UNIVERSITY OF SOUTHAMPTON

Faculty of Physical Science and Engineering
Optoelectronics Research Centre

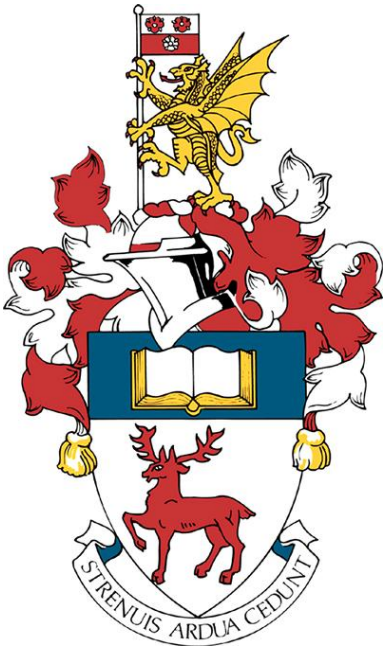

High-Performance and High-Power Applications of Nested Anti-resonant Nodeless Hollow-Core Fibres

by

Viktor Zuba

A thesis for the degree of Doctor of Philosophy

12th March, 2024

University of Southampton

Abstract

Faculty of Physical Science and Engineering
Optoelectronics Research Centre

Doctor of Philosophy

High-Performance and High-Power Applications of Nested Anti-resonant Nodeless Hollow-Core Fibres

by Viktor Zuba

The use of hollow-core fibres (HCFs) for transmitting high-power, high-brightness laser light presents significant advantages over the current standard technology based on solid-core fibres (SCFs). HCFs can deliver much higher optical power levels over longer distances while maintaining a near single-moded beam-quality. This approach has already shown promising results, and this thesis presents important findings on highly efficient coupling and delivery of such laser beams, as well as a relevant application that takes advantage of the hollow core.

The studies conducted in this thesis cover a range of subjects. Initially, the coupling tolerances of an in-house developed, state-of-the-art Nested Antiresonant Nodeless Fibre (NANF) were examined and quantified. This led to the experimental verification of the fundamental limits governing free-space coupling of a near-Gaussian beam into the fibre's fundamental mode. Exploring the opportunity of utilizing high average power lasers, the inevitable thermal load on the optical elements responsible for the input coupling was analysed. The effect of thermal lensing induced by the laser light on the coupling optics led to the degradation of the beam-quality above a certain characteristic threshold (in our experiments ~100 W). The studies showed that using a high-purity lens pair over commercially available alternatives significantly decreased this parasitic effect, resulting in more efficient transmission and reduced thermalisation. Additionally, thermal lensing also modified the input spatial beam distribution, resulting in an increased excitation of unwanted higher order modes. Coupling light into these modes that exhibit greater amount of leakage increases the temperature of the fibre noticeably. A non-invasive technique to extract the excess light not coupled into the fundamental mode was designed and implemented. The decreased thermal load on the fibre coating in turn also reduced the possibility of thermal damage, allowing the further scaling of the coupled optical power.

Based on the findings, coupling efficiency values of ~95 % into NANFs are achieved and maintained at high average powers. This allowed the demonstration of the record delivery of 1 kW average optical power through 1 km of HCF. In addition, the implementation

of the improvements mentioned above allowed an enhanced setup to couple 2 kW of average optical power stably, as well as to deliver it beyond 10 m efficiently. The results achieved in this thesis are limited by the equipment available, and simulations indicate that further scaling in power and transmitted length should be possible.

By combining the efficient methods to couple light into HCFs with the low attenuation offered by NANF technology, the Thesis also examines the optical propulsion of micron sized particles inside the hollow core of such fibres. Initial experiments demonstrate the guidance of 10 µm diameter particles through 1 m of fibre orientable in any spatial direction. By further upscaling the power and fibre length, this preliminary set of experiments indicates the possibility of a remote sensing solution, which can take advantage of the preservation of the high-quality optical beam to trap the microparticles over extended fibre lengths. Furthermore, extrapolations of the measurement results suggest the possibility, in future work, of accelerating such particles beyond 100 m/s in air-filled HCFs.

Contents

Declaration of Authorship

I declare that this thesis and the work presented in it is my own and has been generated by me as the result of my own original research.

I confirm that:

1. This work was done wholly or mainly while in candidature for a research degree at this University;
2. Where any part of this thesis has previously been submitted for a degree or any other qualification at this University or any other institution, this has been clearly stated;
3. Where I have consulted the published work of others, this is always clearly attributed;
4. Where I have quoted from the work of others, the source is always given. With the exception of such quotations, this thesis is entirely my own work;
5. I have acknowledged all main sources of help;
6. Where the thesis is based on work done by myself jointly with others, I have made clear exactly what was done by others and what I have contributed myself;
7. None of this work has been published before submission

Signed:..... Date:.....

1 Introduction

Ever since its first implementation in 1960 [1], systems based on the phenomenon of light amplification by stimulated emission of radiation — or 'lasers' for short — have become one of the most widespread instruments around the globe. Such devices can be found in almost every scientific institute and have undergone tremendous improvements since. They have proved themselves to be indispensable in studies ranging from basic research like detecting gravitational waves [2], to applications in environmental sciences by employing light detection and ranging (LiDAR) [3], laser-based lightning protection [4], or in recent severe acute respiratory syndrome coronavirus (SARS-CoV) related treatment devices [5, 6]. A critical step in most applications is the delivery of laser light into the location of its intended use. As the optical power of the available laser sources are constantly increasing, accordingly, it is becoming progressively more difficult to transmit their output. This Thesis summarizes the steps taken to develop a feasible and reliable way to transmit high-power optical beams beyond km-scale distances through hollow-core fibres, which are emerging as promising solutions.

Historically, the first optical fibre capable of confining and propagating the light from a source to the desired area of work with the advantages mentioned before were the so-called solid core fibres (SCFs). A great summary of the most relevant milestones for the evolution of optical fibre technology is written by Ballato and Dragic [7]. In 1966 Kao and Hockham reported that such optical apparatus can be improved significantly, and envisioned them as next generation alternatives for traditional coaxial-cable and radio systems. For his "groundbreaking achievements concerning the transmission of light in fibres for optical communication", Kao has received the Nobel Prize in Physics in 2009. Using SCF technology is still a common practice nowadays.

However, with the evolution of available laser sources, the fibre technology also had to progress, and so, the concept of hollow-core fibres (HCFs) was proposed, which in theory can withstand the increasing high fluence values. With its first pioneering experimental realization in 1999 [8], these novel fibres make it possible that most of the transmitted power is propagated in air, immensely reducing the limitations set by light-glass interactions.

Confining laser light into a physically isolated domain — i.e. a fibre — have many practical advantages. First of all, the beam path can be altered flexibly, opposed to more complicated free-space solutions, that requires several other optical components, and regular maintenance to preserve stable performance. Secondly, the coupled laser field distribution is essentially conserved during its transmission, shielded from minor

disruptions, e.g. air-turbulence. Furthermore, the technique enables the reliable delivery of high brightness beams over km-scale distances, which is orders of magnitudes larger than the limit set by the Rayleigh-length for free-space optical systems with similar beam diameter. This observation is relevant to several fields, including, but not limited to; telecommunations [9] research [10], military [11], industry [12–14], healthcare [15] or environmental sustainability [16] related applications. Finally, physical constrains imposed by the fibre just as importantly reduces the probably of accidental emission compared to free-space transmission-based approaches.

As a specific example, the laser processing industry is one of the fields, where the combination of maintaining a high beam quality over long distance transmission is valuable [17]. High quality material processing with great precision can only be achieved by using high brightness, single-mode beams. Moreover, delivery fibre lengths of tens or even hundreds of meters allow safer operation and more flexibility. The combination of these two qualities is favourable for applications like high-quality remote welding [18], cutting of carbon fibre reinforced polymers (CFRP) [19], or during the decommission of a nuclear power plant [14, 16, 20], or the prospect of the so-called Power-over-Fibre (PoF) concept [10, 21].

As the main interest of the Thesis, the case of transmitting a continuous wave (CW) beam is considered. In general, there exists an upper limit set by the nonlinearities that can arise in conventional systems employing SCFs. The exact value typically also depends on the fibre core material, more specifically its most relevant parameters — e.g. the Raman and Brillouin gain coefficients. There are several techniques which can ease this limitation (e.g. effective area enlargement), but there is always a trade-off that must be considered (i.e. beam quality or bending loss), even when these improvements are utilized. However, as mentioned, HCFs propose a promising alternative to the more prevalent SCF technology. Figure 1.1 presents some of the greatest milestones in experimental realization of state-of-the-art HCFs.

One of the central objective of the present research is to go beyond the current limitations in power transmission using conventional SCF. Previous results published using these type of fibres — e.g. 1 kW-over-300 m by Matsui et al. [37], 5 kW-over-20 m by Shima et al. [17], 1 kW-over-100 m Rohrer et al. [38], or 9.1 kW-over-30 m Okuda et al. [13] — all argue, that the main limiting factors are determined by the nonlinear effects that starts to emerge near the respective power levels. The goal is not only to transmit greater power values with higher efficiencies, but also to employ orders of magnitude longer lengths of novel fibres. Furthermore a high brightness, near single mode beam quality should be maintained as well. This is due to the fact, that high-quality, high-precision material processing generally requires such high-quality optical beams, respectively. Furthermore, understanding the maximum coupling efficiency (CE) that

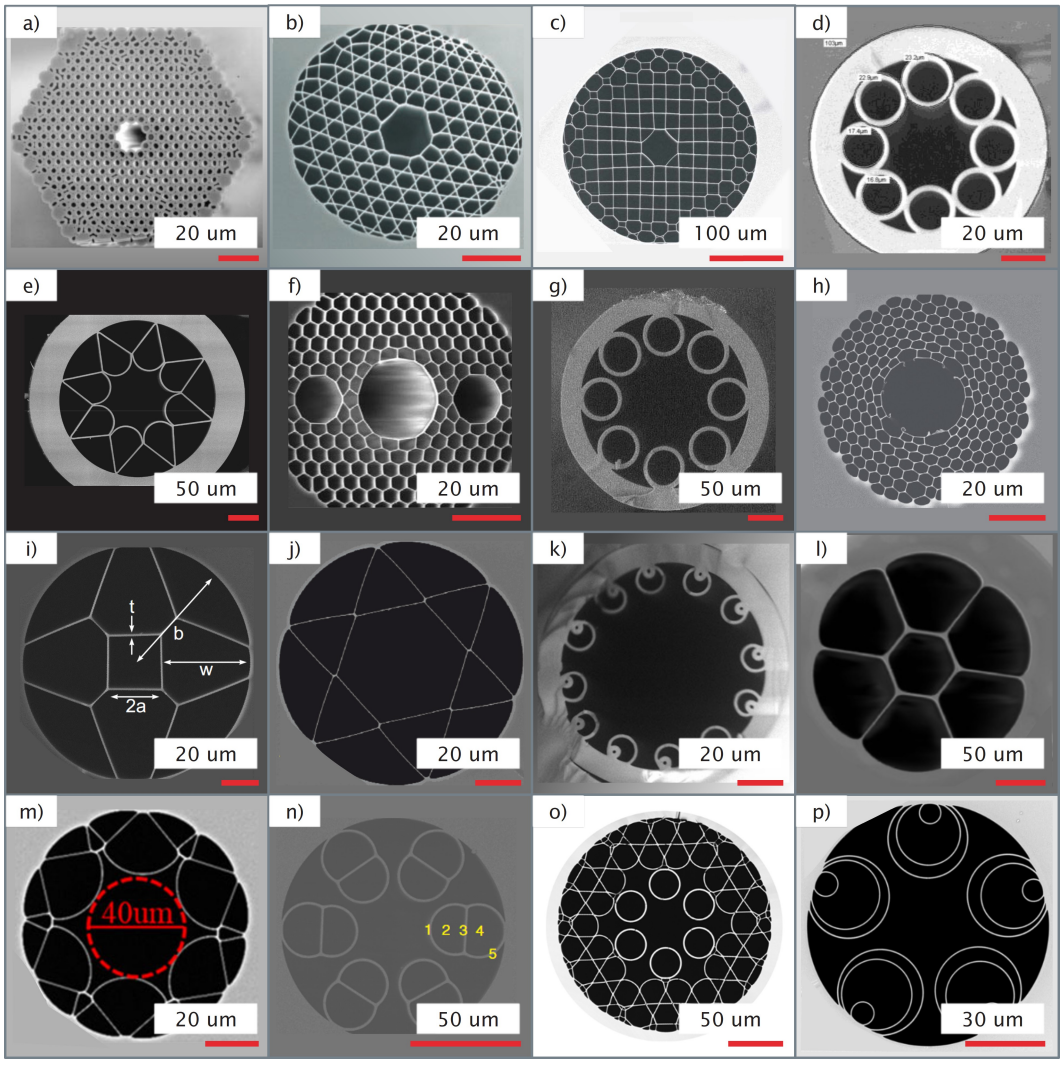

FIGURE 1.1: **Novel HCF Cross sections** | Cross section captures of some of the most impactful milestones results of experimental realizations of novel HCFs: a) First realization of a hollow-core photonic bandgap fibre (HC-PBGF) by Cregan et al. [8], b) First Kagomé fibre drawn by Benabid et al. [22], c) Square lattice Kagomé fibre by Couny et al. [23], d) First Revolver type anti-resonant (AR) HCF by Pryamikov et al. [24], e) Ice-cone shaped structured AR-HCF by Yu et al. [25], f) Polarization maintaining PRISM fibre by Fini et al. [26], g) First non-touching AR-HCF by Kolyadin et al. [27], h) Surface mode free PBGF by Poletti et al. [28], i) Double AR-HCF by Hartung et al. [29], j) Hexagram AR-HCF by Hayes et al. [30], k) First nested anti-resonant nodeless hollow-core fibre (NANF) by Belardi et al. [31], l) Single ring hexagonal HCF by Tsiminis et al. [32], m) Lotus shaped AR-HCF by Nawazuddin et al. [33], n) Pill shaped conjoined-tube negative curvature HCF by Gao et al. [34], o) Hybrid-lattice hollow-core photonic-crystal fibre by Amrani et al. [35], p) First demonstration of a HCF with lower loss values as SCFs: the double nested anti-resonant nodeless fibre (DNANF), by Jasion et al. [36]. Reference scales in red depicting the respective dimensions are also shown for each cross section. Note the great variation of core diameters.

one can achieve when launching light into an HCF from a free space laser beam is essential in all these studies. Since such analysis is scarcely reported, a dedicated Chapter will be provided for related investigations.

To give an example of the intensity range that will be discussed in the Thesis; fibre lasers are routinely capable of providing >1 kW of average input power in CW mode of operation, around the central wavelength of $\lambda_0 \approx 1075\,\mathrm{nm}$. In order to couple this field into an optical fibre, it has to be focused into a spot with a beamwaist of $w_0 \approx 15\,\mu\mathrm{m}$ — a common value assuming that a HCF is utilized. This translates to an average flux density of $I \approx 1.5 \times 10^{12}\,\mathrm{W/m^2}$, which is comparable to those present at the focal point for laser material processing applications. Assuming a Gaussian approximation, the Rayleigh length is given by the relation $z_R = \left(\pi \cdot w_0^2\right)/\lambda_0 \approx 0.6\,\mathrm{mm}$. This is over 6 orders of magnitude less than a typical HCF drawn in-house, in which the same beam waist can be maintained over kilometre length scales. More importantly, SCFs are generally unable to preserve a coupled beam of similar average power, over comparable distances, because of the aforementioned nonlinearities. Additionally, an estimation of the scalability of the technology will be discussed.

Lastly, in combination with the work of other researchers, possible applications based on the gathered findings will be also discussed. In the final part of the Thesis, stimulated by an observation during high power experiments, we extended our interest to the possibility of delivering micron sized particles through HCFs. This capacity has the potential to unique devices, such as a long-distance remote sensor [39] — just to name one example.

Outline of the thesis

The thesis is structured as follows:

- In Chapter 2, the basic theoretical background of both solid- and hollow-core optical fibres, including optical modes, different guiding mechanisms, main loss sources and non-linear effects are discussed. The optical forces acting on micron sized particles in a tightly focused beam, and the basic principles of optical trapping are also introduced.

- Chapter 3 reports findings regarding the highest possible coupling efficiency of laser light experimentally achievable into in-house drawn NANFs. After the mathematical definition of CE given, based on prior simulations, an experimental setup has been designed and built, to verify the assumptions suggested by the theories. Measurements conducted show great agreement with expectations. Furthermore, the requirements of precise alignment and positioning of the optical fibre — along both the translational and angular axes— for maximum CE are also examined. Finally, a comparison with similar HCFs of different kinds is also made.

- The specific case of delivering over kW level of average power is discussed in Chapter 4. Both the physical and virtual version of the experimental setup — i.e. a digital twin — are introduced. Evaluation of the measured and simulated data will highlight the current limitations of the layout. Based on this insight, experimental techniques to reduce these (essentially absorption related) bottlenecks are suggested and realized. The influence and improvement thanks to these steps taken to ease these restraints are demonstrated, and best-effort results — limited only by the equipment available — are presented. Lastly, multiple directions for further work are proposed.
- Chapter 5 introduces a distinctively unique opportunity; the possibility of delivering micron-sized particles through HCFs. In contrast to the more industrial, application focused research discussed in the previous Chapter, here a more fundamental analysis of a growing field of interest will be conducted. Starting from the first observation of phenomenon, an individual experimental setup design is introduced in detail. Initial results are presented, highlighting the capabilities and limitations of the currently employed layout, showing encouraging results. The Chapter is concluded with discussions about future applications of the system.
- Finally, Chapter 6 concludes the Thesis by summarizing the results discussed, as well as providing a brief outlook on possible future work.

2 Theoretical Background

In this Chapter, the theoretical foundation relevant to the Thesis is summarized and the most widely used terminology is established. To begin with, the most important concepts and definitions are introduced through the example of solid-core fibres (SCFs), including the derivation of optical modes. This is followed by a brief description of the non-linear phenomenon, that can be observed when high power optical fields are confined in such fibres. As a potential solution to avoid these (for the scope of present Thesis) unwanted effects, different kind of hollow-core fibres (HCFs), utilizing distinct guiding mechanisms are presented. Practical analogies with their SCF counterparts are drawn, their performances are compared, and newly enabled applications are also mentioned. Next, the main characteristic loss mechanisms are categorized, and the interfacing of the fundamentally different optical fibres is reviewed. Finally, the optical forces acting on micron sized particles that can be optically propelled inside the hollow core of the fibres are described.

2.1 Solid-core fibres

Although the focus of this Thesis is to demonstrate novel applications of the hollow-core fibre (HCF) technology, for historical reasons many practically used definitions have analogues derived from those used for describing solid-core fibres (SCFs). For this reason, it is sensible to introduce these concepts through the simpler example of SCFs. However, only a brief summary is provided here, since there already exist several great sources dedicated to discussing said fibre type; Prof. Govind P. Agrawal's *Nonlinear Fibre Optics* is provided here as an example [40].

In its simplest configuration, a SCF refers to the common step index fibre depicted in Figure 2.1 a). In this case, the fibre consists of an optically denser, axisymmetric material is covered with another material, which has a smaller real refractive index value. According to Snell's law:

$$n_1 \cdot sin\theta_1 = n_2 \cdot sin\theta_2, \tag{2.1}$$

where n_i is the refractive index, and θ_i is the angle of incidence of the optical ray in the material, indexed with $i = 1, 2$. Assigning $i = 1$ for the core, and $i = 2$ the surrounding cladding, the light cannot escape into the cladding, if the incident angle at the surface border is above a given threshold. This phenomenon is called as index-guiding, and the exact value of the critical angle is given by:

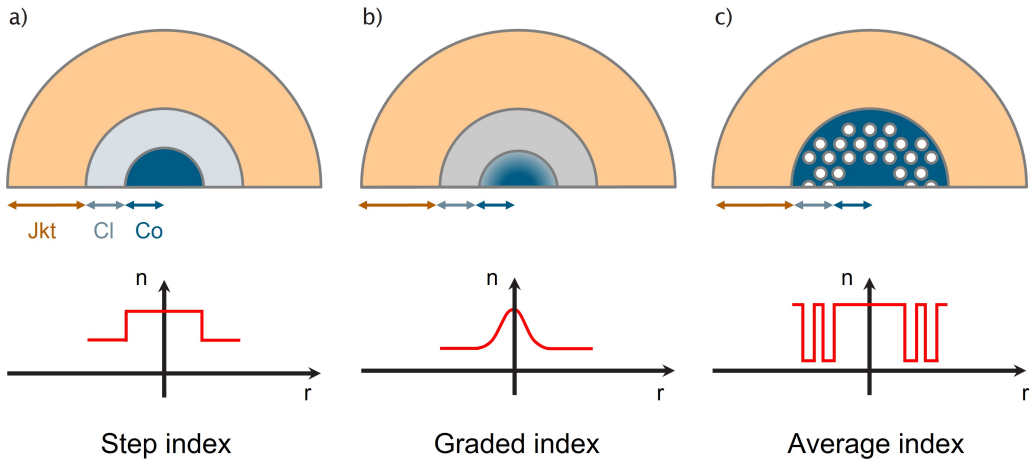

FIGURE 2.1: **Most common solid-core fibre cross sections schematics** | a) step index, b) graded index, and c) average index guiding solid core fibres. The core (Co), cladding (Cl) and Jacket (Jkt) regions are marked and labelled for the simplest structure. For the other geometries, the corresponding counterparts are marked with the respective arrows as well. On the bottom row graphs, the refractive index as a function of the radial coordinate is also illustrated.

$$\theta_{\text{crit}} = sin^{-1}\left(\frac{n_{\text{clad}}}{n_{\text{core}}}\right). \tag{2.2}$$

Usually a third layer (coating or jacket) is also deposited, which generally does not interact with the coupled light, but provides mechanical support and protection.

However, Equation 2.2 is only true, if the relation $n_2/n_1<1$ holds, that is, if the material of the fibre core is considered optically denser — and even more precisely only for multimoded guidance. From this θ_{crit} critical angle, the ϕ_{max} maximum acceptance angle of a fibre can be calculated. Assuming a right-angled fibre tip, and n_{env} refractive index for the environment around the fibre, it is given by:

$$\phi_{\text{max}} = sin^{-1}\left[\frac{n_{\text{core}}}{n_{\text{env}}} \cdot sin\left(90° - \theta_{\text{crit}}\right)\right], \tag{2.3}$$

In this arrangement,the considered fibre can only accept or release rays with angles respective to the axis of symmetry below this threshold. Another widely used figure of merit, the numerical aperture (NA) is also defined based on this maximal angle via:

$$\text{NA} = n_{\text{env}} \cdot sin\left(\phi_{\text{max}}\right) = \sqrt{n_{\text{core}}^2 - n_{\text{clad}}^2} \tag{2.4}$$

From a practical point of view NA a dimensionless value, which makes it an ideal point of comparison for certain aspect of different types of fibres. This is even more convenient in cases when fibres with more complex geometries are considered. One significant advantage of engineering a more sophisticated cross section is that it allows certain

aspects of the fibre to be enhanced, and in turn, can also open new possibilities for applications. As an example, a parabolic refractive index distribution in the radial direction of the fibre — schematically illustrated in Figure 2.1 b) — is also achievable. This profile constantly refocuses the coupled light, which helps minimising the modal dispersion, that is beneficial for instance in telecommunications [41].

Furthermore, it is also possible to fabricate fibres with fine structures, also called microstructured optical fibres or MOFs for short. Figure 2.1 c) shows a common example of this category. In this instance, the cladding is defined by the domain including the air holes around the central core region. In this scenario, for a more accurate physical description, the parameters of cladding structure should be approximated by average, or "effective" values; for instance, in Equation 2.4, n_{clad} should be substituted with $n_{\text{clad, eff}}$ and similarly, all following relations will depend on $n_{\text{clad, eff}}$ instead. Due to the presence of the holes, the average refractive index in the cladding is lower than that of the core. Because of that, this type of fibres practically behaves like step-index fibres, however, the main guiding mechanism in this case is called effective index guidance. Such a fibre was proposed and first realised in 1996 by the Russell group [42] and was an important step towards micro structured hollow-core fibres. The significance of fabricating such an optical fibre will be detailed in Section 2.3.

Note that so far, all the parameters introduced are only strictly valid for what is called multimoded guidance, and for a more refined description, wave guidance must be considered. It is therefore important to explicitly define what an optical mode is.

2.2 Optical modes and the V-number

2.2.1 Core modes

The general distribution of the electric field can be given as:

$$\mathbf{E}\left(\vec{r},\tau\right) = A\left(\vec{r}\right)\cdot e^{-i\omega\tau}\cdot e^{-i\Phi_0}. \tag{2.5}$$

Here, the electric field vector $\mathbf{E}$ is represented by a plane wave, where $\omega = 2\pi c/\lambda$ is the angular frequency of the optical field with wavelength λ, c is the speed of light in vacuum, while $\vec{r}$ and τ denotes the spatial and temporal coordinates, and A and Φ_0 are the amplitude and an initial phase, respectively. Deriving from the Maxwell-equations, it can be shown that — in non-magnetic materials within linear approximation — the electric field vector must satisfy the Helmholtz equation:

$$\nabla^2\mathbf{E} + n^2\left(\omega\right)k^2\mathbf{E} = 0, \tag{2.6}$$

where $k = 2\pi/\lambda$ is the wavenumber, and n denotes the refractive index of the light propagating medium. For every wavelength, there exists a finite number of self-consistent modes, which are confined and guided along the length of a fibre. These discrete modes can be categorized into core or cladding modes — depending on which part of the fibre geometry they are guided — they have a unique, well-defined spatial distribution, and satisfy equation 2.6. Complementing them are a continuum of radiation modes, which are not confined in the fibre. While plane waves are the simplest and one of the most useful mathematical approximations, because of their infinite transverse dimension, they cannot describe real optical fields.

The discrete modes guided in the core of the fibre can be denoted in general as $|\psi_j\rangle$, where the subscript j labels the distinct mode considered. Without any loss of generality, while also including the $\mathbf{H}$ magnetic field vector, assuming the direction of propagation as $\vec{z}$, such modes satisfy the relation of orthonormality [43]:

$$\iint \vec{z} \cdot \left(\mathbf{E}_j^* \times \mathbf{H}_{j'} + \mathbf{E}_{j'} \times \mathbf{H}_j^* \right) dA = \delta_{j,j'}, \tag{2.7}$$

where $\delta_{j,j'}$ denotes the Kronecker delta. Moreover, $\mathbf{E}_j$ and $\mathbf{H}_j$ express the electric and magnetic field distributions of the mode $|\psi_j\rangle$, respectively, such that:

$$|\psi_j\rangle = \begin{pmatrix} \mathbf{E}_j \\ \mathbf{H}_j \end{pmatrix} \cdot e^{-i\beta_j z}, \tag{2.8}$$

where β_j is the propagation constant of the j-th mode.

Within a more explicit framework, the previously discussed $|\psi_j\rangle$ modes are vector modes strictly speaking, and are leaky in nature. For the sake of simplicity, however, it is feasible to transition to the corresponding scalar mode terminology. In this approach, the previously introduced transverse vector modes (e.g. the pair of the fundamental HE_{11} modes) can be categorized into scalar groups, which gather the original vector modes of similar intensity, but different polarization distribution (e.g. LP_{01}, respectively) [44].

Figure 2.2 shows a schematic plot of the fundamental and the first few higher order linearly polarized (LP) core modes. They can be easily derived from the wave equation of an electric field similar to Equation 2.6. By utilizing a cylindrical coordinate system and applying constrain equations arising from the symmetry of the field, a set of equations, called Bessel functions can properly describe the set of modes guided by a simple step index fibre. Separating $\mathbf{E}$ into translational and longitudinal components (which also matches with the cylindrical axes), an analogy to the prior properties can be made. The longitudinal distribution is constant along the fibre throughout the propagation, while — in a lossless approximation — the phase of the plane wave evolves following $e^{-i\beta_j z}$.

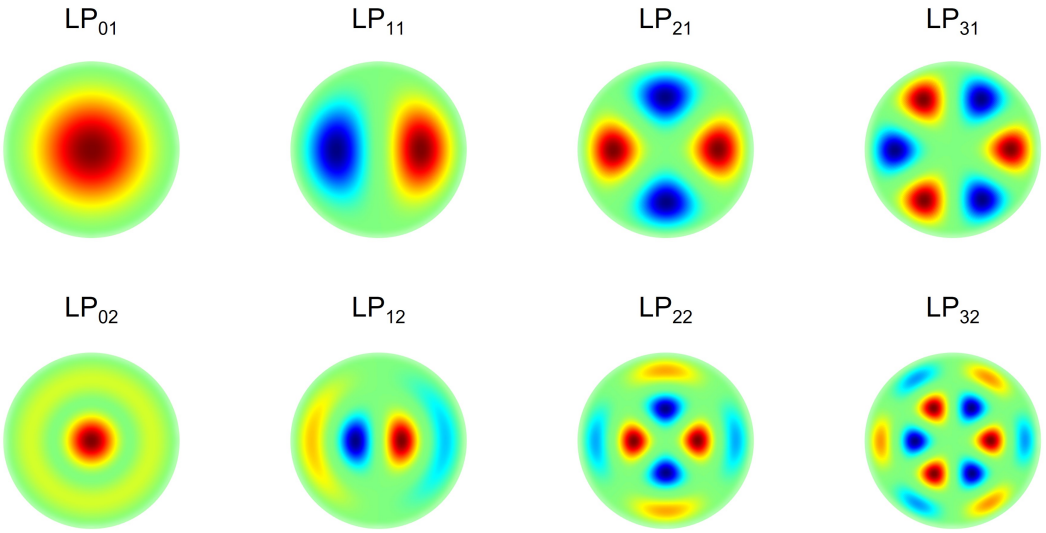

FIGURE 2.2: **Schematic illustrations of the first few LP core modes** | The different signs of the electric field are highlighted with blue and red. Note that for all modes there exist 2 orthogonal polarization states.

The V-number

The number of supported modes can be practically described for step-index fibres by introducing the so-called V-number:

$$V = \frac{2\pi}{\lambda} \cdot r_{\text{core}} \cdot \text{NA} \tag{2.9}$$

where r_{core} is the core radius. For a step-index fibre, this V-number must be under ~2.405 for it to be considered single-mode [45], that is the fibre only supports its fundamental mode (FM). From equation 2.9 it can be also seen that for any given λ wavelength, this can be achieved by carefully engineering the r_{core} core diameter and the NA of the fibre. The greater the V-number, the more higher-order modes (HOMs) the fibre can efficiently confine. For large values, the number of supported modes (including the different polarization states) can be estimated by $N_{\text{modes}} \approx V^2/2$.

Multi-modality is an important feature, that has to be considered and evaluated on a case-by-case basis. The choice to employ single- or multi-mode fibres (SMF and MMF, respectively) generally depends on the specific application, its requirements and tolerances, and usually includes inevitable trade-offs to be made. It is also worth noting, that each mode has their own characteristic parameters — e.g. attenuation or group velocity. Furthermore, coupling light from one mode to the other (cross-modal interaction) is possible, given the appropriate matching conditions (i.e. phase-matching) are met.

SMFs can in general have lower attenuation values, as they can be highly optimized for a given wavelength. This precision, however, also limits the bandwidth of the wavelengths the fibre can support. From Equation 2.9, it can be also expected that the core radius of such fibres are also typically smaller (r_{core} ~few µm's). Clearly, the lack of HOMs

also makes any modal crosstalk impossible, and since only the FM of the fibre can guide light efficiently, the output beam distribution is independent on the input beam quality. From a practical point of view, the alignment of these fibres are more difficult, as better precision is required for efficient coupling, which in turn also means higher sensitivity to environmental disturbances. Lastly, the necessarily more intricate manufacturing process that is required, can usually result in an increase in production costs.

MMFs on the other hand can more efficiently propagate beams with poor beam quality, and can tolerate higher optical power levels. This is mainly thanks to their generally larger core diameters — as can be anticipated from Equation 2.9. They also guarantee more robust guidance (e.g. less sensitivity to bending), but generally have higher attenuation, as the fibre cannot be engineered and optimized for all supported modes simultaneously. Moreover, modal cross-talk is common, and interference of the different modes can change the local beam distribution significantly along the length of the fibre. While launching light into MMFs are practically easier, the previous point also means, that the output beam quality highly depends on the input beam distribution, and the less intricate manufacturing requirements also allows the fibres to be less expensive.

2.2.2 Cladding modes

So far only guided modes in the core region were discussed. However, when specific conditions are met (i.e. phase-matching), the cladding can also support optical modes (or radiation modes) that can propagate along the fibre. These modes usually have orders of magnitude higher loss values than those of the core, and their exact "shape" are also unique to their cross-section geometry. Cladding modes will become more relevant during the discussions about the hollow-core fibres, for which the cladding region is usually defined by a characteristic microstructure, and such, more detail will be provided there.

2.2.3 Gaussian beam

Another practical model to introduce is the concept of a Gaussian beam, named after German mathematician and physicist Johann Carl Friedrich Gauß. Assuming free-space propagation, the transverse intensity profile of the beam in this case is defined by the Gaussian distribution as:

$$I(r,z) = \frac{P}{\pi \cdot w(z)^2 / 2} \cdot exp\left(-2\frac{r^2}{w(z)^2}\right), \tag{2.10}$$

for a beam travelling in the z direction. Here P is the optical power of the beam, while $w(z)$ is called the beam radius, and denotes the distance from the z-axis, at which the intensity drops to $1/e^2 \approx 13.5\,\%$ of its maximum.

Note that the polarization properties, as well as the transverse phase profile of the distribution is omitted here. Rigorously speaking, Gaussian-like beams of similar intensity-profile, but with a phase distribution that is more complex than what can be reasonably described using a second-order polynomial function is not considered to be a Gaussian beam. The main advantage of using this terminology is that it is a practically applicable approximation to describe the fundamental fibre mode in a mathematically more simplistic way [40].

Within the limits of the paraxial approximation, that is the ϕ angle of convergence is small enough that $\tan\phi \approx \sin\phi \approx \phi$ is a reasonable estimation — i.e. the beam is not focused really strongly — the evolution of the beam radius $w(z)$ along the z-axis can be described simply by

$$w(z) = w_0\sqrt{1 + (z/z_R)^2}, \tag{2.11}$$

where z_R is the Rayleigh length, defined as:

$$z_R = \frac{\pi w_0^2}{\lambda}. \tag{2.12}$$

Moreover, w_0 is the beam waist, that is the minimum value of the beam radius. From Equation 2.11, it can be easily seen that this minimum is obtained at the location $z = 0$, which is called the focus. In fibre optics, it is generally favourable to focus the beam such that the double of this beam waist equals to the mode field diameter (MFD $= 2w_0$) supported by the FM of the optical fibre to be used, as in that case, the maximum coupling efficiency is attainable. This will be discussed in more detail in a later Section. Note that while its impact is not analysed explicitly here, the focusing conditions — i.e. the ϕ angle of convergence, and the related NA (through 2.4) — are also crucial.

Finally, the beam quality is generally quantified using an ISO standard [46], which is based on the Gaussian beam terminology. It is called the M^2 value, or beam quality factor, following the definition of:

$$\phi = M^2\frac{\lambda}{\pi w_0}. \tag{2.13}$$

The relation $M^2 \geq 1$ must always hold true, with the equality $M^2 = 1$ describing the case of a perfect Gaussian beam. In reality, M^2 is generally >1, but the smaller the difference, the closer the beam is considered to be a high-quality fundamental beam — i.e. similar intensity distribution to that of LP_{01}. It is worth noting though, that the M^2 value is a single scalar number, and such cannot accurately describe the beam quality itself. However, because it is a practically useful figure of merit, it has found a widespread use in the field of laser beams. For the sake of simplicity — while still maintaining

explicitness — in the following, optical beams with beam qualities of $M^2 < 1.2$ will be generally referred to be quasi-single-moded (QSM) beams.

Nevertheless, even for the highest quality of beams, the fundamental limitation on the performance of SCFs is set by their constituting material(s) — mainly that of the core. As an example, the physical properties of silica glass (SiO_2) — which is arguably the most common material for commercial optical fibres — ultimately limit the minimum theoretical loss value achievable [47]. This in turn restricts the maximum power levels that can be coupled into SCFs before material breakdown damage can happen. The desire to overcome these restrictions is one of the main incentives for hollow-core fibre related research.

2.3 Hollow-core fibres

It has been remarked earlier in Section 2.2, SMFs tends to have small core sizes. This means, that through the fluence of the focused beam at the input facet of the fibre, the damage threshold of the core material ultimately sets the power limit that a fibre can handle. An obvious suggestion to eliminate this upper bound is to remove any material from the core. However, if one wants to confine a significant electromagnetic field inside what can be called hollow-core fibre, then a new approach for guidance is necessary. Confinement based on total internal reflection can only be applicable for highly multimoded fibres, because when the core diameter becomes small enough to be comparable to the used wavelength ~10λ, the contribution from phenomena like interference become even more significant.

Probably the most straightforward approach is to simply have a hollow tube or capillary covered with a reflective coating on its inner surface, so that light is guided by external reflection [48]. These hollow waveguides, however, generally have significant losses due to each Fresnel reflection instead of total internal reflection. Even with very high reflectance, a large core area (100s of the used wavelength) is required in order to reduce the loss values below a reasonable level, which ultimately leads to multimodal transmission. From a more practical perspective, the handling of such fibres with regards to bend sensitivity and splicing possibilities are also inconvenient.

While the very simple capillary structure found a low number of applications, the model itself, on the other hand, is a very good aid to understand the more complex, microstructured optical fibres. For the points to be discussed in the Thesis, the most important fibre types are the hollow-core photonic bandgap fibres (HC-PBGFs), the antiresonant fibres (ARFs) in general, and a subgroup of the latter: the nested antiresonant nodeless fibres (NANFs). The following Subsections aim to give a brief overview of the guiding mechanisms of these fibres mentioned.

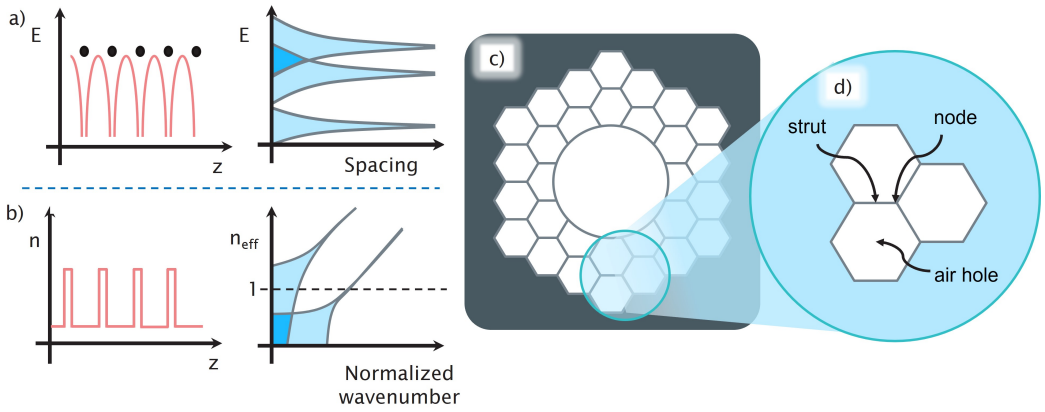

FIGURE 2.3: **Visual aid for photonic bandgap hollow-core fibres** | a) Typical schematic illustration of a solid state physics bandgap structure b) Analogous refractive index structure for PBGFs with the air-line depicted by the black dashed line at $n_{eff} = 1$. (Adopted from [50]) c) Schematic cross section of a typical microstructured photonic bandgap fibre, with d) introducing the used terminology for the specific parts of the cladding structure

2.3.1 Guidance using photonic bandgaps

The first hollow-core fibre with a micro-structured cladding consisting of an array of air holes was realised in 1999 [8]. This fibre only confined a specific wavelength range, corresponding to the photonic band gaps originating from the periodic cladding structure. The group of fibres received their name from said phenomenon; the photonic bandgap [49]. An exhaustive and remarkably detailed article about photonic bandgap fibres (PBGFs) is summarized by Benabid and Roberts [50].

A greatly simplified description of its guiding mechanism can be derived from a solid-state physics analogy. Assuming a perfect, periodic crystal lattice, the allowed potential states are well defined. Based on these exact states, there are several forbidden bands, which consists of a continuum of forbidden electronic states, as depicted schematically in Figure 2.3 a). Based on this electric band structure, both the allowed and the forbidden photon frequencies can be calculated. Approaching the problem from the opposite direction, it can also be shown that a periodic structure can be engineered, such that there exists a given domain of forbidden states, in which no photon is allowed, as illustrated in Figure 2.3 b). Fabricating a HCF with a cladding structure of such a photonic bandgap, the electromagnetic field within the given wavelength range would be confined inside the core.

Another important condition is that the ratio between the transverse components of the wave vectors for both media must satisfy the relation $k_{\mathrm{tr},\,1}/k_{\mathrm{tr},\,2} > \rho_{\mathrm{crit}}$ between the k wavenumbers. The index tr represents the transverse component of the vector, while the indices 1 and 2 denotes that the values are given by the materials of the glass and the air respectively. The exact critical value ρ_{crit} of the ratio can differ greatly based on the specific fibre geometry, but in general it translates to large refractive index differences.

Assuming that only in-plane propagation is allowed in the transverse plane, available materials would be greatly limited. However, when out-of-plane propagation is considered, HC-PBGFs can be manufactured from standard glasses [8], bypassing the strict condition about wavenumbers mentioned. This is justified by the fact that dominant direction for propagation is orthogonal to this transverse plane. A typical cross section for this type of fibres is depicted in Figure 2.3 c).

Through extensive research and characterisation experiments many important features of the PBGFs were pinpointed, and eventually clarified by theoretical descriptions. First of all, as mentioned earlier, stable cladding modes can be excited and guided along the length of the fibre. These can be classified into 3 different groups in a typical geometry, like the one in Figure 2.3 c); i) the airholes inside the cladding structure, ii) the struts, building up the structure, and iii) the nodes, where said struts connect to each other. These are also labelled in Figure 2.3 d). Based on simulations, it was suggested and later experimentally confirmed, that the most dominant contributor of the cladding modes are those confined in the connecting nodes [50].

To minimize the interplay between the core and cladding modes, substantial effort was made to fabricate more sophisticated optical fibres. This resulted in even more complex cladding structures, which in turn made the fabrication processes more intricate. Nevertheless, the aspiration also led to characterization of the intricate effect of resonance-conditions on fibre attenuation [51]. While the approach was successful in the sense that it presented the lowest attenuation achieved in any PBGFs, the thicker membrane allowing the manipulation of resonance conditions also lead to reduced transmission bandwidth of the fibre. Subsequently, novel fibres were designed with the intention of using the phenomenon of resonance as the main guiding mechanism, in order to fabricate HCFs with even lower propagation losses.

2.3.2 Guidance by anti-resonance and inhibited coupling

One specific geometry discovered during the progression of fibre cross section optimisation was the so-called Kagomé-lattice [22]. These fibres can be distinguished from the PBGF cross sections presented previously in Subsection 2.3.1, by the distinct cladding structure. In this case a “David-star”-like pattern, with smaller triangular airgaps between the hexagonal ones can be noticed, as depicted in Figure 2.4 a). The final structure shows resemblance with a traditional Japanese basket weaving pattern; hence the name was coined.

It has been reported, that even though for the Kagomé-fibres the core and cladding modes co-exists — similarly to PBGFs — there is only minimal interaction between these fields. While these fibres were initially believed to be using the same guiding mechanism as the PBGFs, it was later demonstrated that they have no bandgap structure [52]. It has been proven that another phenomenon is responsible for achieving guidance: the wavenumbers of the core and cladding modes also shown to have a mismatch, putting

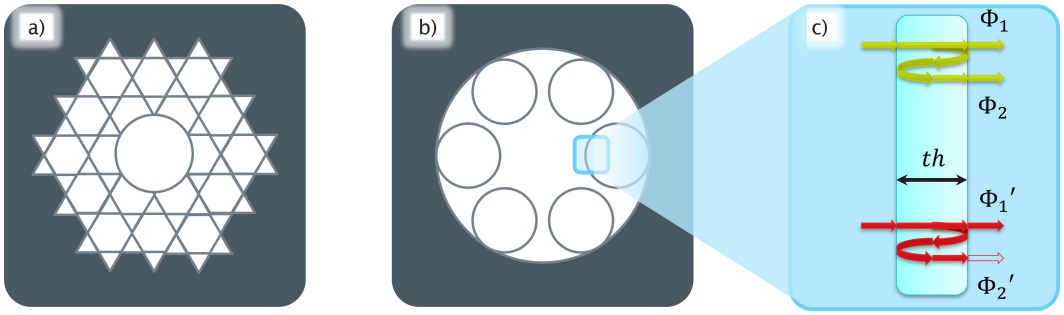

FIGURE 2.4: **Kagomé and Revolver-type anti-resonant hollow core fibre schematics** | Typical a) Kagomé, and b) Revolver type HCF microstructures. c) illustrates the phase relations required to be satisfying the resonance conditions. For a cladding structure with th thickness, a certain λ_R wavelength (plotted with green, top half) might interfere with its twice reflected replica constructively, satisfying Equation 2.14, or destructively (λ_{AR} plotted with red, bottom half) satisfying Equation 2.15

further restrictions on how much the modes can interact. The combined phenomenon of both the reduction of the modal overlap and a wavenumber mismatch is also referred to as inhibited coupling (IC) [23, 53]. Utilizing this design approach resulted in a waveguide, which allowed a broader transmission window bandwidth.

Ultimately, it had been theorized and consequently experimentally verified that the surface of the innermost cladding interface, closest to the core can have a significant impact on the transmission performance of such fibres. Having a negative curvature — that is an inverted curvature of the core surround — is preferred as such fibres have been observed to have an attenuation almost an order of magnitude lower compared to the more conventional circular core [54]. Nevertheless, it has been also concluded that the dominant limiting factor of low loss, highly efficient transmission is still the strong coupling between core and cladding modes — which is localized in the silica struts. Therefore, in order to further enhance the performance of HCFs, the nodes and struts supporting such cladding modes have been avoided. With the intention of eliminating these coupling sources, a simplified cladding structure has been proposed, that transformed the field of HCF fabrication technology.

The previously mentioned phenomenon of anti-resonance in Subsection 2.3.1 was used as the foundation of guidance for the so-called anti-resonant fibres (ARFs). A typical cross section of the one of the simplest geometries, also called tubular or revolver fibres (RVF) is shown in Figure 2.4 b). For this type of fibre, the hollow-core is surrounded by thin tubes made of a material with refractive index n_{glass} and thickness of th. Depending on the thickness, well defined wavelengths exist at which the fundamental transmitted and the twice reflected transmitted fields will be in resonance. This guiding mechanism is based on the phenomenon used in anti-resonant reflecting optical waveguides (ARROW) [55]. Using the same notations as in of 2.4 c), this is true for a slab waveguide approach depicted in the inset, if $\Delta\Phi_{\text{Res}} = \Phi_1 - \Phi_2 = 2m\pi$, where $m \in \mathbb{Z}$.

This accumulated phase difference depends on the material properties of the glass through the relation $\Delta\Phi(\lambda) = n_{\text{glass}} \cdot 2\pi/\lambda \cdot th$. Subsequently, the resonant wavelengths are then given by:

$$\lambda_{\text{Res, m}} = \frac{2 \cdot th}{m} \cdot \sqrt{\left(n_{\text{glass}}^2 - n_{\text{air}}^2\right)}. \tag{2.14}$$

The maximum achievable transmission is at the resonant wavelengths. This can be interpreted as the wavelengths considered will not be confined inside the core, but are essentially transmitted into the cladding. The other extremity can be defined from the same approach. In this case, however, the antiresonance condition is met if, $\Delta\Phi'_{\text{ARes}} = \Phi'_1 - \Phi'_2 = (2m-1)\,\pi$. The wavelengths at which the material theoretically does not transmit is given by:

$$\lambda_{\text{ARes, m}} = \frac{4 \cdot th}{2m-1} \cdot \sqrt{\left(n_{\text{glass}}^2 - n_{\text{air}}^2\right)}. \tag{2.15}$$

For every wavelength apart from λ_{Res} and λ_{ARes}, the leakage from the central domain can also be determined based on the value of $\Delta\Phi(\lambda)$. In general, the domains ranging between the neighbouring $\lambda_{\text{Res, m}}$ wavelengths can have low enough loss characteristics to be used for high bandwidth confinement. Moreover, since there are multiple numbers of these wavelength windows, the number of possibly usable wavelengths with these types of fibres are also greatly increased.

Note that during the discussions above, the term 'transmission' has been used for the interaction between the laser light and glass material forming the microstructure, and *not* the transmission of the optical fibre itself. On the other hand, while the anti-resonant wavelength is guaranteed to have minimal penetration into the region surrounding the core, other effects also must be considered for fabricating ultra-low-loss fibres. Electromagnetic field leaking into the cladding structure can still produce stable cladding modes. By itself, low overlap of the core and cladding modes is not a sufficient condition for efficient transmission.

2.3.3 Modal content of HCFs

Naturally, a similar argument can be discussed here regarding HCFs, as it has been detailed in the prior Section for SCFs. For this reason, it is practical to formulate an analogy between the 2 cases in order to examine the optical modes. Note that as mentioned earlier, the core modes supported by all the previously discussed HCFs are considered 'leaky modes', and intermodal coupling can take place if they are not accounted for properly during the fibre designing process. Furthermore, for the case of microstructured RVF-type ARFs (and by extension NANFs), the cladding modes can become more influential, as the self-similarity of the microstructure and bandgap/antiresonance conditions enable the forming of stable cladding modes [56]. Therefore,

engineering fibres in a way that effectively reduces the modal coupling by employing the concept of inhibited coupling, can have far reaching influence.

Similarly, higher-order core modes can be also supported by HCFs granted that the microstructure enables it. One of the key parameters to be mindful of is the characteristic attenuation of the different optical modes. When maintaining a high-brightness beam is desirable, SM guidance is generally achieved by engineering the HCF in a way that the HOMs have significantly larger attenuation. This results in the fibre effectively acting as a quasi-modefilter after some characteristic length. The efficiency of this filtering can be characterised by the higher order mode extinction ratio (HOMER), which is the ratio between the HOM of the lowest attenuation and that of the FM, as given by: HOMER $= \alpha_{\text{HOM, min}}/\alpha_{\text{FM}}$. The higher the HOMER value, the more similar the fibre performs to that of a truly single-moded SCF. From an experimentalist perspective, paying extra attention to precisely excite only the FM supported by the fibre considered, can also help to achieve better single-moded performance. This is due to the fact that if less HOMs are coupled initially, the total propagation loss of the fibre is also reduced.

For the findings to be discussed in the following Chapters, single-moded guidance will be given priority. The results to be presented will be most beneficial for applications requiring high-brightness beam profiles (e.g. precision manufacturing). However, it is also important to note, that understanding the behaviour of both cladding modes [56] and higher-order core modes [57] can be highly profitable in achieving even better single-mode performance. In the following Subsection a number of approaches using simulation tools as means to provide insight into better FM confinement will be provided.

2.3.4 ARF Simulations

There exists a wide array of literature of simulations regarding how the optimization of different geometrical parameters of ARFs can enhance their performance in one or more aspect, based on the desired application. Setting a typical revolver type fibre cross section as a point of comparison, numerous approaches have been proposed; Figure 2.5 summarizes some of the most recent designs. As it can be seen from the schematic illustrations, there is a wide array of suggestions for improved performance. Hu and Schülzgen [58] used reinforced learning to suggest cross sections optimized for minimal confinement loss — parts d) and e) — Zheng et al. [59] introduced an U-shaped element into the RVF — part f) — to achieve higher HOMER values, and wider operational wavelength, while the structure proposed by Wang and Chang [60] also suggest excellent bending tolerances — part h) — to give a few examples.

However, one would expect that some of these cross sections could be really challenging to fabricate. Considering the case of 2.5 d), realizing a HCF with a microstructure consisting of such unique curves, bends and sharp corners at the touching points is not trivial. Furthermore, the geometry is also expected to be unchanging for the length

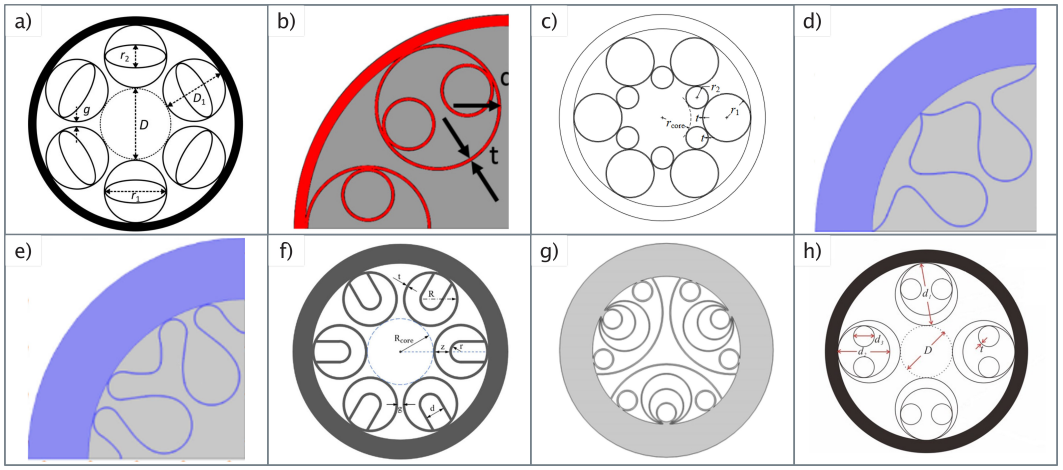

FIGURE 2.5: **Next generation ARF cross section simulations** | Some of the most recently proposed directions of improving the performance of ARFs. a) Positive-negative curvature nested ARF by Hasan et al. [61], b) Antiresonant Leakage Inhibited Fibre (ALIF) by Jasion et al. [62], c) Double negative curvature ARF by Chen et al. [63], d)-e) Reinforced learning based negative curvature designs by Hu and Schülzgen [58], f) U-shaped ARF by Zheng et al [59], g) Triangular ARF by Zhu et al [64], h) Dual-tube Dual nested atiresonant nodeless fibre (DT-DNANF) by Wang and Chang [60].

of the fibre sample. For these reasons, it is beneficial to briefly consider the current capabilities of fibre manufacturing facilities.

2.3.5 Fabrication techniques

While it has been mentioned before repeatedly, how the desired cross section of HCFs can be achieved with careful engineering, little detail has been provided about how these fibres are actually manufactured. In general, the most common way to fabricate HCFs is the so-called "stack-and-draw" technique [49, 65]. In essence, this method involves the initial tight stacking of small capillaries (diameters ~mm regime), as well as optional spacing elements that resemble a "scaled-up" version of the desired cross section. This assembly is then inserted into a thinner covering 'jacket' tube, and then heated and drawn into what is usually referred to a 'cane'. The produced cane is then again covered with a considerably thicker jacket, and drawn again, in a second stage into the final desired fibre structure. However, there are other promising novel techniques, such as extrusion [32, 66], drilling [67] or 3D-printing methods [68] to produce suitable preforms. These are usually favoured for unique application, requiring more exotic materials, like soft-glasses or polymers [66, 68].

While the brief summary provided above sounds deceptively simple, there are several, sensitive factors that must be continuously monitored and adjusted if necessary to manufacture optical fibres of high quality. The intricate physics behind the drawing process includes but is not limited to delicate balancing of the surface tension present in the molten glass of the structure during drawing. Some of the degrees that the fabricators

can manipulate during fibre drawing amongst others are: (i) the gas pressures within the hollow regions (both the core and cladding tubes), (ii) speeds of feed and draw, or (iii) temperature of the furnace. For a comprehensive overview about this fabrication technique for ARFs, Reference [65] provides a great and exhaustive analysis.

In the preforms the capillaries can be tightly packed — e.g. for HC-PBGFs or Kagomé-fibres (Figures 2.3 c, and 2.4 a, respectively) — or non-touching — e.g. for ARFs (Figure 2.4 b). For the latter, it is also important to mention the phenomenon of *mid-draw contact* [65]. It has been modelled and experimentally verified that during drawing the capillaries first expand and then contract, before attaining their final shape [69]. This means that the tubular elements have a temporary stage at which their diameter is larger than their finalized one. Considering the tight spacing that is usually present at typical ARFs, this over-expansion must be always considered. Failing to account for this phenomenon can lead to the touching and merging of these elements. In turn, these contact points effectively establish glass nodes, as they will not separate in the subsequent stages of the drawing procedure. It has been shown in the previous Subsections that these nodes can cross couple core and cladding modes, and such can contribute significantly to the degradation of the performance of the fibre — therefore it is of uppermost importance to avoid mid-draw contact.

Impact of variations in the microstructure

As mentioned previously, the tolerance towards variance of the microstructure is an important factor, and the earlier cited simulational results considered the impact of such aspects; like the uniformity of the structure, the thickness of the capillaries, or the orientation of the cladding elements, just to name a few [59–61, 65]. Since a minor variance of the structure is virtually unavoidable, constant monitoring and adjustment of the fibre drawing parameters is another tool that can be effectively used to manufacture long, homogeneous fibre pieces. While taking samples of the as-drawn fibre periodically during the fabrication process is a possibility, non-invasive alternatives (originally proposed by Frosz et al. [70]) are also being developed at the University of Southampton [71]. Devoting such meticulous approach towards high-precision manufacturing is a key enabler for providing highly consistency HCFs with lengths in the km regime. Such fibre pieces are essential for applications to be discussed in the following Chapters, as significant deviations considered in the prior references can lead to orders of magnitude larger loss parameters, subsequently leading to subpar performance.

2.3.6 Scalability and Outlook

Echoing the opening statement of this Section, one considerable advantage of utilizing HCFs over SCFs is the improved power handling capabilities of the former. The material-less core allows significantly increased power levels to be coupled and delivered by employing HCFs. On the contrary, SCFs in general can be limited either by laser

induced damage or nonlinear effects. The experimental measurements to be discussed in the appropriate Chapters in this Thesis used a CW light source. To cause laser induced damage (LID), such sources usually require rather high power levels — typically on the MW-scale. Comparable values are more readily present as high peak powers, when sub-ns pulsed lasers are utilized. For this reason, it is the latter feature which will be the more relevant concern, and such, the nonlinear phenomena be reviewed in more detail in Section 2.5. Additionally, the upscalability of high-power CW delivery will be estimated considering these limiting factors in Section 4.3.

Furthermore, it is worth highlighting some of the most appealing applications that can be enabled by utilizing HCFs instead of SCFs. Possibly one of the most promising qualities of the hollow-core fibre technology is its modularity that is enabled by the nature of its hollow core. This unlocks the opportunity of filling the core with various materials, from gases [32, 72–74], through liquids [73, 75, 76], to even small particles [75, 77]. Furthermore, all of these introduced materials can also interact with the light coupled into the fibres in manners that previously were impossible.

Examining the capacity of loading the core with gaseous media, as an example, one can propose an alternative technology to gas cells [78]. This technique also has the inherent advantage of increased interaction length, as the highly intense beam distribution can be effortlessly maintained along the entire length of the fibre. Moreover, it is also possible to manipulate the dynamics of the phenomena, simply by adjusting and fine-tuning the pressure of the filling material [79]. As long as the materials are not reacting with each other, the filling of the core and cladding tubes can be replaced and adjusted as desired. It is also possible to enhance the guidance by introducing a differential gas composition into the core and the cladding tubes [74]. The change of the refractive index of the gaseous media from air also alters the resonance conditions defined in Equations 2.14 and 2.15. Exploring the opportunity from the opposite direction, the same feature of the HCFs allow the detection of different gas species either when the core is filled with the sample [32, 80], or when the gas is dissolved in liquid [81].

Another interesting possibility is the coupling and guidance of small (µm to nm scale) liquid droplets or solid particles inside the core of an HCF. In a similar fashion, this opportunity enables long-range remote sensing applications [39]. Moreover, due to the fact that the beam distribution is maintained, the optically trapped element can be manipulated along the length of the fibre, respectively. Since the optical trapping and propulsion are some of the main topics of discussions of the Thesis, a separate Section has been dedicated for more detailed review of the field.

However, so far only an idealized lossless theoretical model has been introduced and discussed. More realistically, though, there are always impurities and small deviations that could significantly alter the coupling and transmission efficiency of any kind of

fibre. The following Section will provide a general overview of the most relevant sources of losses of optical power in HCFs.

2.4 Loss mechanisms

An excellent up-to-date tutorial review on the current understanding loss mechanisms of HCFs, including guidance on how to minimize the total loss through proper engineering is summarized in [82]. While the contribution to the total loss of the separate loss mechanisms is different for the different types of HCFs, 4 major contributors can be distinguished. The exact contribution of each is beyond the scope of present report, but relevant important articles will be referred. It is also worth noting here that while these separate loss sources can be categorized by their characteristic behaviour, it is practically hard to measure their independent contributions experimentally, as they are usually intertwined in complex ways.

Nevertheless, a brief analysis is also provided here with additional attention given to discussions regarding physical realizations of the theoretical considerations. Moreover, presenting practical insights will have a higher priority, and more extensive theoretical investigations will be referenced.

2.4.1 Confinement

Contrary to SCFs, the modes confined in HCFs are generally not bound. In the case of SCFs, if an optical ray incident at a larger angle on the core-cladding interface than the critical angle defined by Equation 2.2, it experiences a perfect reflection, in accordance with Fresnel's law. This is not the case for HCFs, since the guiding mechanism is fundamentally different as discussed before. In this case, the outer silica layers have higher wavenumbers than the propagation constants of the core modes. Because of that, a small portion of the electromagnetic field can leak into the cladding of the fibre. The actual extent to which this happens in general depends on the design of the fibre and can be reduced with careful engineering [49].

The confinement, or leakage loss (LL) can be interpreted in somewhat, but equally useful ways [82]. Building a model based on the ray-optics approximation, there are a few important points to mention [48]. First of all, the LL can be reduced (in theory, to arbitrary low levels) by increasing the core size of the HCF. However, as discussed in Section 2.2, through Equation 2.9, an increased core diameter leads to larger V-numbers, which in turn results in the fibre supporting a growing number of modes. Furthermore, these higher modes generally have larger LL as well. Lastly, in this interpretation, the reflectance of the microstructure is crucial to achieve low loss values. Practically, this can be achieved by employing a cladding structure consisting of more rings of structural elements. Taking a simple RVF as a baseline, this is achieved by inserting additional

tubular elements — as it can see by the improved performances of NANFs (1 nested tube) [31, 83], and likewise DNANFs (2 nested tubes) [36].

In a somewhat different concept, the LL loss can be also illustrated by considering the $|\psi\rangle$ waveguide modes of the HCF. As mentioned, along the core modes, there exist a continuum of cladding and jacket modes. Based on calculation using the coupled mode theory (CMT) [84, 85], it can be showed that the power confined in these modes of all kinds, can be transferred between each other. Since the non-core modes typically have higher attenuation values, the transfer of optical power is not symmetric. These observations show the importance of careful design of the fibre, through minimizing the coupling between modes by adjusting the propagation constants of the different modes [82], or by engineering the innermost surface of the core, such that it has a negative curvature, for example [54].

2.4.2 Material absorption

One of the most fundamental of light-matter interactions is how the energy of photons can be absorbed by the material they are incident on. In this semi-classical interpretation the electromagnetic radiation interacts (most frequently) with the electron structure of said material, and is transformed from electromagnetic energy of the field to internal energy of the absorber. This inevitably results in a reduction of the intensity as light propagates further in the matter following the Beer-Lambert law — which is observed as loss.

In the case of SCFs, the obvious contribution in material related attenuation is induced by the core material (most commonly fused silica, SiO_2), where the most intense part of the optical beam propagates. Considering HCFs, similarly, it is the material structure of the fibre, that is responsible for absorption related losses. However, the air holes confined by the struts and nodes add another domain that should be considered.

As mentioned before, having a low overlap between the optical field and the constituting material is one of the many benefits of employing HCFs [82, 86]. Nevertheless, a small fraction of the coupled light inevitable enters the material that forms the microstructure. Taking the Heraeus F300 as one of the most commonly used high-purity fused silica tube for fibre manufacturing, when compared to a NANF of similar parameters, the glass induced absorption is reduced by ~4 to 5 orders of magnitude [82].

Considering the case of HCFs, complimenting the material absorption of the glass structure, is the absorption of gaseous environment filling the air nodes of the microstructure — amongst them, the most influential being that of the hollow core. Similarly, the smaller cross section of gases compared to solid medium significantly reduces the losses experienced by the optical beam. Moreover, the absorption can be decreased even further, by applying vacuum to HCF.

For the reasons discussed above, it is reasonable to neglect the material absorption of HCFs when total loss is considered, as their contribution is practically non-existent, compared to other more dominant sources, e.g. the confinement loss.

Nonlinear effects

It is worth noting here, that nonlinear (NL) mechanisms are strictly speaking not significantly different or independent from the material absorption mechanism considered above. However, this is only mentioned here briefly, as the topic can be considerably wide-ranging. For this reason, a more thorough discussion will be provided later in Section 2.5.

2.4.3 Scattering

Rayleigh scattering

Similar to the discussion regarding absorption, the Rayleigh scattering of bulk materials (i.e. glass and gases) have orders of magnitude lower influence on the overall loss of the fibre compared to other components (e.g. leakage loss). Furthermore, the contribution of Rayleigh scattering loss (RSL) coefficients of these materials are also known, and such can be interpreted as a small, additional absorption. For these reasons, it is considered to be justified to neglect the impact of Rayleigh scattering in favour to the other loss sources [82].

Surface scattering

During the fabrication of HCFs, the molten glass that will ultimately create the microstructure can develop dynamically in accordance with laws of thermodynamics and surface tension. Once the drawn fibre is cooled down, the air-glass interfaces froze in, with the capillary surface waves embedded into the microstructure [87]. Any deviation from an ideal flat surface acts as a perturbation, that will deteriorate performance. This decline in essence leads to a reduced power transmission, that is characterised by what is referred to surface scattering loss (SSL).

To estimate the effect of the perturbations of the glass surface on the guided modes, the calculations usually utilize some type of mathematical methods, e.g. CMT [85]. An alternate approach, investigating the effect of surface roughness on the far field image of the scattering is introduced and discussed in detail in Ref [82]. It is worth mentioning, however, that arising from its stochastic nature, only a generalized, averaged picture can be given, as the exact distribution of scattering sources can differ significantly for each fibre drawn. Moreover, the inhomogeneity of the surface can also enable coupling between different modes supported by the fibre. While the intermodal coupling would be otherwise forbidden, the phase-matching conditions can be altered locally, such that power can couple from one mode to the other. This leads to a higher total loss, as the

HOM content is increased, and these modes also usually suffer from larger leakage loss values.

When comparing a PBGF with an ARF, the effect of surface scattering on transmission loss is more pronounced for the former. This can be understood by the fact that PBGFs usually carry a larger fraction of the field intensity closer to the core-cladding barrier, which inevitable leads to more distinct interaction. The theoretical difference between these two types of HCFs usually shows an order of magnitude lower loss values for comparable NANFs. Nevertheless, experimental verification of the exact numbers are not trivial, as measuring the SSL independently is troublesome.

Lastly, it has to be mentioned, that being aware of such scattering sources or defects of the microstructure are even more important when high power levels coupled into the fibre. Additionally to being in general a source of loss, in this case, the confinement of the beam can be significantly reduced. Consequentially, the localized perturbations can ultimately lead to irreversible fibre damage and breakdown of the guidance.

2.4.4 Bend losses

So far, it has been generally assumed that the optical fibres are used in a perfectly symmetric layout. However, small bending of the fibre structure along its length is expected during practical employment. In general, this effect can be distinguished into 2 categories, based on the length of the induced deviation from a straight fibre. Micro- and macrobending losses (µBL, and MBL, respectively) are differentiated, with the former generally referring to distances typically longer than hundreds of the used wavelength.

Micro bending

Localized external impact, such as mechanical forces induced by rough surfaces applying pressure to the fibre structure can alter the curve of the fibre from an ideal straight case. In a simplistic description, these effects introduce scattering nodes that enable the cross coupling of light between optical modes, resulting larger overall loss values because of the increased HOM content. It has been shown, that the microbending loss in ARFs is inversely proportional to the core size of the fibre [82]. The influence of such forces can be reduced by applying more advanced protective coatings using several different approaches [88].

Macro bending

Additionally, such bends and curvatures can be present for longer lengths when being deployed. By utilizing the conformal transformation method, the impact of external macrobending can be interpreted as the refractive index profile of the fibre becomes tilted when coiled [82]. This in turn similarly allow the development of unwanted cladding modes with higher loss values. Compared to PBGFs, ARFs in general are significantly

more sensitive to macrobending, and the loss generally follows an inverse squared relation to the bending radius [82]. Lastly, as expected, a critical bending radius can be defined below which the loss increases sharply, and ultimately the guiding cannot be maintained. From a practical point of view, HCFs wound up on a standard shipping bobbin, that has a diameter of $d_{\text{bobbin}} \approx 30\,\text{cm}$, the macrobending induced loss is negligible.

2.4.5 Summary and comparison

In summary, Fokoua et al. provides a great review of the scaling rules for the previously discussed components that contributes to the total loss of HCFs [82]. In general, for the applications to be considered and the results of the studies conducted to be discussed in the following Chapters, the most important insights for using a NANF are:

- The most dominant contributors for the total loss are the confinement or leakage loss (LL) and microbending loss (µBL).
- There exists an optimal core diameter, where the combined impact of leakage and microbending losses are minimal for a given geometry.
- In order to not introduce any noticeable macrobending loss (MBL), the fibre samples should be kept in an arrangement, the bending diameter of which is always kept above 30 cm at any point along its entire length.
- The scattering (RSL, SSL) and absorption related losses are negligible compared to the previously mentioned other sources.
- When beams with high optical power levels are being used, the nonlinear (NL) response of the materials should be considered. This will be discussed in more detail in the next Section.

The points raised above were used as guidelines for choosing the most suitable in-house fabricated fibre samples. These fibres will be introduced later in Section 3.3.

2.5 Non-linear phenomenon

As the strength of the electric field applied to a dielectric material surpasses a given threshold, the relation governing the induced change in the **P** polarization of the material can no longer be appropriately determined as a linear dependence on the **E** field. This means that terms higher than the 1st order become non-negligible, and as such must be considered to describe the physical effects appropriately.

For the case of SCFs, multiple effects — like Brillouin- or Raman scattering, or Kerr effects (e.g. self-phase modulation (SPM) or four-wave mixing (FWM)), or multiple photon excitation, just to name a few — must be considered. As mentioned earlier, there usually exists a threshold above which these phenomena become important. Considering HCFs as alternative solutions, said threshold is greatly increased, as the most intense

part of the beam propagates inside the hollow core (most commonly filled with air), and the overlap of the field with the fibre glass is very low [86].

Up until now, the relations and equations introduced have only considered a linear response of the system to the influence of the incident beam. While these are practically useful for explaining many key physical phenomena at higher power levels they cannot capture the underlying physical effects appropriately. When stronger electric fields are considered, in order to adequately describe the light matter interactions, terms beyond the first order have to be included.

One of the 4 Maxwell's equations, Gauss's law can be written in its differential form as:

$$\nabla \cdot \mathbf{E} = \frac{\rho}{\varepsilon}, \tag{2.16}$$

where $\nabla\cdot$ denotes the divergence of the electric field $\mathbf{E}$, ρ is the volume charge density, and ε is the absolute electric permittivity of the material partaking in the interaction.

Equation 2.16 can be practically interpreted such that a change in the electric field modifies the material properties, and vice versa. Since the electric field is composed of oscillating waves, these changes are always present. Assuming the central wavelength of the light source to be $\lambda_0 \approx 1064\,\text{nm}$ — comparable to those that will be used in the experiments to be discussed in the following Chapters — the corresponding angular frequency is $\omega_0 = 2\pi c_0/\lambda_0 \approx 300\,\text{THz}$, where c_0 is the speed of light in vacuum. From a macroscopic point of view, the oscillation averages out over time, and for weak fields, the change in the $\mathbf{P}$ polarization vector induced by the incident field can be approximated with a linear relationship.

However, when a stronger field is present, higher order terms must be also considered, since the anharmonic motion of the bound electrons in the material creates a nonlinear response [40]. Mathematically this can be represented by:

$$\mathbf{P} = \varepsilon_0 \left(\chi^{(1)} \cdot \mathbf{E} + \chi^{(2)} \cdot \mathbf{EE} + \chi^{(3)} \cdot \mathbf{EEE} + \cdots \right), \tag{2.17}$$

where the $\chi^{(j)}$ coefficients represents the j-th order electric susceptibility tensors.

Taking silica (SiO_2) as an example — since it is a widely used fibre material —, the second order term does not contribute to the change in the polarization vector, because of the symmetry of the molecule. Some of the other most commonly observed non-linear phenomena in optical fibres, results in the formation of new wavelengths — e.g. high-harmonic generation (HHG) or four-wave mixing (FWM). These are also typically only observed in optical fibres since they either require a distinct, different wavelength other than the original "seed" beam, or specific phase-matching equations must be satisfied. For the latter, any spontaneous signals that is not supported by those equations fade

out quickly along the length of the fibre. These mentioned effects are also elastic, i.e. do not cause any energy exchange between the field and the medium.

Another important non-linear effect that often has to be considered is the Kerr-effect, which is related to the $\chi^{(3)}$ term. The refractive index of the materials usually depends on the intensity of the electromagnetic field applied to it. From by Equation 2.17:

$$n^{(NL)} \approx n + n_2 \cdot I, \tag{2.18}$$

where $n^{(NL)}$ is the nonlinear refractive index, n_2 is called the non-linear Kerr-coefficient, and the optical intensity is given by $I = |\mathbf{E}|^2$. As it can be seen from Equation 2.18, the impact of the Kerr-effect depends on the intensity of the electric field. Practically relevant high enough intensity values can be mainly reached when pulsed laser sources are utilized. This is due to the fact that in that case, the peak intensity values can be orders of magnitude larger than the average intensity a CW source can achieve. As an example, the peak power of a Nd:YAG/Cr^{4+}:YAG microchip laser can reach levels beyond 50 MW [89], while the highest ever reported average power of a CW source — which has a central wavelength near 1 µm — is 300 kW, reported by Lockheed Martin, used by the US military [11], displaying a 2 orders of magnitude difference.

An important note is that this effect is more crucial, where significant fields are present in solid material, i.e. SCFs. For HCFs, only a small fraction of the air guided mode enters the cladding structure, somewhere in the range of $10^{-3} - 10^{-5}$ suggested by simulations [86]. The exact value also depends on the specific fibre type and geometry [90]. Furthermore, the Kerr-coefficient of air is determined to be $n_{2,\,\mathrm{air}} \approx 1.2 \times 10^{-22}\,\mathrm{m^2/W}$ at $\lambda = 308\,\mathrm{nm}$ and ~101 kPa pressure [91], in contrast to that of fused silica, which is measured to be $n_{2,\,\mathrm{FS}} \approx 2.19 \times 10^{-20}\,\mathrm{m^2/W}$ at $\lambda = 1030\,\mathrm{nm}$ [92], highlighting another 2 orders of magnitude difference. As a reasonable figure of merit, the $\gamma_{\,\mathrm{fibre}}$ nonlinear parameter of an optical fibre can be defined as

$$\gamma_{\,\mathrm{fibre}} = \frac{2\pi}{\lambda}\frac{n_2}{A_{\mathrm{eff}}} \tag{2.19}$$

Additionally, it can be appreciated, that since HCFs typically have larger core diameters — as mentioned in Section 2.3 — the nonlinear fibre parameters $\gamma_{\,\mathrm{HCF}}$ are usually 3 to 4 orders of magnitude below to their $\gamma_{\,\mathrm{SCF}}$ counterparts. Lastly, the changes are more influential where the phase properties are crucial, e.g. pulsed operation or in satisfying resonance conditions. From equation 2.18 the resulting phase-shift can be also calculated through:

$$\Delta\Phi = n^{(NL)} \cdot k_0 \cdot L, \tag{2.20}$$

where $k_0 = 2\pi/\lambda_0$ and L is the interaction length, i.e. the fibre length. This effect also results in the so-called self-phase modulation (SPM), which also plays a crucial role in explaining the spectral broadening of ultrashort pulses. For the reasons mentioned above, the Kerr effect will not be of concern for the experiments to be presented in the experimental Chapters, and such will not be discussed in more details.

On the other hand, nonlinear effects (NLE) which do include energy transfer to the medium can be labelled as inelastic scattering. The two main contributors are Stimulated Raman and Brillouin scattering (SRS and SBS respectively). Both SRS and SBS are similar in in the sense that the material absorbs a photon of the radiation field and emits another photon with either lower or — if possible — higher frequency, corresponding to the Stokes or the anti-Stokes waves respectively. The significant difference between the two is that the particle participating in the interaction is an optical phonon for the SRS, while it is an acoustic phonon in the case of SBS.

For both SRS and SBS, the optical power of the signal can be calculated [40] by:

$$dP^{(\mathrm{R/B})} = \left[g^{(\mathrm{R/B})} \frac{P_{\mathrm{seed}}}{A_{\mathrm{eff}}} - \alpha^{(\mathrm{R/B})} \cdot P^{(\mathrm{R/B})}) + C^{\mathrm{SR/SB}} \cdot P^{(\mathrm{R/B})} \right] dz. \tag{2.21}$$

In Equation 2.21 above, z is the longitudinal position along the fibre length, P_{seed} is called the seed power of the originally coupled field, and A_{eff} is the effective cross section area of the light inside the fibre. The coefficients g, α, and C are the small signal gain coefficient, the attenuation coefficient and the spontaneous response coefficients, respectively, while $P^{(\mathrm{R/B})}$ is the power of the Raman/Brillouin scattering. Since the equations are identical, the cases describing the Raman/Brillouin effects are labelled with R/B, respectively.

It is also worth mentioning here that for both SRS and SBS, a substantial $P^{(\mathrm{R/B})}$ signal is only generated above a certain P_{seed} threshold input power level. Considering a SMF as an example, this threshold can be 3 orders of magnitude lower for Brillouin scattering [40]. This would suggest that when high power fields are present, SBS would be the first limiting factor to acknowledge. However, another important feature is that SBS also exhibits an inverse dependence on the bandwidth of the seed [93]. For this reason, the scalability of power transmission is restricted by either SRS or SBS, based on the linewidth of the laser source. As the fibre laser used for the experiments to be discussed in Chapter 4 displays an intrinsically broad bandwidth, it can be appreciated that SRS will be the main limiting factor for the results to be presented there.

Another more practical insight obtained from Equation 2.21, is that considering the same material composition, the SRS/SBS signals depend inversely on the A_{eff} effective area of the fibre. While a larger effective area generally results in lower non-linear responses — as shown by Equation 2.9 — at the same time, it also increases the V-number, which in turn increases the number of supported modes. This could be detrimental for applications like high quality material processing, where single-moded beams are

preferred. Another important practical aspect mentioned earlier, is that a larger core size also requires smaller NA. This in turn increases the bending sensitivity of the fibre, and such could be another disadvantage for certain purposes.

When comparing specifically SCFs with HCFs, the most obvious difference is the reduced power entering the glass in the latter case, significantly reducing the light-matter interactions [86]. As an example, consider the case of high power delivery of a CW beam from fibre laser source — similar to what will be introduced in Section 4.1. In this scenario, the most relevant NL phenomenon is SRS, which arises from the combination of the broadband nature of the laser source and the air molecules inside the core. Based on simulations reported by Mulvad et al. [94], it has been concluded that the power delivery results to be reported in the following are still well below the threshold for any of the aforementioned nonlinear phenomena to have a significant contribution. The impact of SRS will be discussed in more detail from a practical point of view in Chapter 4.

2.6 Interfacing of different optical fibres

Even though the rapid development of HCF technology can be clearly seen by the continuous reports of world-record results [36, 95, 96], showcasing their capabilities to their fullest extent is not trivial. Probably one of the most sought after target goal of such tenacious effort towards ultra-low attenuation is to replace the already existing and well-established network of SCFs with HCFs. This would also preserve the already favourable properties of an all-fibre setup — e.g. flexibility and compactness. Realistically speaking, however, it is only practical to upgrade the currently employed system gradually. Thus, interfacing the most widespread, commercially available SCFs with next generation HCFs would be necessary.

Several studies have investigated different practical solutions to couple light from SCFs into HCFs, with the shared goal to find a practically convenient, robust, resilient, and highly efficient way for interfacing them. The main challenge to overcome in this undertaking is that the core diameters of commercially available and most widely used SCFs and HCFs can vary to a great extent. While the d_{core} core diameter of a single-moded SCF operating near the wavelength of $\lambda \approx 1\,\mu\text{m}$ can be ranging between 5 to 6 µm, it more commonly falls between the 25 to 35 µm domain for HCFs.

While strictly speaking, not a specifically a fibre related loss mechanism, it is important to discuss the loss suffered during coupling of the optical beam into any kind of fibre. As a very simplistic explanation, based on the work of Marcuse [97], any arbitrary $|\psi\rangle$ field distribution consisting of electric and magnetic field vectors $\mathbf{E}$ and $\mathbf{H}$ respectively, can be represented as the linear combination of the $|\psi_j\rangle$ modes supported by the fibre (introduced in Section 2.2), that is:

$$\mathbf{E} = \sum_j c_j \mathbf{E}_j, \qquad \mathbf{H} = \sum_j c_j \mathbf{H}_j, \tag{2.22}$$

where the coefficient c_j denotes the relative amplitude of the given mode of the field under examination. After combining Equations 2.7 and 2.8, the c_j coefficients can be obtained through:

$$c_j = \iint \vec{z} \cdot \left(\mathbf{E} \times \mathbf{H}_j^* + \mathbf{E}_j^* \times \mathbf{H} \right) dA \tag{2.23}$$

It can be shown that the total power carried by the field is simply $P = \sum_j |c_j|^2$. Normalizing this expression, by setting $P = 1$, we can define the power coupling efficiency into a given $|\psi_j\rangle$ mode, or CE for the sake of simplicity, as the respective $|c_j|^2$ coefficients.

It can be also seen from Equation 2.23, that maximum coupling is achieved when the supported mode of the optical fibre and the distribution of the focused beam is identical. Achieving perfect, lossless coupling is essentially impossible because of the inevitable imperfections of both the optical beam and the fibre structure. On the other hand, the introduced terminologies of linearly polarized (LP) optical modes and the concept of a Gaussian beam in Section 2.2 provide a practical point of comparison for estimating the maximum attainable CE.

Wagner and Tomlinson reported a great overview of coupling efficiency related calculations, considering an arbitrary case, including possible misalignments of the system [98]. The provided equations can properly describe a general coupling problem for single-moded fibre components. Moreover, they are greatly simplified for an ideal case; that is when all the optical elements (including the source) are centred on the same optical axis. The impact of misalignments will be discussed in more detail in Section 3.4.

There have been several more unconventional and promising methods reported that could be employed to overcome the challenge of interfacing SCFs with HCFs. Without the intention of providing an exhaustive list, this can range from using a tapered nano-spike [76, 99], a reverse tapered splice [100], or a capped fibre end [101]. The required preparation procedures can also include low temperature gluing [102] or high temperature splicing [100, 103]. While the techniques show great prospects, there are some important aspects that have to be mentioned here. First of all, the techniques inevitably require cautious preparation of the fibre samples used. This could prove to be disadvantageous while operating in less forgiving experimental conditions (e.g. on-field deployment), as maintenance can become inconvenient. Secondly, some of the studies report relatively low CE (e.g. ~87.8 % for the nano-spikes used by Xie et al. [99]), while those quoting high CE values utilize additional materials (e.g. glued fibre caps used by Suslov et al. [102]). From the point of view of the research to be discussed later, the main concern is the power scalability of these techniques. In both examples, no

discussion have been provided about the behaviour of the techniques when ~kW-range optical powers are used.

In general, it can be claimed that an ultimate interfacing method is yet to be presented. So far, all approaches are intentionally optimized to tackle one specific concern (e.g. suppression of back-reflection), with a trade-off given to a less important aspect. For this reasons, the arguably most commonly used concept of utilizing a lens pair for coupling of an optical beam is preferred — as it will be discussed in more detail in Chapters 3 and 4.

2.7 Optical forces on micron scale particles

Another interesting proposal for taking advantage of the hollowness of the core of the HCFs is the possibility of manipulating micron sized particles inside the fibre. This is achieved by using the coupled beam as the means to control the propulsion. While the phenomenon of light exerting optical force has been observed as early as the beginning of the 17$^{\text{th}}$ century by Kepler [104], any practical application of the effect required centuries of technical advancement. One of the most recent utilization has been proposed by Ashkin's research in 1970 regarding the trapping of particles using only optical forces [105]. Soon this was followed by the optical levitation of such particles [106], and later the realization of the first, truly 3 dimensional optical-tweezer in 1986 [107]. Ultimately, it is now routinely possible to trap [108, 109], push [110], pull [111], rotate [112], or cool to sub-μK temperatures [113] small (~μm and below range) sized particles and aggregates. The extension of optical manipulation of macro-scale objects are also of scientific interest — e.g. near-space light sails — and are also being investigated rigorously [114]. Here, the relevant theoretical relations will be summarized with the intention to support the discussions that will be presented in Chapter 5.

In order to appropriately describe the physics governing the dynamics of such particles illuminated by tightly focused light beams, employing a full wave-optical frame is generally required [109]. However, for certain cases practical approximations can be applied to reduce the complexity of the used equations, while maintaining validity of the model. There are three distinct regimes that can be distinguished, based on the particle size parameter ξ, which is defined by:

$$\xi = 2\pi \cdot a \cdot n_{env} / \lambda_0, \tag{2.24}$$

where a is the characteristic size of the arbitrary particle to be trapped (e.g. the radius of a sphere), n_{env} the refractive index of the environment surrounding it, and λ_0 denotes the central wavelength in vacuum of the trapping beam. These 3 main regimes that can be differentiated are:

1. In the case of "large" particles, when $\xi \gg 1$, using a simple ray optics approach can describe the system under examination with sufficient accuracy.

2. For "small" particles $\xi \ll 1$, if $|m|\xi \ll 1$ also holds true (where $m = n_{par}/n_{env}$ is the relative index of refraction between the particle and its surrounding environment) the dipole approximation (or sometimes also called Rayleigh approximation) can be applied.

3. In the "intermediate" regime between the previous two points, when the a size of the particle is comparable to the λ_0 wavelength of the laser light, neither of the approximations can be considered valid any more, and the electromagnetic theory must be utilized.

In the following, optical manipulation of particles of the first group (i.e. $\xi \gg 1$) will be discussed. This is reasoned by the fact that the main driving force of the research to be discussed in Chapter 5 (i.e. remote sensing by using optically guided particles) falls into this category. Consequently, the designed and built experimental setup will also accommodate the requirements of this approach. In the scenario to be discussed, the diameter of the particle is $d_{\text{ptcl}} = 10\,\mu\text{m}$, and the wavelength of the used source is $\lambda_0 = 1064\,\text{nm}$, resulting in a particle size parameter of $\xi \approx 31.4$. In the following the manipulated particles will be generally referred to as microparticles (McPs). For a more comprehensive review, Pesce et al. provides a great summary article about calculations covering all 3 groups mentioned above [109].

2.7.1 Ray-optics approximation

In the rest of the Section, the ray-optics formalism, a simple, quantitative, semi-classical approximation will be used. In this interpretation, the photons of the laser field exchange momentum with the trapped object. The incident trapping beam with power $P_{\text{trap, 0}}$ can be considered as a bundle of light arrays. The distribution of the electric field can be translated to the distribution of the rays, by considering their spatial and angular distribution with appropriate weighting [115]. Since most of the work to be presented in this Thesis will be using a near-Gaussian beam, the discussions will be limited to the analysis of such beams. However, based on the work of Malik and Boruah, the calculations can be extended to more complex profiles [116].

According to Crooker et al. [115], it is possible to decompose a Gaussian beam into optical rays. This way, the more demanding calculations that would be required by using a wave-optics based approach can be significantly simplified. Moreover, by introducing the concept of statistical rays and utilizing basic tools used in matrix-optics, the evolution of the field distribution can be appropriately described. In this case, the total optical power can be written as $P = \sum_j P_j$, where j covers the fundamental N number of rays that builds up the original beam.

Figure 2.6 depicts the case of a single optical ray incident on an arbitrary spherical particle. Considering a single ray of optical power Ω_1 hitting the dielectric sphere with refractive index of $n_{\text{ptcl}}(\lambda_0)$ at an arbitrary wavelength λ_0. Ignoring the material absorbance, following the geometrical optics consideration, $R \cdot \Omega$ part of the power will be reflected under the same θ angle of incidence relative to the $\hat{n}$ surface normal. Additionally, the $T \cdot \Omega$ part will enter the sphere refracted under the angle φ, following Snell's law (Eq. 2.1). Here R and T are the reflectance and transmittance of the environment-particle interface. Strictly speaking, in accordance with the Fresnel formulas, these values also depend on the polarization of considered ray. In order to simplify the calculations, a circularly polarized beam will be considered, and such $R = R_{\text{eff}} = 1/2\,(R_S + R_P)$, with the indices S and P denotes the respective polarization states. Furthermore, since the material is assumed to have no absorbance, $T = T_{\text{eff}} = 1/E_{\text{eff}}$.

The optical force induced by a single ray acting on the sphere can be calculated by summarizing the total exchange of momentum induced by each reflection. While in general this leads to the summary of an infinite geometric series, typically, the impact of the first 2 scattering events is dominant [109]. This $\mathbf{F}_{\text{opt, ray}}$ total optical force can be separated into $\mathbf{F}_{\text{axl, ray}}$ and $\mathbf{F}_{\text{rad, ray}}$ axial and radial components, respectively. These vectors are perpendicular to each other, and their direction align with the coordinate system illustrated in 2.6, such that $\hat{n}_{\text{axl}}$ is parallel with $\hat{n}_z$, and $\hat{n}_{\text{rad}}$ is parallel with $\hat{n}_r$. Based on Ashkin's work [117] Phuoc [118] also provided the equations for these forces via the equations:

$$F_{axl} = \frac{n_{\text{ptcl}}P}{c_0} - \left\{ \frac{n_{\text{ptcl}}PR}{c_0}\cos(\pi + 2\theta) + \sum_{j=0}^{\infty} \frac{n_{\text{ptcl}}P}{c_0} T^2 R^j \cos(\alpha + j\beta) \right\}, \tag{2.25a}$$

$$F_{rad} = 0 - \left\{ \frac{n_{\text{ptcl}}PR}{c_0}\sin(\pi + 2\theta) + \sum_{j=0}^{\infty} \frac{n_{\text{ptcl}}P}{c_0} T^2 R^j \sin(\alpha + j\beta) \right\}, \tag{2.25b}$$

where $\alpha = 2\,(\theta - \varphi)$, and $\beta = \pi - 2\varphi$.

Considering a ray that is not parallel with the optical axis, but is incident on the particle with an angle of convergence ϕ, $\mathbf{F}_{\text{opt, ray}}$ can be also defined by another pair of orthogonal optical forces: $\mathbf{F}_{\text{sctr, ray}}$ and $\mathbf{F}_{\text{grad, ray}}$, denoting the scattering and gradient forces, respectively. When using this coordinate system, the direction of $\mathbf{F}_{\text{sctr, ray}}$ is parallel with the incident optical ray, while $\mathbf{F}_{\text{grad, ray}}$ is perpendicular to both. In figure 2.6, for the ray Ω_1, the force pairs $\mathbf{F}_{\text{axl, ray, 1}} = \mathbf{F}_{\text{sctr, ray, 1}}$ and $\mathbf{F}_{\text{rad, ray, 1}} = \mathbf{F}_{\text{grad, ray, 1}}$ are the same. However, considering ray Ω_2, these relations do not hold, as in this case, $\phi_2 \neq 0$. In general, it is possible to define a transformation rule between the 2 coordinate systems by scaling the forces with the appropriate trigonometrical function: $\mathbf{F}_{\text{sctr, ray}} = \cos\phi \cdot \mathbf{F}_{\text{axl, ray}}$ and $\mathbf{F}_{\text{grad, ray}} = \sin\phi \cdot \mathbf{F}_{\text{rad, ray}}$.

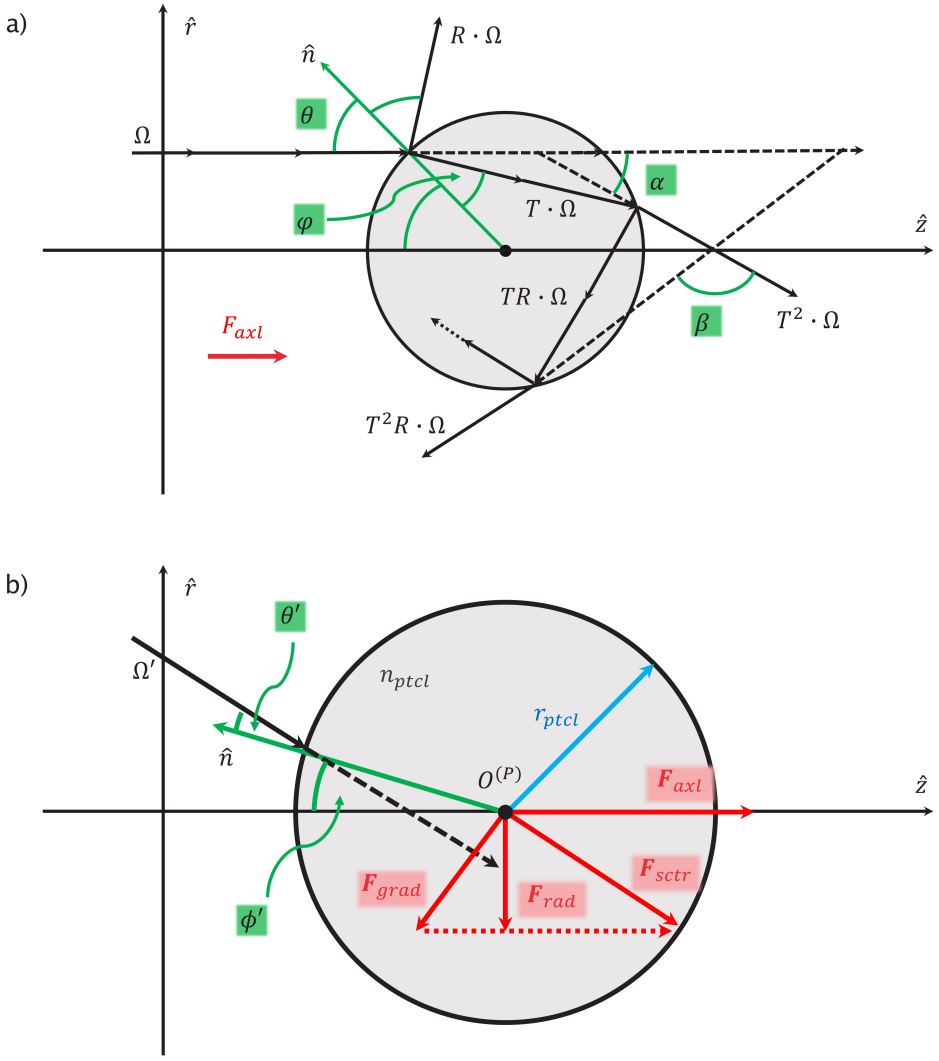

FIGURE 2.6: **Optical beam path of a singular ray interacting with a spherical micro-sphere** | a) The ray with optical power Ω initially propagates in a medium with refractive index n_{env}, parallel to the optical axis $\hat{z}$. It is incident on the sphere with refractive index n_{ptcl}, under the angle of incidence θ, relative to its surface normal labelled $\hat{n}$. It is partially reflected under the same angle with its power reduced by a factor of R. The remaining $T \cdot \Omega$ power is refracted and enters the sphere, under the angle of refraction φ. Assuming no absorption is present, $T = 1 - R$ hold true. Then this refracted ray is incident on the particle-environment interface, and the same partial reflection occurs. Here $\alpha = 2\,(\theta - \varphi)$, and $\beta = \pi - 2\varphi$. b) Shows an ray of optical power Ω' incident on the same sphere with radius of r_{ptcl}, but in this scenario, the direction of the ray has an angle of convergence ϕ', relative to the $\hat{z}$ optical axis. The optical forces are defined as $\mathbf{F}_{\text{sctr}}$ and $\mathbf{F}_{\text{grad}}$ for the components of the total force, that is parallel or perpendicular to the initial direction of the incident beam, respectively. Similarly, the transformation from this basis to the one using the directions set by the optical axis $\hat{z}$ and the radial direction $\hat{r}$, leading to the forces $\mathbf{F}_{\text{axl}}$ and $\mathbf{F}_{\text{rad}}$ are also illustrated. Adapted from [117]

As a point of reference for calculations, McPs made of polystyrene (PS) with a diameter of 10 µm, and a refractive index of $n\,(\lambda = 1064\,\mathrm{nm}) = 1.5717$ have been chosen. This is justified by the fact that McPs with such properties will be used extensively in Chapter 5, where the relevant experiments will be discussed. Assuming that the particle is surrounded by air, the amplitude of the **F** optical force can be easily approximated by

$$F = \frac{n_{prtcl}}{c_0} \cdot Q_{\mathrm{opt}} \cdot P, \tag{2.26}$$

where Q_{opt} is a dimensionless quality factor. Since it can be seen that the absolute value of Q_{opt} and $|\mathbf{F}|$ is only different by a constant factor, Q_{opt} is sometimes also referred as the normalized force factor. This normalized force factor summarizes the impact of multiple physical quantities, from the wavelength, spatial intensity and phase profile of the used optical beam, to the material, size and shape of the McP considered. The maximum value of this coefficient is attained, when the incident ray is perpendicular to a perfectly reflecting surface, for which scenario $Q_{\mathrm{opt,\,max}} = 2$. However, in most experiments which utilize optical manipulation in any manner, its value is practically $Q_{\mathrm{opt}} \leq 0.1$ [110].

Figure 2.7 shows the calculated relative magnitudes of the $Q_{\mathrm{sctr,\,ray}}$, $Q_{\mathrm{grad,\,ray}}$ and total $Q_{\mathrm{opt,\,ray}}$ normalized forces induced by an individual optical ray acting on the dielectric sphere, based on Ashkin's derivation of the governing equations [117]. Typically, there is a preferred frame of reference, which is generally based on the actual experiment, and makes the interpretation of the observation easier. In the following, the *axial* and *radial* directions are chosen, and will be used, as the former is practically defined by the HCF for the relevant experiments, and such easier to visualize.

It can be seen from Figure 2.7, that the optical forces becoming more impactful, when they are incident on the sphere under a larger θ angle. It can be seen, that the Q_{opt} total optical force is always positive, resulting in the particle constantly being pushed away from the source. On the other hand, above the threshold of $\theta_{\mathrm{th}} \approx 85°$, negative values of Q_{grad} are anticipated. However, in practical applications, optical rays with such large angle of incidence are usually are either not present (e.g. weak focusing, with low NA), or contain a small fraction of the optical power (e.g. outer ring of a Gaussian beam)

The main objective of the study to be discussed in Chapter 5 is to employ HCFs and take advantage of their unique possibilities regarding the optical manipulation of McPs. As detailed in Section 2.6, maximum CE is achieved if the beam distribution of the focused beam matches well with of the HCF — practically its FM. Furthermore, the most recently reported quasi-singlemoded HCFs show exceptionally low attenuation values [36], which ensures that a near-Gaussian beam profile is maintained for km-scale distances. Because of this, the actual distribution of the trapping beam is going to be determined by the optical modes the fibres can support. This modal distribution — and in turn, the optical force acting on the particles — is preserved along the length of the fibre, and as

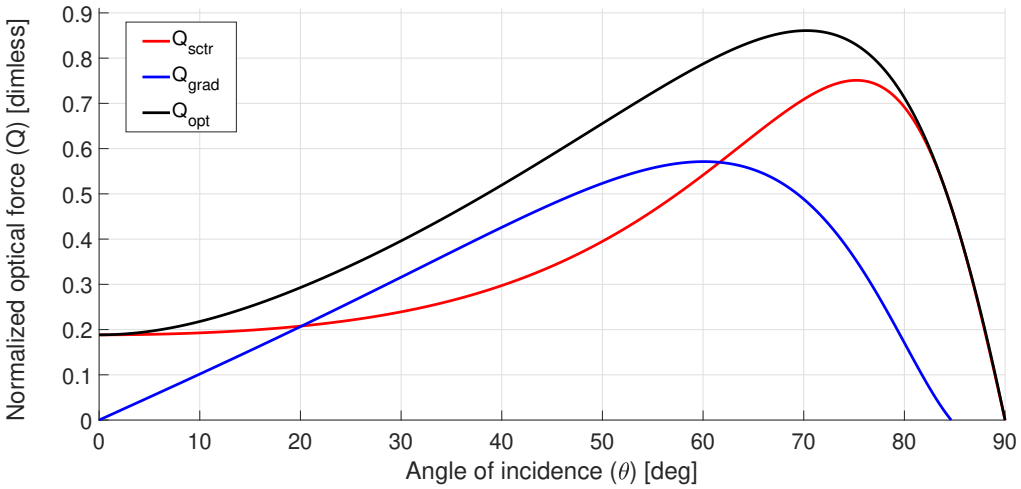

FIGURE 2.7: **Normalized optical force of a singular ray incident on a spherical microparticle** | The case of a microsphere made of polystyrene (with a refractive index of $n_{\text{ptcl}} = 1.5717$) that surrounded by air ($n_{\text{air}} \approx 1$), is considered, assuming no absorption. The red, blue and black curves shows the amplitude of the Q_{sctr}, Q_{grad}, Q_{opt} normalized scattering, gradient and total optical forces, respectively, following the naming convention set by Figure 2.6 b). More detailed discussion is provided in the text. Adopted from [117]

such, the stable trapping conditions will be also maintained. Consequently, the guidance of McPs over a significant distanced is also secured. Furthermore, it has been reported, that high quality beam profile, good pointing and power stability is a must for achieving stable trapping [109]. HOMs can perturb the dynamics of the trapping, such that a more complex model is required for proper description of the trapping mechanism [75, 119]. While it is clear that using a laser-tweezer with high NA optics and tight focusing is advantageous and results in a stronger optical trapping [120], this degree of freedom is not applicable when the beam path is determined by the conditions to achieve optimal coupling into the HCF.

Considering a steady state, this $\mathbf{F}_{axl}$ is counteracted by another, usually non-optical force (e.g. gravity or drag), such that the particle has a constant velocity. These will be discussed in more detail in the next Section.

On the other hand, in equilibrium $\mathbf{F}_{rad} = 0$ as the particle is kept in a stable position. Because of the symmetry of the focusing beam, the radial component of the opposing, individual optical rays cancel out each other. Furthermore, the calculation of the optical forces of these single optical rays takes a more complicated form, which depends on the focusing strength of the optical trap, i.e. the NA of the beam [117, 118].

2.7.2 Relevant non-optical forces

In general, there are 4 relevant non-optical forces that also have to be considered. These are:

(a) The van der Waals force

First of all, the discussions so far have been based on the assumption that the McP is already airborne, and is not mechanically attached to any surface. However, McPs are generally provided in some sort of a container. In reality, individual, levitating particles must be prepared accordingly in advance. They are usually commercially available in large numbers either in a fine powdered form, or as a suspension, mixed with the appropriate liquid. Particles tend to stick either to each other or to the surface of such containers, and such mechanical forces must be applied to break the relatively strong van der Waals force that forms.

In order to compare the arising forces, considering the example particle defined above ($r_{\mathrm{ptcl}} = 5\,\mu\mathrm{m}$, made of PS) is attached to optical grade glass. This case can be interpreted as the McP has escaped the trapping (that can happen for a number of reasons) inside the HCF, and hits the inner side of the core structure. Assuming a smooth surface of the fibre geometry, according to Hamaker's approximation [121], the typical force values are in the $F_{VdW} \approx 10$ to $100\,\mathrm{nN}$ range. This force is generally typically 3-5 orders of magnitudes larger than the optical forces present for light sources with $P_{avg} \approx 100\,\mathrm{mW}$ average powers. Hence, either a powerful mechanical influence is necessary for separation, or significantly larger power levels (near the $P_{avg} \approx$ kW regime) are required. While the former approach will be examined in more detail in Section 5.2, the first observation of McP propulsion (introduced in Section 5.1) has been observed due to the latter.

Figure 2.8 considers the example of a $r_{\mathrm{ptcl}} = 5\,\mu\mathrm{m}$ McP made of polystyrene, and the focusing of an ideal Gaussian beam, with beamwaist of $w_{foc} = 11\,\mu\mathrm{m}$. It can be seen from part a) that considering the $\mathbf{F}_{\mathrm{sctr}}$ optical scattering force, a minimum of $P_{min} \approx 35\,\mathrm{mW}$ optical power is required to counteract the $\mathbf{F}_{\mathrm{grav}}$ gravitational force. Furthermore, the inset of a) highlights the orders of magnitude larger force Van der Waals force present, when a particle radius of $5\,\mu\mathrm{m}$ is assumed. Part b) demonstrates the behaviour of $\mathbf{F}_{\mathrm{grav}}$ as a function of the particle radius. As expected the inverse third order dependence on size shows a sharp rise of the gravitational force that has to be countered. Lastly, part c) illustrates, the same dependence of the Van der Waals force. Note the orders of magnitude different scale of the Y-axis, compared to b).

(b) Gravitational force

Furthermore, once the McP is airborne, the obvious F_{grav} gravitational force must be counteracted at all times if any kind of optical trapping is desired to be maintained. As it will be discussed later in Subsection 2.7.3, from the point of view of optical forces, a McPs with larger d_{ptcl} particle diameters are preferred, as they allow a larger fraction of the beam to be utilized. On the other hand, this comes at the obvious cost of increased size, in turn mass, and ultimately larger F_{grav}. The actual force will depend on the ϱ_{ptcl} density of the particle, and will scale the cube of its r_{ptcl} particle radius — assuming spherical symmetry:

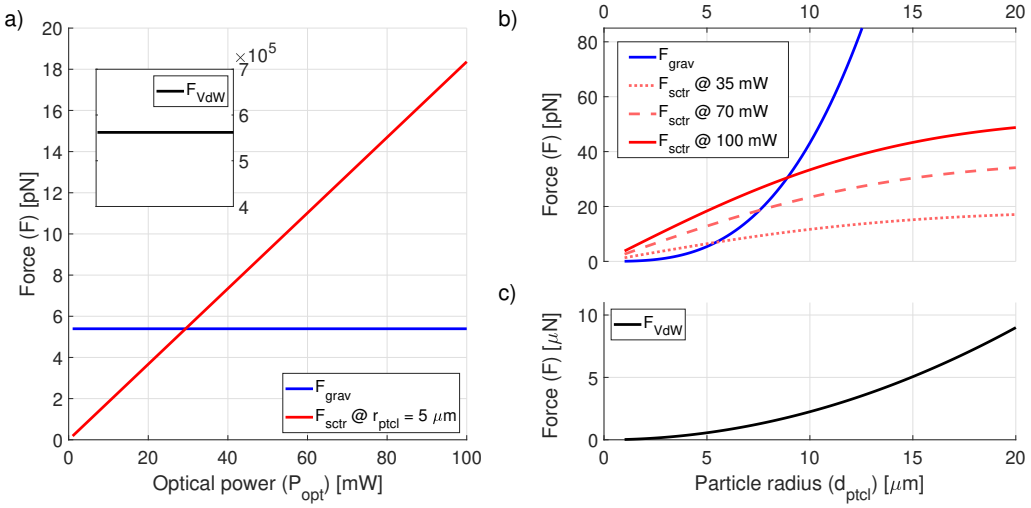

FIGURE 2.8: **Relevant Van der Waals, gravitational and optical scattering forces acting on polystyrene microsphere particles** | a) Considering a polystyrene McP with a particle radius of $r_{\text{ptcl}} = 5\,\mu\text{m}$, the simulated scattering force as a function of the incident optical power is shown, assuming a focused Gaussian beam, with a beamwaist of $w_{foc} = 11\,\mu\text{m}$. The calculated gravitational and Van der Waals forces are also shown. Firstly, it is demonstrated, that a $P_{min} \approx 35\,\text{mW}$ of optical power is required for optical levitation against gravity. Secondly, it can be seen, how the latter force is ~5-times larger then the other 2 forces considered. b) and c) shows the same group of 3 forces, as a function of the particle radius, while the difference in Y-axis scaling highlights the dominance of the Van der Waals force over its counterparts.

$$\mathbf{F}_{grav} = \frac{4\pi}{3} \cdot r_{ptcl}^3 \cdot \varrho_{ptcl}. \tag{2.27}$$

Considering the example of a 5 µm diameter PS MCPs, the gravitational force would be ~5.4 pN. This value is comparable to both F_{sctr} and F_{grad}, assuming a $P_{avg} \approx 100\,\text{mW}$ light source, that is optical levitation of such particle with such beam is in theory possible. The dependence of F_{sctr} as a function of the incident optical power is shown in Figure 2.8 a). Furthermore, the relevant gravitational force acting on the example particle is also marked. Based on the calculations, it is estimated, that an optical power of >35 mW would be sufficient to trap a PS McP, with a particle radius of $r_{\text{ptcl}} = 5\,\mu\text{m}$. Part b) of Figure 2.8 illustrates the relationship between the F_{grav} and F_{sctr} forces, as a function of the particle radius — assuming that the focused ideal Gaussian beam has a beam diameter of $w_0 \approx 11\,\mu\text{m}$.

(c) Stochastic thermal force

Another important element to consider for maintaining a stable optical trap is the always present Brownian motion. This can be originated from the particle's temperature related potential energy. In order to maintain a stable trapping of the particle, the potential walls of the trap introduced by the light beam must be greater than its thermal energy. Following the work of Zemánek [110], this can be translated to the relation:

$$W_{lat} = -\int_0^{\infty} \mathbf{F}_{opt}\left(\vec{r}\right) d\vec{r} \gg k_B \cdot T. \tag{2.28}$$

Here k_B denotes the Boltzmann constant, and T is the temperature of the particle.

(d) Viscous drag

Finally, possible high-power applications are considered. The maximum achievable $v_{\text{ptcl, max}}$ speed of a particle propelled by the light coupled into the HCF, is ultimately limited by the drag, which can be written as:

$$\mathbf{F}_{drag} = 6\pi\eta \cdot r_{\text{ptcl}} \cdot v_{\text{ptcl}} \cdot K. \tag{2.29}$$

Here η is the dynamic viscosity, v_{ptcl} is the instantaneous speed of the particle, and K is the so-called wall correction factor, respectively. The latter is characteristic to the inner structure of the fibre core — in analogy how the inner surface of a cylindrical channel would have an impact on the fluid dynamics passing through it — but also depends on the $\Lambda = r_{\text{ptcl}}/r_{\text{core}}$ particle radius to channel radius ratio. Assuming typical values of $r_{\text{ptcl}} \approx 10\,\mu\text{m}$, and $r_{\text{core}} \approx 30\,\mu\text{m}$, $\Lambda \approx 0.3$, which translates to a particle-channel ratio of $K \approx 2-3$ for cylindrical channels [122]. However, this estimation is only valid as a first degree approximations, since the NANF structure has greater complexity than a cylindrical channel.

2.7.3 Microparticles inside HCFs

Note that so far, no relations regarding the optical forces included the d_{ptcl} particle diameter explicitly. However, considering the applications involving the utilization of HCFs, the first obvious constraint is imposed by the fibre core, setting an upper limit for the particle size. Furthermore, as mentioned in Subsection 2.7.1, the fibre structure also determines the supported optical modes. Consequently, the focusing and therefore the coupled beam distribution and beamwaist is also fixed. Figure 2.9 shows that larger relative particle sizes — that is the ratio of the particle radius and the beamwaist of the focused beam: $\Lambda_{\text{MFD}} = r_{\text{ptcl}}/w_{\text{MFD}}$ — allow a larger fraction of the beam to interact with the McPs. Assuming that both the beam has an perfect Gaussian distribution, and the McP is a symmetric sphere, the dependence follows the trend of an error function. The highlighted section also indicates that only up to $Q_{\text{MFD}} \approx 60\,\%$ of the optical power can be practically utilized. This is due to the fact, that near ~1 relative particle size, contact between the McP and the inner microstrucure of the fibre has a higher probability. Such an event would result in "clogging" the fibre, ultimately leading to the point of contact needed to be removed. This can be highly troublesome, depending on the exact location of the accident, especially if significant lengths of fibre pieces are utilized.

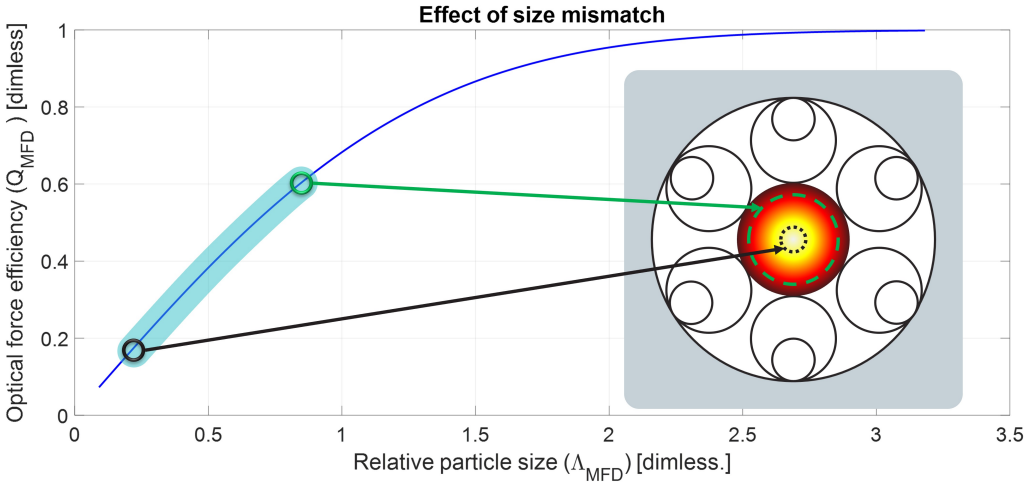

FIGURE 2.9: **Dependence of the $Q_{\mathbf{MFD}}$ optical filling quality factor on the relative particle size for a focused Gaussian beam** | The plotted curve illustrates the fraction of the optical power utilized by the particle it is incident on, as a function of the relative particle size, defined by $\Lambda_{\mathrm{MFD}} = r_{\mathrm{ptcl}}/w_{\mathrm{MFD}}$. Assuming an ideal Gaussian beam distribution, and that the microshpere is centered on the optical axis, the dependence follows the trend of an error function. While the larger relative particle sizes leads to an increased efficiency, a practical upper boundary usually exist, that is determined by the core size of the HCF. A reasonable range for applications is highlighted with blue shaded region. The inset illustrates how the central, most intense part of the beam contributes more compared to the less intense outer rings of the beam. The extremes of the size range considered here are shown with green and black markers.

3 Fibre coupling optimization measurements

In the present Chapter an in-depth investigation about the coupling efficiency (CE) into HCFs will be discussed. This is an important aspect to consider, since by optimizing the efficiency of the coupling, it can be ensured, that maximum power from the source is being delivered to the work-piece. Furthermore, having high CE also helps simplifying possible heat management concerns, by foregoing any unwanted effects in the fibre that could arise because of light not captured by the fibre's modes. Since this field has yet to be explored in enough detail, such a study will be provided here. The insight gained by the investigations will prove to be a valuable foundation for high-power measurements. Results will show that the in-house fabricated HCFs are capable of achieving and maintaining high CE.

To begin with, based on expectations set by theoretical considerations lined out in Section 2.6, an experimental setup has been designed and built with the intention to verify said predictions via experimental demonstrations. After the setup has been introduced, a set of characterisation measurements, which will quantify the requirements of precision positioning of different HCFs will follow. Both translational and angular misalignments of the input fibre tip will be examined, and a preference for the optical transmission window to be used for ARFs to guarantee maximum CE will be provided. Finally, the Chapter is concluded with a brief summary, highlighting the most relevant findings for the high-power delivery experiments that will be discussed in the succeeding Chapter.

3.1 Coupling efficiency

As discussed in the theoretical background (Section 2.6), mathematically, the CE can be calculated by the overlap integral of the $|\psi_{\mathrm{Beam}}\rangle$ field distribution of the beam to be coupled, and the $\sum_j |\psi_{\mathrm{Fibre,\,j}}\rangle$ field distributions supported by the modes of the fibre considered [98]. Simply put, the CE into the FM of a NANF can be calculated as $\mathrm{CE_{FM}} = \langle\psi_{\mathrm{Beam}}|\psi_{\mathrm{NANF,\,FM}}\rangle$. Experimentally, this can be determined in a quite straightforward way. After the total transmission of the fibre sample has been measured, the attenuation induced by the propagation along the length of the fibre is subtracted, leaving the CE separated from other loss sources.

As summarized earlier in Section 2.6, highly efficient interfacing of already commonplace SCFs with the emerging technology of HCFs is of high importance for many research groups. While many of the mentioned approaches show quite promising initial results, the option of free-space coupling using a pair of lenses was chosen here. There have been 2 main reasons for this choice: First of all, this technique offers the most flexibility

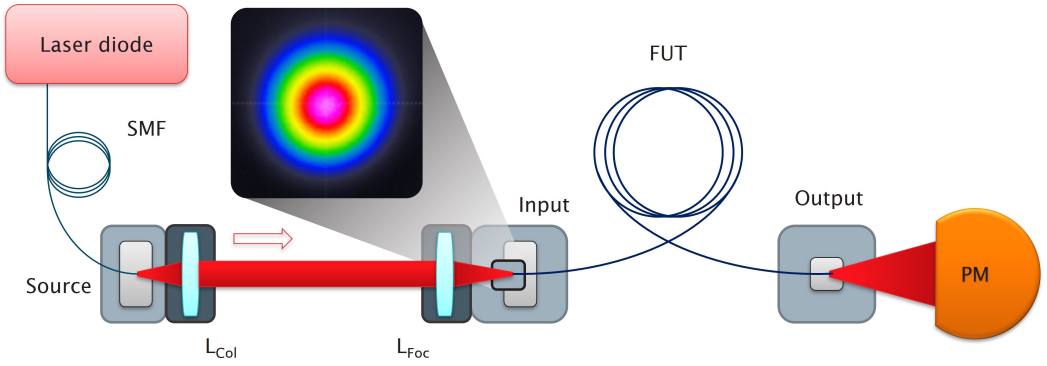

FIGURE 3.1: **Schematic of the experimental layout of the high-precision coupling setup |** The output of the diode laser is coupled directly via an FC/PCA connector to a mode-filtering loop (SMF). This patch cord consists of a tightly coiled PM-980 fibre which guarantees a quasi-single-moded (QSM) initial beam (the cross section of which is shown in the inset). The output of this patch fibre is mounted on the 5-axis stage (Source). The collimating (f_{col}) and focusing (f_{foc}) lens are chosen such that their combined magnification matches with the ratio of MFD of the SMF and fibre under test (FUT), and the separation of the lenses is approximately 30 cm. The re-focused beam is incident on the receiving input tip of the FUT, which is mounted on a similar 5-axis stage (Input). Finally, the transmitted beam is out-coupled (Output) and is measured by a photodiode power sensor (PM). More details are provided in the text.

for experimental realization by allowing to fine-tune the incident beam diameter in a straightforward way. Moreover, the output of the laser source needs no special preparation (compared to tapered nano-spike [76, 99], reverse tapered splice [100], or capped [101, 102] approaches as examples), and is similarly relatively less sensitive to unwanted environmental effects (e.g. vibrations and air convention). Furthermore, coupling in free space has the most potential for power-transmission scalability, as better thermal management of the coupling elements is possible in contrast to other approaches. At higher power levels, the inevitable (mostly absorption related) losses become more important to be handled appropriately. As thermalisation related issues are becoming more prominent a number of other possible coupling solutions — like low temperature gluing [102] or high temperature splicing [100, 103] to fibres — are yet to prove themselves as capable alternatives. The realized experimental setup based on these considerations, that has been used for the CE experiments will be introduced in the next Section.

3.2 Low power transmission setup

Figure 3.1 shows the schematic layout of the transmission setup assembled for the CE experiments. The laser source is a Bookham LC96A1060-20R laser diode (LD), emitting a $\lambda_{\mathrm{LD},\,0} = 1064\,\mathrm{nm}$ quasi-single-moded (QSM) beam — as defined in Subsection 2.2.3 — with $\Delta\lambda_{\mathrm{LD}} = 10\,\mathrm{nm}$ spectral bandwidth. Its average power level is set at $P_{\mathrm{LD},\,0} \approx 100.0 \pm 0.7\,\mathrm{mW}$. The output of the laser diode is connected to a PM-980 fibre that is commercially available ($d_{\mathrm{LD,\,core}} = 5.5\,\mu\mathrm{m}$, $NA_{\mathrm{LD}} = 0.12$).

The output of the LD patchcord (which terminates with a standard FC/APC connector) is mounted on top of an stage assembly, that incorporates a ThorLabs MicroBlock Stage (MBT616D/M) and a compatible Pitch and Yaw (P'n'Y) platform (APY002/M). The former allows the accurate alignment required in the 3 translational axes (XYZ), while the latter enables the adjustment of the angular directions along 2 angular axes (pitch and yaw), ensuring that the alignment of the launched beam is possible though a combination of 5-axes.

The collimating and the focusing lenses are two ThorLabs achromatic doublets, with focal lengths of $f_{\mathrm{col}} = 10\,\mathrm{mm}$ (AC080-010-B-ML) and $f_{\mathrm{foc}} = 50\,\mathrm{mm}$ (AC127-050-AB-ML), respectively, both with <0.5 % reflectance anti-reflection coatings at $\lambda_{\mathrm{LD},\,0} = 1064\,\mathrm{nm}$. This lens pair is chosen so that — assuming a typical collimating and refocusing layout depicted in Figure 3.1 — their magnification ($M_{\mathrm{Lens}} = f_{\mathrm{foc}}/f_{\mathrm{col}} = 5$) matches reasonably well with the ratio of the mode field diameter (MFD) of the incident beam, and that of the FM supported by the hollow-core test fibres. More specifically, these MFDs are $w_{\mathrm{LD}} \approx 6.6\,\mu\mathrm{m}$ and between $w_{\mathrm{NANF}} \approx 21 - 24.5\,\mu\mathrm{m}$, for the PM-980 fibre and the hollow-core NANF samples to be discussed in more detail in Section 3.3, respectively. The latter w_{NANF} range is estimated by the theoretical expectations, that is, the MFD is close to ~70 % of the core diameter for HCFs, when optimal coupling is achieved [123]. Consequently, a magnification corresponding to $M_{\mathrm{MFD}} = w_{\mathrm{NANF}}/w_{\mathrm{LD}} \approx 3.2 - 3.7$ is expected by using the aforementioned lens pair. The discrepancy between the magnifications M_{Lens} and M_{MFD} is then corrected by adjusting the exact position of both lenses along the optical axis. Based on a simple ray transfer matrix analysis, the required displacement of the lens pair to ensure better matching of the magnification values can be calculated. Finally, the lenses are fine-tuned, until the optimal transmission efficiency — and such, a corresponding coupling efficiency — is experimentally achieved. A magnified image of the intensity profile of the beam incident on the NANF as recorded by a CMOS detector is also shown by the inset on Figure 3.1.

Furthermore, the choice to employ the achromatic doublets introduced in the previous paragraph is made in order to reduce the impact of spherical aberration. The relatively short focal lengths of the optical elements allow the setup to remain compact. On the other hand, the small radius of curvature that would be required assuming that conventional singlets have been used, would introduce significant aberrations. Thus, increasing the number of refractions by utilizing the cemented achromats lessens the influence of these errors. Lastly, since only a relatively small power level of $P_{\mathrm{LD}} \approx 100\,\mathrm{mW}$ is incident on the lenses, any absorption related effects are expected to have minimal contribution, and as such can be neglected.

An identical stage assembly as described previously was also built to provide the same 5 degrees of freedom for alignment of the input of the fibre under test (FUT). Since the exact position of the output of the FUT does not require the same precision for appropriate power transmission measurements, a simple 3-axis translational stage provides

adequate alignment for the experiments. The fibre samples have been always cleaved with a Fujikura CT-100 precision mechanical cleaver, which can reliably and repeatably provide flat facet cleaves with <0.3° precision according to the specifications. Once both fibre ends are prepared, they are mounted on top of their respective mounting platform. As the PM-980 patch fibre is terminated with an FC/APC connector, no special preparation of the output of the laser-source is required.

Since the fibre samples can range between $10 - 2000\,\mathrm{m}$, they are either wound up on a commercially available plastic bobbin, or kept in a loose coil. Nevertheless, the coil diameter is always ensured to be >30 cm for all these cases, minimizing any possible macro-bending induced losses to a reasonably negligible level. Note that, as discussed prior in Section 2.3, HCFs are effectively single-moded only after a certain length of propagation. This is explained by the different attenuation of the different mode groups. As a result, in general, longer length of fibre pieces (usually >10 m) are used, when achieving a high modal purity is of importance. Furthermore, special care was taken during the alignment procedure of the setup, such that only the FM of the fibre samples will be excited, with minimal excitation of HOMs.

The optical power levels at different locations along the experimental layout are measured with a standard ThorLabs photodiode power sensor (S121C — labelled as PM) and a compatible console (PM100D) is used for data recording and calculating the relative statistics. The sensor head is always positioned such that the incident beam fills the same expanse on the detector surface, ensuring that power readings are reliably comparable by having reduced margin of error. In the following Section, the NANFs that have been used during data acquisition of the Thesis will be discussed.

3.3 Fibre samples

As mentioned in the previous Section, the optical elements responsible for highly efficient coupling of the laser source were chosen such that they are optimized for the fibre samples that are used in the experiments. In this Section, relevant NANF samples will be introduced. Furthermore, unless specifically indicated otherwise, this (NANF) geometry will be assumed during future discussions.

Table 3.1 summarizes the most relevant parameters of the fibre samples that has been used in the Thesis, while Figure 3.2 shows their respective cross sections and FM attenuation. It can be seen from the Table that such a simple geometry still has quite a few adjustable parameters. For instance, while keeping other parameters fixed, the impact of different membrane thicknesses (th) of the microstructure — and in turn the choice of optical transmission window for a given wavelength — can be investigated. This will be discussed in more detail in Section 3.5, comparing NANF-1 and NANF-2, which have thicknesses $th \approx 360\,\mathrm{nm}$ and $\approx 750\,\mathrm{nm}$, respectively. At the same time, it can be appreciated that all NANFs listed have comparable $d_{\mathrm{core}} \approx 29 - 33\,\mu\mathrm{m}$ core diameters. This

TABLE 3.1: Summary of the relevant characteristic parameters of the fibre samples used for the experiments discussed in the Thesis. More detailed discussions is provided in the text.

Parameter	**NANF-1**	**NANF-2**	**NANF-3**	**NANF-4**	**NANF-5**
Colour code [−]	Blue	Red	Gold	Black	Green
Number of tubular elements [−]	5	5	6	6	6
Antiresonance window order for $\lambda_0 = 1\,\mu m$ [−]	1^{st}	2^{nd}	2^{nd}	2^{nd}	2^{nd}
Avg. core diameter (d_{core}) [µm]	30.0	29.4	33.2	31.2	32.0
Avg. membrane thickness (th) [nm]	360	750	720	770	780
Avg. FM attenuation					
$\lambda_{LD} = 1064\,nm$ [dB/km]	1.58 ± 0.13	0.35 ± 0.05	–	–	–
$\lambda_{SPI} = 1075\,nm$ [dB/km]	–	–	0.56 ± 0.06	0.74 ± 0.05	1.29 ± 0.09

allows their respectively measured coupling and transmission efficiencies to be compared in a more justifiable manner when similar coupling conditions are present.

It should be also noted that this Table provides an exhaustive list of fibre samples that have been used for all the measurements and results to be discussed. As such, the corresponding labelling will be used in the rest of the Thesis. Similarly, unless specified otherwise, all fibre samples were always prepared using the same Fujikura precision cleaver. Lastly, the NANF samples undergo a brief inspection before the actual measurements take place. Once they are aligned for optimal transmission in the previously discussed setup, the fibres are checked for any substantial scattering visually observable using a commercially available IR viewer scope. After it has been confirmed that there are no localized defects in the FUTs, the pieces are considered to be ready for the appropriate experiments.

3.4 Misalignment sensitivity

Inspired by the work of Siwicki et al. on the coupling tolerances of ARFs [124], firstly, the required accuracy for highly efficient coupling has been investigated for in-house manufactured NANFs. As discussed earlier the input tip of the test fibre under examination is mounted on top of a stage assembly, enabling a 5-axes alignment procedure. This covers the 3 translational axes (XYZ) and 2 rotational axes (Pitch and Yaw), while the possibility of any adjustments along the 3$^{\text{rd}}$ rotational axis (Roll) is intentionally

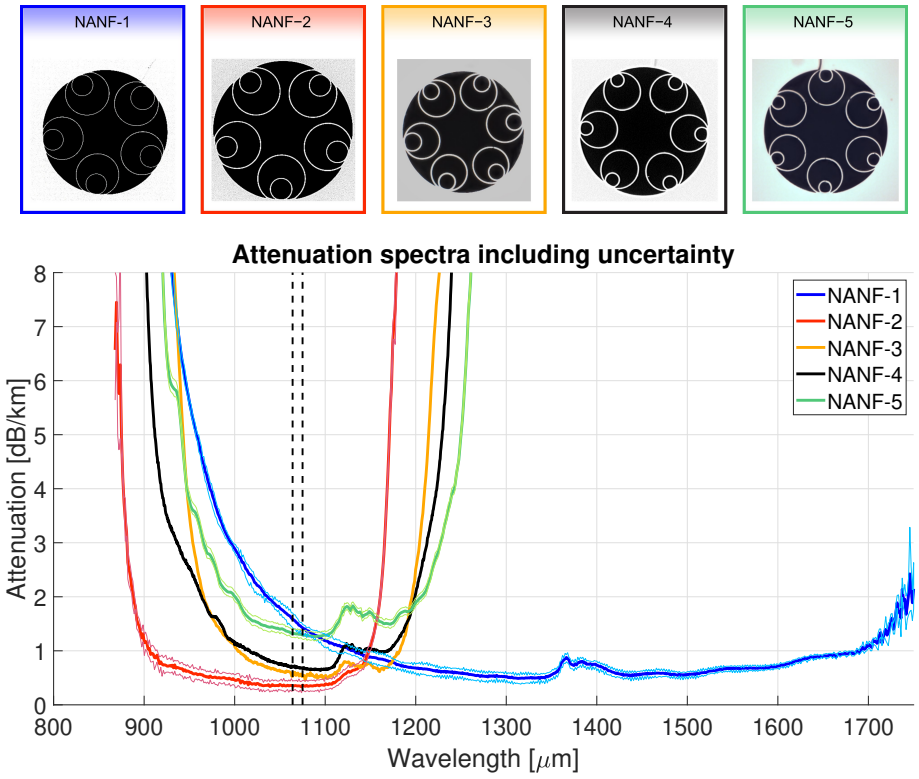

FIGURE 3.2: **Measured spectral attenuation of the used NANFs via the cut-back technique** | Spectral attenuation of the relevant NANF samples summarized in Table 3.1, as measured by the cutback technique. The length of the cutback lengths varies between $50 - 400\,\mathrm{m}$, depending on the specific fibre piece. The curves follow the same colour coding defined at the table; blue, red, gold, black, and green for NANFs 1-to-5, respectively. The lighter shaded boundaries surrounding the main curves illustrate the 1σ error bar of their respective averages. The vertical dashed lines marks the important central wavelengths of $\lambda_{\mathrm{LD}} = 1064\,\mathrm{nm}$ (left) and $\lambda_{\mathrm{SPI}} = 1075\,\mathrm{nm}$ (right) of the used laser diode and SPI fibre laser light sources, respectively. On the top, the corresponding cross sections recorded by scanning electron microscopy (SEM) are also presented.

excluded. This is justified in one part with the reasonable radial symmetry of the quasi-Gaussian beam of the laser diode used as the source for the experiments. Figure 3.3 illustrates the naming convention of these axes.

On the other hand, in order to support the omission of control over the 'Rolling' axis even further, a 3-paddle polarization controller by ThorLabs (FPC564) has been inserted between the laser source and the PM-980 patchchord. Initial power transmission tests with NANF-2 showed no significant dependence of the transmission efficiency on the polarization state of the laser beam — because of symmetry reasons, the other samples are also expected to show similar behaviour. This observation strongly suggest that the polarization dependent loss for these fibres are negligible, confirming that the 5-axes alignment stage is sufficient. For this reason, the polarization controller has been removed from the experimental layout before the measurements that will be discussed have been performed.

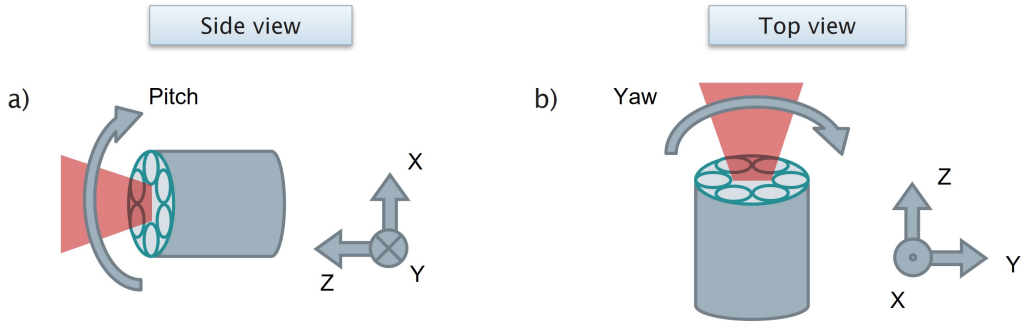

FIGURE 3.3: **Naming conventions for the 5-axis misalignments** | a) side and b) top view schematic of the receiving input fibre tip, respectively. The direction of the arrows points towards the positive change from the optimal position, which is set as the 0 reference value.

Considering first only the translational axes, they can be separated into 2 groups: (i) the axial component, and (ii) the lateral component(s), corresponding to 'Z' for the former and 'X' and 'Y' for the latter in Figure 3.3, respectively.

Taking the z_R Rayleigh length as a point of comparison, an estimate of importance for the respective misalignments can be provided, based on the definition of $z_R = \pi w_0^2/\lambda$, where z_R denotes the Rayleigh length, w_0 is the beamwaist, λ is the central wavelength of the field. Assuming $\lambda = 1064\,\text{nm}$ and $w_0 = 10\,\mu\text{m}$, which are relatively similar values to the cases to be discussed, the Rayleigh length is $z_R \approx 664\,\mu\text{m}$. While such a distance from the beamwaist along the z-axis would reduce the CE significantly, compared with a similar misalignment along the lateral direction would result in no coupling at all — assuming a typical core radius of $r_{\text{core}} \approx 15\,\mu\text{m}$. This more than an order of magnitude larger difference between z_R and r_{core} agrees well with the cited experimental results [124] as well. As such, the aim of my investigation has been set to concentrate on these 2 lateral (X and Y) translational axes, since their sensitivity towards misalignment also leave less room for error. According to the findings of [123], it has been stated that the best coupling is achieved, when the beam-core ratio — defined by the ratio of the MFD and the d_{core} core diameter — is ~70 %. As future results will show, the experimentally achieved CE values are in great agreement with the theoretically expected maxima. Therefore, it can be reasonably assumed, that the alignment procedure positioned the input of the FUTs, where this ideal ratio is obtained.

Secondly, it is only [124] that reports about investigating the influence of angular variations for HCFs in an actual experimental setup. While it is obvious that special care is always given to minimise such misalignments, a better understanding of the impact of them could be beneficial for numerous applications, where maintaining high CE is desirable. As an example, for high power applications precise and repeatable positioning of the input fibre tip is mandatory. Maximizing and preserving high CE, as well as managing misalignments are critical when intense laser fields are to be coupled into the fibres. This will be explored in more details in Chapter 4. Another specific scenario could be

the case when the fibre tip has to be precisely positioned inside a smaller chamber that contains micron-sized particles, with the intention that they can be optically trapped and propagated inside the HCF along its length. In this example accessibility of the input tip of the FUT is greatly limited, as it will be discussed in more detail in Chapter 5.

3.4.1 Angular tilt

The set of fibres that have been introduced previously in Section 3.3 have been first measured for their coupling tolerance towards angular misalignments. The best coupling positions are determined by optimizing all the available 5 axes, and are set as the 0 mrad reference positions. Then, the coupling is intentionally misaligned along the respective axes. First, the transmitted power levels have been recorded and the transmission efficiency values have been calculated. Then, the attenuation induced propagation losses has been accounted for, and finally, the CE values have been normalized with respect to the maximum. Figure 3.4 summarizes the results of the measurements conducted on 4 of the NANF samples summarized in Table 3.1.

Taking the work of Wagner and Tomlinson [98] on SM fibre coupling as a benchmark, Gaussian curves have been also fitted to the data points. The choice of a Gaussian fit is also based on their findings for spatial misalignments — i.e. translational and angular deviations — of the receiving fibre tip from the optimal position. The thick black curve shows the theoretically predicted sensitivity, based on the parameters set by the experimental layout (distance between receiving fibre tip and the surface of the focusing lens closest to it: ~35 mm, the estimated $1/e^2$ spot radius at that surface ~1 mm), for an arrangement of optical components with perfect radial symmetry, assuming an ideally matched proper beam-core ratio (~70 %). Because of symmetry reasons, the pitch and yaw axes are not differentiated for the theoretical curve.

Note, that assuming that only the FM of the FUT is excited and transmitted, the attenuation induced losses during propagation affects all measurements identically for the given NANFs, respectively. Because of this, it can be considered as a background offset that does not impact the coupling sensitivity in any significant manner, and could have been ignored. However, the impact of the attenuation, and more importantly the uncertainty of it can be clearly seen on the Figure, as for a longer length ($l \approx 800$ m) of NANF-1, the 1σ error bars near the optimal position of the input tip are visibly larger than the other FUTs. This could be improved by either using a shorter sample, or by more precise knowledge of the $\Delta\alpha$ uncertainty of the attenuation — the impact of the latter is visible when contrasted with NANF-2 ($\Delta\alpha_{\text{NANF-1}} = 0.13\,\text{dB/km}$, in contrast with $\Delta\alpha_{\text{NANF-2}} = 0.05\,\text{dB/km}$), as an example.

Examining the figure in more details, it can be observed, that on the one hand, the two different angular axes (pitch and yaw, plotted with solid and dashed lines respectively) show reasonable agreement, as expected from the symmetry of the cross sections of

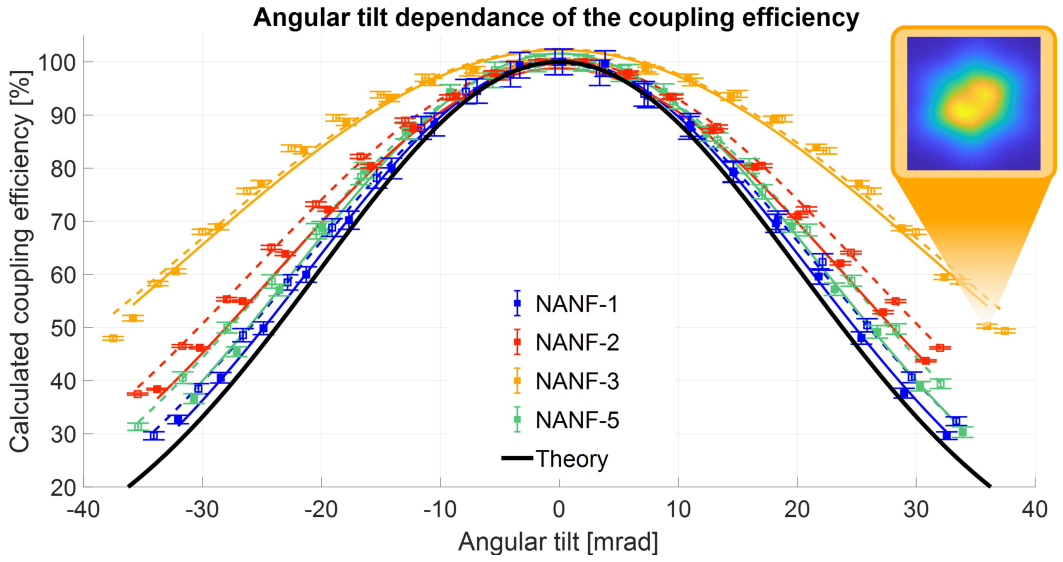

FIGURE 3.4: **Angular misalignment sensitivity plots of in-house NANFs** | Filled and empty boxes with error bars show the calculated CEs while the solid and dashed lines plot the fitted Gaussian curves, for the pitching and yawing axes, respectively. The thick solid curve illustrates the theoretical expectation based on equations provided in [98]. The visibly wider curve is attributed to HOM transmission, as suggested by the inset showing the transmitted beam distribution at the largest misalignment. More details are provided in the text.

the fibres. The minor discrepancy between the pitching and yawing angle can be an indication of some slight astigmatism inherent to the coupling setup. On the other hand, there is a clearly distinct difference in performance between NANF-3 (yellow) and the other 3 samples tested. NANFs 1,2, and 5 show better agreement with the theoretical expectations. However, NANF-3 visibly separated from the former group of samples. The most likely reason for this behaviour was considered to be related to observed transmission of HOMs by this fibre piece.

As an attempt to compare the curves quantitatively, the full width at half maximum (FWHM) of the respective plots were used as a figure of merit. The calculated values, as well as the lengths of the inspected fibre lengths are summarized in Table 3.2. While this measure is not intended to adequately characterize the acceptance range on its own — as this terminology cannot sufficiently account for multi-moded behaviour — it still can be used as a reasonable point of comparison. Losing half of the input power is absolutely unacceptable, especially for high power applications. For instance, at the 2 kW power level, a drop of ~2 % of the CE already translates to ~40 W of absolute power.

Comparing the FWHM of the different fibres, the slightly larger values for the yawing axis compared to the pitching axis could indicate minor experimental misalignments in the coupling setup — not related to the fibre samples. Furthermore, NANF-3 shows significantly larger value, up to 150 % of the other NANFs, while as mentioned, this is also attributed to the transmission of HOMs. As can be seen by the inset of Figure 3.4, when substantial misalignment has been introduced, the output beam of this specific fibre

TABLE 3.2: PnY results of own fibres including a 1σ confidence interval. Note that NANF-4 of Table 3.1 has not been tested. For comparison, values based on theoretical considerations [98] is also presented in the last column. More details are provided in the text.

Parameter	**NANF-1**	**NANF-2**	**NANF-3**	**NANF-5**	**W&T [98]**
Length of fibre samples used [m]	~800	~50	~400	~1200	N/A
FWHM of pitching angle [mrad]	49.53 ± 2.47	56.68 ± 2.88	75.01 ± 2.06	51.74 ± 0.82	44
FWHM of yawing angle [mrad]	52.20 ± 2.88	60.46 ± 3.70	76.49 ± 2.88	55.20 ± 3.29	44

was indeed, visibly different from that of a quasi-Gaussian — indicating a significantly lower HOM loss relative to the other fibres. This explains the larger relative power transmission for more significant misalignments, since the excited HOMs were not filtered out even after propagating a significant length (~400 m) through the fibre. Moreover, a similar conclusion was reached by [124], for the same characteristic feature observed. Unfortunately, no explicit data is available for the HOM loss values of those specific HCFs. A comparison with the results reported there is shown in Figure 3.5. Note that since the two different axes (pitch and yaw) show no significant differences, only one of them — pitch — is chosen to be plotted. Furthermore, in order to compare the results with those provided by Siwicki et al., the total transmission efficiencies will be compared for better clarity. The fibre samples detailed in [124] are:

i) ~10 m long step-index single-moded SCF (d_{core} ~5.8 µm),

ii) ~1 m long "ice-cream" cone type fibres (d_{core} ~25.0 µm), and

iii) ~40 cm long revolver-type tubular fibres (d_{core} ~23.8 µm).

While all plots are following the same trend, the results can be arranged into 3 different groups:

a) First, the ARF-2 curve (red dashed line) with the least sensitivity towards angular misalignments was attributed to the lack of optimization for single-moded guidance for that specific fibre before its fabrication. As mentioned before, this means that the HOM loss values for the fibre were not large enough to suppress the HOMs for the given fibre length, resulting in multimoded transmission. When put in contrast with the other HCFs by the authors, a similar behaviour can be observed as with the in-house NANF-3 and the other NANF samples.

b) Secondly, it has been debated the other HCFs tested by Siwicki et al. (ARF-1, ICF-1 and ICF-2, with purple, black and blue colours respectively) might still contain some HOMs, as they show similar behaviour to the in-house drawn NANF-3

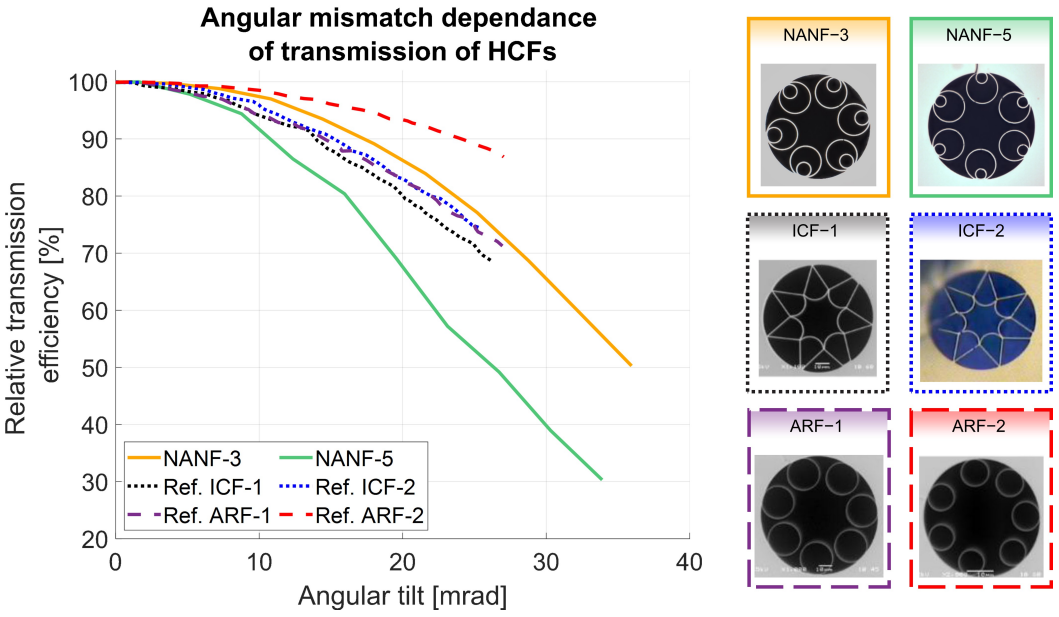

FIGURE 3.5: **Angular misalignment sensitivity plots in comparison to other relevant HCFs** | Solid, dotted and dashed curves illustrates the average relative transmission efficiencies normalized to their respective maxima, for in-house NANFs, Ice-cream cone type HCFs and single element revolver type ARFs from Siwicki et. al [124], respectively. For better readability only one direction of misalignment is shown. More detailed discussion is provided in the text.

(yellow), which is known to support multimoded transmission. Since unfortunately no exact description for HOM losses is provided for the quality of the transmitted beam, it cannot be concluded without a doubt.

c) Finally, the remaining curve (green, NANF-5) show high-brightness single-moded guidance. This is supported by the better agreement with the calculations from the theoretical expectations [98].

3.4.2 Lateral shift

A similar study, this time focusing on the lateral misalignment has been also conducted. Comparison is shown in Figure 3.6 including the corresponding cross sections of the respective fibres. Note that for an appropriate comparison of the impact of such misalignments, a correct figure of merit should also take into account that the core diameter of both solid- and hollow-core fibres considered can wary greatly. Following the works of Wagner and Tomlinson [98], it is feasible to normalize the translational changes to the size of the focused (to be coupled) beam waist. Since Siwicki et al. clearly took great care to achieve the best alignment possible, it can be safely assumed, that this translates to a case, when the beam-core ratio is ~70 % for HCFs, as suggested by [123]. On the other hand, for the step-index SCF, an MFD of 6.2 µm is used for the normalization, as provided by the manufacturer of the sample.

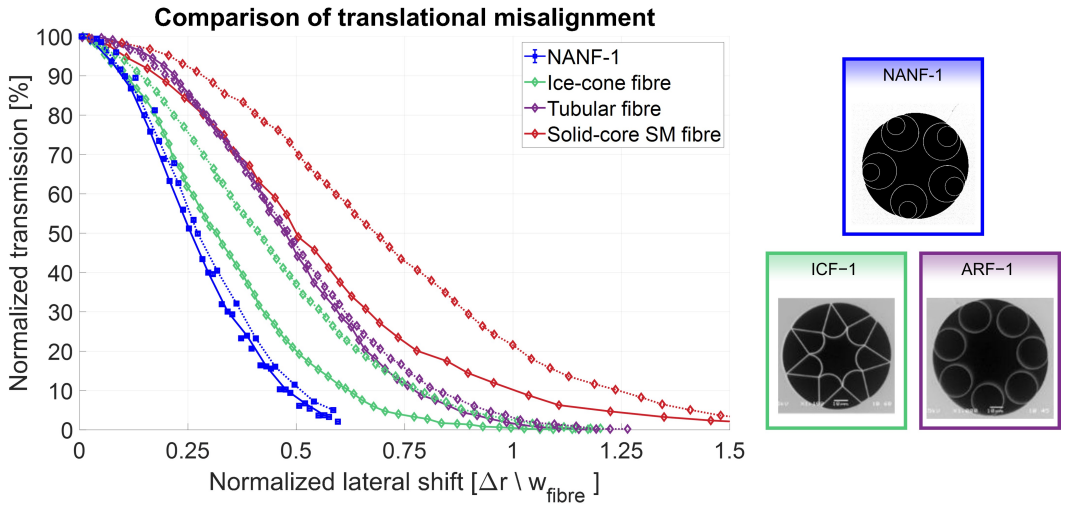

FIGURE 3.6: **Lateral misalignment sensitivity plots in comparison to other fibre types** | All lateral shift (Δr) data points are normalized to the beam waist (w_{fibre}) of the respective fibres, while the values recorded are normalized to the respective maxima. The blue curve shows the sensitivity of the in-house drawn NANF-1. Compared to that are plotted the SM SCF, (dark red), Ice-cream cone HCF (green), and single element tubular ARF (purple) from [124]. Solid and dotted lines represents displacements along the X (vertical) and Y (horizontal) axes, respectively. For more in depth discussion, see text.

As mentioned before, achieving and maintaining high CE is even more crucial for high power transmission, where the significantly more intense beam can overlap with the cladding structure more, and therefore it can possibly induce permanent damage as well. Moreover, since all in-house fabricated NANFs showed similar behaviour, only one of them (NANF-1, blue) has been included here. From Figure 3.6 it can be also seen that all the HCFs show slightly worse sensitivity compared to the SCF step-index fibre (plotted with dark red). The visibly different behaviour of the solid-core step index fibre is explained by 2 separate effects. Firstly, it is experimentally challenging to cover optimal coupling by matching the beam-core ratio to ~70 % for such a large distribution of core sizes ($6 - 25\,\mu$m). Because of that, it has been suspected that a certain degree of mode-mismatch could be present for the SCF, resulting a lower than expected transmission and in turn, sensitivity to misalignments. Furthermore, it has been argued by the authors of [124], that the different physical confining mechanism of SCFs and HCFs could also play a role. Additionally, it has been also considered that the stronger focusing might result in a beam that is incident on the fibre tip under an angle that exceeds its maximum acceptance angle supported by its NA.

The difference between the sensitivity of the X- and Y- axes (discerned by solid and dotted curves respectively) for the ICF and SCF fibres are claimed to be related to fibre structure variations in the referred article [124]. The difference between the ICF and ARF (green and purple) curves are claimed by the authors to be connected to their structural difference, i.e. the lack of nodes in case of the tubular ARF. Measurements

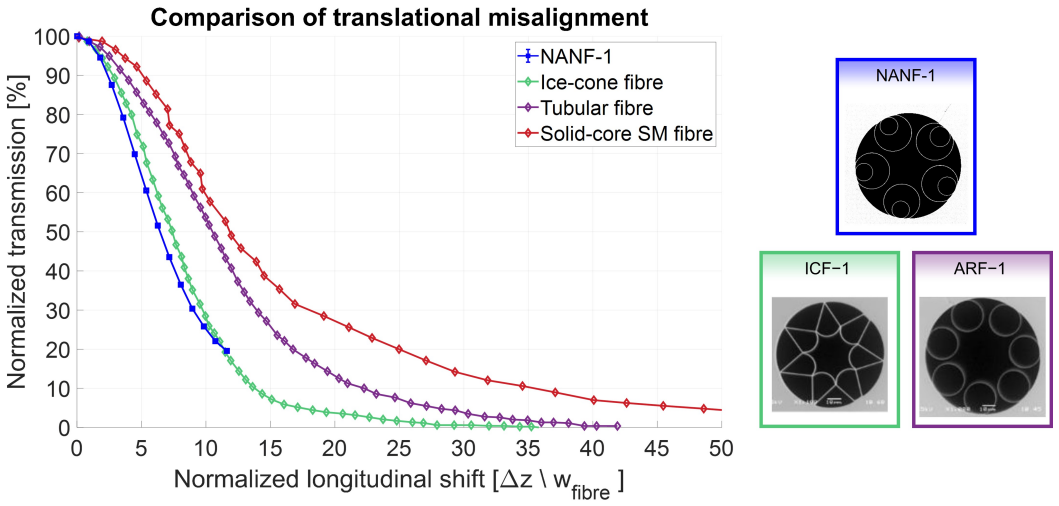

FIGURE 3.7: **Longitudinal misalignment sensitivity plots in comparison to other fibre types** | Complementary plot analogous to Figure 3.6, demonstrating the impact of longitudinal shifts (Δz) — normalized to the beam waist (w_{fibre}) of the respective fibres. The values recorded are similarly normalized to the respective maxima. The blue curve shows the sensitivity of the in-house drawn NANF-1, while the red, green and purple markers represents the SM SCF, Ice-cream cone HCF, and single element tubular ARF (purple) from [124], respectively. Note the scale of the horizontal axis. For more in depth discussion, see text.

using NANF-1 are shown with blue markers. The data shows a similar trends compared to the ice-cone HCFs, however, it also have better symmetry along the 2 axis.

3.4.3 Longitudinal shift

Analogously, misalignments along the optical axis have been also investigated, Figure 3.7 showing the corresponding curves. In this case, similar behaviour to that of Figure 3.6 can be observed. The most sensitive fibre piece towards misalignments along this axis is likewise the in-house fabricated NANF. On the other hand, the SCF sample seems to be the most resilient to such errors. However, it is important to highlight that here, the abscissa is more than 10-times larger compared to the lateral shifts. This practically translates to the fact that a slightly larger deviation in the longitudinal direction from the focal point still supports a relatively high coupling efficiency. It must be noted, that the reduced number of data points plotted — also covering a narrower domain — are limited by the resolution and travel distance of the mounting stage used in the experiments. Finally, as it will be discussed in Chapter 4, this greater tolerance will also results in the procedure of compensating for thermal lensing becoming easier to manage when kW-scale optical beams are coupled. Due to the fact that the induced focal shifts will not lead to instantaneous degradation of the coupling efficiency, the necessary corrections can be done manually even with a slight time delay present.

Lastly, it must be noted that the typical core diameters for all the HCFs discussed here — in both Subsections 3.4.2 and 3.4.3 — were $\sim 23 - 34\,\mu\text{m}$, while for the step-index

SCF it was closer to ~5.8 µm. These values correspond to supported w_{fibre} beam waists of ~16.6 – 22.4 µm for the HCFs, while, as mentioned earlier, it is closer to ~6.2 µm for the step-index SCF. Again, it must be noted that this could result in a less reliable comparison because of a wide range of core diameters covered.

Since the impact of misalignments have been discussed here, the influence of some of the main geometrical parameters of the NANF structure will be examined in the following Section.

3.5 Impact of the optical transmission window

As discussed in the theoretical introduction (Subsection 2.3.4), there are numerous proposals on how the performance of a HCF can be improved by careful engineering, which are supported by simulations [123]. However, as also mentioned, the actual realization (i.e. the fabrication) of such advanced fibres geometries suggested can become very challenging. In this Section, the influence of arguably the most principal parameter of the NANF geometry will be examined in more detail; the thickness (th) of the glass membranes of the microstructure (see Figure 2.4). It has been shown before — through Equations 2.14 and 2.15 — that this thickness can have a significant impact on the spectral transmission of a NANF. Additionally, it is also important, that which optical transmission window of the fibre does the λ_0 central wavelength of the laser source fall into.

It has been shown theoretically, that the order of the optical transmission window of any ARF — and by extension the NANF and DNANF geometries too — determines the maximum coupling efficiency achievable for the fibre considered [123]. Based on the findings of this cited study, I have conducted several high-precision experiments using the previously introduced experimental setup to verify these theoretical expectations [125]. The further expansion of the combined results of these conference proceedings have been also published in [126], and will be discussed in this Section.

Visually, the impact of using an optical transmission window of a different order can be seen on Figure 3.8. In this case, a 6-tube NANF with $d_{\text{core}} = 32$ µm core diameter is considered. Assuming an ideal lossless structure, the characteristics of different optical windows are demonstrated by shifting the λ wavelength of the field, while maintaining the th thickness of the antiresonant membrane constant — through Equation 2.15. Plotting the x-component on the electric field, it can be seen that for the 1$^{\text{st}}$ window, the field changes sign only once across the glass membrane, while for the 2$^{\text{nd}}$ window, this change happens twice. When comparing these fields with that of an ideal Gaussian beam as an example, whose magnitude does not change sign, it can be seen that the electric field for the latter case is better matched than for the former. This observation can be also extended to the higher order windows, however, the discrepancy between odd- and even-numbered windows will decrease as the order of the window order increases.

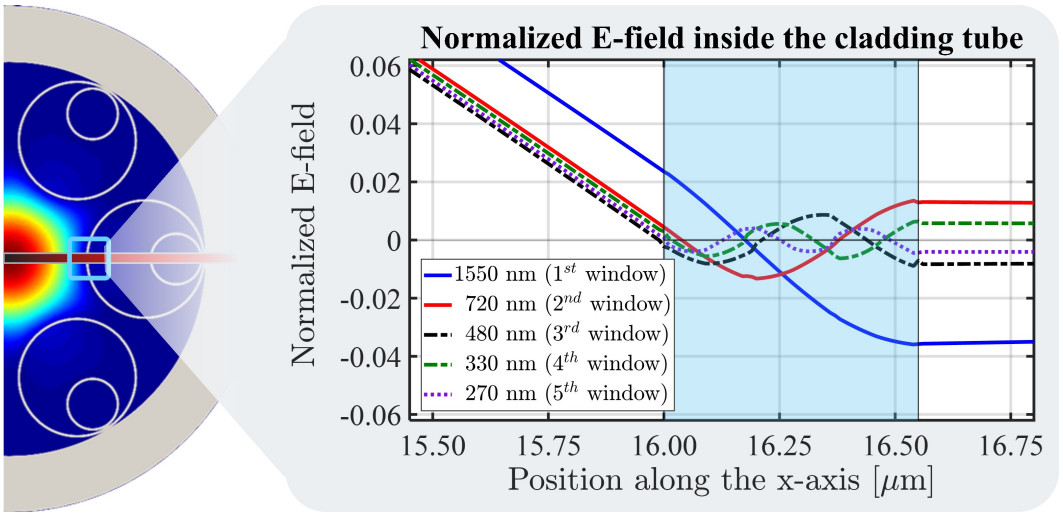

FIGURE 3.8: **Illustration of the electric field inside the glass membrane of an ARF** | Normalized electric field distribution of the fundamental LP_{01} mode of a typical 6-tube NANF. Highlighted are the curves of the x-component of the electric fields of different wavelengths, corresponding to different optical windows, along the marked cut of the fibre cross section. It can be seen that the electric field changes sign an m-number of times inside the cladding membrane (illustrated by the light-blue section), where m is the order of the respective transmission window. These curves show an increased overlap with a strictly-positive Gaussian distribution for the case of even-numbered windows, with the best fit correlated to the 2nd order. (Figure adopted from [126]

Also influential is the role of the number of nested tubes. Again, for operation in the first window, the same argument leads us to conclude that coupling efficiency into the simple ARF would be the lowest. The NANF geometry (with 1 nested element) improves this slightly as the field would change signs twice as it crosses the two membranes and a DNANF (with 2 nested elements) would again see a slight decrease in coupling efficiency, although the difference would grow smaller as the number of nested tubes increases.

As can be seen from Figure 3.8, the biggest contrast is present between the 1st and 2nd windows, and can be as high as 1.4 percentage point (p.p.). It is also clearly visible that the higher order windows (3rd, 4th, and so on) do not suggest better overlap and in turn, better coupling performance. Ultimately, we can conclude that the most effective way of optimizing the CE for a specific application is to operate in the second 2nd window. Therefore, I will use two NANFs, which operate in the 1st and 2nd antiresonant windows for $\lambda = 1064\,\text{nm}$, respectively, to compare this theoretically predicted 1.4 p.p. discrepancy, with what is experimentally measurable. These samples have been introduced in Table 3.1 — labelled NANF-1 and NANF-2. They will be colour-coded by red and blue, respectively, for the rest of this Section.

3.5.1 Methodology

Using the same experimental layout introduced and discussed in detail in Section 3.2, the fibres are prepared according to the standard procedure mentioned in Section 3.3,

and are mounted on top of the 5-axis assembly. In order to demonstrate the reliability and repeatability of the measurements, a set of 4 independent cleaves are used as inputs for 4 individual experiments with identical coupling conditions. After each cleave, a slight re-alignment of the input fibre tip to the incoming beam is required to optimize the power throughput, which will be referred to P_{out}. Similarly, the P_{in} reference input power is measured by removing the FUT, and positioning the power meter at a position after the focal position of the lens assembly, such that the beams incident in the 2 cases had identical spot sizes, minimizing any error related to the spot size and spot position on the detector surface.

Each individual experiment is recorded over a time window of ~30 s, corresponding to ~5000 data points in order to provide a data set that enables quantifying and averaging of the instabilities of the light source. Once the total measured transmission efficiency M-TE $= P_{\text{out}}/P_{\text{in}}$ has been recorded, the calculated coupling efficiency is extracted by excluding the propagation loss accumulated over the length of 10 m. This procedure has been performed for both FUTs of the same length, for the NANF-1 and NANF-2 samples, respectively. Once the propagation losses are accounted for, the calculated experimental results can be compared with the theoretical expectation, detailed in the next section.

3.5.2 Results

After recording the output power for 4 separate input cleaves, I calculated the transmission efficiency as the ratio between the P_{out} output power and the P_{in} reference input power. The average CE was then extracted from the transmission efficiency by accounting for the average loss accrued after propagation over 10 m of fibre. The propagation efficiencies (including the uncertainties) were calculated from the values in Table 3.1 to be 99.60 ± 0.03 % and 99.92 ± 0.01 % for NANF-1 and NANF-2, respectively. It can be seen that the contribution of the attenuation can account for a measurable (~20 %) portion of the expected CE difference (0.32 p.p. compared to 1.4 p.p.) between the 2 fibres. Separating the losses experienced during propagation (by assuming Gaussian propagation of error) leads to the calculated coupling efficiency values of 93.3 ± 0.3 % and 94.7 ± 0.3 % for samples NANF-1 and NANF-2, respectively, showing an average difference of 1.4 p.p. or 1.5 % relative change.

Figure 3.9 illustrates my measurement results in terms of the FM CE of the fibre samples. The results shaded in blue correspond to NANF-1 whiles those in red correspond to NANF-2, respectively. Moreover, the different hues indicates the results of separate measurements (input cleaves $1-4$). After post-processing the recorded power values over the mentioned 30 s time windows for each cleave, such that the propagation losses are accounted for, I grouped the corresponding CE values shown on the x-axis into 0.125 % wide bins for better visual representation. The count percentages along the y-axis refer to the number of occurrences of the given average CE value of the bins, relative

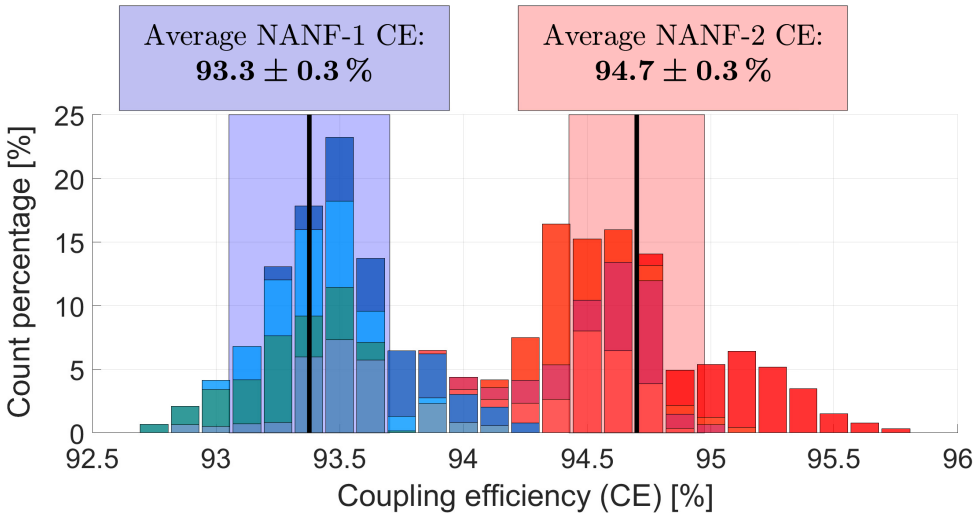

FIGURE 3.9: **Histograms of the coupling efficiency** | The y-axis covers the counts of coupling efficiency recorded for given bins for each fibre piece, blue and red for NANF-1 and NANF-2, respectively, each bin aggregating a range of 0.125 %. The different colour shades illustrate the results from independent experimental conditions. The average across all measurements and confidence interval is highlighted with thick black lines and shaded backgrounds, while the corresponding numerical values are shown above the respective histograms. The uncertainties arise from the power fluctuations of the source.

to the total number of sample points for the respective NANF. Records from different experimental conditions, i.e., individual precision cleaves and re-optimized alignment, are contrasted by the distinct colours shown on the stacked bar chart. Highlighted on the labels are the average experimental results of 93.3 ± 0.3 % and 94.7 ± 0.3 % for NANF-1 and NANF-2, respectively.

This measured CE difference of 1.40 ± 0.06 p.p. already shows excellent agreement with the theoretically predicted 1.4 p.p. reported by the simulation of [123]. However, the achievable maximum CE values quoted there are 97 % and 98.4 %, respectively, for 1st and 2nd window NANFs — while only 93.3 % and 94.7 % CEs were measured experimentally, respectively. This ~3.7 % discrepancy is assumed to be related to the fact that the simulations assumed a perfectly symmetrical Gaussian beam, and flawless microstructure. The difference between the previously presented measurements and the earlier theoretical predictions can be explained by the shape of the laser beam which is in fact not an ideal Gaussian, and the cross section of the fibre, which also includes some minor variations.

To verify this hypothesis, a finite element simulation has been repeated by colleagues in the group for the CE calculations with updated inputs: the FM distribution supported by the fibres were determined based on their parameters defined by the SEM images — also depicted in Figure 3.2. Similarly, the electric field distribution was provided by capturing the output beam using a CMOS camera. Using the same optical elements, the beam had to be magnified in order to ensure an adequate resolution of the distribution

for the numerical simulations. The CE maxima from these simulations — which are now based on measured properties of the experimental setup — are 93.2 % and 94.5 %, for NANF-1 and NANF-2 respectively, indicating a difference of 1.3 p.p., or 1.4 % relative deviation. These values show remarkable agreement within 1σ error with the experimentally measured 93.3 % and 94.7 % CE values, and a difference of 1.4 p.p., or 1.5 % relative deviation. Similarly, the findings also confirm the role of both the asymmetries in the cross section of the fibre, as well as in the profile of the experimental laser beam.

3.6 Conclusion

In summary, by using the NANF structure as an example, I have experimentally shown that a CE of 94.5 % can be achieved. In order to attain such a high value, it is important to realize and maintain adequate coupling conditions of the setup and the delivery fibre. Based on prior theoretical expectations suggested by simulations [123], I have built an experimental layout capable of verifying these predictions. I have measured the coupling efficiency into two nearly identical NANFs fabricated in-house and operating at 1064 nm in the first and second antiresonant windows, respectively. My results verified the difference in CE between these fibre samples, also showing great agreement with the theory. Of particular relevance, I have identified for the first time the advantage of launching into the 2^{nd} optical transmission window. Additionally, theory suggest this is the highest CE achievable utilizing any of the transmission window orders.

Note that the seemingly negligible 1.3 p.p. or ~0.06 dB difference in coupling loss between the first and second window is comparable to the loss incurred by propagation in as long as 350 m for a fibre with attenuation of 0.174 dB/km — the lowest experimentally measured value reported [36]. While there has been tremendous amount of improvement in the HCF fabrication processes to accommodate the transmission of more commonly used optical beams, there is still room for improvement, and further progress is expected, as claimed by the authors.

The next Section concludes the Chapter by providing a few examples, where the findings presented can be valuable.

3.7 Outlook

The results presented here show that using NANFs, and in theory by extension other antiresonant fibres operating in their second antiresonant window, are the preferred choice for various applications where coupling efficiency into the fibres is critical. One such example where the findings can be beneficial is the PoF concept [10], as mentioned in the Introduction. Furthermore, exploring the coupling and delivery of other, more exotic beam distributions, such as optical vortex beams, is also a recent, emerging field of study. This example has already found application in areas such as laser micromachining

or optical trapping and manipulation using HCFs [127]. Lastly, using different optical windows might be favoured in specific cases. It has been shown that using the 1st optical window allows the transmission of a wider spectral broadband — as can be seen in Figure 3.2. Moreover, such fibres also provide better draw yield [65]. The advantage of using other higher order windows over the previously mentioned ones are yet to be recognized and capitalized on.

For the scope of this Thesis, however, the results are invaluable for high-power laser delivery, where HCFs promise to be the next generation solutions [94]. In this latter application, optimizing the launch efficiency not only ensures delivering the maximum power from the source to the work-piece, but also helps simplify heat management and avert damage to the fibre by light not captured by the fibre's modes — i.e. the FM. In fact, one of the main driving forces behind the investigations presented in this Chapter was to establish a strong and reliable foundation for delivering kW-scale average power beams through the novel NANFs. Thus, the following Chapter is dedicated to discussions about the research leading to the demonstration of long-haul high-power delivery of such scale.

4 High power transmission experiments

Building on the results of achieving high coupling efficiency (CE) — as presented in Chapter 3 — here, the prospect of high-power transmission of high-brightness CW laser beam through hollow-core fibres (HCFs) will be considered. As mentioned in the Introduction (Chapter 1), one of the greatest potential of HCFs is the unique feature of having a material-less core. This enables significantly larger power levels to be delivered practically penalty-free, in sharp contrast to their solid-core fibre (SCF) counterparts. A number of applications, like subsurface rock drilling [128] or high-speed lithium ion battery welding could benefit from employing the HCF technology.

In this Chapter, the upscalability of power transmission through HCFs — more specifically through in-house fabricated nested antiresonant nodeless fibres or NANFs — will be analysed. First of all, the used experimental setup will be introduced. This will be followed by presenting the latest state-of-the-art results; the transmission of 1 kW average optical power beyond the distance of 1 km. After evaluation of the measurement data, relevant limiting factors (i.e. absorption related degradation) will be identified. Besides the experimental results, insight provided by simulations will be also discussed. The proposal of extracting the excess cladding light as a technique to enable further scaling of power delivery by overcoming the previously mentioned boundaries will be investigated and characterised experimentally. Findings will show that the suggested approach is practically applicable and it demonstrates improved transmission with better handling of the observed thermal effects, enabling the stable coupling of the available 2 kW average power, and its delivery over 10 m. Finally, the Chapter concludes with a brief summary and outlook at possible future works and applications.

4.1 High power delivery layout

The schematic layout of the high-power delivery (HDP) transmission setup used for the experiments is shown in Figure 4.1. For safety measures the entire arrangement has been built inside an interlocked enclosure, such that the system can be operated remotely during experiments. The laser source is an SPI 2kW QUBE CW fibre laser, with a central wavelength of $\lambda_0 = 1075\,\text{nm}$, providing a beam via a SCF delivery fibre with $d_{\text{SPI}} = 20\,\mu\text{m}$ core diameter and $\text{NA}_{\text{SPI}} = 0.075$ numerical aperture. This output is terminated with a water-cooled, thin, plane-parallel beam-delivery optical (BDO) glass window, which protects the delivery fibre connected to the source from any contamination. The maximum available output of the laser is limited at $P_{\text{SPI,max}} \approx 2.2\,\text{kW}$.

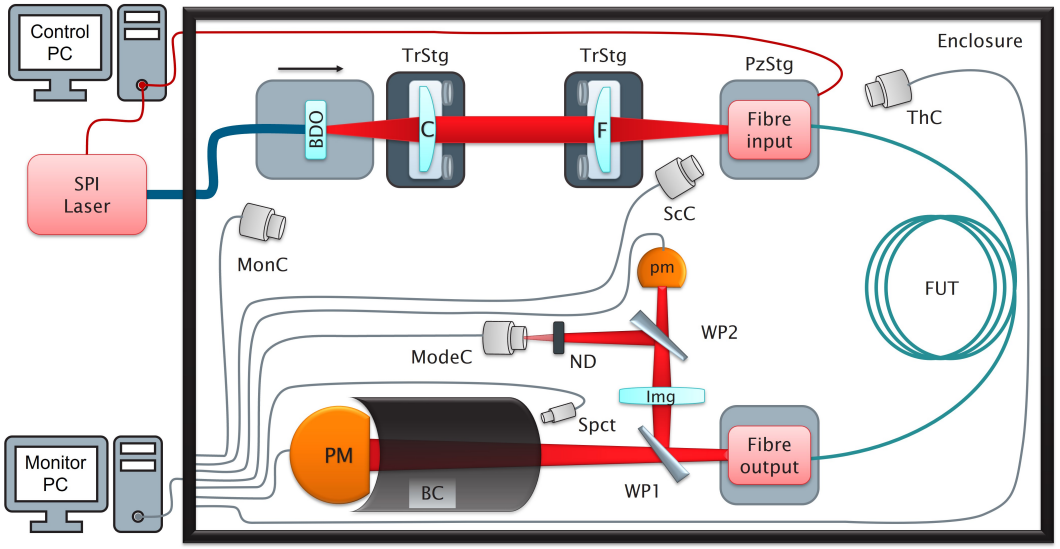

FIGURE 4.1: **Schematic layout of the HPD transmission system** | BDO: Beam delivery optics, C: Collimating lens, F: Focusing lens, TrStg: Translation stage, PzStg: Piezo stage, FUT: Fibre-under-test, ScC: Input scattering monitor camera, ThC: Thermal camera, MonC: General monitor camera, ModeC: Output mode detector, Spct: Spectrum sampling fibre, connected to the optical spectrum analyser BC: Beam path covering screen, WP1 and WP2: Wedge pairs (for better visibility, only one of each pair is illustrated) , PM and pm: Power meters, ND: Neutral density filter. Control and Monitor PCs are also included, summarizing the remotely controlled and monitored components, respectively.

The diverging beam is collimated (C) and refocused (F) using commercially available UV graded fused silica (UVFS) plano-convex singlet lenses from ThorLabs. These optics are coated with -YAG anti-reflection (AR) coatings (providing lower, sub-0.3 % reflectance at the wavelength of 1075 nm, than the broadband alternative) and have focal lengths of $f_{\mathrm{col}} = 50\,\mathrm{mm}$ (LA4148-YAG) and $f_{\mathrm{foc}} = 75\,\mathrm{mm}$ (LA4725-YAG) respectively. The choice for the focal lengths is analogous to the case of the low power laser diode experiments discussed in Section 3.2. However, in this instance relatively high CW power levels — beyond 1 kW — are expected to be incident on the optical components. Therefore the absorption of these lenses become crucial, presenting an important difference to the experiments detailed in Chapter 3. For this reason, singlets were preferred, allowing the thermalisation and consequently the temperature induced changes to be more homogeneous. The predicted worsening of spherical aberration in the system is then partly compensated by employing lenses of larger diameters. Utilizing only the central segment of the optical elements, the marginal part of the beam experience smaller deviation, which is favourable, as the spherical aberration is directly proportional to the 4^{th} power of the distance from the optical axis. Both lenses are mounted into low distortion Polaris Kinetic Mirror mounts with minimal thermal hysteresis, which are fixed on top of two, separate, 3-axis ThorLabs translation stages (TrStg). Finally, the focused beam is coupled into the fibre-under-test (FUT), which is fixed on an in-house water-cooled

V-groove atop of a 3-axis translation stage with stepper motors and piezo actuators (PzStg).

It is worth noting here, that for alignment purposes, a different, dedicated laser of the SPI QUBE has been used. This secondary source shares the delivery fibre with the main beam, however, its maximum output power is limited below 1 mW. Moreover, its central wavelength is ~650 nm. The combination of these 2 parameters enabled a more practical approach to align the system, since a beam can be provided, even when the safety enclosure is open. Following the same procedure, as discussed in Section 3.2, optimal coupling conditions can be established. It is evident, however, that in this case, the optical components will be aligned for the aforementioned visible source. By calculating the optimal lens positions for the wavelengths of the alignment and the main laser, the difference of the lens positions for both of these scenarios can be easily determined. Following the adjustment of the lenses to be optimized for the latter 1075 nm beam, the system is confirmed to be aligned for high power operation.

The input end of the FUT is stripped longer than usual of its coating (for ~10 cm), ensuring proper thermal connection and heat management along the entire length of the V-groove. This is crucial, as the fluence of the beam is the highest in this segment of the fibre. Any light that is not coupled in here could be incident on the V-groove indirectly, and such its cooling is advantageous. The FUT is mounted using Kapton-tape as shown in the photo of Figure 4.2 a). This both assures mechanical fixing and helps to achieve better thermal conduction. The latter is due to the fact that a single piece of Kapton-tape has a thermal conductivity of $k_{\text{Kapton}} \approx 1.75\,\text{W}/(\text{m}\cdot\text{K})$, compared to the $k_{\text{air}} \approx 0.25\,\text{W}/(\text{m}\cdot\text{K})$ for air, an approximately 7-fold increase, assuming an ambient temperature of ~20 °C [129]. Note, however, that overlapping a number of Kapton-tape pieces did not provide any additional benefit.

As mentioned in Section 3.4, the input tip of the FUT should be as close to the edge of the mounting as possible for minimal bending. However, the Kapton tape also should not be placed too close to the source-side edge of the water-cooled V-groove, as that could lead to overheating of the tape, ultimately resulting in a breakdown of coupling and permanent fibre damage. In practice, the most stable operation was achieved, when <1 mm of the fibre tip was sticking out of the V-groove. Additionally, the first few mm's of the stripped fibre was only in contact with the V-groove and the ambient air, while the rest of the uncoated section was secured with the Kapton tape — similarly to what is depicted in Figure 4.2. Since the entire setup is enclosed during operation, the final 3-axis stage (PzStg) is also remotely controllable.

Note that, opposed to the experimental setup presented in Section 3.2, this layout lacks the 2-angular axes of alignment of the input tip of the receiving FUT. However, the employed Polaris mounts can practically fulfil the same purpose in this case, as the coupling optical lenses can be adjusted along the angular axes if necessary. Moreover, as it will be

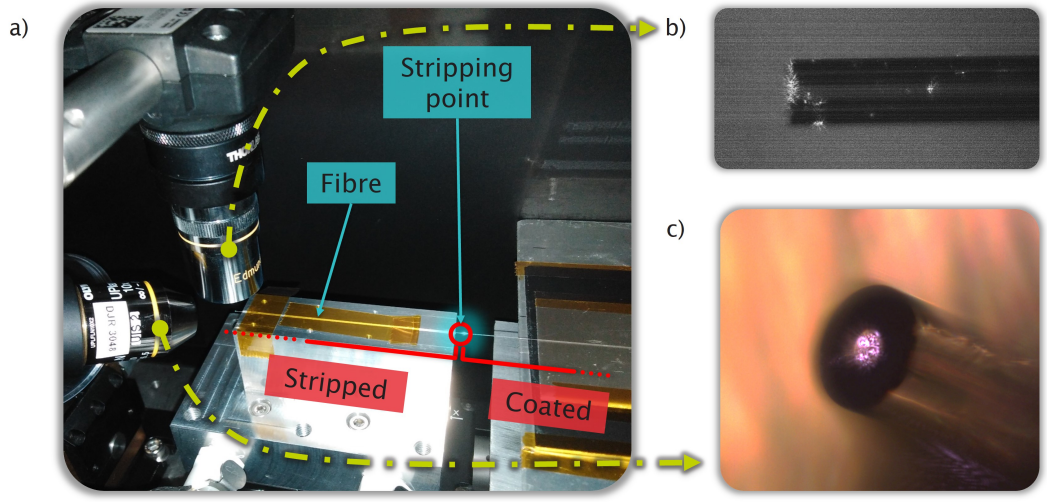

FIGURE 4.2: **Input tip monitors** | a) Photo of the water cooled V-groove mount, with a sample fibre piece mounted on top of it. Blue labels mark the position of the fibre piece and the location of the stripping point, before which the initial section is stripped, while the following length still has its protective coating on. These segments are also highlighted with red indicators. The 2 cameras with microscope objectives, monitoring the scattering (ScC in Figure 4.1) from the top and from the profile are visible on the left hand side of the photo. Illustrations of typical images captured by the b) top and c) profile cameras also indicated by the arrows during operation. The scattering of the incident beam is observable by the brighter white and purple sources respectively.

shown in Section 4.2 and later in Section 4.5, the measured transmission efficiencies, and in turn the calculated coupling efficiency (CE) values are in great agreement with the respective maxima predicted by the theory. This indicates that the coupling conditions are close to the experimentally attainable optimum. Based on these points, it has been concluded that the realized experimental setup can satisfy the precision and accuracy needs of the NANF samples (detailed in Section 3.4), which are essential to achieve and maintain high (>95 %) CE.

Several diagnostic cameras have also been installed to monitor the system during operation. Scattering at the input of the test fibre is recorded using 2 ThorLabs CMOS cameras, equipped with a microscope objective (ScC). One of the cameras provides a top view of the input tip, while the other one captures the scattering from its profile. An example for each of the scattering images as seen by the monitoring devices during operation are shown in Figure 4.2 b) and c), respectively. Here, the bright white and purple areas highlights the sources of scattering for the cameras, respectively. Note, that these illustrations were captured at low power demands for better visibility, since at higher levels, stronger attenuation before the detectors are required to avoid the saturation of the cameras. Lastly, the temperature of the initial segment of the fibre is captured with a FLIR A-300 Series thermal camera (ThC), while the entire setup is also constantly monitored using a commercial web camera (MonC).

After being propagated through the fibre, the out-coupled beam is first incident on the primary wedge pair (WP1). Most of the power is transmitted by the pair, and without any other intermediate optical element, it is collected by a water-cooled Gentech Power Meter (PM). Furthermore, this high power beam path is also covered with anodized aluminium screens (BC) in order to block any unwanted scattering, protecting the other devices of the setup. On the other hand, the reflected beam from W1 is then focused with a $f_{\mathrm{Img}} = 60\,\mathrm{mm}$ bi-convex lens (LB1723-B) labelled (Img). A secondary wedge pair (WP2) transmits most of the remaining power to a S130C ThorLabs power meter (pm). This secondary power meter can measure significantly smaller power fluctuations and have a faster response time compared to the main PM. These characteristics allow more delicate optimization and operation of the system by providing feedback with higher resolution. Finally, the reflected beam from WP2 is attenuated with a neutral density filter (ND), before it is incident on a HAAS camera (ModeC), which records the transmitted near-field beam profile. Note, that for better readability, only one of the WP wedge pairs is shown in Figure 4.1.

Furthermore, the spectrum of the transmitted beam is also recorded using a commercial multimode fibre (Spct) pointed at the Gentech power meter, that captures the scattered light from detector's surface. The fibre is connected to an ANDO AQ6317B optical spectrum analyser (OSA) which can cover the 600 to 1750 nm wavelength range. All monitoring and diagnostic devices are displayed continuously during operation. Based on the feedback provided by them, the input tip of the fibre under examination is constantly kept at an optimal position (remotely and manually, without any dedicated automatic software) to maintain maximum transmission. Once the highest coupling efficiency is achieved, the power level of the source is gradually increased.

As for recording the reference input parameters (e.g. output spectra of the laser source and power calibration of its control software), a commercially available broadband dielectric mirror with >99 % reflectivity is introduced before the focusing 2^{nd} lens. This way the beam can be steered such that it directly illuminates the water cooled power meter. Adjusting the position of the collimating 1^{st} lens, it is possible to ensure the same beam diameter incident on the detector, as it is during the transmission experiments. Correspondingly, the Spct fibre tip collecting the scattering from the detector surface is also re-positioned. These steps allows reliable comparison of both the power levels and the spectra recorded, in a similar manner, as discussed previously in Chapter 3.

It is also worth noting here, that the experimental setup presented in Section 3.2 also provides a convenient platform to review the fibre samples. As part of the fibre preparation procedure, it is a mandatory step prior any high-power experiment, to examine every fibre sample to be tested. This is practically done by observing the FUT with a commercial infrared viewing scope (IR-viewer), when low average power (<100 mW) light is coupled. As the fibre is transmitting the coupled beam, its outer surface can be observed along its tangent — from the direction opposing the direction of propagation

— with the IR-viewer. If any increased scattering is noticed, further checks are required. Initially, the degree of the localized loss induced thermalisation has to be characterised. This is practically done by focusing the thermal camera at the suspected point of defect, and monitoring the induced temperature increase when a relatively low power of the SPI laser source is being coupled (less than a few hundred W's). By extrapolating, the expected peak temperature at maximum power demand can be estimated. If this value is above what is determined to be the maximum temperature of safe operation (~100 °C), an approximately ~1 m segment that includes the localized defect has to be cut from the fibre sample.

4.2 1st Generation results

Using the experimental layout previously introduced in Section 4.1, the power delivery performance of some of the fibre samples have been examined. In general, all high-power measurements were terminated at their respective power level because of one of 3 main reasons: i) optimizing the position of the input fibre tip was not sufficient to regain an acceptable transmission efficiency, ii) temperature values on the thermal camera reached >70 °C, which was agreed to be a safety limit, or iii) small particles captured by the laser light propagating along the fibre lengths became dangerous by blocking or absorbing too much power (and possible threatening causing damage in the fibre). The latest point will be examined in more detail in Chapter 5.

1001m transmission

First, the performance of NANF-4 (see Table 3.1 for reference) has been analysed. The original total fibre length for this piece was ~1010 m. However, a small localized defect had been observed during inspection with a low power laser diode, ~300 m from one end, which had to be cut out. In an attempt to demonstrate delivery over 1 km of distance, the 2 (now ~300 m and ~700 m) pieces were fusion spliced together, resulting in a final re-combined length of 1001 m. The splicing was performed with great care, using a standard arc-fusion splicer, and the localized splice loss were estimated to be ~0.1 dB. For safety reasons, the 2 bands were kept in a free-coil arrangement, with bend diameters $D_{\text{bend}} > 30$ cm, while the splicing point was submerged in water, in order to guarantee better local heat dissipation. *The results to be presented here have been also published in* [94].

The transmission efficiency over ~1 km of the NANF-4 fibre is shown in Figure 4.3. Absolute transmitted power levels (P_{out}), as well as calculated transmission efficiency values (TE) of a given input power level (P_{in}) are presented corresponding to the left vertical axes, with black and blue, respectively. Moreover, the secondary, right hand axis also shows the peak temperature measured at the initial section of the fibre. The black markers show a highly linear correlation between the input and the output power levels, which can be examined in more detail by observing the blue TE curve, calculated

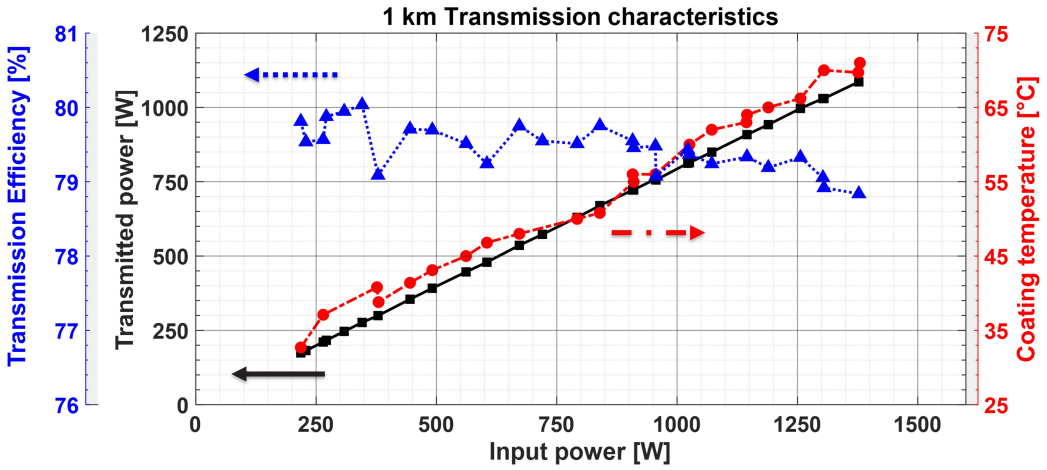

FIGURE 4.3: **Characterization plots of the** 1 km **transmission measurement** | Black markers connected with solid lines show the transmitted power of the 1 km long NANF piece, as a function of the coupled input power, displaying good linearity. The corresponding transmission efficiency is shown with blue markers connected by dotted lines, indicating only a ~1 % reduction over the entire ~1.3 kW power demand range. Red markers joined by dash-dotted lines indicate the measured peak temperature values of the initial section of the FUT, suggesting a similarly linear dependence on the input power. All data points correspond to their respective vertical axis of the same colour which is also indicated by the respective arrows with corresponding line styles.

by the ratio of the power values. Note that the slight sawtooth-like behaviour of the TE displays qualitatively the previously briefly mentioned procedure; that is, as higher optical power levels are being transmitted through the coupling optical elements, the phenomenon of thermal lensing begins to appear. This is observed by a small, but noticeable (~1 to 2 %) drop in the transmission efficiency. Nevertheless, the lost TE can be recovered by repositioning the input fibre tip, until the coupling conditions are optimal again. Ultimately, however, above some characteristic threshold input power, the realignment procedure gradually restores a smaller fraction of the lost power. Consequently, the CE progressively starts to decline, until the maximum achievable efficiency is considered hazardous, and the experiment is stopped. Note that the specific value of this threshold can depend on many factors, from the optical properties of the coupling elements to the modal loss of the FUT — in this case it is concluded to be ~1300 W. The relatively small (~1 %) variation in the measured TE is explained by a rigorous and frequent re-alignment approach that was taken during the experiments.

Examining of the practical considerations of the setup, two important points have to be mentioned. First, since optical power levels on the kW-scale are coupled into the FUTs, exceptional care was taken to maintain the input facet in immaculate condition. This was generally achieved by conducting the high-power experiments on fibre samples with fresh cleaves on both ends, as any potential contamination could lead to irreversible fibre damage. When the same cleaves have been used over the span of several days, a reduced transmission efficiency even at lower power levels was observed, signaling the need for a

clean facet. Studying the degradation of the facets over time is an important work, and accordingly, efforts to provide more insight about the dynamics are investigated [130]. Additionally, it must be noted, that an approach this careful can require a considerable ramp up time. Typically a few minutes are spent at every power increment step — every data point in Figure 4.3 — to ensure secure and stable operation, which becomes even more relevant above the kW threshold. Consequently, this could represent a possible bottleneck and make the concept discussed here less feasible for applications that demand the guidance of comparably high intensity beams at a faster pace.

After accounting for the $\alpha_{\text{NANF-4}} \approx 0.74\,\text{dB/km}$ attenuation, the calculated CE is ~95 %, showing good agreement with the expectations based on the results from the previous results discussed in Section 3.5. It can be noticed that the total TE is slightly decreased by 1 % (from ~80 % to ~79 %). This is attributed to the thermal lensing induced distortion of the beam profile. Moreover, the temperature of the initial stripped section of the fibre is also plotted with red data points as the function of the input power. When compared to the behaviour of the black transmitted power curve, a similar linear dependence when compared to the output power's can be observed. Note that the maximum temperature recorded is 72 °C, still well below the damage threshold of the coating, which should be able to withstand temperature levels exceeding 100 °C. However, for further power scaling, implementing other techniques to improve the coupling and transmission are highly recommended to be adopted. More details about these methods will be provided in the following Sections.

On the other hand, Figure 4.4 demonstrates the sturdiness of the experiment. The spectrum of the input reference beam is plotted by the dash-dotted black curves, while the transmitted one is shown in red. Considering the spectral evolution over 1 km of delivery, it can be seen that there is only a minor development — a small redshift can be noticed (~1 nm) in the output spectrum, compared to its input counterpart. This is most noticeable on the central inset highlighting the wavelength range around the main peak. Furthermore, the smaller artifact like features observable near the wavelengths of 540 nm and 1260 nm (magnified on the right hand insets), are not generated by any specific physical phenomena during the transmission through the FUT. Since these are already observable in the reference input spectrum, they are attributed to other non-relevant sources: either nonlinear effects already present in the laser system, or a characteristic feature of the OSA used. The artifact near 540 nm is suspected to be related to a ghost signal of the 2$^{\text{nd}}$ harmonic of the central peak around the wavelength of $\lambda_0 = 1075\,\text{nm}$.

As an effort to investigate the origin of the slight redshift observed, a finite element simulation method has been adopted by Dr. Seyed Mohammad Abokhamis Mousavi, in order to model the propagation of the light inside the NANF. This approach utilizes the generalized nonlinear Schrödinger equation (GNLSE), including a semi-quantum mechanical description of the rotational and vibrational Raman responses of air [94]. It can be appreciated that an almost identical redshift is suggested by the calculations,

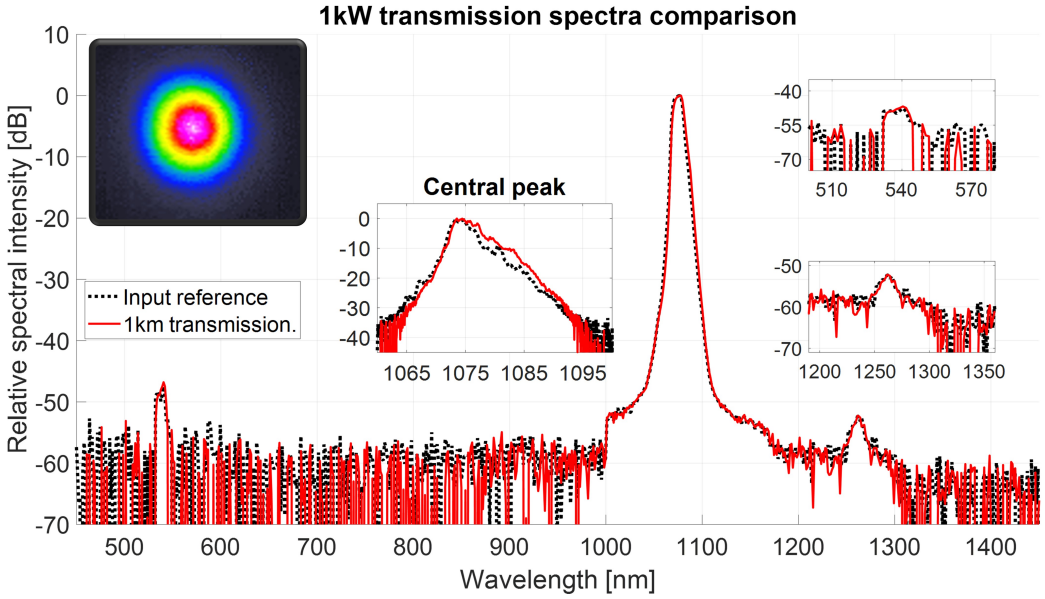

FIGURE 4.4: 1 km **spectral and modal transmission** | The input and output spectra are shown after propagation through 1 km of NANF. The input power is ~1.3 kW, corresponding to 1 kW transmitted power. Additional inset graphs highlight the evolution of the central main peak, and the lack of dynamics for the 2 artifacts (recognised to be inherent to the laser source) at wavelengths near 540 nm and 1260 nm, in the middle and on the right, respectively. On the top left, the captured output mode image at the highest power level is also depicted.

corresponding to the Raman response of the atmospheric air inside the core of the NANF. As discussed prior in Section 2.3, the small overlap between the high-intensity electric field and the glass structure of the NANF (in the order of $\sim 1 \times 10^{-5}$) found to play no role in the spectral evolution at these power levels and length scales, as also supported by the simulations. The top-left inset of Figure 4.4 shows the recorded near-field mode profile of the 1 kW transmitted beam, visibly presenting a near-Gaussian beam profile. However, since the experimental setup was built inside an enclosure for safety reasons, conducting a more diligent M^2 beam quality factor measurement was practically unfeasible. Nevertheless, a separate M^2 measurement has been conducted using the setup discussed in Section 3.2, showing an experimental value of $M^2 \approx 1.1$, strongly suggesting that the beam quality has been conserved throughout the long distance delivery.

In summary, we have shown, that it is possible to transmit a high-brightness beam with over 1 kW average power beyond 1 km distance through a NANF, without any significant spectral penalty. The sole reason for concluding the experiment at this stage has been the existence of the splicing point. As mentioned at the end of Section 4.1, any localized scattering source induces localized heating, which has to be considered and managed by applying proper cooling procedures. While every measures have been taken to ensure safe operation, it has been acknowledged to be too hazardous to pursue transmission of even higher power levels with this fibre piece.

In the next Section, the scalability of NANFs for high-power laser delivery applications will be examined. Based on the findings discussed here, an estimate for the maximum practically transmissible power and feasible transmission length will be given. After identifying the potential bottlenecks, experimental solutions will be proposed and implemented to overcome these limitations. This aim will be also supported by simulational tools. After analysing their impact on the performance, results of measurements using a next generational system will be presented. Furthermore, during the detailed discussion that will follow, all representative values will be compared with similar relevant studies, and most importantly, with the current state-of-the-art SCF technology.

4.3 Current limitations

Presumably, one of the most powerful commercially available CW laser source near 1 µm central wavelength is the Yttermium doped fibre laser (~10 kW), while the highest ever reported up-to-date source considering the same central wavelength has been developed by Lockheed Martin for the US military, at an extreme average output power of 300 kW [11]. This latter laser system follows the design of spectral beam combining [131], in order to achieve such remarkable average power levels. However, it must be also noted, that this approach generally leads to a slightly reduced beam quality ($M \geq 1.5$), which can be detrimental for applications that require high precision — e.q. material processing.Ultimately, delivering high-power beams of such scale through optical fibres of any kind will be limited in distance by non-linear effects (e.g. spectral broadening), and by attenuation. As an example for the latter, considering the earlier used NANF-4 as a reference, assuming the highest CE discussed previously (>95 %), the total transmission will be only 50 % after 4 km of propagation, because of the $\alpha_{\text{NANF-4}} \approx 0.74\,\text{dB/km}$ attenuation at $\lambda \approx 1064\,\text{nm}$. Based on these parameters as guidelines, the practical bottlenecks of scalability will be explored in the following.

4.3.1 Spectral degradation

The recorded reference spectra of the SPI laser source is shown in Figure 4.5. It can be seen that the spectrum of the source slightly broadens as power level increases. This is attributed to be an intrinsic characteristic of the laser source. This observation will be used for the simulations that estimate the spectral penalty the beam suffers from during propagation in HCFs.

In order to make reasonable comparisons, a few definitions will be introduced here. As a figure of merit, the terminology of the spectral power overlap ratio function S has been adopted. In silica fibres, the critical input power for stimulated Raman scattering (SRS) is defined as the power level, at which the output optical power will be equally distributed between the pump and the Stokes signal wavelengths. This condition corresponds to $S = 0.5$, which will be therefore defined as the critical spectral broadening for the following. Based on the term 'high power transmission capability' (HPTC), originally coined by

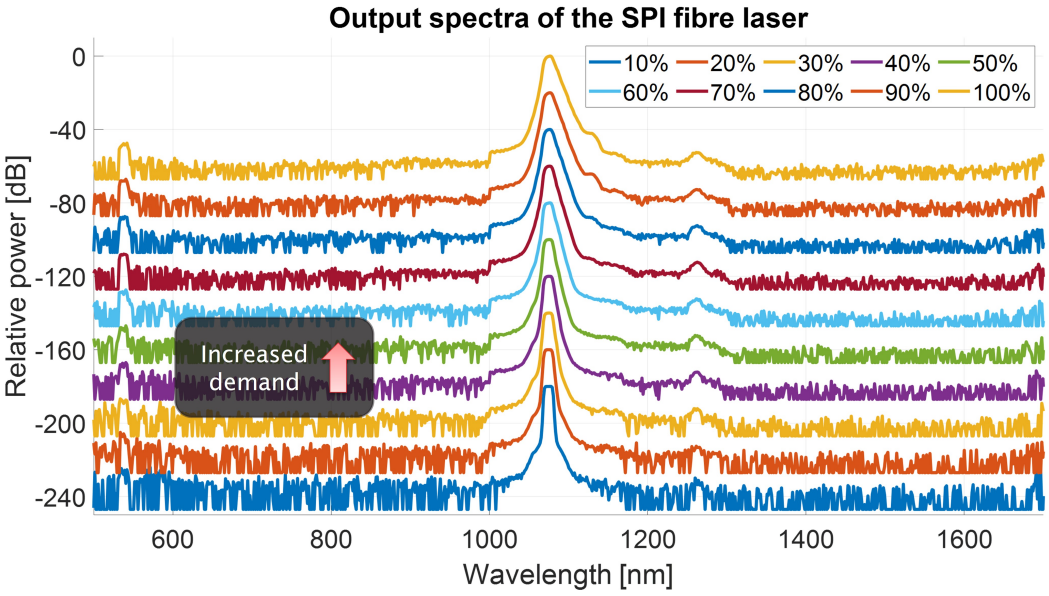

FIGURE 4.5: **SPI spectra at different power demands** | The respective curves show the relative power of the spectral components in 10 % increments of the power demand of the SPI fibre laser, with $P_{max} = 2200\,\mathrm{W}$. Note that the plots are shifted on top of each other by a 20 dB offset, starting from the lowest average power on the bottom going towards the highest on the top. All spectral components not within the central range are >50 dB below their maximum.

Okuda et al. [13], the figure of merit 'power-distance product' (PDP) corresponding to the product of the transmitted optical power and the transmission distance will be also used for the sake of comparison. Additionally, it will be assumed that during propagation a high quality ($M^2 \approx 1 - 1.1$) beam profile has been maintained.

It had been presented in the Supplementary material in [94] how the measured spectra shown in Figure 4.5 can be scaled up to the case of ~11 kW in a sensible way, based on the spectral evolution observed from 0.1 to 2.2 kW. Furthermore, the evolution of all spectra after propagation through an optical fibre with identical geometry as NANF-4 over the length of up to 10 km has been discussed as well. Based on the simulations detailed there, it has been also concluded that even at the maximum output average power level of $P_{\mathrm{SPI,\,max}} \approx 2.2\,\mathrm{kW}$, transmission over 5 km of appropriate NANF is possible without any serious spectral penalty, which corresponds to a PDP of $\sim 1 \times 10^7\,\mathrm{W \cdot m}$. When compared to previous results of PDP $= 1 \times 10^5\,\mathrm{W \cdot m}$ [17], $3 \times 10^5\,\mathrm{W \cdot m}$ [37] and $4.2 \times 10^5\,\mathrm{W \cdot m}$ [13] — with all of the cited sources using microstructured SCFs — the advantage of using HCFs is clearly visible. Moreover, simulations using a similar cross section to the SCFs reported in the cited publications also show that these PDP values are also close to their fundamental limit as expected from their corresponding HPTC. The cited publications will be compared to other relevant results in Subsection 4.5.1, and visualized in Figure 4.16.

Based on the insight gained from this analysis, it has been confirmed that there is still room for progression, as the results reported in Section 4.2 (1 kW delivered over

1 km length, corresponding to a PDP of 1×10^6 W · m) can be enhanced further by approximately one order of magnitude. It should be also noted that until this point, only HCFs with their cores filled with ambient air have been considered. Assuming a case where the HCF is under vacuum, or is filled by a Raman-inactive gas (e.g. Argon), the same simulations predicts PDP values possible beyond the maximum power levels and transmission lengths available at the time of conducting the experiments. Ultimately, in those scenarios, the theoretical PDP limits will be determined by the available laser power and fundamentally achievable attenuation of the HCFs.

On the other hand, as also presented in Section 4.2, the main limitations of the scaling of high-power delivery experiments are more practical, and related to the available coupling technique and equipment. So far, none of the simulations discussed in this Section considered the impact of beam distortions that can be present in the beam that is being coupled into the FUT. In the experimental layout used here (i.e. free-space coupling), the practical boundaries are related to absorption and heating of the used optical elements, namely the BDO, the collimating and the focusing optics. While at relatively low power levels (i.e. the CE measurements discussed in Chapter 3) these effects are insignificant — hence can be safely neglected — above a certain threshold, they must be considered. The actual value of such threshold can depend on many experimental factors. As a specific example, using the commercially available ThorLabs lens pair for coupling (detailed in Section 4.1) altered focusing conditions were observed above ~250 W of average output power of the SPI laser source, and such, remote realignment of the fibre tip was necessary — as revealed by the saw-tooth shape of the transmission efficiency plots in Figure 4.3. In order to estimate the scalability of high-power, high-brightness transmission of HCFs, another simulational tool has been utilized, which can take these thermally induced effects into account.

4.3.2 Digital twin in COMSOL

As an attempt to gain more insight about the thermalisation of the lens pair, I have designed a digital twin of the high-power delivery setup in the COMSOL finite element simulational environment. The very simplistic layout is presented in Figure 4.6. On the left side of the schematic, the bare fibre tip of the previously introduced SPI laser source is set. As the light propagates towards the right, it interacts with the 3 main optical elements, the BDO, the collimating and focusing lenses, respectively in that order. The results of the COMSOL model were initially verified by an independent MatLab simulation developed by Dr. Hans Christian Hansen Mulvad, which considers the paraxial propagation of a Gaussian beam, employing a thin lens approximation. This MatLab code has been already used effectively as a multifunctional tool to aid the alignment of the free-space coupling setup. The simulation can calculate the ideal positions of given lenses to achieve a desired focal spot to match the MFD of the FM of the HCF. Moreover, it is also capable of estimating the thermally induced focal length change. All of these figures of merit will be compared in the following.

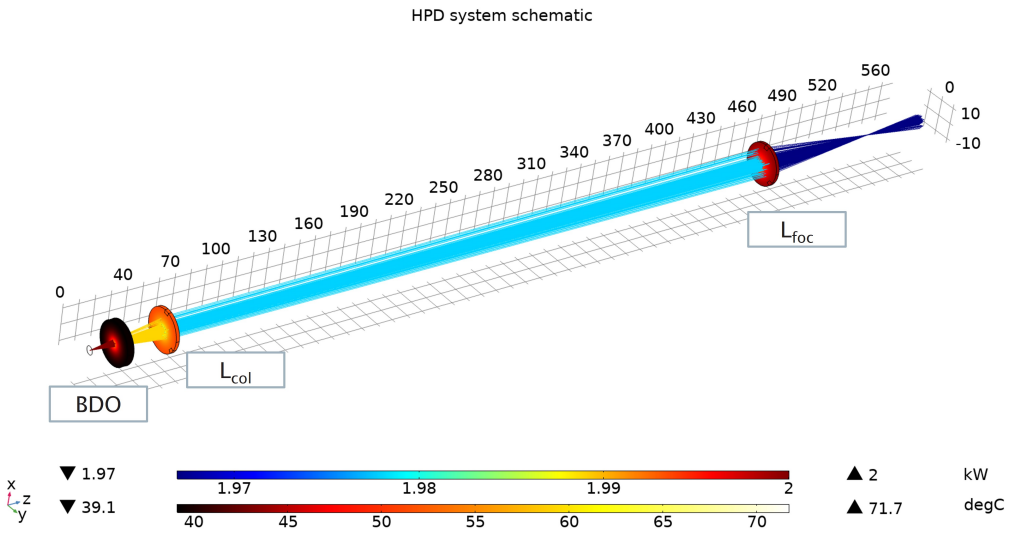

FIGURE 4.6: **Layout of the COMSOL digital twin of the high-power delivery experimental setup |** As the light is propagated from left to right, it is incident on the labelled optical components of BDO, L_{col}, and L_{foc} in that order. The combined optical power of the rays is subsequently reduced, as fractions of it is being absorbed by the optics. This is represented by the change of colour in the rays, following the upper colour scale. Similarly, the induced temperature increase is also shown inside the optical elements, highlighted by the bottom scale. All grid lines are separated by 10 mm, positioning the focus near 530 mm from the fibre tip of the source.

For the COMSOL simulation to be introduced and discussed here, the "Bidirectionally coupled ray tracing" approach, using the ray-optics approximation has been implemented. Unfortunately, this method also limits the capabilities of the code, as the actual electromagnetic field distribution near the focus cannot be determined precisely. The designed ray tracing simulation uses the exact laser-related, geometrical, and material specifications of the coupling optics provided by the producers to solve the related equations. Table 4.1 summarizes the most relevant and important values used. While almost all parameters are precisely specified, some approximations had to be made. As an example, while the reflectance of the AR-coating was given, its absorption was not, and as such the latter was neglected. However, since measuring the thermalisation of the optics was experimentally possible, the simulation can be verified to a certain extent — this will be discussed in more detail in Subsection 4.3.3. Accordingly, the imaginary refractive index of the UVFS lens material (κ, marked by an asterisk in Table 4.1) had to be estimated by matching it to the experimental results. The value of $\kappa = 3 \times 10^{-9}$ used here translates to an absorption loss of $\alpha_{abs} = 4\pi\kappa/\lambda_0 \approx 350\,\mathrm{ppm/cm}$, corresponding to a total loss of 175 ppm total loss for each lens — where ppm denotes parts per million or 1×10^{-6}. Comparing this to a realistic estimation of $210 - 230\,\mathrm{ppm}$ total loss (based on typical values of $20 - 50\,\mathrm{ppm/cm}$ absorbance for UVFS, and 100 ppm per surface loss for electron-beam coatings) a reasonable agreement is achieved.

Nevertheless, the model still makes minor predictions, like mechanical properties of the optical elements, or the change of the focal length reasonably accurate. Considering the

TABLE 4.1: Summary table of parameters and boundary conditions used for the simulation of the HPD setup using the COMSOL code. The value of the imaginary part of the refractive is approximated, as marked by an asterisk (more detail about its validation is in the text)

Parameter	**Value**	**Unit**
Laser source central wavelength	1075	[nm]
Antireflection coating reflectance @ 1075 nm	0.2697	[%]
Laser source output diameter	18	[µm]
Imaginary refractive index of the UVFS lens material *	3×10^{-9}	[−]
Laser source numerical aperture	0.075	[−]
Temperature dependence of the refractive index (dn/dT)	1×10^{-5}	[1/K]
Laser source output power	$1 - 2200$	[W]
Heat transmission coefficient	10	$[\mathrm{W}/(\mathrm{m}^2 \cdot \mathrm{K})]$
Distance from source to the centre of the 1st lens	50	[mm]
Distance between the lens pair	400	[mm]
The maximum mesh element sizes are <100 nm at the source, and <1.5 mm for each lens surfaces		
Mounted parts of the lenses are thermally insulated, but heat can radiate at the clear interfaces		
Mechanical expansion is only allowed on the clear surfaces, but not at the fixed mount sides		

case 2 kW input power, as an example, Figure 4.7 a) shows the first surface of the first (collimating) lens. Contour colours represent the isothermal lines (right scale). It is evident that the lens heats up from the initial room temperature of ~21 °C to over 70 °C near its centre, where the most intense part of the beam is incident. The cross section is coloured such that the absorption induced refractive index change is presented (left scale). The impact of the thermal lensing is twofold. On the one hand, as seen on the scale labels, the change of refractive index has a positive sign. This is due to the fact that the temperature dependence of the refractive index (dn/dT) of the lens material has a positive sign, as shown in Table 4.1. Practically, this translates to stronger focusing, resulting in a paraxial focus shift, translating the focal point closer to the source, as well as reducing the beamwaist. On the other hand, it is also clearly visible, that the change is not homogenous, but rather there exists a radial thermal gradient. This means that the optical rays closer to the optical axis experience a relatively larger change in the direction of refraction than those incident on the cooler, outer region of the lens. As a result, the intensity profile of the beam will be also altered.

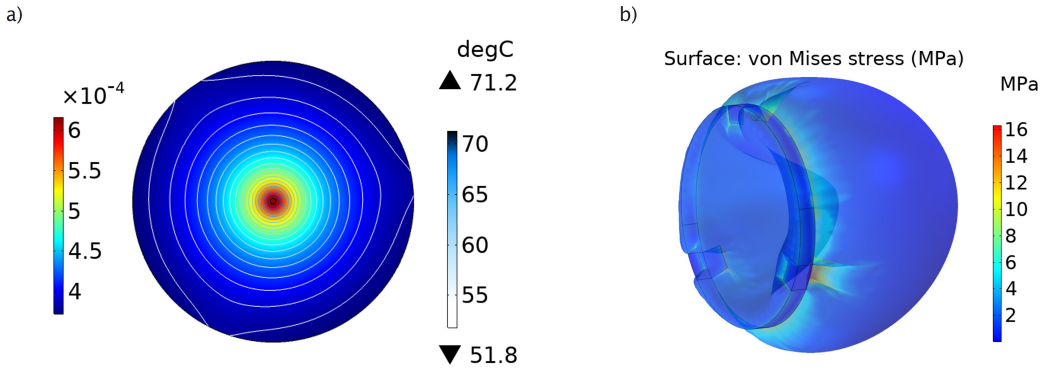

FIGURE 4.7: **Simulated impact of thermalisation of the collimating lens** | Calculated changes of a) opto-thermal and b) mechanical properties inside the collimating lens, assuming 2 kW of incident power. Part a) shows isothermal lines of the temperature according to the right hand scale, and refractive index change shown by the left hand colour legend of the first surface, closest to the laser source. b) illustrates the effect of the thermally induced Von Mises stress (deformation is upscaled by 5×10^4 for better visibility).

Additionally, Figure 4.7 b) highlights the mechanical stress induced by the thermal expansion of the lens. Note that the deformation is over-exaggerated by 4 orders of magnitude for better visibility. Calculating the von Mises stress is generally used to give an upper limit, above which a failure event can happen. In this case, the maximum simulated stress is 16 MPa. As a point of comparison, according to the data provided by Corning, for its high-purity fused silica glasses, the threshold value called the modulus of rupture (MoR) — where permanent damage would be expected — is set at 52.4 MPa, still well above the calculated maximum. The distinct triangular feature visible in both a) and b) plots are attributed to the fixing points defined by the Polaris mounts.

Furthermore, it is also possible to de-couple different aspects of the simulation. Assuming that the thermal absorption does not change the index of refraction of the optics, but only leads to mechanical expansion induced by stress, the beam distribution is only impacted negligibly. The actual bulging of the lens only contributes to ~<0.1 % of the combined deviation. Additionally, it can be also seen that the highest von Mises stress is located near the edge of the lens, where no optical ray is incident. This demonstrates, that the temperature dependence of the refractive index is the dominant factor responsible for altering the focusing. These findings indicate that the current bottleneck of coupling is not determined by mechanical, but by thermal effects — and as such, the phenomenon and its impact has been investigated further and will be discussed next.

4.3.3 Thermal lensing

Figure 4.8 a) shows the peak temperature values of the 1st collimating lens, as a function of the P_{in} average input power. The data points plotted with red represents the experimentally measured values, as captured by the thermal camera, while the blue markers depicts the calculated values based on the simulations, respectively. Parts b) and c)

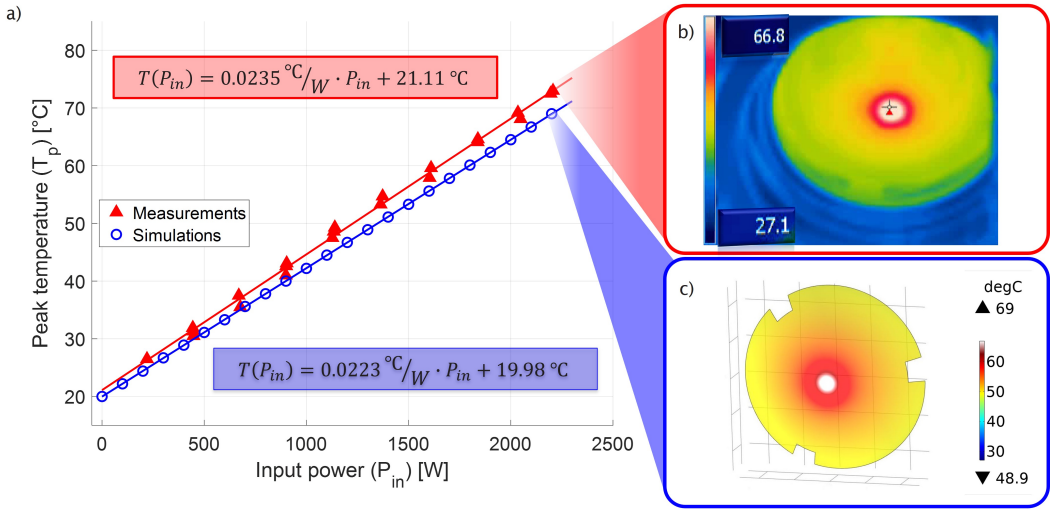

FIGURE 4.8: **Thermalization of the collimating lens** | a) Temperature dependence of the lens as the function of the incident power. The red and blue markers denote the measured and simulated temperatures, respectively, including the equations describing the linear fit of both data set. Example thermal distributions of same lens as b) recorded during the measurements c) calculated by the simulations, at the maximum 2.2 kW incident power levels. Note that the scales for both scenarios are set to be the same, allowing better visual comparison.

illustrates the total temperature distribution for $P_{\text{in}} \approx 2.2\,\text{kW}$, corresponding to the experiments and simulations, respectively. As the colormaps were set to be the same, it can be appreciated that the distributions shows reasonable similarity. Nevertheless, the simulated values are also limited by the approximations/uncertainties in parameter values used – e.g. coating properties. Note that the calculations also consider the influence of the BDO on the beam, as it is also susceptible to thermal lensing, and consequently introduces beam distortions. Furthermore, when compared to Figure 4.7 a), a ~3 °C peak temperature difference can be noticed. This is explained by the fact that here, the 2$^{\text{nd}}$ surface of the collimating lens is being analysed (in contrast to the 1$^{\text{st}}$ one illustrated in the previous Figure). The only reasoning behind this choice is that it is experimentally more feasible to capture this surface with the thermal camera.

Examining the data more quantitatively, linear curves have been fitted to the available discrete data points. Highlighted are the parameters of the linear dependence, including regressions values of $R^2_{\text{meas}} = 0.997$, $R^2_{\text{sims}} = 0.999$, for the measured and simulated cases, respectively. Furthermore, the slopes of 0.0223 and 0.0235 °C/W are within ~6 % difference between the measured and calculated temperature values, respectively, suggesting reasonable agreement. The discrepancy is attributed to the simplifications and approximations (e.g. the coating properties of the lens, or the material absorption of the substrate) used by the simulation. As an example, it has been also shown that the cleanness of the surfaces of the optical elements can have a significant impact on the quality of the focusing [132], however, its contribution through the calculations can be difficult to capture precisely.

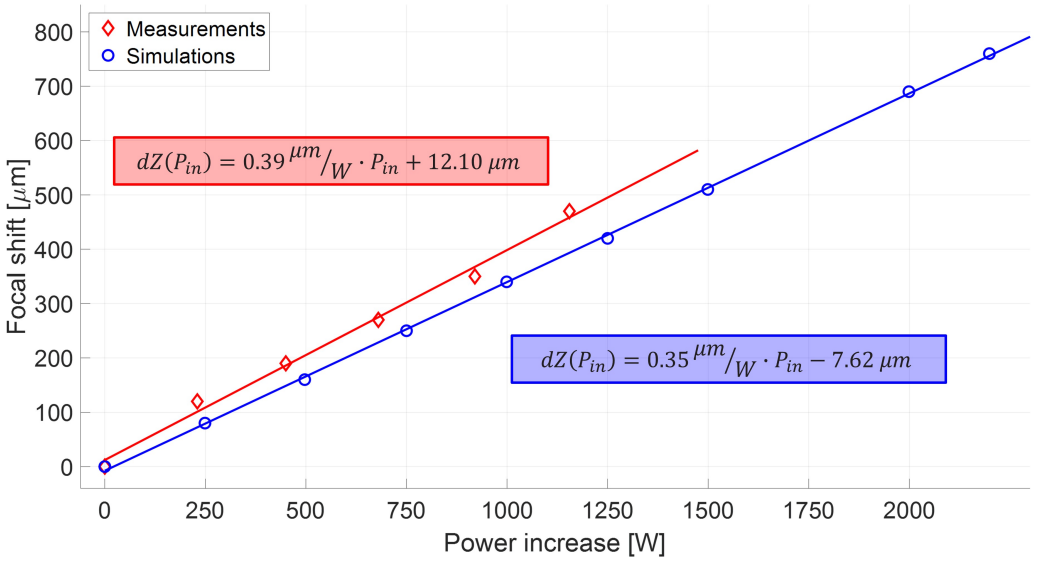

FIGURE 4.9: **Comparison between simulation and experimental values of thermal focal shift** | Red markers indicate the required realignment along the Z optical axis during the high power experiments. Blue circles denotes the focal shifts calculated by the simulations. A linear curve has been fitted to both set of data, with their equation displayed alongside, with regressions values of $R^2_{\text{meas}} = 0.993$, $R^2_{\text{sims}} = 0.998$, respectively. The estimated focal shift of 800 µm beyond the 2 kW power difference ensures that the fibre tip can be always positioned near the focus during high-power operation.

Now that it has been verified that the simulation provides comparable results to the measured values, the thermally induced focal shifts for the 2 cases will be examined and contrasted. Figure 4.9 shows the recorded adjustment of the input tip of the FUT required along the optical (Z) axis in red, while the change of the focal position predicted by the simulation is displayed with blue, as a function of the power increment. The former values have been practically logged by Kinesis software (ThorLabs), which has been used for precise control of the fibre tip remotely during the experiments discussed previously in Section 4.2. For the simulations, the focal position is determined by the smallest MFD given by the study, corresponding to the beam waist. Still, as calculations are based on ray optics approximations, this position is defined as the minimum total distance from the optical axis summarized for all optical rays considered. On the far right hand end, an estimated shift assuming maximum power demand from the laser source is included. The predicted focal shift of ~760 µm is confirmed to be within the travel range of the remotely controllable piezo-stage (3.5 mm) on top of which the fibre input is mounted. This ensures, that assuming the same experimental conditions, the available equipment is capable of accommodating the requirements for efficient coupling — when only the phenomena considered so far are being taken into account.

On the other hand, up until this point, only the focal shift along the optical axis has been examined. As a point of reference, the calculated Rayleigh length, as given by $z_R = \pi w_0^2 / \lambda_{\text{SPI}}$, for this case is $z_R \approx 660\,\mu\text{m}$. This suggests that the previously estimated

760 µm focal shift at the highest power levels available could change the beam diameter by a factor of $\sim\sqrt{2}$. Considering that the ideal beam-core ratio has been set as 70 %, this change in the size of the beam waist can have a significant impact, and must be accounted for. Just as important is the possible distortion of the beam distribution near the focus, which has been neglected so far. However, as discussed earlier, since the CE is defined by the overlap integral of the respective fields, these alterations can have a significant impact.

The current limitations of the COMSOL simulation described here are two-fold. Firstly, the beam distribution is expected to deviate from a quasi-single-moded beam cross section due to the non-homogeneous thermally induced refractive-index change illustrated in Figure 4.7 a). Secondly, during the previous discussions, the phase distribution of the incident beam near the focus has been considered constant. While this was a reasonably approximation and simplification for the calculations at low power levels ($P \approx 100\,\mathrm{mW}$), this estimation is expected to lose its validity as the power is increased.

4.3.4 Discussion

In summary, the transmission at the highest possible power in the experimental setup (2.2 kW) should be achievable. As discussed prior, the spectral penalty would be negligible for fibre lengths of 5 km. Furthermore, the results of the COMSOL model suggest that within its limitations -– i.e. without fully characterizing the electromagnetic field — it is possible to compensate for the thermal lensing induced focal shifts. The constant re-positioning of the fibre tip of the FUT is practically easy to achieve, and would allow to maintain a high CE.

However, because of the inhomogeneous change of the refractive index inside the optical elements, at higher power levels, not only the position of the focus, but the diameter of the focal spot, and its actual beam distribution is also expected to change. These predicted beam distortions are more complicated to manage. The simulated focal shift indicates a smaller beam waist at the altered focus, which results in a deviation from the ideal ~70 % beam-core ratio discussed previously in Section 3.4. Furthermore, the beam distribution is also expected to deviate further from the FM distribution supported by the fibre microstructure. Combining these 2 phenomena leads to the conclusion, that the bottleneck for maintaining high CE is limited by effects, which cannot be compensated by simple repositioning of the fibre tip.

Generally, 4 main directions have been proposed to minimize the impact of thermal lensing. Firstly, using optical lenses made out of higher purity material would reduce their absorption, and in turn lessen the thermally induced refractive index change. This approach limits the impact of unwanted effects (prevention) instead of attempting to manage them (treatment). Nevertheless it must be mentioned, that the cost of such optical components can be significantly higher. Furthermore, based on the available manufacturing techniques, while the impact of thermalisation can be lessened, because

of the unavoidable defects that could materialize during fabrication, it cannot be nullified completely.

Secondly, the possibility of pre-compensating has been considered. In this approach, the coupling optics are aligned in such a way, that the coupling conditions are not optimized for low-power transmission, but the beam waist is slightly larger when compared to an ideal case. However, due to the absorption of the lenses, the thermally induced distortions will eventually alter the focusing. Taking this effect into account, the coupling can be intentionally misaligned to ensure that at the cost of a slightly reduced CE (~2 %) at low power levels, the altered beam waist will match better with the MFD of the test fibre, at higher power levels, where the handling of the losses become more critical. Initial measurements showed promising results to confirm this theory experimentally. Considering the thermalisation related requirements to achieve the state of equilibrium, this approach might also provide some improvement by lowering the ramp up time — with the exact improvement depending on the maximum peak power employed. However, such a trade-off can be also considered more dangerous, as other factors could become more dominant over time, e.g. the contamination of the optical surfaces [132]. Additionally, while it is possible to adjust the beam diameter as intended, the actual beam distribution cannot be compensated in this simple approach either. Consequently, above approximately 1 kW input power, the temperature of the fibre coating reached above 70 °C values, and such the idea to further explore this suggestion has been discarded.

Another proposal could be to 'heat up' the optics in such a controlled way, that when the effect of absorption is included, the combined temperature distribution becomes closer to being homogeneous. In theory, a "negative" of the expected thermal distribution can be determined and through simulations, a heating solution capable of providing it can be calculated. Some of the main disadvantages of this approach is that it can be energy inefficient and practically inconvenient. Furthermore, as temperature of the optical elements is expected to reach values near to ~70 °C, heating components capable of precise temperature control at this level is required. Similarly, the used equipment (e.g. mounting solutions) must be able to operate safely under such environmental conditions. Because of these concerns regarding safe operation, this direction has not been investigated further either. Nevertheless, by carefully designing a heat management arrangement, the scaling of this approach could theoretically go beyond the capabilities of prior suggestions. This is due to the fact, that in contrast to those proposals, which try to minimize the influence of thermalisation, and such the arising deviations, here, the heating is actively controlled.

Lastly, a coupling setup which consist of optical materials with refractive indices that show temperature dependence with opposite signs (dn/dT) has been considered. In this approach, a system can be designed where the individual thermally induced beam distortions are such that the sum of them practically cancels out any deviations [13, 132].

This could lead to an unaltered beam distribution, independent on the incident power to a certain extent. While this solution is the most refined way to handle the discussed phenomenon, it is also the one, which requires the most resources, both from the side of appropriate designing, as well as the cost of manufacturing those optical elements. It is also worth noting, that the material of the employed lenses (UVFS) provides one of the lowest absorption at the relevant wavelength of ~1 µm. Consequentially, inserting another material with the desired property of negative dn/dT coefficient, would also lead to an unwanted increase of absorption and the related phenomena. For these reasons, it has been concluded that this direction is not feasible at the moment, and has been postponed as future work if desired.

After considering and comparing the introduced prospects, trade-offs and complexities of the options, the first suggestion has been followed. The impact of employing optical lenses of higher quality will be presented and discussed in Section 4.5. However, before that, another technique to handle another absorption related concern will be addressed.

4.4 Cladding light extraction

While the previously reported ~>95 % CE values in Section 4.2, are practically the highest achievable, assuming a $P_{\text{in}} \approx 1\,\text{kW}$ average input power, the corresponding localized coupling loss of $P_{\text{Cpl-Loss}} \approx 50\,\text{W}$ is quite substantial. The exact length along which this power dissipates can depend on many factors (e.g. core-HOM and cladding mode losses, thermal conduction, etc.), but reasonably can be estimated to be around a few metres. Since the fluence of the laser field is the highest at this segment of the fibre, a considerable loss over a relatively short distance is expected as a result of the coupling loss. Therefore the temperature of this section is being constantly monitored during high-power operation. The recorded peak temperature values have been already presented in Figure 4.3, however, very little explanation was provided there. In this Section, a more thorough examination will be detailed.

In order to control this thermal dissipation at the initial section of the fibre, several approaches have been proposed to extract the excess light from fibres, and are commonly called cladding light strippers (CLS). These techniques range from laser [133] or chemical aided etching [134] of the fibre structure, to methods reducing the cladding diameter [135]. While the results show significant reduction in temperature and good thermal handling properties, the main drawback of these procedures are that they alter a section of the fibre permanently. Another desirable proposal is the practice of applying a refractive index-matching material to the exterior surface of the uncoated fibre [136]. This allows the excess light from the fibre cladding to enter the surrounding medium. By doing so, not only does the material act as a heat sink to reduce the thermal load by increasing the heat capacity of the ensemble, but also manipulates the total surface,

where thermal conduction can be utilized to reduce the heating. This approach could be a non-invasive alternative, which could be very practical for research purposes.

Figure 4.10 a) depicts my implementation of this non-invasive method to extract the excess light from the test fibre. After stripping the coating of the initial segment of the fibre for approximately 10 cm it is mounted onto the water-cooled V-groove block — identically to what has been already discussed in Section 4.1. However, in this case, only the very beginning is fixed with commercial Kapton tape, to ensure a reasonable mechanical stability of the input tip. In addition a small amount of index matching gel (ThorLabs G608N3) is applied along the initially uncoated length of the fibre inside the water cooled V-groove, until it is fully covered to ensure better heat conduction. Furthermore a single UVFS uncoated substrate of UVFS ground glass diffuser (ThorLabs DGUV10-220) has been also placed on top of the gel-covered part of the fibre. This enables light to be extracted from the cladding (via the gel) and safely diffuse into the surroundings. The glass piece is placed closer to the other end of the V-groove, such that, together with the Kapton tape, they provide a more secure way of fixing the FUT. Parts b) and c) show the improvement achieved by implementing the CLE technique. Note, that the colour-scale on the right of each capture is different for better contrast. Additionally, the contour of the glass piece is also visible in the bottom left corner of Part c), when the method is applied.

The refractive indices of the materials are $n_{\text{fibre}} \approx 1.509$, $n_{\text{gel}} \approx 1.450$, $n_{\text{UVFS}} \approx 1.443$ for the fibre, for the index matching gel and for UVFS glass diffuser, respectively, at the used central wavelength of $\lambda_{\text{c,SPI}} = 1075\,\text{nm}$. While the values do not match precisely, by implementing this technique, the handling of the thermal load is significantly improved, as it will be shown in the following. It is also expected that as the input power is increased, the exact refractive index values will slightly change, and similarly, the efficiency of the extraction of the excess light may also vary. In general, quantifying the exact values would certainly be valuable. However, because of the complex nature of the phenomenon, developing a reliable way of measurement has been postponed to be a dedicated future project. As the results in the following Section will show, the technique enables the coupling of the highest power provided by the available laser source. Because of that, there was no intention to take other actions to optimize this technique to the fullest extent possible — e.g. by employing glass pieces or gels of different materials.

To demonstrate the improved performance here, a ~13 m long piece of NANF-5 has been tested initially. Along with the transmission efficiency, the hottest temperatures measured at the initial section of the test fibre vs input power are presented in Figure 4.11. While the red plots show the measurements without the implementation of the CLE technique, the blue curves represent those which were conducted with it. It is evident from the graph, that extracting the excess cladding light does not degrade the CE considerably. This suggests that the method does not introduce significant mechanical stress on the fibre piece, consequently, the microbending loss values are not changed

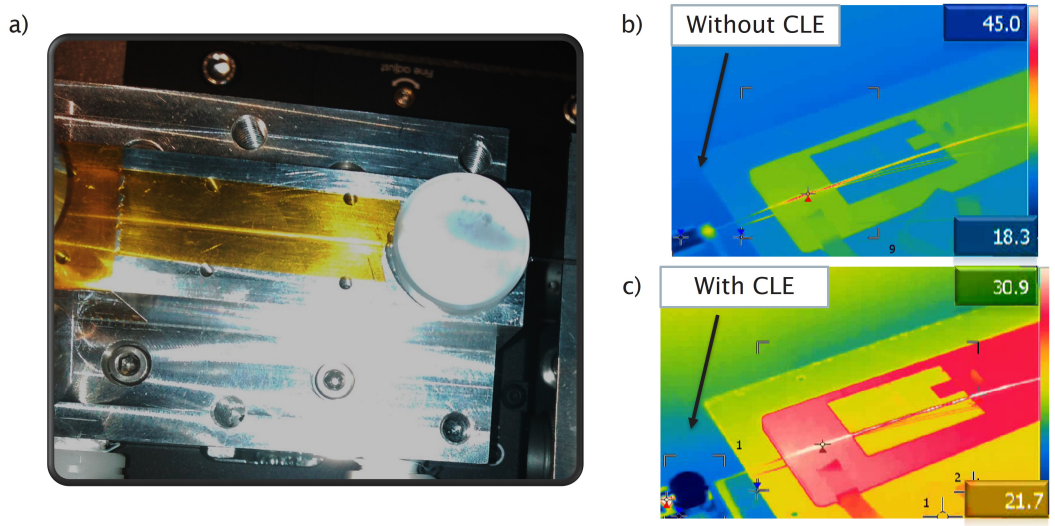

FIGURE 4.10: **Cladding light extraction visual aids** | a) Photo of the realized CLE layout. The fibre is laid out horizontally on the image, with the input facet on the left. The glass diffuser substrate is placed on the other end to ensure better clamping on the fibre piece. Note that the longer, horizontally placed Kapton tape is only for visual purpose here, as during the high power operation it is removed, and the initial, stripped fibre section (including the part below the glass piece) is covered with an index matching gel. See text for more details. Thermal captures b) and c) show the temperature distributions as captured by the thermal cam with and without the CLE technique implemented, respectively. Notice the contour of the diffuser plate on the bottom left as indicated by the arrows, and the change of range on the colourmap scales.

noticeably. Comparing the maximum temperature reached with CLE above 1.5 kW, the 'safe' level was already exceeded without the CLE technique at around 700 W of input power, as highlighted by the horizontal black dash-doted reference line. The experiment without any extraction was terminated because the fibres were not tested for operation above 70 °C, while the one with CLE was stopped because of the larger number of travelling defects observed — this phenomenon will be examined in more detail in the following Chapter. Notice, that the 'roll-off' of the blue transmission efficiency curve also coincides with a steeper increase of the peak temperature above 1400 W, further indicating a connection between the CE and the heating of the initial section of the fibre. Assuming that this thermalisation is the main limitation for achieving the best transmission, the CLE technique significantly reduces this bottleneck, enabling the scaling of the used setup to even higher levels, following the trend, most likely above the 2 kW output capacity of the SPI laser.

In conclusion, in this Section I have shown that it is practically feasible to extract the excess light, that has not been coupled into the FM of the FUT. I have demonstrated that this can be accomplished in a non-invasive way, such that no delicate preparation of the fibre is required. The measurement results show no decline in maintaining a high coupling efficiency, while the temperature of the initial section can be reduced by as

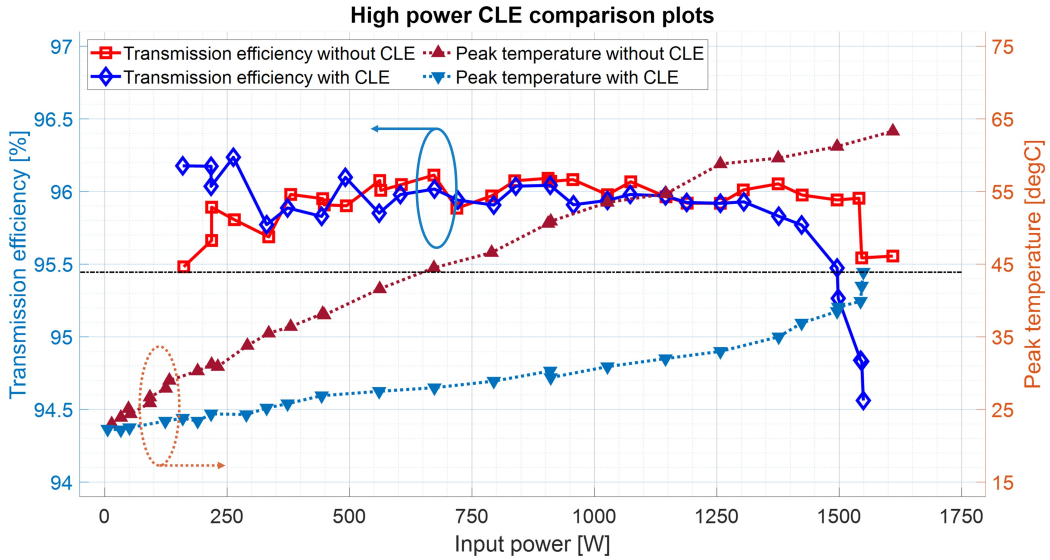

FIGURE 4.11: **CLE induced improvement comparison curves** | Comparison plot for presenting the impact of extracting the excess light, as observed during measurements employing the 13 m long NANF-5. Transmission efficiency is marked with squares and diamonds connected by solid lines, scaled to the left y-axis, as indicated by the arrow. On the other hand, the measured peak temperatures are plotted with upwards and downwards pointing triangles and dotted lines, corresponding to values on the right-hand y-axis, as also indicated by the arrow. Both pair of curves are additionally shaded red and blue for the cases without, and with the CLE technique employed, respectively. Furthermore, the highest temperature value reached when the CLE method has been applied is indicated with a black, dash-dotted horizontal reference line, slightly below 45 °C.

much as 20 °C at ~1.5 kW incident power. The concept of CLE developed and discussed here will become advantageous for the experiments leading to the next milestone result to be presented in the following Section.

4.5 2nd generation results

Building on the insight gained from studies discussed earlier, in this Section, the combined impact of 2 main techniques to improve on previous results — that is employing optical lenses of high optical purity and the application of cladding light extraction — will be examined.

It has been argued, that the high CE can be more easily maintained for free-space coupling, even at higher power levels, if transmissive optical elements of higher purity are employed. This has been reasoned by the fact that those pieces of equipment are less prone to absorption compared to the UVFS ones — e.g. those introduced in Section 4.1. Therefore, thermal lensing and related beam distortion effects are expected to be significantly reduced. This enhancement could enable the upscaling of the transmitted power to exceed the previously reported 1.5 kW average power level, above which the impact of the phenomena becomes clearly visible.

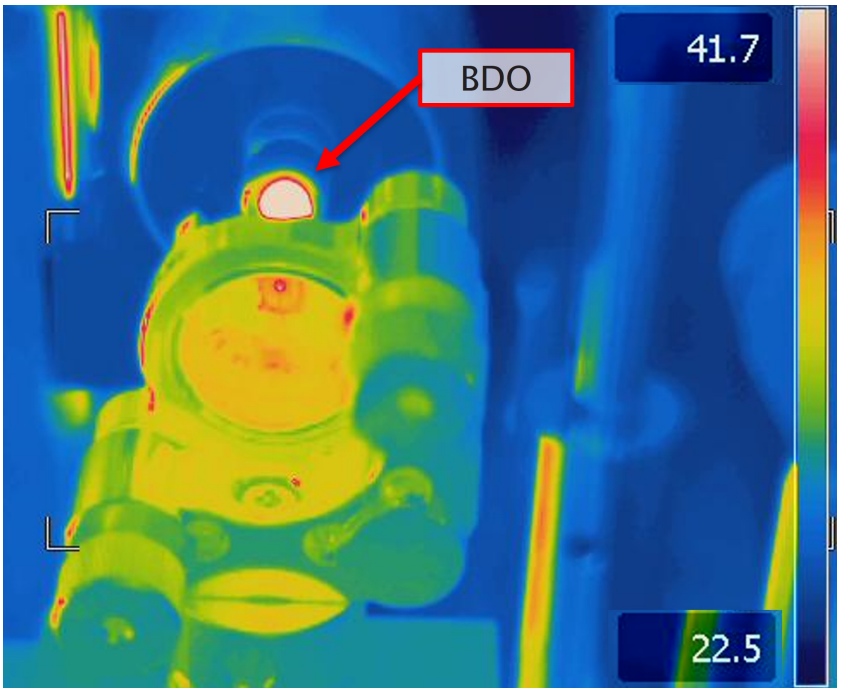

FIGURE 4.12: **Temperature distribution of the high-purity collimating lens at 2 kW incident power** | The thermal image as captured by the thermal camera illustrates the advantage of employing optical lenses made of HPFS material. Compared to the temperature distribution of the commercially available components, this lens shows negligible amount of heating, suggesting similarly minor absorption. Only the BDO (highlighted by the text box with arrow) demonstrates measurably increased temperature — suggesting that plano-parallel window to be the dominant contributor of the experienced focal shift.

To explore the experimental capability of this approach, the previously discussed commercially available ThorLabs lens pair has been replaced by a pair of custom made lenses provided by II-VI Infrared (Coherent). Both of them are bi-convex aspheric lenses, made of high purity fused silica (HPFS), claimed to have less than 10 ppm (parts per million) contaminants, according to the manufacturer. This value agrees well with expectations based on typical absorption values of ~1 ppm/cm for low-OH silica, and 1 ppm per surface loss considering a coating layered by ion-beam sputtering. The collimating and focusing optics have focal lengths of $f_{\mathrm{col}} = 60\,\mathrm{mm}$ and $f_{\mathrm{foc}} = 80\,\mathrm{mm}$, and central thicknesses of $th_{\mathrm{col}} = 12\,\mathrm{mm}$ and $th_{\mathrm{foc}} = 11.3\,\mathrm{mm}$, respectively. Lastly, both have an appropriate anti-reflection coating for $\lambda_{AR} \approx 1080\,\mathrm{nm}$ (no additional reflectance value has been provided). It should be noted, however, that these elements are also 100-times more expensive than their 1$^{\mathrm{st}}$ generation counterpart.

In order to quantify the improvement resulting from the utilization of HPFS lenses, first, the setup was aligned in a similar way, as discussed in Subsection 4.1 and depicted in Figure 4.8 b). Here, Figure 4.12 shows the captured temperature distribution of collimating HPFS lens, at the highest demand of 2.2 kW. Note that this is indeed the highest output of the SPI fibre laser, meaning that the results to be discussed here are limited by the available laser source.

There are 2 important features to consider here. First, in contrast to the previous discussions, this lens does not show a Gaussian-like heat distribution. In fact, apart from the reflections originating from the BDO, no deviation from a homogeneous distribution is visually observable. Furthermore, the thermal camera itself was not able measure any excess heating on the lens either. This suggests that the thermal load, and in turn the thermal focusing induced by the optical lenses is expected to be significantly reduced. On the other hand, as also visible on Figure 4.12, it is clear, that in this case, the heating of the BDO will be the dominant factor in limiting the coupling into the FUTs. Unfortunately, since this piece of optics also acts as an inherent protective sealing for the laser source itself, replacing it with another one of higher purity was not possible. After updating the digital twin introduced in Subsection 4.3.2 with the appropriate geometrical and material values, the simulation shows good agreement with the experimental results; the calculated temperature changes in the HPFS lenses are negligible, furthermore, the model similarly indicates that the main source of the observed thermal effects is the BDO.

Using the same, 13 m NANF-5 fibre piece presented in the prior Section, while also applying the same CLE technique, Figure 4.13 shows the final experimental results achieved, using the upgraded 2$^{\text{nd}}$ generation layout. The light green square markers corresponding to the left hand y-axis shows the measured transmitted power as a function of the incident power coupled into the FUT. Considering the loss accumulated during transmission, using the attenuation value presented in Table 3.1, the calculated transmission loss is 0.0167 dB, which translates to ~99.6 % transmission efficiency. After accounting for this, the calculated CE is shown by the darker green upwards triangle markers, corresponding to the right-hand vertical axis. For comparison, the grey dots and black downwards triangle markers represents the previously discussed scenario (see blue markers on Figure 4.11), that is, using the old pair of commercially available (ThorLabs) lenses, respectively. Furthermore, both data sets, correspond to measurements where the same CLE technique was applied. The improvement can be appreciated by observing how the new layout results in both higher CE values, while the more moderate "roll-off" also allows higher power levels to be coupled. This latter point also demonstrates the impact of the higher purity lens pair. Due to the lower absorption of the material, the alteration of the beam distribution at the focus from the initial, low-power case has been reduced. This results in maintaining the same overlap integral — and in turn CE — even when larger power levels are incident on them. It can be noted that for both cases, the roll-off is observed above similar power levels. This suggest that the BDO (which remained unchanged), and in turn its thermalisation, plays an important role in determining the actual power threshold.

To examine the thermally induced effects in more details, Figure 4.14 a) shows the required compensation of the position of the input tip of the FUT, in order to maintain maximum CE. This can be basically interpreted as the thermally induced focal shift. The

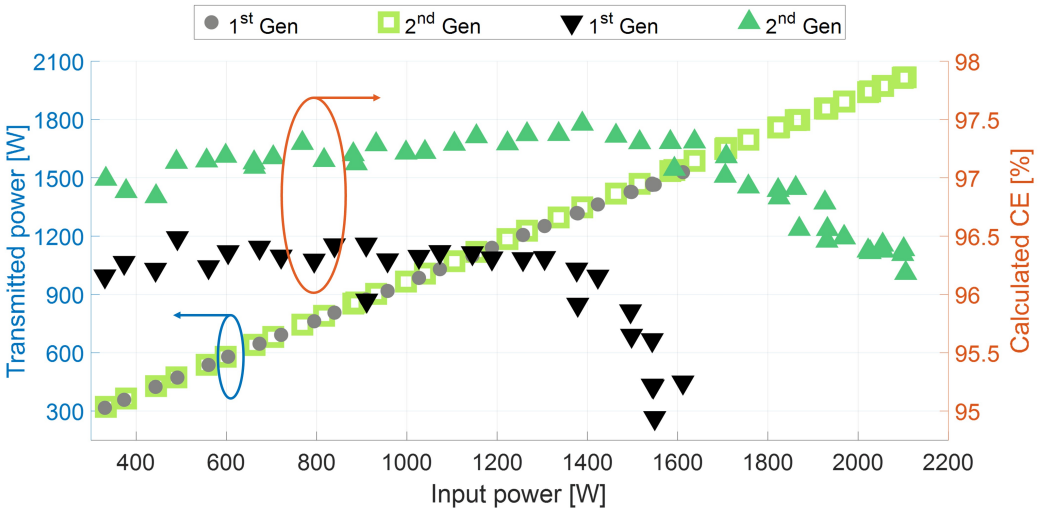

FIGURE 4.13: **Comparison plot of 1^{st} and 2^{nd} generation power delivery results** | Corresponding to the left vertical axis, grey dots and green square markers show the transmitted power as a function of the incident coupled power, when the 1^{st} and 2^{nd} generation experimental setup has been used, respectively. The calculated coupling efficiency values for the respective data points are also shown with downwards and upwards pointing triangle markers of black and green, respectively, scaled to the right vertical axis. The improvement is clearly visible both by the ~1 % increased CE, and by the notably slower roll-off above the 1500 W input power level.

3 cases presented are i) when a new pair of out-of-the-box commercial lenses have been used, ii) when the same lens-pair has been employed, after everyday usage for several months, and iii) when the new high-purity lens pair have been utilized, depicted by blue, red, and green markers, respectively. Comparing the impact of maintaining a clear surface of the optical elements is clearly visible between the red and blue markers, which aligns well with the expectations based on the works of Bonhoff et al., as the authors claim that the influence of thermally induced effects depends greatly on the degree of contamination present at the surface of the optical components [132]. Furthermore, it can be also appreciated, that the high purity lens pair performs even better than both of the previous cases, as less realignment is required to manage the thermal focusing and preserve the high CE.

Moreover, Figure 4.14 b) highlights the contribution of the CLE technique on the peak temperature measured on the initial section of the FUT. In this case, the 3 scenarios presented are when a fresh pair of commercial lenses were employed, without and with the CLE technique, and when the high purity lens pair have been installed, for red, blue and green, respectively. The former 2 data sets are the same as those shown in Figure 4.11. In addition, here, the green markers show almost identical effect on the coating temperature, regardless of the used lens pair. Below ~1.5 kW of input power the blue and green markers behave practically identical. However, above this level, when the commercially available lens pair has been used, as the CE started to roll off (as can be seen in Figure 4.13), the increase of the temperature values measured can be also

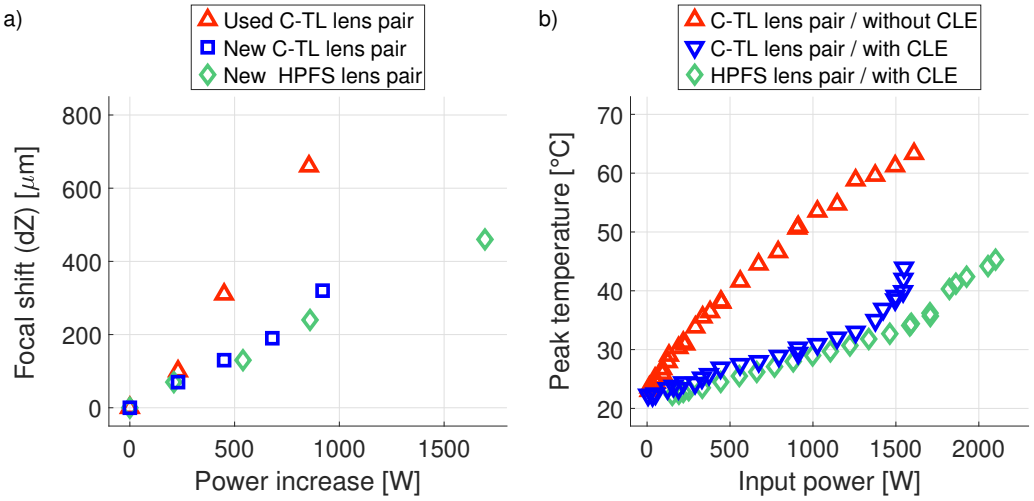

FIGURE 4.14: **Impact of thermal effects influencing the coupling efficiency at high incident power levels** | Part a) shows the results of applying CLE and the usage of high-purity lens on the paraxial shift of the focal position of the beam. This is measured by the travel distance of the fibre tip stage required to achieve the best transmission efficiency. On the other hand, b) demonstrates the highest measured temperature of the coating, as the function of the incident power, as recorded by the thermal camera. The latest results using both the high-purity lens pair, and CLE technique are plotted with green, while the red-blue contrast indicates different performances of the same commercially available lens pair of lower purity, demonstrating the impact of weariness (a) and of employing the CLE method (b), respectively. Note that for a), the ΔP power difference is shown on the horizontal axis. The reference 0 position is set at the highest respective power level, at which no repositioning of the input tip from its initial position was required.

observed. On the other hand, the slope of the green markers (i.e. the case when the HPFS lens pair has been used) changes only slightly above this threshold — showing similarities with the behaviour of the respective CE curve in Figure 4.13.

Concluding the list of observations, Figure 4.15 presents the hardly noticeable spectral evolution of the transmitted beam at the maximum demand of 2 kW average power. Compared to what has been already shown in Figure 4.4, an indication implying the development of an even smaller shift might be observable. This is the due to the ~2 orders of magnitude lower PDP, which results in a significantly smaller nonlinear interaction with the air-filled hollow-core. However, the noticed difference might be due to fluctuations in the laser output spectrum. These findings agrees well with the expectations from Subsection 4.3.1, that is the transmission should not impact the spectrum in any significant way. The captured cross section of the transmitted beam is also presented, displaying that the high-brightness, quasi-single moded intensity distribution has been also preserved.

4.5.1 Discussion

In summary, Figure 4.16 shows most recent and relevant CW power delivery results reported in the literature up until the date of submission. Studies employing both SCFs

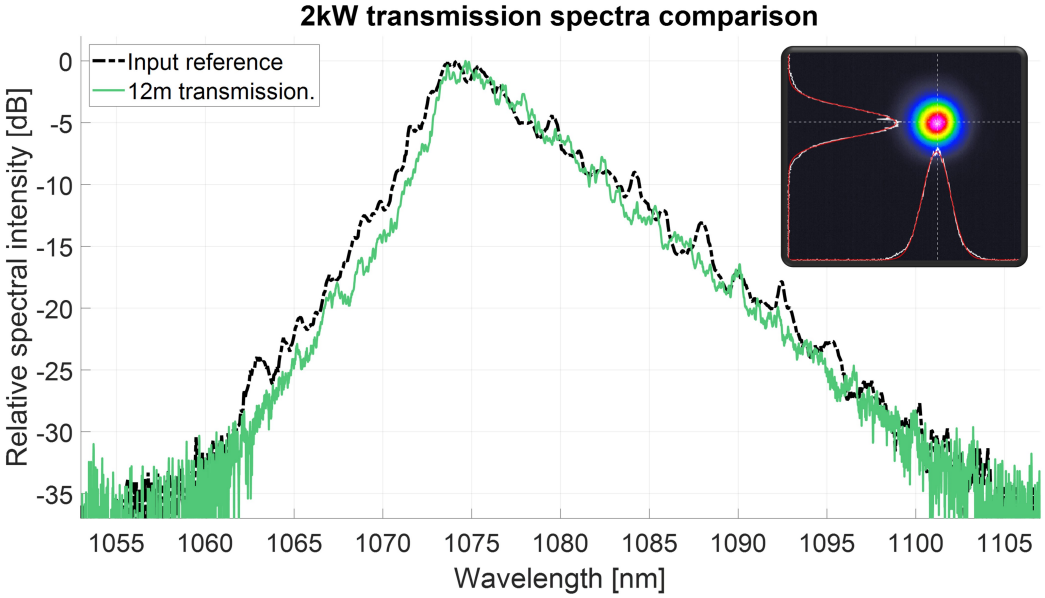

FIGURE 4.15: 2 kW **spectral and modal transmission** | Spectra of the 2 kW CW beam before and after propagating through 13 m of HCF, as recorded by the optical spectrum analyser, depicted by black and green curves, respectively. Both spectra are also normalized to their respective peak intensity. A slight red shift is noticeable, which is expected from the simulations, and are contributed to rotational SRS. The inset also indicates the high-quality output profile of the transmitted beam.

(solid markers) and HCFs (hollow markers) are included, while red symbols mark the outcomes of the experiments discussed in this Chapter — T1 and T2 for the 1st and 2nd generation setups, respectively. The diagonal lines indicates the PDP threshold levels that correspond to the case of $S = 0.5$, for the scenarios labelled by the shaded regions. At these boundaries only half of the output optical power is expected to remain within the wavelength range defined by the input beam, while the rest of the transmitted power is shifted to Stokes signal wavelengths considering the respective circumstances.

Firstly, the 1 kW-1 km result (labelled T1) reported in Section 4.2 is clearly beyond the capabilities of SCFs of any kind. Nevertheless, it can be also seen, that it is still well below the capabilities of HCFs. As it has been discussed in [94], a 6-to-10-fold improvement in PDP is still possible. However, this estimation also considers that the core of the fibre is filled with air — assuming that the fibre is evacuated, PDP values orders of magnitude larger are predicted.

Secondly, similar, independent research conducted by Cooper et al. [143] — labelled as H8 on Figure 4.16 — align well with the results presented in this Section. (Note that at the time of submission, only a pre-print version of the article is available.) The group also reports the transmission of over 2.2 kW average power over 6.25 m of their own in-house fabricated 5-tube NANF, using a laser source providing a CW beam with narrow spectral bandwidth around the $\lambda_0 = 1080$ nm central wavelength, and excellent $M^2 = 1.045$ beam quality. Unfortunately, while the authors seems to employ a similar

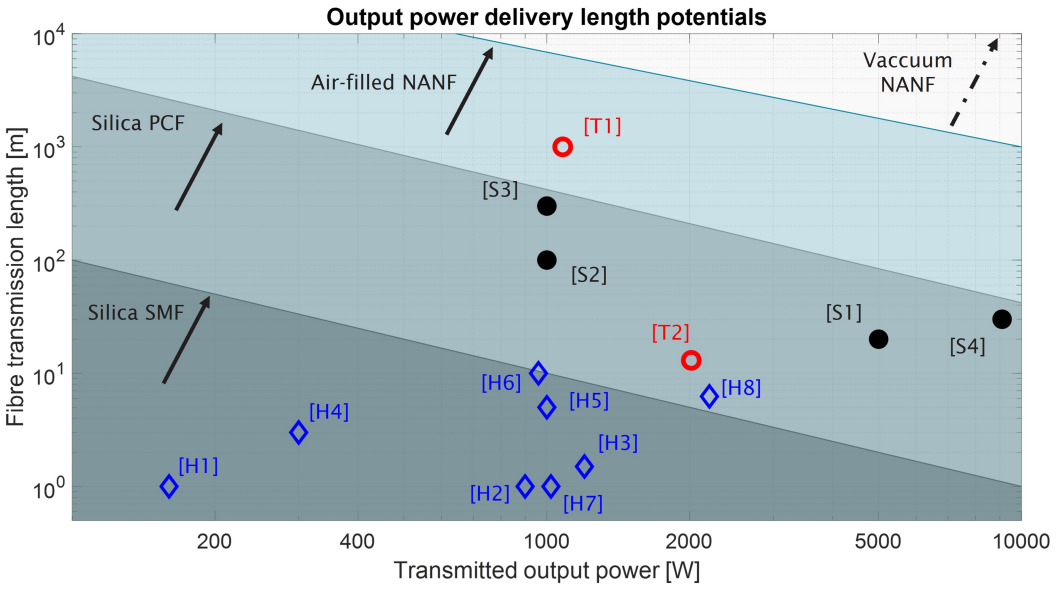

FIGURE 4.16: **Scalability of high-brightness high-power CW beam delivery through optical fibres** | Solid diagonal lines represents the power-distance product (PDP) thresholds, above which the labelled fibre type would transform the transmitted beam to have $S = 0.5$ spectral power overlap after propagation. Solid dots, and empty diamonds depicts experimental demonstrations of other groups using SCFs and HCFs, while open circles indicates the results presented in this Thesis, respectively. The markers denotes the following works: **S1** - Shima et al. [17], **S2** - Röhrer et al. [38], **S3** - Matsui et al. [37], **S4** - Okuda et al. [13], **H1** - Jones et al. [137], **H2** - Hädrich et al. [138], **H3** - Palma-Vega et al. [139], **H4** - Zhu et al. [140], **H5** - Zhu et al. [141], **H6** - Cooper et al. [142], **H7** - Cui et al. [103], **H8** - Cooper et al. '23 *Pre-print available* [143], **T1** - 1st generation results, published Mulvad et al. [94], **T2** - Most recent, 2nd generation result discussed in this Section. Figure adapted from [94].

free-space coupling approach using a pair of lenses, they do not provide much detail about their optical purity or absorption. Information about such parameters of the optical elements could be crucial, as they claim that *"[...] no additional adjustments to the NANF input coupling were performed for the entire duration of high power testing"*. Considering the discussions above, this suggest that Cooper et al. have also found an adequate way to manage the absorption related effects that can have detrimental impact on the CE. Nevertheless, the findings reported in this Thesis presents the highest average CW power level ever transmitted through any kind of HCFs up to date, and such are world record results, and another significant stepping stone for future high-power delivery research.

4.6 Conclusion

In conclusion, in this Chapter the state-of-the-art results of long-haul, high-brightness CW power delivery using hollow-core anti-resonant fibres have been presented. After the realized experimental setup had been introduced, the highest power distance product (PDP) of $1 \times 10^6\,\mathrm{W \cdot m}$ — i.e. 1 kW average power over 1 km distance — has been

experimentally demonstrated. Examining the measurement data in more details, showed that it is possible to further improve on this value. Analysing the spectral evolution of the beam when transmitted over 1 km indicated only minor spectral broadening. This has been attributed to rotational Raman scattering of the ambient air molecules inside the hollow-region. However, simulations suggested that even at 2.2 kW average power — that is at the maximum demand of the available laser source — transmission over 5 km of HCFs is achievable without significant spectral penalty.

Based on this insight, I have coded a simulation, which acts as the digital twin of the experimental setup. Once the model had been verified against the measurements, it has been used to identify the possible bottlenecks that could scale down the capabilities of the experimental layout. I have found that the main limiting factor for maintaining a highly efficient coupling and robust transmission is related to the management of light absorption along the system. After pinpointing the relevant sources of material absorption both in the coupling optics and the fibre structure, I have proposed 2 techniques that could lessen the restrictions they impose on the power delivery.

Firstly, by implementing a method to extract excess light that has not been confined in the fundamental mode of the HCF, I have demonstrated that the peak temperature of the initial section of the fibre can be significantly reduced without having any impact on the CE. Furthermore, by employing optical elements of higher optical purity, I have shown that the quality of the incident beam can be preserved even at higher power levels. Combining these 2 techniques allows the same, high CE to be maintained over a larger power range, which led to the independent demonstration of transmitting 2 kW of optical power over 13 m of NANF.

The results discussed in this Chapter paves the way for new applications, which require long distance transmission of single-moded optical beams with considerable average power. Such operation would not be possible by using conventional SCFs, due to their limitations; namely that the most intense part of the beam is confined inside a material can lead to significant nonlinear effects. As pointed out previously, this can be efficiently avoided by utilizing a HCF-based technology.

4.7 Outlook

Finally, this Section concludes the Chapter by providing a range of possibilities, where the findings presented can be of interest. While there are a huge number of possible directions to explore that could take advantage of the results presented in the prior Sections, the 6 main distinct directions with the most promising prospects for future work has be considered:

4.7.1 Upgrading the COMSOL model

A powerful next step for the simulations would be the implementation of the COMSOL wave-optics module. This would significantly increase the complexity of the software; nonetheless, it would also help in understanding the evolution of the focal spot as the input power level is increased. Combining the upgraded model with the mathematical definitions of optical aberrations introduced in [98] could provide meaningful insight for further scaling of the power levels. Understanding the thermally induced deviations of the beam distribution could also allow better compensation of it, e.g. by introducing an additional optical element, the refractive index of which changes with temperature with an opposite sign compared to those already in use.

4.7.2 Characterization of light extraction efficiency

It has been presented how implementing the CLE technique reduces the thermal load on the FUTs, without having any measurable impact on the CE. However, it has been also stated in Section 4.4, that during the experiments no special effort was given to optimize and characterize the efficiency of the extraction of the excess light. From Figure 4.14 b) it can be also observed, that even at the highest demand of the laser source, when utilizing the CLE routine, the maximum temperature reached is $<50\,^{\circ}\mathrm{C}$. This is far below the $100\,^{\circ}\mathrm{C}$ threshold value considered at the time as the limit of safe operation. Since the available power levels are limited by the laser system, there were no incentive to further characterize the CLE technique. This insight, however, could become important if laser sources of even higher output powers will be used.

One proposal that has been considered is the utilization of a device similar to an integrating sphere. In that case, the optical power of excess light extracted could be more precisely quantified. This metric then in turn could be correlated with several other parameters, ranging from characterization of the excited cladding modes, to providing a feedback to monitor and maintain high CE. Furthermore, if it can be assumed that no cladding modes have been excited, even at lower power levels, optical attenuation of higher-order core modes might be possible to measure. This is reasoned by the fact that for ARFs optimized for SM transmission, the attenuation of HOMs are significantly larger. While these are distinctly different from the cladding modes, in this scenario, the higher loss values would lead to higher temperature values measured. Comparing this case to that of lossless, purely SM transmission, all thermal contributions could be attributed to the HOMs.

4.7.3 Enhanced drilling

Over the last decades, many of the essential minerals required by several industries have to be excavated from deeper locations, usually surrounded by harder geological formations as well. It has been reported, that the main contributor of the cost of such extractions is related to the drilling process. Taking the development of geothermal

resources as an example, Jamali et al. states that the relevant cost can account anywhere from 50 to 70 % of the total investment, and that it can follow an exponential dependence on the depth of the procedure [128]. This is mainly reasoned by the high wear of the drilling bit during operation. However, by pre-conditioning the material — via laser induced thermal rock softening — the excavation can be made easier, and in turn cheaper.

It has been shown that it is possible to enhance the hardness of industrial steel by laser surface engineering [144]. Similarly, characteristics of hard rocks can be also altered by using high power laser systems [128]. By employing a remote technology which can modify the underground environment by locally making it more brittle, the earlier mentioned wear related costs of the tools used can be decreased significantly. Furthermore, the exponential growth of the depth related costs can be also reduced, as it has been shown in this Chapter, that delivery of high-power, high brightness laser light is possible on the km-scale. To explore another one of the examples, the drilling of deep-sea mineral nodes can be also considered. These nodes have enormous mineral reservoirs, ranging from cobalt, through zinc, to lithium amongst many others [145]. Some of these are essential resources for one of the most recently emerging sector: the electric vehicle industry.

Finally, to revisit the first example in this Subsection, the field of a promising next generation renewable and carbon-free energy sources of geothermal systems is considered here. In general, the energy output of solar and wind farms can fluctuate significantly over time based on factors out of human control. However, it has been shown recently, that it is possible with geothermal power plants to store and harvest energy on demand as necessary — without relying on batteries to store the excess [146]. While this would not lead to the other more common techniques (e.g. power plants) becoming redundant, geothermal energy can become a practical counterpart complimenting those. Similarly, the previously discussed results presented can help with the laser-aided excavation, that is required to establish such facilities.

4.7.4 Delivery of narrow bandwidth optical fields

As mentioned earlier in Section 2.5, in this Thesis, optical beams with relatively broad bandwidth have been considered and used. However, another similarly important field is the employment of narrow bandwidth light sources. In that case, the first nonlinear phenomenon that limits the possibilities of using SCFs is the stimulated Brillouin scattering (SBS), as the corresponding input threshold power is practically ~3 orders of magnitude lower, than the stimulated Raman scattering (SRS) detailed in this Chapter [40]. For this reason, such sources are expected to experience some degree of unwanted nonlinear degradation even when only a few metres of SCFs are used. Therefore, fibre amplifiers of narrow bandwidth beams are generally limited to similar length scales. On the other hand, by using HCFs, this distance can be increased to beyond tens of metres.

However, faster ramp up time of the coupled power would be also required, which might be practically challenging as it has been discussed in Section 4.3, since the appropriate management of the thermalisation and the induced thermal lensing is not trivial. Nevertheless, the approach of spectral beam combining for power scaling — akin to the system used in References [11] and [131] — could greatly benefit of research studies similar to those condected by Cooper et al [143].

4.7.5 Power transmission in vacuum

As mentioned earlier, a promising and still not yet well explored domain for high power CW delivery is the prospect of evacuating the fibres in order to lessen the impact of any nonlinear phenomena [94]. Probably the most interested fields would be mainly industrial ones, where the delivery of multi-kilowatt power levels over multi-kilometre distances are necessary. Without the intention to provide an exhaustive list, the technology could be feasible for example during the decommission of nuclear power plants [14], or when utilizing laser-aided drilling of subsurface and underwater rocks for oil, gas, or coal harvesting — as discussed in the prior Subsection. In these scenarios, the target area for material processing can be hazardous and/or the access to it can be difficult, and such, controlling the position of processing precisely remotely can be advantageous.

4.7.6 Long-haul delivery of optical pulses

Another obvious and straightforward step from CW power delivery would be to shift the attention towards the transmission of pulsed laser light [147]. First of all, the air-filled core would significantly reduce the experienced spectral dispersion (i.e. chirp). Furthermore, it could be possible that filling the core instead with an appropriate gaseous medium would lead to a self-sustaining soliton, with the additional advantage of having a conveniently interchangeable core. Similar pulsed power delivery has been very well demonstrated and studied by numerous other groups [147–150].

Understandably, however, exploring this possibility would deserve a study on its own. Firstly, a distinctly different laser source capable of delivering short pulses would be required. This in turn would also demand more refined optical components that have minimal spectral shift along the broader range of spectral components of the light pulse. Furthermore, an ARFs that can accommodate the spectrum of the source is just as essential. For these reasons, the conversion towards laser pulse delivery would not be straightforward. From the designing process to the actual realization of an experimental setup, it was acknowledged to be such a serious undertaking, that this direction was not pursued further, as it lies far beyond the scope of present Thesis. Nevertheless, the demonstration of delivering ultrashort ($<$100 fs) pulses trough HCFs with negligible dispersion could be a stimulating opportunity from academic research purposes [150] to industrial applications [128, 148].

4.7.7 Propulsion of particles

Last, but not least, by virtue of having a solid material-less core, HCFs are also capable of delivering small particles in the micron and sub-micron size range. Originating from what at the time was considered an unwanted phenomenon, the next Chapter is dedicated to discussions and experimental demonstrations of the propulsion of such particles.

5 Particle guidance inside hollow core fibres

During the high-power delivery experiments discussed in the prior Chapter, for some of the tested fibre samples, an unusual phenomenon was occasionally witnessed. Above some not too sharp input power threshold, it appeared that localised scattering of light from distinct points were propagated along the length of the fibres under test (FUT). This observation was developed into a study driven by curiosity, and as the investigation matured, progressively more possible applications were identified. While the initial aim was to conduct experiments at high powers, the practical problems encountered actually restricted the analysis to focus on lower power experiments thus far. Unfortunately, considerably more time than initially envisaged were spent on trying to solve the seemingly obvious (but actually rather complex) problem of creating freely suspended particles that the laser could trap and guide through the fibre — as it will be presented in Section 5.2.

In this Chapter, the initial observation of the mentioned phenomenon will be discussed first. Subsequently, potential explanations will be a reviewed. Comparing and contrasting the different options that can be employed to verify the assumptions, the designed experimental setup will be introduced and the choices made for the final layout will be justified. This is followed by an overview of the materials of the micron sized particles and droplets that could be guided during the experiments. Then, the gathered data from the experiments is presented and evaluated, and the demonstration of particle delivery is presented. Furthermore, current limitations of the setup and the approach is reviewed. Finally, the Chapter closes by providing concluding remarks, and recognizing potential applications.

5.1 Initial observation

Figure 5.1 displays a captured still image of NANF-5 during high-power operation (>500 W), highlighting the unexpected high scattering sources with red arrows. Visually, their scattering pattern showed resemblance to those originating from static imperfections that can appear during the fibre drawing process (e.g. touching tubular elements in a revolver-type fibre). However, they also displayed other features that proved any suggestion trying to connect the two phenomena false. First of all, they were not static, but moving along the length of the fibre — hence the term travelling defects was coined. Their path along the fibre was observable by their increased scattering. Moreover, while they were clearly visible, the transmitted power measured also dropped. The exact

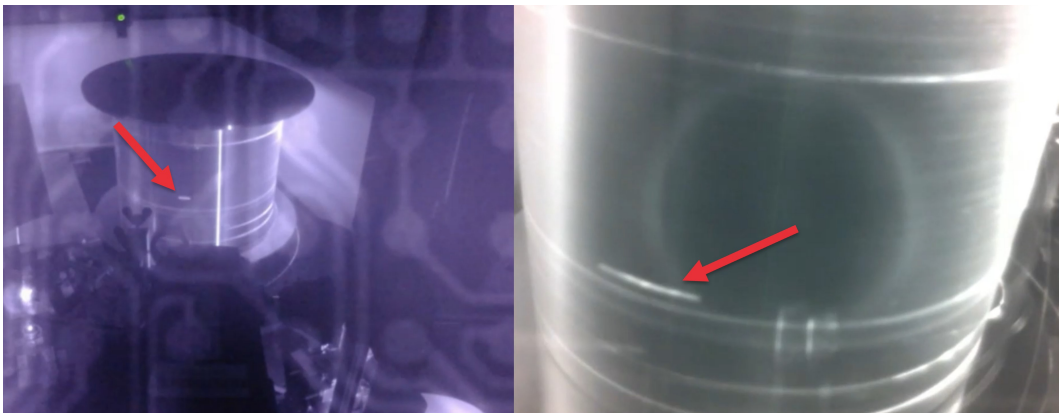

FIGURE 5.1: **Static image of inside of the HPD enclosure, during high-power (>500 W) operation** | The fibre in the figure is wound on an in-house aluminium drum. Red arrows mark the scattering induced by travelling particles propelled by the laser beam. These are suspected to be ammonium chloride particles, which are formed from the chlorine trapped inside the fibre during fabrication. At high power levels these particles are captured and being propagated along the fibre.

value could greatly vary based on factors like the 'intensity' of the scattering, the coupled power, and the number of defects being present at the same time, but typically around $0.2 - 1\,\%$ of the input power was observed to be lost. However, once the defects left the beam, the lost power was regained. Lastly, these events were never observed at lower power levels, but usually required substantial optical power to be coupled into the FUT for the phenomenon to arise.

Since at that time, this was regarded as a parasitic phenomenon (considering the power delivery efficiency and stability), significant effort was made to search for explanations regarding the origin of the phenomenon. As their behaviour (e.g. scattering intensity, or speed) depended on the coupled power, as well as they were observed to exit the fibre, they were suspected to be travelling inside the hollow core of the fibre — opposed to the smaller tubular elements of the NANF structure — and consequently, their maximum physical dimension was determined to be less than the core diameter. According to the scientific literature, 2 possible explanations have been proposed:

1. The phenomenon of optical discharge (OD) has been reported in HCFs [27, 151] that showed some similarities. However, there are 2 main significant differences that were conflicting with the observations:

   (a) The intense scattering from the OD was travelling towards the source, while our findings showed that in our case, the defects were propagating away from it.

   (b) The travelling discharge permanently altered the structure of the fibre that ultimately led to catastrophic fibre damage, and as a result, to the failure of confinement of the beam.

For these reasons, the phenomenon of optical discharge could not satisfyingly describe the event observed, and was discarded as a proper interpretation of the encounter.

2. The other plausible explanation was that the travelling defects were small particles, captured and trapped akin to Ashkin's laser tweezers [105]. Since this assumption was not contradictory, but rather a suitable interpretation of the observations, this direction was investigated further.

5.1.1 Microparticle delivery

As mentioned, it was speculated, that particles with diameters in the micron scale were being guided inside the fibre during the experiments when higher power levels were utilized. After the first demonstration of guiding atoms in HCFs in 1995 by Renn et al. [152], the delivery of particle with much larger diameters (50 nm to 10µm) were also reported shortly after, by the same group in 1999 [153]. However, 2 main questions still remained: What are these particles that are being propagated, and where are they coming from?

Based on the findings reported by Bonhoff et al. [132], the origin of the particles observed could be explained by considering the atmospheric lab conditions. For this reason, a commercially available air-purifier (Levoit LV-H132, with HEPA filter) and an accompanying particle counter device (Tera Groupe - NextPM sensor, supplied by RS Components) were both installed. Note that as discussed earlier in Section 4.1, the entire high-power delivery system had to be built inside a safety enclosure. This solution also had the added benefit of sealing the setup from unwanted air movements to a certain extent. However, based on the insight provided by the particle counter, it has been concluded that no unwanted particles above its detection threshold were present inside the enclosure during high power experiments. For this reason, the concept of trapping and propagating ambient dust particles was dismissed.

On the other hand, both of the former questions can be seemingly explained by the observations made by Lyngsø et al., during their experiments using their own in-house fabricated HC-PBGF [154]. The group reports, that during examination of the fibre performance, the ro-vibrational spectra of HCl can be witnessed, which originates from the fused silica that makes up the fibre structure. Building on this conclusion, Rikimi et al. conducted a rigorous study monitoring the long-term performance of HCFs [130] over time. Advancing on the work of Lyngsø et al., Rikimi et al. also report the detection of ammonium chloride (NH_4Cl). They argue that the NH_4Cl develops on the fibre facets, and speculate that the material is produced during fibre fabrication, when the temperature can reach values beyond 2000 °C. Therefore, the theory of capturing and propelling these ammonium chloride particles have been adopted. Additionally, the intention to replicate the witnessed phenomenon of particle guidance in a more controlled manner, as a mean to better understand the underlying physical aspects has been formed.

Moreover, by taking advantage of such a unique opportunity, other applications have been conceptualised.

Motivated by the ambition to showcase the capabilities of the in-house fabricate NANFs to their fullest extent, the possible implementation of a remote sensing device, based on the utilization of an optically levitated microparticle (as originally proposed by Bykov et al. [39]) has been considered. This concept acts as the main driving force behind the studies to be presented in the following. In order to achieve this objective, an essential first step is to gain more insight about the dynamics of the observed particle guidance through HCFs. Therefore, an experimental setup that allows the controlled launch and study of such particles is proposed and discussed in the next Section.

5.2 Particle delivery setup

The previously discussed high-precision, low power laser diode based experimental layout has been considered as a starting point to develop a system capable of launching and optically delivering micron-size particles. Figure 5.2 depicts the general flowchart of demonstrating controllable particle guidance. The process of particle propulsion can be broken down into 5 specific steps:

1. Preparation and deposition
2. Trapping and coupling into the fibre
3. Propulsion and confinement
4. Ejection or extraction
5. Evaluation of the recorded data

The following Subsections will describe each of the aforementioned stages of particle delivery. Finally, the Section will be concluded by presenting the designed and realized experimental setup.

5.2.1 Preparation and deposition of particles

In practice, particle samples are generally available in 2 physical forms: either a) as a powder, or b) as an aqueous suspension. As mentioned in Section 2.7, one of the first fundamental steps required before the optical manipulation of microparticles (McPs) of any kind can be performed, is to break the relatively strong Van der Waals forces present between the sample and its container — even if the particles are dispersed in a suspension [121]. There are 2 common methods for making the McPs airborne for experiments, depending on which of the aforementioned groups they belong to. Either mechanical vibration is introduced to the system to force the powdered material off the surface of its holder — usually via a piezo actuator [77, 155, 156] — or the particle suspension is dispersed by using a nebulizer [157–159]. One can also differentiate between active

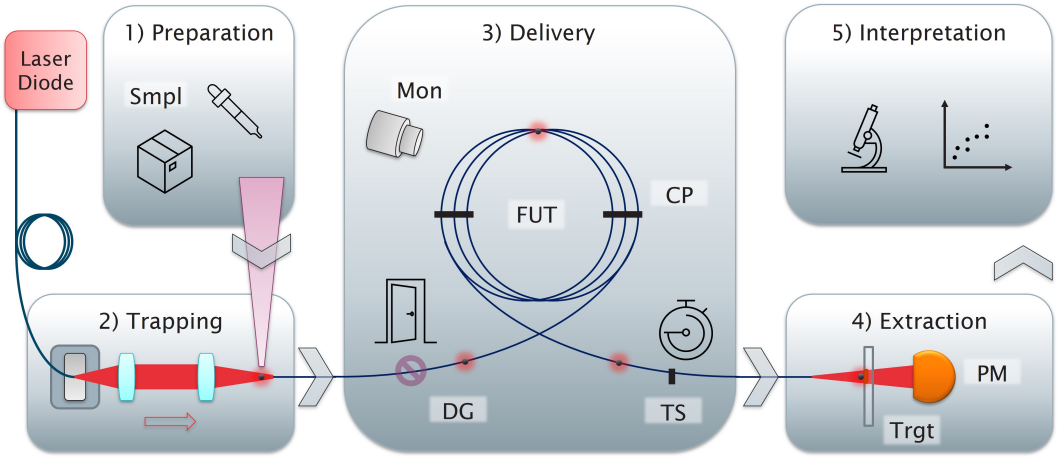

FIGURE 5.2: **Particle guidance setup flowchart** | The schematic illustrates the 5 stages of the experimental setup in a simplified manner. 1) Preparation stage; the sample (Smp) containing the microparticles (McP) is pre-conditioned for the experiments. This step can include the adjustment of the concentration of the suspension, or breaking up any aggregation of McPs, for example. 2) Trapping stage; the particle sample is being locally deposited into the previously aligned optical beam path. 3) Delivery stage; the coupled McPs pass through an initial filtering technique (droplet gating - DG). As the trapped McP is being propagated along the length of the fibre-under-test (FUT), important data regarding its position and visual appearance is collected by monitoring devices (Mon), while at preset checkpoints (CP), a timestamp (TS) is recorded to estimate its velocity. 4) Lastly, the guided McP leaves the FUT, and a target plate (Trgt) captures it. During the measurements, the transmission of the fibre is also constantly monitored by using a power meter (PM) to capture the output power. 5) Finally, the recorded measurements are being evaluated and interpreted.

and passive trapping processes. As mentioned in Section 2.7, because of the relevant van der Waals forces present, it would require a considerable amount of optical power to actively select and lift up a McP into the air — while for McPs that are confined and manipulated inside liquids, this is a far more feasible approach. On the other hand, a cloud of particles can be introduced into a well-defined volume which contains the fixed optical trapping beam. Due to the Brownian motion of the dynamics of these particles, some could eventually drift into the beam path because of the probabilistic nature of their movement pattern. Therefore, it might take some time until a particle travels into the optical path of the trapping beam, and for that reason, this method can be labelled as a more more stochastic, passive solution. A schematic depiction of the working principle of the 3 techniques to be considered here are shown in Figure 5.3.

(a) Piezoelectric vibrational stage

For the case of particles available in a powdered form, a platform is typically used. The sample is deposited into this container, which has piezo membranes attached to it — in most practical cases gluing is applied. By vibrating the piezos at the eigen-frequency of the particle holder, the McPs are forced off the surface of the platform, as the mechanical force exceeds the Van der Waals bonding forces. The exact frequency can depends on many factors including the shape or the material of the sample holder. If a trapping

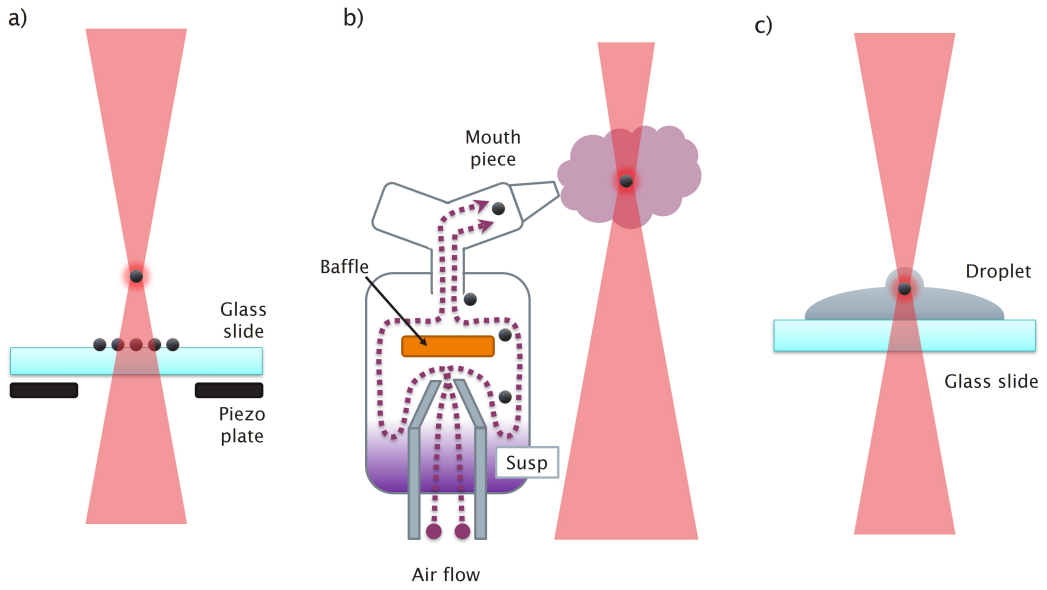

FIGURE 5.3: **Schematic illustrations of the considered particle deposition techniques** | a) A powder of McPs deposited on top of an optically transparent stage can be shaken off in a localized manner, such that the airborne particles can be trapped by the focused beam. The assembly consists of a glass slide and a piezo plate. By oscillating the latter at the eigen-frequency of the former, the mechanical vibrations force the McPs off the glass piece, incident into the beam. b) A jet nebulizer uses a pressurized air flow (disrupted by a baffle) to deliver a suspension (Susp) of particles into a localized volume as a fine mist. These, now airborne McPs — which may also have a shell of the solvent around them — can now pass into the optical beam, allowing them to be trapped. c) By having a drop of McP containing suspension place on top of a glass slide, the particle can be trapped easier while still inside the liquid environment. Then, by evaporating the surrounding medium, the captured McP could possibly remain inside a stiff optical trap, while practically being airborne. Note that this has not been demonstrated yet experimentally.

beam is positioned such that it overlaps with the expected trajectories of the particles as they bounce off the surface of the container, the now airborne McPs can be confined by the laser. The technique was reportedly first used by Thurn and Kiefer [155]. A schematic illustration of this approach is also depicted in Figure 5.3 a).

While this concept generally takes a more active and localized approach for deposition, the supporting electronic devices can also make it more complex. A frequency generator providing the signal to the piezo vibrating stages are expensive, and the stages themselves must be also capable of handling a large enough amplitude that will resonate the particle platform that holds the sample. Furthermore, the actual optimal frequency of the vibration depends on the specific the geometrical parameters of the particle stage, that has to be calculated on a case-by-case basis, and can typically range between 0.1 to 100 kHz. An advantage of this technique is that it is not sensitive to size or material composition of the McPs — opposed to the method of using a nebulizer for deposition.

(b) Dispersing using a nebulizer

On the other hand, a nebulizer is usually employed instead for particles that are suspended in fluids [157]. In this case the suspension containing the McPs is loaded into the device which generates a cloud of airborne liquid droplets, that can contain a number of the particles. A general schematic is depicted in Figure 5.3 b). However, the actual method of nebulization depends on the type of the specific nebulizer. Moreover, the size of the McPs can have a significant impact on the performance of the different devices [160]. Furthermore, some of these concepts also employ a fine mesh for producing the micron sized droplet cloud, which can be easily clogged without careful precautions. Lastly, by the nature of this approach, the material composition of the McP component is restricted by the potential chemical interactions between the solid and liquid parts of the mixture.

One crucial characteristic of the nebulizers to consider is the size distribution of the generated droplet cloud. Not only can this determine an upper bound of the particle size that can be utilized, but it is also an important factor of considering an optimal concentration of the suspension. By diluting the suspension to an appropriate concentration determined by the factors mentioned above, the particle density, that is the average number of particles suspended in the airborne droplets can be manipulated. While the desired density can depend on the actual application, it is generally feasible to achieve a value resulting in having on average only 1 particle per droplet. In order to ensure a more homogeneous mixture, the suspension is also typically pre-conditioned by using a sonicator. Here, an RS Pro 100 W ultrasonic cleaner with 2 L tank capacity has been used. Placing the sample into an ultrasonic bath, most of the agglomerated clusters can be broken up, resulting in a more uniform particle distribution. This enables a much easier regulation of the particle density of the generated droplets, which is beneficial for the experiments.

In general, compared to the case of employing a piezo-stage, the utilization of a nebulizer is considered to be a passive approach. This is due to the fact that the trajectories of the nebulized particles generally follow a stochastic distribution, and the produced cloud is not well localized. As the droplets enter the deposition chamber, they start to fill the available volume uniformly — chiefly because of the existing air movement. It is only when a number of these particle containing droplets enter the already present optical beam that they can be trapped. For better localization a more flexible delivery employing a nozzle can improve the probability of such trapping events to happen by directing the cloud of droplets towards the trapping beam with better accuracy.

(c) Solvent evaporation

Lastly, the possibility of optically trapping a particle inside the suspension then removing it from the liquid environment was briefly explored. For practical reasons, in this case the beam was directed upwards. A microscope slide holder mounted on top of a similar

3-axis ThorLabs MicroBlock Stage (MBT616D/M) has been installed such that the focal point of the beam is slightly above the horizontally placed glass piece. A drop of the sonicated suspension is placed on top of the glass slide, such that the focused beam is incident on it, and the focal point is located inside the mixture. Then, the transmitted beam is strongly attenuated, such that a CMOS camera can image the inside of the drop containing the McPs. The main advantage of this approach is that trapping inside an aqueous medium is practically more feasible, as stronger optical trapping can be achieved even when relatively lower optical powers (~100 mW) are being used [159].

By adjusting the position of the microscope slide via the stage, separate McPs inside the suspension can be captured by the focused beam. It has been speculated that once trapped, the McP can be removed from the mixture, either by relocating the focus outside the suspension, or by removing the solvent from around the particle. An illustration of this concept is shown in 5.3 c). The latter option could be achieved by either normal or externally aided evaporation (e.g. increased air movement). Unfortunately, despite all efforts, such extraction of the McP from the suspension have not been demonstrated. It has been suspected to be caused by the induced mechanical forces on the McP during extraction, as the surface tension of the surrounding medium de-stabilize and ultimately breaks the optical trap. Because of these reasons, this approach was not pursued any further.

Finally, Table 5.1 summarizes the main advantages and disadvantages of the 2 — (a), and (b) — main techniques discussed. Some of the most relevant parameters when considering the final design was the required financial investment, ease of use, modularity and the compatibility of current equipment, with the latter ones being more subjective and specific for our case. After careful consideration, the approach of using a nebulizer has been chosen to be the preferred technique for particle deposition. This is because the required equipment is inexpensive, a wide variety of particle suspensions with precise standards are readily available, and the simple integration into the already assembled experimental setup. A more detailed discussion about the McP samples will be provided in the next Section.

5.2.2 Trapping and coupling of particles into the HCF

One important aspect for the case of trapping in air is that the strength of the trap can be affected to a greater degree by the environment. Air movements, temperature and relative humidity all have a significant influence on how stably a particle can be contained within the trap [161–164]. In order to reduce the impact of such phenomena, the previously discussed delivery solution must be able to provide the particles of appropriate speeds within a few 100's of µm in front of the beamwaist [118]. Those slow enough particles, whose trajectory also overlaps with this cone defined by the focused beam will experience optical forces acting on them that will ultimately lead to stable optical trapping.

TABLE 5.1: Comparison table of the main deposition techniques (piezo stage or nebulizer) contrasting their respective advantages and disadvantages of employment

Aspect	**Piezo stage**	**Nebulizer**
Cost	$ $ $	$
Complexity	Complex	Simple
Method of deposition	In batches	Possible to deposit constantly
Particle size constraint	No strict limitations	Limited by the nebulizing technique
Size distribution	Well defined by the particles	Stochastic distribution of sizes
Localization	Can be localized more precisely	A cloud of fine mist fills a larger volume
Requirements on form of particle sample	Powdered preferred	Suspended in liquid

However, the focusing of the beam is ultimately dictated by the hollow-core FUT, as maintaining a highly efficient transmission is essential. This limits the stiffness of the optical trap, as the beamwaist is determined by the core size of the fibre. Nevertheless, if the previously mentioned conditions are met and the trapping is accomplished, the coupling of the particle into the HCF is practically straight-forward, and self-sustaining. This is due to the fact that for typical non- or weakly absorbing particles, the $\mathbf{F}_{\text{grad}}$ gradient force will always push the particles towards the most intense part of the beam — i.e. the centre. Furthermore, the scattering force will push the particles parallel to the direction of propagation, essentially guiding them into the hollow-core. The governing equations have been introduced earlier in more details in Section 2.7. In the next Section, the impact of the particle size relative to the core diameter of the FUT will be also examined through more specific examples.

5.2.3 Propulsion and confinement of the particle inside the HCF

Generally speaking, once the trapped particle is coupled into the fibre, it will be confined near the centre of the core, assuming that the beam is not altered significantly along the fibre. Meaningful alterations can mean a) natural loss of power as a result of the attenuation of the fibre after a given length, b) too tight bending of the fibre leading to a larger centrifugal force than what can be compensated by the radial optical force, or c) a local imperfection or permanent damage of the fibre structure inducing a significant drop in power, just to give a few examples. Lastly, the HOMs can also have an influence on the guidance [119]. However, since additional care is always taken to excite on the FM of the FUT, the possible impact of HOMs is not considered here.

So far, only a single beam has been considered to be coupled into the fibre. In this case, the speed of the particle can be regulated simply by adjusting the power output of the laser source. It is, however, important to note that while the axial force acting on the particle is proportional to the optical power — it scales linearly according to Equation 2.26 — there is also an obvious lower threshold, below which, the radial forces cannot stably trap the particle. The results to be reported in the following are based on a system using the previously introduced low power laser diode source ($P_{\mathrm{LD,\ max}} \approx 100\,\mathrm{mW}$). This further supports the importance of maintaining a high CE and in turn transmission efficiency, such that the trapping forces will remain sufficiently large along the entire length of the fibre.

On the other extremity, there also exist an upper bound, a maximum delivery speed of the particles. Experiments using the SPI fibre laser source ($P_{\mathrm{SPI,\ max}} \approx 2.2\,\mathrm{kW}$) has been considered, but had to be postponed and will build the foundation of an independent study in the future. An estimation of the practically achievable peak propulsion velocities based on relevant parameters will be provided later in Subsection 5.4.3.

5.2.4 Ejection of the particle from the HCF

Generally speaking the particle can be delivered through the fibre with 3 distinct purposes:

Principal particle delivery

First of all, the delivered particle can be trapped again outside of the fibre (i.e. 'fundamental particle delivery'). In this scenario, the particle should not suffer any degradation during guidance, as the main goal is to re-locate it intact to a target environment. As an example, the transfer of an adequately sized biological sample to a specialized inspection tool can be considered — a schematic of which is depicted in Figure 5.4 a). Utilizing a low power optical beam ensures minimal heating through absorption, while also guaranteeing stable trapping and delivery. It also allows the speed of the propagation to remain slow enough such that it can be re-captured after the guidance. In this case only a modest length of HCFs (~10 to 100 m) are assumed.

Particle gun

On the other hand, by increasing the optical power level, not only stronger trapping, but higher particle speeds are achievable. In this case, the delivered sample could be deposited onto some surface. A variant of a 'particle-gun' is illustrated on Figure 5.4 b). As an example, precision surface patterning with sub-micron accuracy, using material ranging from polystyrene, through sodium chloride (NaCl), to gold (Au) McPs has been already demonstrated [165]. The flexibility of optical propulsion enables a wide variety of materials to be delivered and deposited — the technique is basically limited by the damage threshold of these particles. However, as it will be discussed in Subsection 5.4.3,

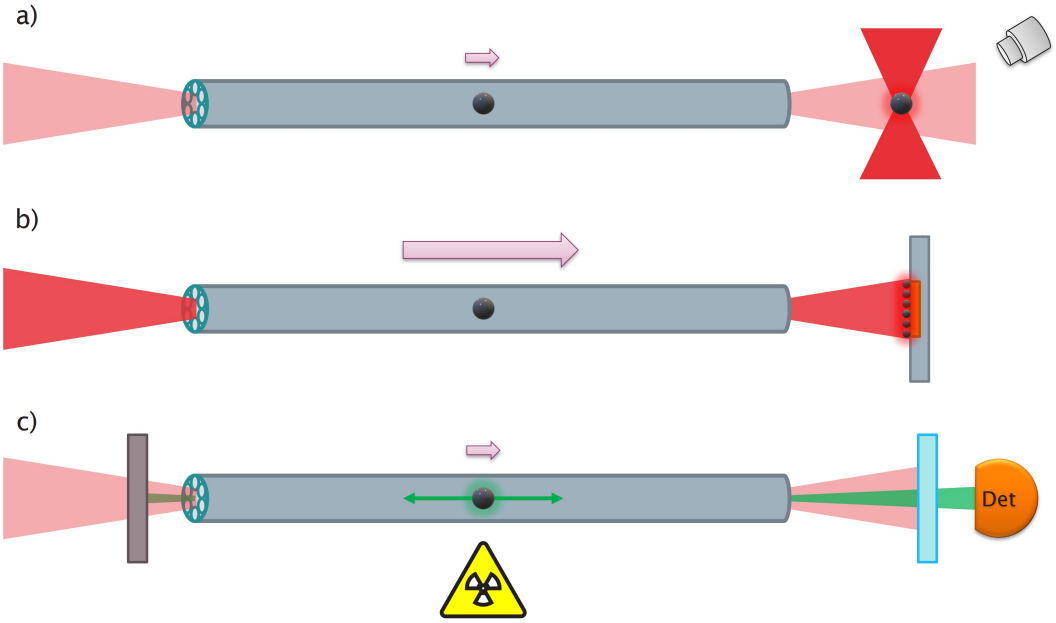

FIGURE 5.4: **Schematic illustrations of different applications and extraction types of microparticles guided inside hollow-core fibres** | a) One of the most fundamental utilizations of optical delivery of McPs is the simple relocation of the particle to a more desirable environment. This could be a specialized laboratory, or even a chamber with reduced air pressure, to give some examples. b) By employing more intense optical beams, the McPs can be accelerated to higher speeds, and can be deposited to a target location. In this scenario, the surface of interest can be processed in micron scale resolution, by practically using the delivery fibre as a particle gun. c) When McPs that have more peculiar features (e.g. radio- or thermal-luminescence), detecting the signals they can give off, and determining their location become the most important tasks to handle. In this case, thanks to their more easily replaceable nature, while still preferable, the extraction of the McP is secondary — assuming limited costs.

this approach might require the HCFs to be kept in a straight position, as tighter bends might not allow the optical forces to counteract the possible centrifugal forces present.

Localized sensing applications

Finally, it is possible to take advantage of the particles during their guidance inside the HCF. For this approach, maintaining a stable trapping along significant distances is crucial. As the most recent reports demonstrated a remarkably low attenuation of 0.174 dB/km [36], conserving significant portion of the optical power over km-scales is possible. The guidance of particles with special properties (e.g. radio-luminescence) presents a unique opportunity to develop a long-haul sensing instrument [39] — Figure 5.4 c) schematically illustrates this scenario. This utilization is arguable considered to be the main driving force behind further studies presented here.

5.2.5 Experimental layout

Based on the considerations discussed so far in the Section, the final layout of the experimental setup is shown in Figure 5.5. The arrangement is a slightly altered version

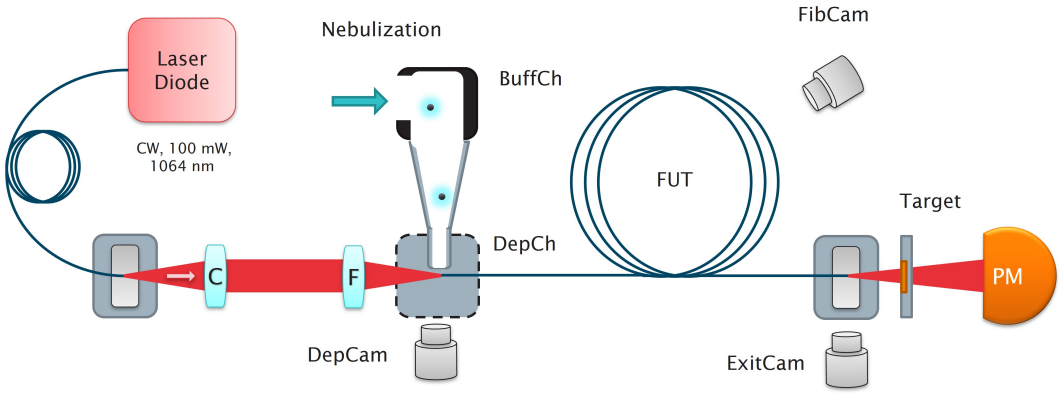

FIGURE 5.5: **Schematic layout of the particle propulsion experimental setup** | Similarly to the experimental setups introduced earlier, a layout based on a free space coupling approach has been realized. A pair of lenses (C and F for collimating and focusing, respectively) are used to manipulate the nebuilzed microparticles through the fibre-under-test (FUT). The transmitted power level is constantly monitored by a power meter (PM) measuring the transmitted light. The laser source is a low power laser diode, with central wavelength of 1064 nm. The microparticles are initially deposited by a nebulizer into a buffer chamber (BuffCh), where the higher speed McPs are passively filtered out via the air convention. Then, the remaining McPs, which have appropriate velocities fall into the deposition chamber (DepCh), where the focused beam can trap and couple them into the FUT. The input fibre tip, the entire length of the fibre used, and the output tip are all monitored using CMOS cameras, labelled as DepCam, FibCam and Exit cam, respectively. Finally, the delivered McP can be captured by a target, that can be placed right after the output interface of the FUT. More details are provided in the text.

of the one used for the low power coupling experiments (Figure 3.1).

Choice of nebulizer

In general, 2 nebulizers have been considered: a) Omron MicroAIR U100, and b) PariBoy Classic. After initial tests employing both instruments, the latter has been chosen as the preferred apparatus. There has been 2 main reasons for this decision; Firstly, the Omron nebulizer houses a vibrating element and a metal alloy mesh of fine holes. The supplier does not provide exact specifications, but inspections under microscope suggest hole diameters of ~50 µm. For practical reasons related to the clogging of the mesh, working with this device has been problematic. On the other hand, the PariBoy does not have such a fine-mesh, but it is a compressor based nebulizer instead. Furthermore, as connection tubing is also provided for the latter, the generated droplet cloud can be more easily directed.

It is also worth noting here, that when a nebulizer is generating the cloud of droplets, it is practical to do so in short bursts. This is beneficial for 2 reasons. Firstly, if a less expensive equipment is employed, the nebulization rate (deposited volume over time, usually $<1\,\mathrm{mL/min}$) is usually fixed, which translates to a constant average droplet velocity. Typical flow rates usually produce relatively high speed droplets that can be difficult to capture with lower stiffness traps. This can be overcome by using a

more sophisticated (and expensive) nebulizer which has the capability to adjust its nebulization rate. Secondly, a continuous flow of droplets can also degrade the beam quality — and in turn the coupling efficiency. The droplets which are not trapped by the beam can induce interference patterns in the field. In an ideal case, only a very limited amount of particles, with the lowest possible velocities should be present in the particle capturing chamber during experiments. The former concern regarding the speed of the particles is addressed by employing an assembly of chambers that can separate and slow down suitable particles, and will be discussed in the following.

Particle deposition chamber

The output of the PariBoy is connected to a buffer chamber, which is sealed on all sides, apart from 2 openings: one on the side for the nebulizer mouthpiece, and one on the bottom, which is directed towards the focused laser beam — as illustrated in Figure 5.5. The main purpose of the buffer chamber is to provide an initial selection process. The droplets with higher speeds will simply hit and attach to the opposite wall. Based on the works of Caviezel et al. [166], and Bolledulla et al. [167], assuming relevant quantities present in the system (e.g. Reynolds number, Weber number, etc.), the droplets will adhere to the surfaces, and are not expected to bounce back from them. Thanks to this, they will not lead to any undesirable interference pattern in the beam distribution either. Furthermore, because of their speeds, it would not be possible to stably trap these droplets with the used laser diode nonetheless.

After the droplets of lower speeds have been separated, they are expected to begin free-falling towards the focal point of the laser beam. They very rapidly reach their terminal velocities of $<15\,\mathrm{mm/s}$, that can be estimated by equating the gravitational force with the viscous drag. Combining Equations 2.27 and 2.29 showing a direct, squared dependence of the velocity on their exact diameter of the droplets, as they leave the buffer chamber via the opening on its bottom. The droplets fall through a straight metal tube, which also enables the evaporation of the surrounding liquid. The advantage of this section is twofold: Firstly, the reduced size would further slow down the droplets. Secondly, by thinning the surrounding outer droplet shell less unwanted effects can interfere with the experiments. Ideally, the aqueous medium should fully evaporate, ensuring that only the McPs are entering the beam path. Observations show, however, that some liquid droplets can remain and be captured by the beam.

Ultimately, the surviving particles and droplets arrive at a 3D-printed nozzle. As discussed by McGloin et al. [158] and subsequently, by Summers et al. [159], *"The design [of the nozzle] can be quite critical with slight alterations significantly altering the flow behaviour"*. The final nozzle fabricated in house is depicted on Figure 5.6 a) including the dimension, and is in essence a scaled version of what is presented in the article cited above. The assembly depicted schematically here is mounted on top of a 3-axis

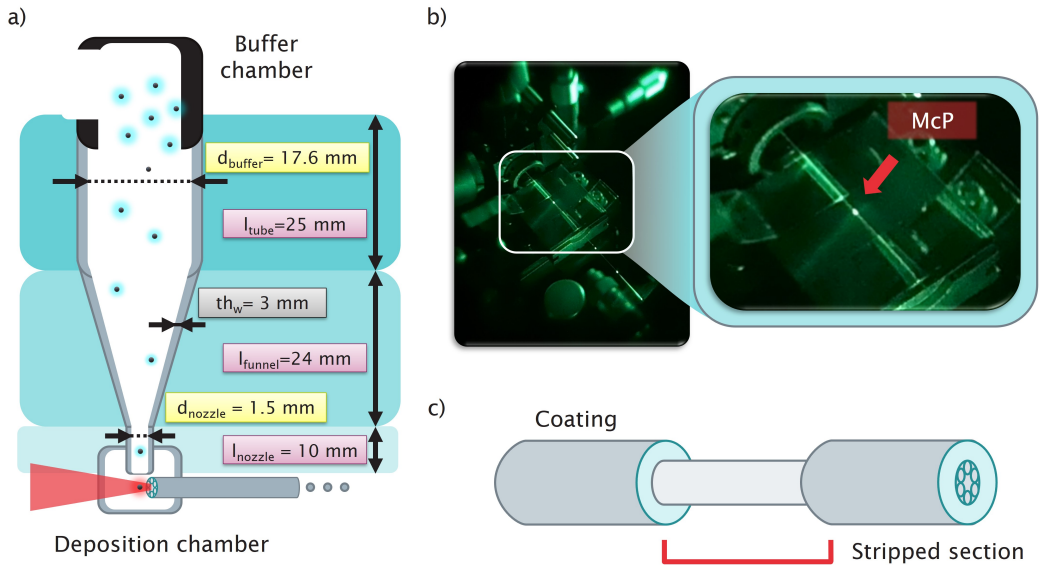

FIGURE 5.6: **Influential parts of the final particle guidance setup** | a) Specifications of the used, 3D printed nozzle connecting the buffer chamber with the deposition chamber. As mentioned in the text, the exact dimensions are critical for optimal McP deposition and trapping. b) Displays a photo of a trapped and guided McP, as it is being propelled along the length of the fibre, as seen through a conventional IR viewer scope. c) Schematic illustration of the droplet gating section, highlighting the intermediate section of the fibre, which is stripped from its coating. This enables to influence the mechanical properties of the core of the HCF more directly.

ThorLabs MicroBlock Stage (MBT616D/M). This enables the precise positioning of the nozzle, allowing the cloud of particles to enter the focused beam at the desired region.

It is worth noting that, unfortunately, no discussion regarding an ideal nozzle structure were provided by either [158] or [159]. Nevertheless, as later results will show, our 3D-printed model performed suitably. Because of that neither did I conduct a proper characterisation on the impact of the nozzle parameters (e.g. sharp angles, final output diameter), as optimization of this part of the setup was not essential. Still, such a study would certainly be beneficial for future works.

Finally, the droplets and particles leaving the nozzle enter the beam path and — because of the stochastic nature of deposition — a number of them are trapped and coupled into the FUT. Figure 5.6 b) shows a typical image of a scattering source — that can be either a droplet or a McP — highlighted by the red arrow, being propagated inside the HCF as seen by an InfraRed viewer. Unfortunately, however, it is not possible to determine if the artifact visible consist of a single free McP, multiple McPs, McP(s) with a liquid shell, or an empty liquid droplet without any McPs inside it, by such a photo on its own.

Droplet gating during delivery

As stated the previously, it is still possible for a pure liquid droplet of the suspension to be coupled into the hollow-core delivery fibre. In an attempt to filter out such events,

when longer (l_{FUT}>1 m) HCF pieces have been used, another gating mechanism has been proposed and implemented. In this case, the fibre has been stripped of its coating for a short segment (~5 cm), after a longer initial section (~30 cm), which is left intact — as depicted on Figure 5.6 c). While such an alteration will not have a significant impact the fundamental core mode, it enables a better control of the physical properties of this uncoated length. As the trapped scattering source is coupled and propelled inside the HCF, it ultimately passes this stripped section, which acts as another method for filtering. The influence of applying such practice (droplet gating - DG) will be discussed later in Section 5.4.

Particle delivery checkpoints

Lastly, when longer lengths of fibre pieces have been examined (l_{FUT}>1 m), multiple locations were labelled along the length of the FUT. During the measurements these positions act as checkpoints for the particle that is being propagated. Knowledge of the distances between these points enables the estimation of travelling speed, by simply recording a timestamp of the particle passing the set checkpoints. Note that such labelling on the fibre should be minimally interfering, as it has been shown by Schmidt et al. that an absorbing marking can have a significant impact on the propelled particle — ultimately it can also halt the delivery [168]. This is explained by the absorption induced gas dynamics inside the HCF. Quantified measurements of the achieved particle speeds will be reported in a later Section.

Now that the experimental setup has been introduced and discussed in detail, it is important to review the available particles that will be used during the study.

5.3 Microparticles

In this Section, the relevant micron-sized materials that have been involved during the experiments will be discussed.

First of all, the McPs of choice will be justified. There are several factors that have been considered. Arguably, the material of the McP is one of the most fundamental properties. An inert, inexpensive option is preferred for the initial experiments. Furthermore, having a low density material is advantageous, since for the same volume, a lower gravitational force will be acting on the McP. This would allow lower optical power levels to be employed, while still maintaining stable optical trapping. Similarly, higher damage thresholds would enable longer exposure to the light source before evaporating the particle, which in turn would translate to longer possible delivery lengths.

Regarding the size of the particle, having a precisely specified dimension with minimal variance is beneficial, as it would enable measurements with better repeatability. Similarly, in order to compare the results more reliably with theoretical models, simple spherical shapes are preferred opposed to more complex shapes, e.g. more elongated,

rod-like structures. Finally, in order to ensure that a more simplified discussion using the ray optics approximation is valid, that the size parameter (defined by Equation 2.24) should satisfy the relation $\xi \gg 1$, promoting larger McPs.

As discussed in the Section 2.7 the first obvious constraint is imposed by the fibre core, as an upper limit for the particle size. Figure 2.9 also showed that larger relative particle sizes allows a larger fraction of the beam to interact with the McPs following the trend of an error function. In general, only up to 60 % of the optical power can be practically utilized, as oversized particles could "clog" the fibre. Such an event would require the contaminated section to be removed, as it will not be possible to transport particles over the obstruction. This can be both inconvenient and undesirable, depending on the exact location of the accident, especially if significant lengths of fibre pieces are utilized.

5.3.1 Polystyrene microparticles

Based on the points discussed in the previous Subsection, microparticles made out of polystyrene (PS) was chosen for the initial experiments. This material satisfies all the prior requirements of an ideal candidate. Merck Sigma-Aldricht has a huge range of available latex beads made of PS with <2 % size variation. I have selected the option of PS particles with $d_{\mathrm{ptcl}} = 10\,\mu\mathrm{m}$ diameter. This size ensures that the maximum fraction of the optical power can be utilized, while also allowing some space inside the core of the HCF such that some degree of instability of the coupled beam would not result in breaking the optical trapping of the McP inside the fibre, causing it to stick to the inner surface of the core.

On the other hand, these McPs are also provided in the form of a suspension. This aligns well with the choice of using a nebulizer to provide airborne McPs for the optical trapping experiments. However, it is also important to mention that the PS-McPs are subject to degradation, when illuminated by laser light over time [107]. This would limit the length over which it is possible to propel such particles without considerably damaging them.

Lastly, it must be mentioned, that the potential impact of micron and sub-micron sized (inert) particles on the human health is still not understood well-enough. Continuous research effort is focused on studying the effect of microplastic particles, as increasing international interest is shown, recognizing its potential threat on the environment, and by extension to humans. At present it is agreed to be at worst have minimal influence. This is important to consider, as one of the most common material of microplastics is indeed polystyrene [169] — which were used extensively in the experiments to be discussed in the following Sections. Considering the point above, all the experiments described in this Chapter had been conducted with appropriate personal protective equipment (PPE).

5.3.2 Liquid droplets

As mentioned previously in Subsection 5.3.1, the PS-McPs are provided as a liquid suspension. Because of this, another important component that must be discussed here is the liquid environment itself. There are 2 main constituents that has to be considered. Firstly, there is the is the original solvent: de-ionized (DI) water. On the other hand, isopropyl alcohol (IPA) has been used to dilute the suspension to a desired concentration. The decision of using IPA over DI-water has been made because of the more favourable evaporation properties of the IPA. In the following, these 2 materials will be discussed.

De-ionized water

Originally, the McPs are already prepared with the de-ionized (DI) water as the solvent of the suspension. Since the nebulization process is expected to generate a number of empty, particle-less droplets as well, the interaction between the laser beam and the DI-water droplets is also anticipated. Unfortunately, the most undesirable property of the DI-water, is that it evaporates relatively slowly. This also enables the possibility of previously separated airborne water droplets to merge, combining both their solvent volume and particle content. Such an event is unwanted, as it can both push the size of the droplet above the limit set by the core diameter of the HCF, and can also lead to a cascade of similar events, as the larger droplet has a higher chance to merge yet again with other droplets as well. As the main objective is to examine the dynamics of the delivery of independent PS McPs by the laser light through the HCFs, another liquid with better vaporization was also used, and will be introduced next.

Isopropyl alcohol

One of the main benefits of using IPA as the solvent of the suspension is that it evaporates significantly faster than the DI-water. This is a preferable trait as it will ultimately lead to less unwanted phenomena related to solvents, most importantly to DI-water. Considering the case of IPA, droplets have enough free-space travel that the surrounding shell is able to evaporate faster than its DI-water counterpart. Control of relative humidity, temperature and air flow can play a significant role, as mentioned earlier [162].

In conclusion, Table 5.2 summarizes the most relevant parameters of the materials discussed in this Section. The table also puts the 2 solvents into contrast. Firstly, their index of refraction at the important wavelength of $\lambda_{\mathrm{LD},\,0} = 1064\,\mathrm{nm}$ is comparable. This suggest that the related optical forces acting on both of them would be consequently similar. On the other hand, their mechanical properties are clearly different. Not only does the IPA have a lower density, but also a lower enthalpy of vaporization. Both of these characteristics are favourable, as the former lessens the impact of gravitation forces, while the latter enables faster evaporation of the liquid.

TABLE 5.2: Summary table of the main materials present during the particle deposition experiments

Parameter	**Polystyrene**	**De-ionized water**	**Isopropyl alcohol**
Index of refraction at 1064 nm (n) [–]	1.572	1.324	1.376
Density (ρ) [kg/m^3]	1050	997	786
Enthalpy of vaporization (ΔH_{vap}) [J/g]	N/A	2257	732.2
Particle radius (r_{ptcl}) [µm]	5	$< d_{\text{core}}$	$< d_{\text{core}}$

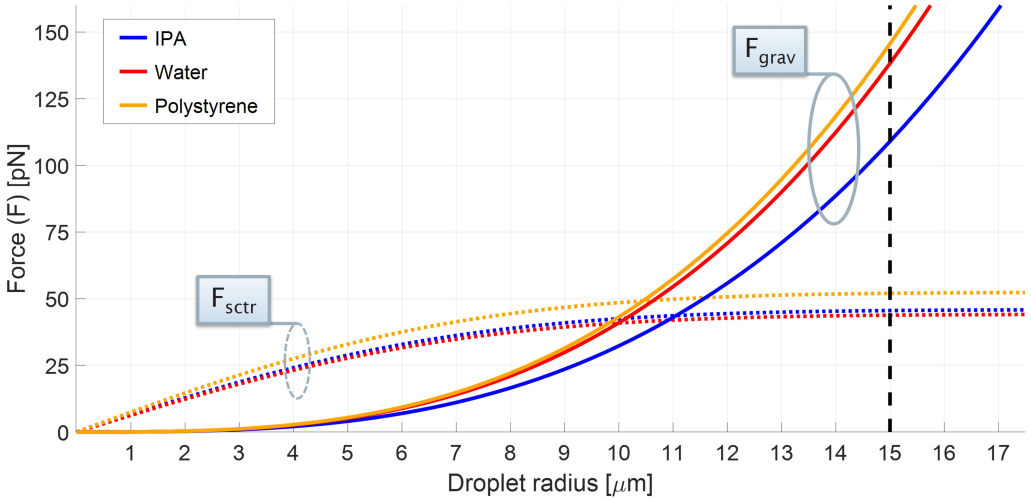

FIGURE 5.7: **Relevant forces acting on different nebulized materials** | Calculated values of the optical scattering force (F_{sctr}) propelling the trapped McP along the length of the fibre, as well as the gravitational force (F_{grav}) acting on it, as a function of the droplet radius, plotted with dotted and solid curves, respectively. The materials considered are isopropyl alcohol (IPA), de-ionized water (DI-water) and polystyrene (PS), with blue, red and gold colours, respectively. It can be seen that up to a radius of ~10 µm, droplets of any material composition is expected to be levitated against gravity. Dashed black line indicates the upper size bound set by the core diameter of the fibre. The calculations assume a total average input power of 100 mW, and a focused beamwaist of 15 µm.

Lastly, Figure 5.7 illustrates how the more relevant optical and gravitational forces (according to Equations 2.26 and 2.27) act on the materials considered in this Section. It can be seen that the absolute value of the respective forces are similar for all 3 materials. Because of that, almost identical behaviour is anticipated from any scattering sources that will be observed, regardless of their material composition.

5.4 Experimental results

5.4.1 Initial experiments

To begin with, the efficiency of the nebulizining process has been examined. For the initial experiments, an extremely short (~10 cm) piece of NANF-2 has been used. The main objective of these studies were to demonstrate the deposition, trapping and coupling of McPs.

Nebulization of empty DI-water droplets

First of all, the PariBoy nebulizer is loaded with pure DI-water without any McPs. The output of the mouthpiece is placed at the input of the buffer chamber, while the assembly is aligned such that the nozzle output is ~1 mm away from the input tip of the FUT — in front of and above it, as it is depicted in Figure 5.6. This alignment procedure is conducted with the aid of the input monitoring camera. During the nebulization procedure, a typical scattering pattern, similar to that shown the left hand side of Figure 5.8 a) was visible. However, note that this photo was taken when another liquid was examined — which will be discussed in the next paragraph. Nevertheless, the observed scattering was practically identical, independent on the material. While it was clearly visible, that airborne droplets have passed through the beam path, no DI-water droplets were witnessed to be coupled into the FUT. On the one hand, this demonstrated that depositing the cloud of droplets at a well defined position is practically achievable. On the other hand, the impact of a relatively long deposition chamber assembly, and the slow evaporation of the water have to be considered. It is assumed that the combination of these 2 phenomena leads to the originally smaller droplets being merged into significantly larger ones, which are now too oversized (both in diameter and weight) to be trapped by the relatively weak trap.

Guidance of empty IPA droplets

On the other hand, as mentioned earlier in Section 5.3, IPA has a more desirable enthalpy of vaporization. Loading the PariBoy nebulizer this time with pure IPA results in somewhat different observations. Because of the quicker vaporization, the environmental conditions outside the fibre play a crucial role on the dynamics of the droplets. Unexpectedly the produced cloud of droplets disappears significantly faster — something that can be seen by the naked eye as well. For this reason, a longer deposition time was also necessary before any scattering was observable. This is suspected to be caused by the increased partial vapor pressure introduced by the evaporation of those droplets generated at the beginning of the deposition. As the concentration of the IPA vapor pressure reaches the level of saturation, the most recently produced droplets evaporate at a reduced rate, enabling them to reach the laser beam. Figure 5.8 a) shows that these droplets are also small enough that (assuming they enter the laser beam) they can be

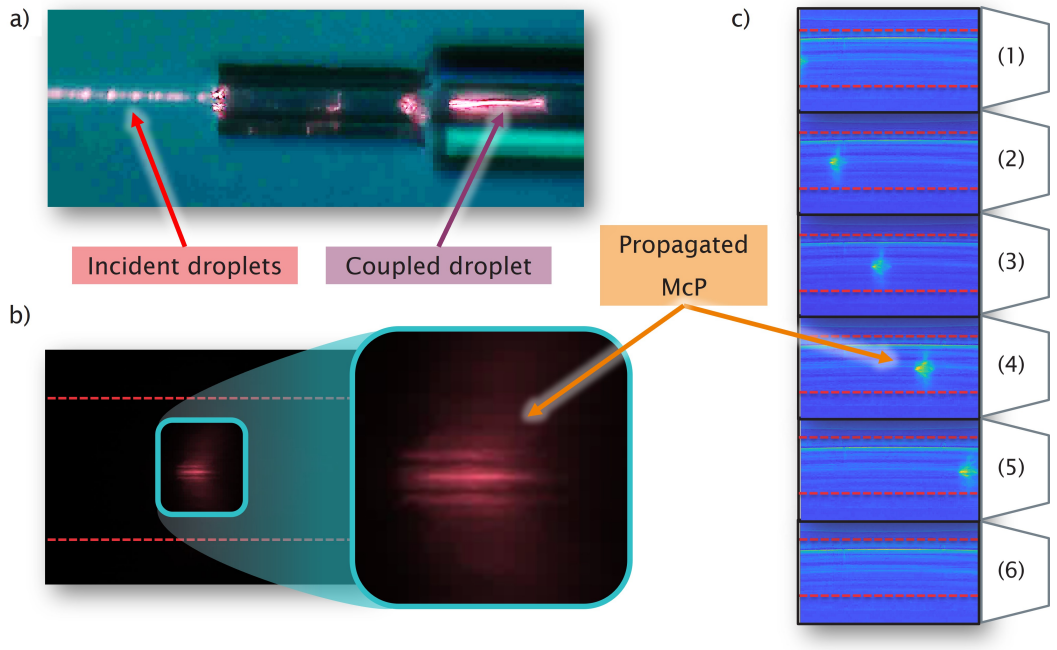

FIGURE 5.8: **Still photos of the laser-microparticle interactions** | For all pictures, the laser light propagates from left to right. a) The deposited fine mist of IPA droplets are incident into the focused laser beam. In front of the fibre tip, scattering from a number of droplets is visible. A single droplet coupled into the NANF can be also seen on the right hand side. Note that the elongated scattering is caused by the ~10 m sec exposure time of the capturing detector. b) A typical scattering image recorded at a stripped section of the fibre under ~40-times magnification. The red dashed lines indicate the outer diameter of the un-coated fibre segment. The inset highlights the propelled PS-McP at even larger magnification. The horizontal darker lines are suspected to be induced by the refraction of the scattered light at the glass membranes building up the cladding structure of the NANF. A dark background capture is shown for better visibility. c) False coloured sequence of an observed particle propagating through the same section after post-processing the images. Similarly, the red dashed lines indicate the outer diameter of the stripped section. The images are recorded at 20 Hz frame rate.

coupled into the NANF. Furthermore, they are preserved while being propagated inside the FUT, and exit the fibre piece at the output end. In contrast to using DI-water, it has been proved that IPA droplets can be captured and delivered through NANFs. For this reason, it has been decided that IPA is the preferred choice of main solvent for the suspension to be used for McP deposition.

Coupling of polystyrene microparticles

The final experiment using the ~10 cm piece of NANF-2 as the delivery fibre also included an IPA based PS-McPs suspension being loaded into the nebulizer. The originally provided mixture had a concentration of 10 %, with DI-water as the solvent. A small amount of this mixture has been diluted with IPA to $c \approx 0.67$ % before pre-conditioning it in an ultrasonic bath for ~15 min. This new concentration has been calculated based on the $d_{\mathrm{MMAD}} \approx 3.8\,\mu$m mass median average diameter (MMAD) of droplets produced

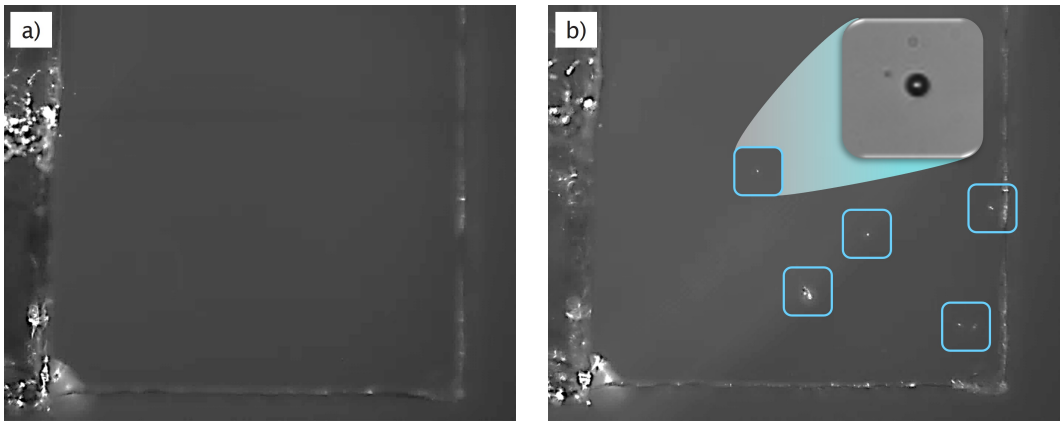

FIGURE 5.9: **Photos the microscope slide before and after the particle delivery experiments** | a) Reference photo before, and b) after particle guidance have been observed through a relatively short 10 cm piece of NANF. A 10x magnification microscope objective has been used, allowing to cover a larger area of inspection. On part b), the deposited particles are highlighted with squares, with the inset showing one of them further magnified (~40x). The highly scattering region on the left hand side of both images is a piece of Kapton-tape, that has been used to mark the glass slide and the area of interest for the experiments, with the bottom and right lines are the edges of the microscope cover slide used as a target.

by the PariBoy device (as provided by its specification), such that most of the generated droplets are expected to contain 1 single McP. The diluting has been done using Eppendorf Research plus mechanical pipettes.

During this set of experiments, similar scattering patterns as what is shown on Figure 5.8 a) were also observed. Furthermore, parts b) and c) also display a still picture and a sequence of photographs of the trapped and propagated McP, as it could be seen by using a microscope objective, respectively. However, just by examining these scattering patterns of such basic still images, the size, material constituent or McP content of the droplets cannot be determined. For this reason, in this scenario, a commercially available precision cover glass with thickness of 170 µm supplied by ThorLabs (CG15KH) were also placed immediately after the output of the short fibre piece. A smaller area of X-by-Y mm's were surrounded with markers on the cover glass slide for inspection. It has been recorded before and after conducting the experiments, as shown on Figure 5.9 a) and b) respectively. It can be seen that there is a clear indication of a handful of particles being deposited onto the cover glass, with their sizes matching well with the expected diameter of 10 µm. Note that a considerably larger number of scattering sources were observed to be propagated during the experiment. However, it is assumed that most of these were indeed droplets of IPA or DI-water — that remained from the original suspension before dilution.

5.4.2 Delivery of PS microparticles

After it was confirmed by the initial experiments, that McPs have been transported through a short piece of NANF-2, the scalability of delivery length has been explored.

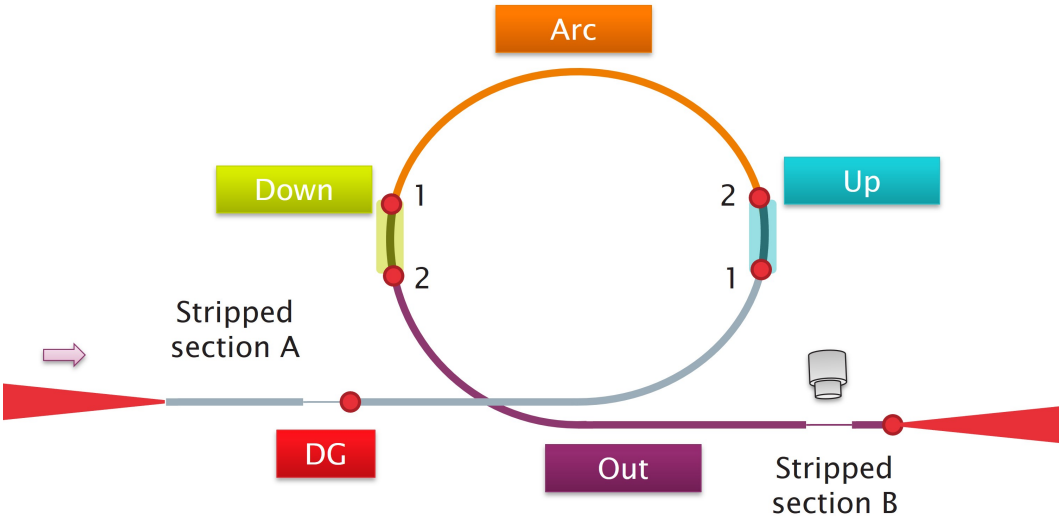

FIGURE 5.10: **Naming convention for the 2 m single-loop fibre experiments** | The schematic illustration labels the important segments of the single-loop particle propulsion experiments. As the light is coupled into the fibre from the left, it first passes the droplet gating section (DG). Then the particle is guided along the length of the fibre first going through the sections labelled 'Up', 'Arc', 'Down', and finally 'Out'. Lastly, it passes through another intermediate stripped section that is monitored with a CMOS camera, before leaving the FUT. The red dots mark the checkpoints (detailed in the text), at which positions timestamps of the propagated particles are being recorded. Note that the sections 'Up' and 'Down' are practically fixed to be vertical during the measurements, while 'Arc', and 'Out' consists of curves and more horizontal segments.

In this step, a slightly longer length of ~2 m from the same fibre has been used. In order to keep the system compact one loop (with $d_{\text{bend}} \approx 30\,\text{cm}$) of the NANF has been introduced between the input and the output facets. As it will be shown, this also had the added benefit of conducting measurements similar to those done by Schmidt et al. [170] previously. The ingenuity of their work takes advantage of the bending introduced to the fibre. By arranging the loop such that the plane it defines is either laid flat horizontally, or fixed vertically, a particle being propagated along its length would experience guidance in all spatial directions. This could demonstrate the capability of delivering McPs along any trajectory determined by the fibre, essentially confirming total 3D maneuverability.

During the measurements to be discussed in this Subsection, all the previously set parameters ($P_{\text{LD}} = 100\,\text{mW}$, $c_{\text{dil}} = 0.67\,\%$) has been kept the same. Additionally, the previously mentioned droplet gating has been implemented, and delivery checkpoints have been established, since the longer length made these improvements practically feasible. Figure 5.10 illustrates the final experimental layout schematically, with the appropriate naming conventions, as they will be used in the following. Note that a secondary stripped section (labelled 'B') has been also introduced. However, the only purpose of this alteration is to enable a better imaging of the guided scattering source as it approaches the end of the NANF.

Horizontal loop

Conducting experimenters when the fibre piece was placed horizontally granted many valuable insights. First of all, the impact of the droplet gating concept has been recognized. Without introducing any additional disturbance to the stripped section (e.g. external heating), during the experiments it was apparent that the DG had an influence on the guidance of the droplets. As the scattering sources entered the uncoated segment of the fibre, in most cases, the reflected light from the laser beam quickly disappeared. It has been considered that there could be 2 possible explanation for this behaviour; either a particle falls out of the trap, or a droplet is evaporated inside the core. Since the transmitted power is constantly monitored, the latter explanation seems to be more plausible. Even after witnessing 10's of such terminations of the scattering, the transmission efficiency has not degraded. As the phenomenon of clogging induced transmission reduction has been observed numerous times during the experiments, the evaporation of droplets is strongly suggested to be the proper explanation. Furthermore, it has been observed that applying any external heating (e.g. an arc-lighter) would also destroy the coupled PS-McPs, and such, any additional alteration apart from the stripping of the coating has not been applied.

After further examination of those scattering sources that did pass the droplet gate (~5 % of all coupled droplets), the extended length of the FUT allowed the observation of other unusual phenomena. As a consequence of the nebulizer providing a distribution of droplet sizes (and similarly McP content), scattering sources of different travelling speeds were witnessed. As a faster droplet approaches a slower one, 2 outcomes are usually observed. It is possible, that they merge together and continue to propagate with a slightly faster speed because of the increased volume, and therefore better interaction between the optical field and the droplet. On the other hand, it has been also observed, that in some cases, the 2 droplets do not collide, but the faster one overtakes the slower one. It has been speculated that this would require the droplets to be guided along non-overlapping trajectories through the HCF. However, in order to obtain a better understanding of this phenomenon, a more rigorous study is necessary.

Additionally, the resilience of the particle guidance have been also tested. It can be appreciated, that introducing minor disturbance (e.g. touching) to the FUT does not impact the trapping and continuous delivery of the particle. Nonetheless, major turbulence (e.g. squeezing or shaking the fibre) can cause the droplet to fall out of the trap. Furthermore, blocking the laser beam momentarily usually does not result in a loss of guidance, since the particle can be re-captured, if the optical forces are re-introduced quickly enough. Practically, dropping the particle required the laser source to be obstructed for >1 s.

Since the particles travelled only in the horizontal plane, all relevant forces are expected to maintain their relative direction compared to each other. Considering the drag as a

TABLE 5.3: Summary table for the distances between the checkpoints set along the length of the vertically positioned ~2 m long NANF-2 piece used for the particle guidance experiments.

Definition	**Label**	**Distance from previous checkpoint**
Beginning of upwards section	Up-1	N/A
End of upwards section	Up-2	67 mm
Beginning of downwards section	Down-1	780 mm
End of downwards section	Down-2	69 mm
Output of the test fibre	Out	456 mm

balancing and limiting force, this leads to a constant speed of propulsion of the guided particles along the length of the fibre. According to the measurements, the calculated values ranged between 1.39 to 6.98 mm/s. The considerable variance is attributed to the slightly different droplet sizes, and multiple scattering sources simultaneously present inside the FUT. The latter point will be discussed in more detail later in this Subsection. Assuming a very simplistic model, an expected particle speed of $v_{\text{model}} \approx 8.3\,\text{mm/s}$ is predicted, indicating a reasonable agreement with the measurements, within its limitations. Lastly, similarly to the original observation introduced in Section 5.1, when a droplet or particle has been trapped, coupled and propelled along the HCF, the transmitted power showed a temporary drop (between 1 to 3 %), which is restored, after the droplet or particle has left the FUT. Note that the increase percentage value compared to that case can be originated from many factors — e.g. the different material or size of the droplet/particle that is being propagated.

Vertical loop

Considering now the case when the fibre loop is positioned vertically, the gravitational force can be parallel with the optical axis at different segments along the FUT — and consequently, with the optical scattering force. Since the direction can be either the same or the opposite, the amplitude of the resulting net force acting on the particle depends on its location along the length of the FUT. Table 5.3 summarizes the relevant distances between the set checkpoints along the length other FUT. Accordingly, Figure 5.11 shows the calculated speed of the scattering sources based on their travel time between the checkpoints. The presented results can be categorized into several groups.

The monitored scattering sources labelled P-01, P-02, P-03, and M-04 can be grouped together by their shared feature of showing a greater speed when they are travelling downwards, as opposed to upwards. This is an intuitively expected property based on how gravity increases or decreases the velocity of the guided particle, respectively. On the other hand, M-04 can be further separated from the rest of this group, as average speed is

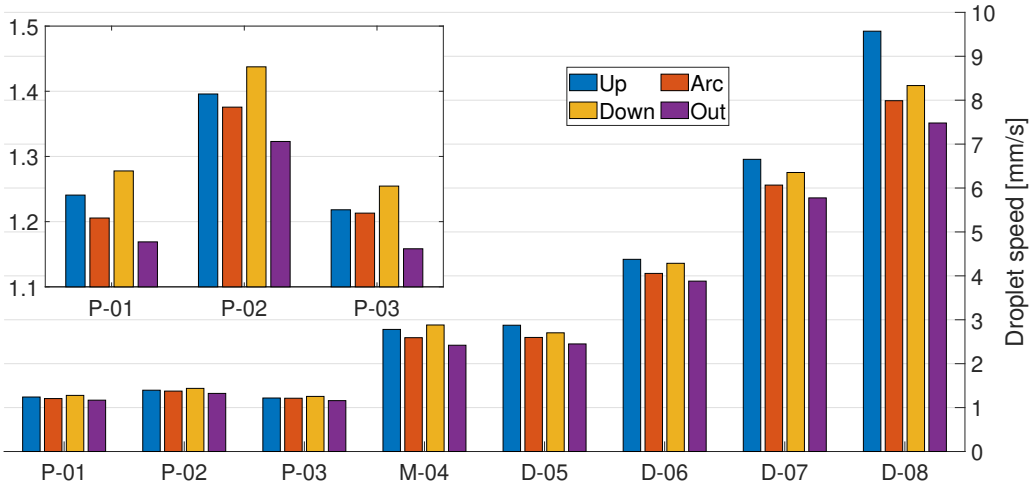

FIGURE 5.11: **Bar plot of calculated particle speeds** | Labels 'P' refer to suspected particles, 'M' denotes droplets containing multiple particles, while 'D' stands for observations when the beam has been disrupted by other scattering sources simultaneously present inside the NANF. The inset highlights the speed differences measured for the slowest droplets observed. Notice how the 'Upwards' particle speeds are lower than their 'Downwards' counterparts for P-01 to M-04, while the relationship is reversed for D-05 to D-08. Note that the segments containing horizontal directions ('Arc' and 'Out') always show lower speeds than the prior 2.

also approximately twice of the previous 3 particles. This behavior strongly suggest that multiple number of particles were present in that case, however, the observed scattering was not significantly different for the two cases.

By using the Equations 2.26, 2.27 and 2.29 provided in Section 2.7, the diameter of the observed scattering sources can be also estimated. Considering the 2 cases of equilibrium, that is $F_{\text{axl}} - F_{\text{grav}} - F_{\text{drag}\uparrow} = 0$, and $0 = F_{\text{axl}} + F_{\text{grav}} - F_{\text{drag}\downarrow} = 0$, for when the particle is propelled upwards and downwards, respectively, assuming that the optical power is the same, the d_{ptcl} can be approximated as a function of the $\Delta v = v_{\downarrow} - v_{\uparrow}$ speed difference of the 2 steady state solutions. The previous assumption is justified by the low loss of the NANF, which over the length of FUT used here is $<0.02\,\%$. In this case, the particle diameter is given by:

$$d_{\text{ptcl}} = \sqrt{\frac{9}{4}\frac{\eta \cdot K}{\rho_{\text{ptcl}} \cdot g} \cdot (v_{\downarrow} - v_{\uparrow})}\,. \tag{5.1}$$

However, the above equation only holds true when only a single particle is present inside the fibre, as it will be shown later.

As an attempt to verify the particle guidance, the d_{ptcl} particle diameters have been estimated using Equation 5.1. The calculated values for P-01, P-02, P-03, and M-04 are shown in Figure 5.12. Furthermore, the other materials present the system (i.e. DI-water and IPA) have been also considered. The calculations suggest particle diameters of 1 to 2 µm, as opposed to the expected 10 µm of PS particles. This behaviour is suspected

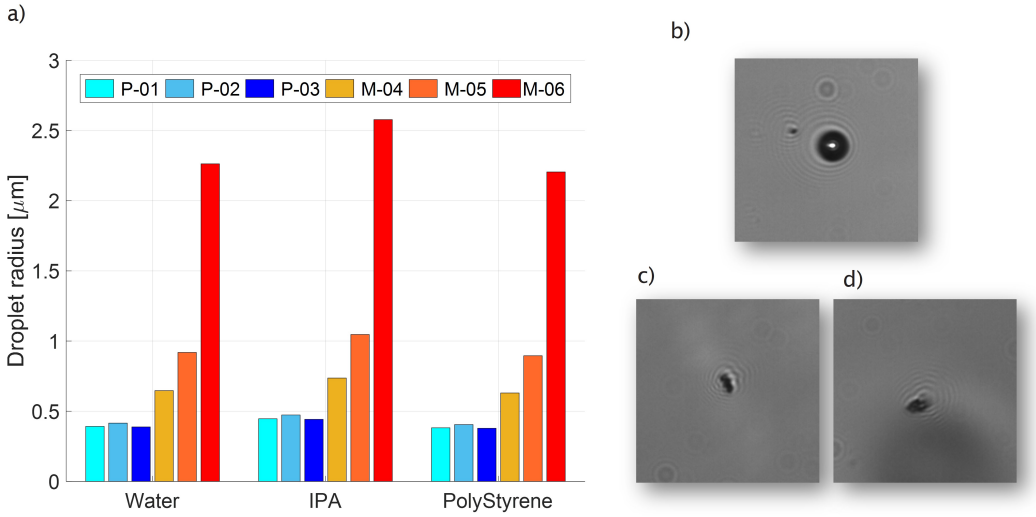

FIGURE 5.12: **Bar plot of calculated particle diameters** | a) presents the calculated radii of some of the scattering sources observed, assuming K = 1 in Equation 5.1. Labels P refer to suspected particles, while M denotes droplets that are believed to contain multiple particles. Note, that for the particle sizes considered here, the validity of the used ray optics approximation becomes problematic. b) shows the 10 µm diameter PS-McP, after being guided through the $l \approx 10$ cm short piece FUT used for the initial measurements discussed earlier as a reference. In contrast, parts c) and d) display captured particles after being delivered over $l \approx 2$ m, clearly demonstrating the degradation induced by the long exposure to the trapping beam.

to be related to the sensitivity of PS towards the extended exposure to a focused laser beam, causing the McP to degrade over time [107]. The assumption is supported by the fact that it can take between 10 to 30 min for the droplets to be transmitted through the significantly longer FUT. Furthermore, on the right hand side insets, the ~40-times magnified image of the transmitted McPs are displayed. These particles illustrates the difference between the delivery over shorter ($l \approx 10$ cm) and longer ($l \approx 2$ m) lengths of FUT — as they have been deposited onto the microscope cover slide glass piece placed right after the output tip of the respective FUTs.

On the other hand, in contrast to all of the previously mentioned 4 scattering sources, Figure 5.12 also displays the group of D05-08, for which the earlier discussed trend is opposite: they show a greater speed when they are travelling upwards, as opposed to downwards. Because of this, their sizes cannot be estimated by using the same equation. Figure 5.13 shows that assuming that the same optical power (100 mW) is incident on the same McP, the travelling speed upwards (golden curve) should never be larger than its downwards counterpart (red curve). It can be also appreciated that even if a change in particle size is considered, the respective curves do not cross, indicating that evaporation alone cannot explain the phenomenon.

Assuming that the optical power is not identical at the 'Up' and 'Down' segments, however, can indeed recreate a case similar to the observed phenomenon. This can be seen more clearly on the highlighted inset by the dashed blue curve, which assumes a

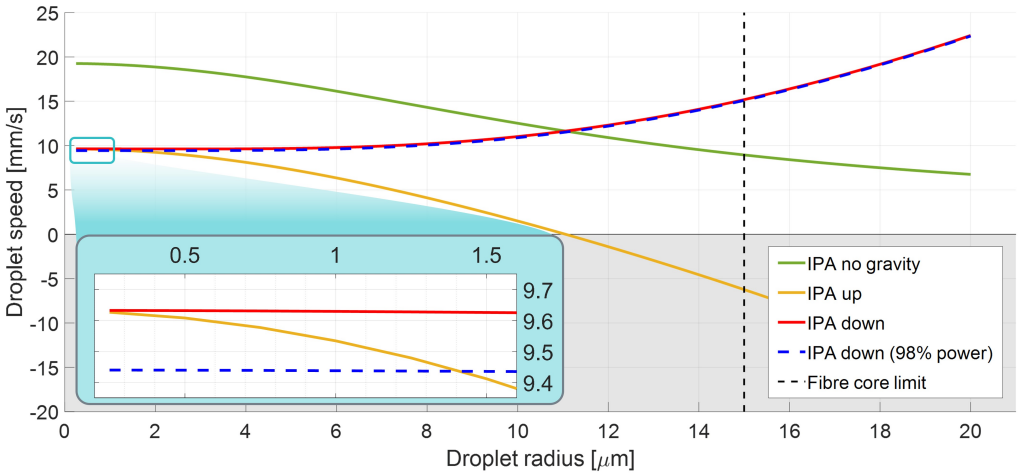

FIGURE 5.13: **Different calculated droplet speeds as a function of droplet radius** | Considering IPA as the constituting material, the green, gold and red lines illustrate the different cases, when the gravity is neglected, it points to the opposite (upwards propagation) or same (downwards propagation) direction compared to the optical force, respectively. It can be seen that assuming the same 100 mW incident optical power the red curve is always above the gold one. However, even a relatively small (~2 %) drop in power can result in an intersection of the two (dashed blue and solid gold) curves, as highlighted by the inset. Assuming that every other parameters are kept identical, this scenario corresponds to the case when another droplet is present in front of the measured one, causing a fraction of the power to not reach the latter, as it interacts with the former. The shaded area highlights the droplet sizes above which the droplet could not be propagated upwards against gravity. Furthermore, the black dashed line indicates the upper radius limit imposed by the fibre core.

minor power reduction of ~2 %. This change in optical power can be interpreted as a result of multiple scattering sources being present inside the FUT during the same measurement. As it has been discussed earlier, the guided particles causes the beam distribution to be slightly disturbed after the location of the scattering source. This results in a somewhat altered modal content of the beam, leading to a slightly increased HOM intensities, which have higher attenuation values, and in turn the transmitted power is reduced while the McP is inside the FUT.

Lastly, for all the scattering sources measured and presented here, it can be also seen that they have been propagating slower, when the fibre is positioned horizontally (segments labelled Arc and Out), as opposed to the cases when it is directed vertically (segments Up and Down). This is suspected to be caused by the impact of gravity causing the position of stable trapping (i.e. $F_{\text{grav}} = F_{\text{rad}}$) to be slightly off the optical axis. As a result, for these segments, the incident optical power, and in turn the F_{axl} is also reduced, leading to slower propulsion speeds.

5.4.3 Peak speeds achievable

Finally, as mentioned earlier, one field where the acceleration of McPs to high velocities could be appreciated for experiments is the analysis of the impact of colliding micrometeorites with spacecraft [171] in a laboratory environment. This could be a desired, less expensive alternative approach, proposed to improve the longevity of satellites. Here, based on the data presented earlier in Subsection 5.4.2, an expected particle speed range will be extrapolated.

In order to give an estimate of the maximum achievable v_{max} velocity, the scenario when the axial optical force is balanced by the drag, that is $\mathbf{F}_{axl} = -\mathbf{F}_{drag}$ is considered. Mathematically, inserting the Equations 2.26 and 2.29 and reordering the terms leads to:

$$v_{max} = \frac{1}{6\pi \cdot c_0} \cdot \frac{1}{\eta} \cdot \frac{n_{\text{ptcl}}}{r_{\text{ptcl}}} \cdot P \cdot Q_{\text{sum}}. \tag{5.2}$$

As can be seen from Equation 5.2, the relevant terms to be considered are:

1^{st} term Constant scaling factor.

2^{nd} term Viscosity shows that v_{max} is inversely dependant on η. This can be reduced to some extent by manipulating the material of the environment surrounding the particle, e.g. decreasing the pressure of the filling gas.

3^{rd} term Describes how v_{max} depends on the material properties of the McP to be accelerated. Qualitatively, a smaller particle would experience less drag, and a higher index of refraction would guarantee larger optical forces — assuming that the ratio of the particle radius r_{ptcl} and the w_{foc} beamwaist of the focused beam (i.e. the d_{core} core diameter of the delivery fibre) is the same.

4^{th} term P shows a linear dependence on the average power of the light source,

5^{th} term Finally, Q_{sum} includes all the previously discussed quality factors, e.g. Q_{opt} or Q_{MFD}. This unified quality factor scales the efficiency of the interaction between the laser beam and the MCP, as discussed earlier in Subsections 2.7.1 and 2.7.3.

In the following, the example of a SiO_2 McP will be considered. This is justified by the observation made previously in Subsection 5.4.2, that is polystyrene based MCPs suffer from the significant disadvantage of fragility. When illuminated for an extended amount of time, McPs made out of PS are degraded and ultimately destroyed.

Figure 5.14 shows the estimated maximum achievable propulsion speeds. The calculations assumed a particle density of $\varrho_{SiO_2} = 2650\,\text{kg}/\text{m}^3$, $\eta = 18 \times 10^{-6}\,\text{Pa}\cdot\text{s}$ viscosity of ambient room environment [77], and a $Q_{\text{opt}} = 0.1$ quality factor [110]. The blue and red curves represents the scenarios, when the incident average optical power is 1 and 2 kW,

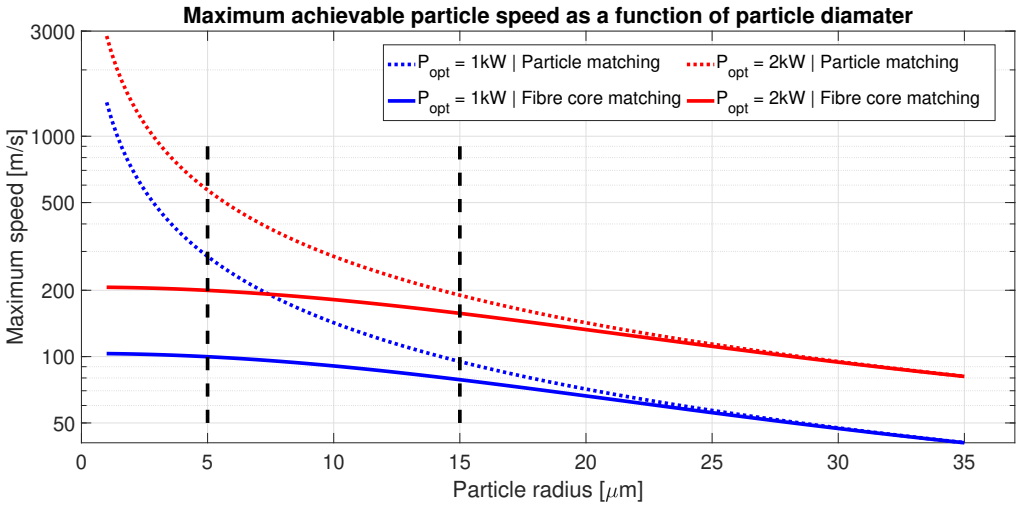

FIGURE 5.14: **Maximum expected propulsion speeds of SiO_2 McPs |** The blue and red curves illustrates the expected delivery speeds, as a function of particle radius. A steady state condition is assumed, such that the optical scattering force is balanced by the drag, resulting a net force of 0. The solid lines shows the case where ideal coupling of a Gaussian beam into a HCF with a core diameter of $d_{\text{core}} = 30\,\mu\text{m}$ is considered. On the other hand, the dotted curves corresponds to the scenario where the total optical power of the beam is utilized, as the focusing is such, that it matches perfectly with the relevant particle size. Lastly, the dashed vertical lines marks the important values of $r_{\text{ptcl}} = 5\,\mu\text{m}$ and $r_{\text{core}} = 15\,\mu\text{m}$.

respectively. As expected from Equation 5.2, because of the linear dependence, the doubled power results in twice as fast particle speeds. On the other hand, the dotted curves denotes simulations, where the relative particle size is $\Lambda_{\text{MFD}} = 1$, while for the solid curves, the core diameter is set at $d_{\text{core}} = 30\,\mu\text{m}$, a typical nominal value for NANFs. The former case can be interpreted as the particle is coupled into a fibre, which has a core diameter ~1/0.7 times the particle diameter, that is ~140 % larger — in accordance with the predictions from [123] about achieving maximum CE. While the realization of a fibre with such parameters is practically not feasible, the influence of the Q_{MFD} factor is clearly visible, when compared with the more realistic solid lines. Lastly, the 2 vertical dashed lines mark the previously mentioned important sizes of the $r_{\text{ptcl}} = 5\,\mu\text{m}$ particle radius, and $r_{\text{core}} = 15\,\mu\text{m}$ fibre core radius.

Furthermore, it is important to review how McPs moving at speeds between 100 to 200 m/s can restrict the flexibility of fibre deployment. Considering the previously discussed particle diameter of $r_{\text{ptcl}} = 5\,\mu\text{m}$, a standard spool diameter (and in turn bending diameter of a fibre) of $d_{\text{spool}} = D_{\text{bend}} = 30\,\text{cm}$, and a theoretically achievable speed of $v_{max} = 150\,\text{m/s}$, the calculated centripetal force, according to

$$|\mathbf{F}_{\text{cpt}}| = \frac{m_{\text{ptcl}} \cdot v_{max}^2}{r_{\text{spool}}}. \tag{5.3}$$

would be $|\mathbf{F}_{\text{cpt}}| \approx 208\,\text{nN}$. Based on Equation 5.2, this would required an optical power of

$P \approx 1.5\,\mathrm{kW}$. According to Equation 2.26, the corresponding axial force is $F_{axl} \approx 254\,\mathrm{nN}$. Practically, this is usually more than 2 to 3 times the F_{rad} force component — for strong optical traps, using high NA objectives and correspondingly strong focusing. This is generally not the case when HCFs are used, as these fibres have significantly acceptance angles leading to aforementioned discrepancy between axial and radial components of the F_{opt} total optical force.

The above observations strongly suggest that if a McP of such speed ($v_{max} = 150\,\mathrm{m/s}$) would approach a section of the HCF, that has a bend diameter of $D_{\mathrm{bend}} = 30\,\mathrm{cm}$, the F_{rad} force would not be sufficient to counteract the expected F_{cpt} centripetal force. In order to keep the propagating particle inside the fibre spool, the relation $F_{cpt} \leq F_{rad}$ must hold. Otherwise, the McP in theory could pierce the fibre structure at its bend and leave it along the tangent. Considering identical parameters, and a comparable $F_{rad} = 100\,\mathrm{nN}$, an estimated bend diameter of $D_{\mathrm{bend}} \approx 145\,\mathrm{cm}$ is required. Practically, this translates to the necessity of employing a straight fibre piece, if particle speeds beyond $100\,\mathrm{m/s}$ are desired.

Lastly, it must be mentioned that the average velocity of such micrometeoroids is on the scale of $10\,\mathrm{km/s}$ [171], approximately 2 orders of magnitude beyond what has been estimated using the parameters of the currently available equipment. From Equation 5.2, it can be also seen, how this gap could be reduced. First of all, the material properties (i.e. n_{ptcl} and r_{ptcl}) are determined by the composition of the micrometeoroids, and as such can be considered constants for the sake of this discussion. Next, the most straight-forward step would be to increase the optical power. As shown in Chapter 4, however, the thermal load on the coupling elements practically set an upper bound on the maximum optical power that can be coupled into a HCF. Additionally, the Q_{MFD} quality factor can be increased by reducing the Λ_{MFD} relative particle size, through the utilization of a fibre with smaller core diameter — as shown in Figures 2.9 and 5.14. Similarly, this approach is limited by the available fibre fabrication techniques and capabilities. Lastly, the viscosity of the core material (i.e. air) can be reduced by evacuating the fibre piece. While the realization of an experimental setup combining these points is indeed a challenging task, it is an essential step for on-the-ground space debris related research efforts.

5.4.4 Current limitations

As mentioned earlier, degradation of the PS-McP is suspected to be the main limiting factor for long haul particle delivery [107]. Since this restriction is imposed by the material itself, the only viable option is to use McPs of different constitution (e.g. SiO_2). This would enable the reliable and intact delivery over significantly longer distances. On the other hand, the results discussed strongly suggest that the used particle diameter of $10\,\mu\mathrm{m}$ is adequate for the NANFs used here, as the Λ_{MFD} relative particle sizes leads to reasonable Q_{MFD} quality factor values. Furthermore, while the nebulization

of the suspended McPs is satisfactory, it could be potentially improved by optimizing the depositing nozzle design. It has been also proposed that by implementing a counter propagating airflow, both the initial speed of the droplets inside the nebulized cloud can be reduced, as well as the evaporation of the surrounding liquid shell can be accelerated. The former allows more particles to reach low enough velocities, such that they can be trapped, while the latter reduces the solvent ratio of the particle cloud during deposition [162].

Additionally, by upgrading the laser source used, a number of opportunities would be unlocked. Smaller power fluctuations would assure more secure trapping of the particles, and in turn more reliable guidance could be achieved. Moreover, since no internal cooling system had been implemented for the laser diode used in these measurements, the available average optical power was limited to ~100 mW. This, however, was not considered a serious restraint at the time of conducting the initial measurements, because of the already mentioned sensitivity of the PS-McPs to long exposure of high fluence beams.

Lastly, for the sake of simplicity, and with the aim to gain initial expertise with optical guidance of McPs, only one beam has been utilized. This also limited the manoeuvrability of the McPs, as only one-directional propulsion was possible. By splitting the original beam, and introducing a counter propagating beam that is being coupled into the same HCF from the opposite end of the FUT, an optical force of opposite sign can counteract the axial force of the initial beam. Then, by simply adjusting the power ratio of the two arms, it is possible to maintain the particle at a given position along the fibre, or even propel it in the opposite direction. Meanwhile the radial components of the coupled beams are combined, resulting an optical trap of similar stiffness, compared to if only one beam would be used [39, 119, 172].

Similarly, the broadband spectrum of the laser diode used here only allow optical trapping based on the exchange of momentum between the McP and the photons. By employing a source with narrow linewidth, more precise control could be enabled by interfering the counter propagating beams such that a standing wave is achieved. This effect, however, also depends on the relation between coherence length of the laser, and the length of the fibre piece as well.

5.5 Conclusion

In summary, I have designed and built an experimental setup that is capable of demonstrating the guidance of micron sized particles, for the first time utilizing an in house fabricated NANF for such application. I have set up a particle dispenser solution that can create a localized cloud of McPs that can be captured by the beam incident on the delivery fibre. I have presented the capacity of the NANFs to propagate these McPs over a reasonable distance of >1 m in virtually any spatial direction. The results discussed

in this Chapter indicate that the realized setup will be able to take advantage of the record-low attenuation of NANFs. As the steps to follow, with the acquired know-how, the guidance of more durable (e.g. SiO_2) McPs over record distances beyond 100 m are achievable. Such an advancement could pave the way to the realisation of a long-distance remote sensing device which would discussed in the following Section.

5.6 Outlook and possible applications

Further work based on the promising results of the initial experiments presented in this Chapter has been considered. The main proposals are:

5.6.1 Long term fibre performance monitoring

One distinctly different direction of research that is worth mentioning here can be derived from the initial observation of the optical propulsion phenomenon. Considering, that NH_4Cl has been witnessed to accumulate inside the fibre underlines the importance of constant monitoring of the fibre characteristics over time [173]. Better understanding of the alteration of the transmission of the fibre samples will be also beneficial for high-power delivery applications. Similarly, gaining more insight about the process of fibre transmission degradation can be influential for applications from telecommunications to those requiring the adjustment of the gas composition in the hollow regions of HCFs [74], to give some examples.

5.6.2 Optical guidance of highly evaporative liquid droplets

Another fascinating study could be the closer inspection of highly evaporative droplets. Using IPA as a solvent was preferred, because of its quick evaporation in ambient conditions as it has been discussed. On the other hand, once an evaporative equilibrium has been reached, it was possible to trap and couple the IPA droplets into the HCF. Furthermore, thanks to the low gas diffusivity of the fibre, it is possible to maintain this equilibrium for practically the entire length of the fibre sample. The ability to trap and optically manipulate materials of similar volatility could enable new opportunities of fundamental research. This could provide insight about these liquids that has not been possible yet because of the sensitivity of these materials towards environmental forces.

5.6.3 Short fibre sample characterisation

A similarly feasible application where the propulsion of McPs can be of great benefit is the field fibre characterisation. Measor et al. proposed a characterization method that is "simple, inexpensive, non-destructive, non-contaminating, and can be used for very short sample lengths" [174]. The scattering of the delivery beam from the trapped particle propagated inside a liquid-filled waveguide was observed. From the particle trajectories along the samples, the attenuation of both single- and multi-moded waveguides

pieces with lengths <5 mm were calculated. Results from the measurements showed great agreement with theoretical models, demonstrating a promising step towards next generation HCF characterisation techniques.

5.6.4 Droplet lasers

Another possible method to interact with droplets (as well as McPs) inside the HCF is by using them as high-quality resonators. Such droplets can support stable whispering gallery modes of the incident light by acting as resonators. Although the first micro-droplet laser has been already introduced in 1984 [175], the challenges of localizing and trapping such fragile droplets have been improving slowly. Nevertheless, new developments (from liquid crystal lasers to more efficient integration with microfluidic based techniques), there seems to be encouraging prospects for further advancement of droplet lasers [176].

5.6.5 Optical conveyor belt into high vacuum

Relatively shorter fibre pieces can be also utilized for delivering nanoparticles into environments that are otherwise practically troublesome to access. It has been demonstrated by Grass et al., that it is possible to delivery particles of $d_{\mathrm{ptcl}} = 387\,\mathrm{nm}$ diameter into fine vacuum ($\sim 1 \times 10^{-1}\,\mathrm{mbar}$), by using a HCF of $l = 15\,\mathrm{cm}$ length [177]. The reported $1 \times 10^{4}\,\mathrm{mbar/m}$ pressure gradient combined with a lower attenuation, slightly longer fibre piece could allow the delivery of particles to even higher vacuum levels, thanks to the low gas diffusion. Applications for fundamental physics, like force sensing, matter wave interferomety, or quantum mechanics [177, 178], could greatly benefit from such instrumentation.

5.6.6 Remote sensing

Nevertheless, the previously mentioned ideas did not take advantage of the low attenuation of the in-house fabricated NANFs just yet. One of the main inspiration for establishing the research discussed in this Chapter has been proposed by Bykov et al [39]. The main limiting factors in the previous reports have quoted the lack of conservation of optical power and beam distribution along the length of the HCFs as a considerable limiting factor. The transmission efficiencies reported in earlier Chapters clearly indicates that using the latest NANF technology, the possible delivery lengths can be significantly increased. Furthermore, since these fibres can preserve a high-brightness beam distribution, while also having a comparably larger core diameter to conventional SM-HCFs, making them an ideal method for long-haul micron sized particle delivery.

Arguably one of the most attractive proposal is the optical trapping and guidance of materials with special properties. As an example, zinc sulphide — which displays radioluminescent behaviour — can be considered. With proper engineering, NANF samples can be manufactured that have optical transmission windows both at the wavelength of

the trapping beam, as well as around the wavelength of luminescence of the particle. Moreover, the low attenuation enables the precise manipulation of the McP, while also allowing the emitted luminescent signal to be detected at the output of the HCF. Localization techniques, such as those based on Doppler-velocimetry [39, 75], can determine the precise position of the particle with great resolution. It is possible to install a considerable length of km-scale HCF in more dangerous or sensitive environments — e.g. nuclear power plants or hospitals — where early detection of radiation leakage is crucial. The practically simple replacement of possibly contaminated particles can be also done distant from the hazardous surrounding. This further indicates the desirability of this technique, compared to similar radiation detecting methods based on SCFs, which are more susceptible to radiation related bleaching effects, while HCFs are far more robust [179].

5.6.7 Coating of the inner walls of HCFs

By using a secondary laser beam to ablate the already coupled particles guided inside the core of a HCF, novel post-treatments of optical fibres can be enabled. One of such application of precise control of McPs inside HCFs is the opportunity to layer the internal surface of the core-cladding boundary. Romodina et al. reported the rocket-like backward propulsion of optically trapped microparticles in HCFs [180]. As a possible application, the authors mentioned the deposition of the material of the trapped particle inside the fibre structure. By using a secondary fs-laser source with optimized parameters, the trapped microspheres acted as micro-lenses, and the focused beam damaged the particle, scattering their material inside the core. This allows to coat the inner structure of HCFs, with a wide array of materials, at positions hardly accessible otherwise, far inside the end facets. Such coatings can shift the anti-resonance transmission windows of ARFs, and unlock the integration of wavelength filters, Bragg-grating mirrors or amplifiers.

5.6.8 High-speed particle launching

Lastly, as it has been briefly mentioned in Section 2.7, by coupling laser beams of kW scale average power level, particle speeds of 100 to 200 m/s are possible for air filled HCFs. Furthermore it has been discussed in [94] that by evacuating the core of a NANF, the threshold above which unwanted nonlinear effects start to have significant impact can be pushed beyond 10 kW average power. Additionally, this would also reduce the drag acting on the trapped and guided McPs. Such studies could enable particle speeds that could be relevant for the field of micrometeorite collisions.

The impact of micrometeoroids and orbital debris on man-made instruments has shown to be a threat to space missions since one of the earliest studies on the topic, conducted back in 1957 [181]. Ever since, the designing process of virtually all space equipment — from space suits to spacecrafts — has to consider the harsh environment, that has been

compared to sandblasting [171]. For both financial and practicality reasons, conducting relevant important research should be feasible on ground instead in space. However, the acceleration of micron sized particles beyond km/s levels still remains a challenging task. By combining the exceptional power handling capabilities with the unique feature of having a hollow core, NANFs could become a valuable asset to future research in this field, thanks to their potential of achieving propulsion of relevant McPs at comparable speeds.

A very simplistic case study is provided here with the intention to give an impression of the scale of the parameter space of such an investigation. Consider a spherical silica particle ($n_{ptcl} \approx 1.4496$ at $\lambda = 1064\,\text{nm}$) with particle radius of $r_{ptcl} = 5\,\mu\text{m}$ and material density of $\varrho_{ptcl} = 2650\,\text{kg/m}^3$. Assuming a realistic normalized force factor of $Q = 0.1$, and an optical beam with $P = 2\,\text{kW}$ power, under ideal, size-matching focusing conditions, using Equation 2.26, the corresponding total optical scattering force is $F_{\text{axl}} \approx 9.66 \times 10^{-7}\,\text{N}$. According to Newton's law of motion ($F = m \cdot a$), the calculated acceleration of the McP is $a_{\text{ptcl}} \approx 6.965 \times 10^5\,\text{m/s}^2$, if the scattering force pushes the McP towards the direction of propagation of the beam. In order for the particle to reach an estimated velocity of $v \approx 10\,\text{km/s}$, it would only take $t = 14.4\,\text{ms}$, assuming linear motion at constant acceleration inside an evacuated environment (i.e. the drag is neglected). Lastly, supposing that the optical beam distribution is maintained during this time, a distance of ~71.79 m would be required. This finding based on a highly simplified scenario shows, that by using a HCF of <100 m — with its core evacuated and kept in a straight arrangement, such that the centrifugal force can be omitted — it would be possible to simulate the impact of micro-meteorites on ground. Unquestionably, however, there are many other other practical concerns that must be solved, before it is possible to realize such an experiment.

6 Conclusions and future work

In summary, my key scientific results and contributions can be compiled into 3 distinct points, that have been discussed in much detail in the 3 main Chapters establishing my Thesis. These are:

- I have conducted experimentally investigations leading to the demonstration of highly efficient coupling of a quasi-single-moded, continuous mode laser beam, with central wavelength $\lambda_0 = 1064\,\text{nm}$ into a hollow-core fibre with a nested anti-resonant nodeless geometry, using a free-space coupling approach. By comparing the transmission of 2 almost identical fibre sample, that only differs in their respective optical window at the important central wavelength of the laser source used, I have experimentally verified previous theoretical expectations. My findings show that anti-resonant hollow-core fibres operating in their 2^{nd} optical transmission window are the preferred choice over their counterparts that operate in any other ordered window, for applications, where the coupling efficiency is a crucial aspect. The results can have significant contributions to fields, like the delivery of high-brightness, high-power optical beams, as an example.

- Building on the past work of the research group, I have proposed, designed, and realized experimental methods to further advance the capabilities of high-brightness, near-infrared, high average power continuous wave laser beam delivery. By upgrading the optical components of the preceding experimental setup with ones of higher optical quality, furthermore by employing a cladding light extraction technique, I have presented independently the transmission of $>2\,\text{kW}$ average power through a nested anti-resonant nodeless fibre of $>10\,\text{m}$. This result is comparably the highest power value for any kind of hollow-core fibre transmission at the date of submission, and is only limited by the available equipment. Furthermore, as discussed extensively in Chapter 4, such a performance goes beyond the fundamental limitations of solid-core fibre technology, that is set by optical nonlinearities. Lastly, as field of hollow-core fibres continuously advances, the ultimate capacity of air-guiding fibres is yet to be fully taken advantage of. The reported findings can enable more advanced applications from those that utilize material processing, such as subsurface drilling or the decommissioning of nuclear power plants, to new opportunities in particle acceleration or long-path interferometry based gravitational wave detection.

- I have designed and installed an experimental layout, that can reliably demonstrate the optical trapping and delivery of micron sized particles through in-house drawn

nested anti-resonant nodeless fibres. While the phenomenon of optical guidance in hollow-core fibre have been reported nearly 30 years ago, the required experimental instrumentation that could be capable of presenting long-haul application of the technique has not been realized before. I have built an experimental setup, that can act as a foundation for future work, with the aim of demonstrating the capabilities of hollow-core fibres as long-distance remote sensing devices.

Based on the above mentioned main pillars, several possible directions for future work have been already proposed at the end of each experimental Chapter. Without the intention of providing an exhaustive list, here I will summarize some of the main points, a number of interesting next steps that could follow the studies discussed in the Thesis:

- Extending the scope of highly efficient coupling and delivery of quasi-single-moded optical beams into hollow-core fibres, the demonstration of similarly effective guidance of otherwise sensitive optical vortex beams is considered. The protection granted by an optical fibre enables the preserved transmission of beams with such unique properties.

- The quantified characterization of the developed cladding light extraction technique show promising applications from low-power coupling efficiency related studies to improved safety consideration of systems used for high-power material processing procedures.

- As discussed, the experimental results presented in the previous Chapters were limited by the available equipment. Thus, the ultimate capabilities of hollow-core fibre technology are yet to be demonstrated. Simulations suggest that a nested anti-resonant nodeless fibre with the parameters comparable to those used in the Thesis are still not utilized to their fullest potential. A further 7 to 10-fold improvement of the power-distance product is expected considering a fibre the core of which is filled with ambient air. Assuming that the core is evacuated instead suggests an improvement over 2 orders of magnitude beyond what is possible with conventional glass fibres [94]. The obvious challenge to be solved for these applications is the proper thermal management of the coupling approach used, as well as the heating of the fibre coating.

- Furthermore, hollow-core fibres with significantly lower loss values — below the limits set by Rayleigh scattering for silica — have been already presented [36]. Other novel geometries, implementing a double nested cladding structure are predicted to reach attenuation levels below 0.1 dB/km, and speculated to revolutionize a number of scientific fields, from telecommunications, through sensing, to power delivery [82].

- Throughout the Thesis, a near-Gaussian beam profile was considered to be desired. As such, the possibility of employing few- or highly multi-moded antiresonant fibres

have not been explored. This field is largely unexplored, and consequently shows promising opportunities by enabling the transmission of 10s of kW average power levels beyond slightly reduced, but still in the range of 100 to 1000 m distances [57]. For applications where preserving a high-brightness beam is not essential, this approach can provide a substantial improvement and greater flexibility (through the extended delivery length) over their solid-core counterparts.

- Arguably one of the more attractive applications of the earlier discussed proposals is the precise control of optically manipulated particles through hollow-core fibres. The long-haul guidance of such microparticles of different kind shows so many promising possibilities from remote sensing to coating the inner structure of the fibre core, that this direction of investigations will most certainly influence the future of research efforts exploring the capabilities of employing a hollow-core fibre based technology.

- Lastly, the complete combination of experimental Chapters could lead to the demonstration of a highly efficient coupling of high-power optical beam, into a in-house drawn hollow-core fibre, that can launch micron sized particles with speed values beyond $>100\,\mathrm{m/s}$. As this capability proposes an unique solution to possibly simulate the impact of micrometeorite collisions on the ground, it is a field of study that is certainly worth further investigations.

Acknowledgements

> If I have seen further [than others], it is by standing on the shoulders of giants.
>
> *Sir Isaac Newton*

First of all, I would like to express my deepest gratitude to my supervisors: Prof. David J. Richardson, Prof. Francesco Poletti, and Dr. Hans Christian Hansen Mulvad. They accepted me as their PhD student and provided me the opportunity to advance my academic career, for which I will be forever indebted to them. Their continuous support, encouragement and most importantly patience towards me will be always highly appreciated. Working under their supervision has been a life-changing experience for me. I am especially grateful to Dr. Hans Christian Hansen Mulvad, who has been a true mentor for me, inside and outside the lab. Without his valuable feedback and our discussions at lunch or over a coffee, the quality of this Thesis would be without a doubt of a lesser quality.

I am thankful for all the members of the Pulsed Fibre Laser Group, with whom we regularly discussed the progression of our individual research and always provided useful insight: Dr. Yongmin Jung, Dr. Lin Xu, Dr. Sijing Liang, Dr. Qiang Fu, Dr. Duangyang Xu, Yudi Wu, Ibrahim Abughazaleh, Panuwat Srisamran, Matthew Gerard, Kunhao Ji, Xin Huang, Jing Meng, and Jikun Yan.

I am grateful to those with whom we started and struggled through these tiring years, the soon-to-be-Dr's: Ann Lanari, Greg Jackson, Tom Kelly, Leonard Budd, and Xuhao Wei.

I would like to praise the help and support I have received from Prof. Radan Slavík, Dr. Eric Numkam Fokoua, Prof. Hendrik Ulbricht, and Tiberius Georgescu.

Similarly, I owe my thanks to those who contributed to the fabrication of and provided me the exceptional fibres that have been used extensively: Dr. Gregory Jasion, Dr. Hesham Sakr, Austin Taranta, and Konstantin Vidiajev.

Likewise I give my special thanks to my mentors and former colleagues, without whom I wouldn't be where I am now, and who always found a few minutes for me in their busy schedules: Dr. Roland Flender, Dr. Péter Jójárt, Dr. Roland Nagymihály, Réka Krisztin, Bence Gábor, Imre Seres, and Zsolt Bengery.

This thesis would not be the same without the support and infinite patience of my partner, Kamila Klejny. Thank you so much, for pushing me to be the best possible version of myself, and also being there for me whenever I needed.

S végül, de nem utolsó sorban köszönettel tartozom családomnak, akik mindig bíztattak és támogattak, végtelen jótanáccsal láttak el, még ha mindet nem is fogadtam meg, és gyakran emlékeztettek, hogy ne felejtsem el honnan indultam.

Last but not least, thank You, who considered my work worthy of your time and effort to read it.

Symbols and Notations

This list summarizes the notations and symbols used in the report

Acronyms

µBL	Micro bending loss
ARF	Anti-resonant fibre
BDO	Beam delivery optics
CE	Coupling efficiency
CLE	Cladding light extraction
CLS	Cladding light stripper
CMT	Coupled-mode theory
CRFP	Carbon fibre reinforced polymers
DG	Droplet gating
DNANF	Double nested anti-resonant nodeless fibre
FM	Fundamental mode
FUT	Fibre under test
FWM	Four-wave mixing
HCF	Hollow-core fibre
HHG	High-harmonic generaion
HOMER	Higher order mode extinction ratio
HOM	Higher order mode
HPD	High power delivery
HPFS	High-purity fused silica
LD	Laser diode
LL	Leakage loss (sometimes also referred to as confinement loss)

LP	Linearly polarized
MBL	Macro bending loss
McP	Microparticles
MFD	Mode field diameter
MMF	Multi-mode fibre
MOF	Microstructured optical fibre
MoR	Modulus of rupture
NANF	Nested anti-resonant nodeless fibre
NA	Numerical aperture
NLE	Non linear effects
NL	Non linear
OD	Optical discharge
PBGF	Photonic bandgap fibre
PDP	Power distance product
PnY	Pitch and yaw
PoF	Power over fibre
PS	Polystyrene
QSM	Quasi-single-moded
RSL	Rayleigh scattering loss
RVF	Revolver type fibre
SBS	Stimulated Brillouin scattering
SCF	Solid-core fibre
SMF	Single-mode fibre
SPM	Self-phase modulation
SRS	Stimulated Raman scattering
SSL	Surface scattering loss
TE	Transmission efficiency
UVFS	UV grade fused silica

Constants

ε_0	Electric permittivity of vacuum	[$8.854 \cdot 10^{-12}$ F m^{-1}]
c_0	Speed of light in vacuum	[$\sim 3 \cdot 10^{8}$ m s^{-1}]
k_B	Boltzmann constant	[$1.38 \cdot 10^{-23}$ J K^{-1}]

Notations

$\alpha^{R/B}$	Raman/Brillouin attenuation coefficient	[m^{-1}]
α_{idx}	Attenuation	[m^{-1}]
β_{idx}	Propagation constant	[µm^{-1}]
$\chi^{(j)}$	j-th order electric susceptibility tensor	[—]
η	Dynamic viscosity	[kg m^{-1} s^{-1}]
$\lvert\psi_{idx}\rangle$	Arbitrary wave function	[—]
Λ	Particle to channel ratio	[—]
λ_{idx}	Wavelength	[nm]
$\mathbf{E}$	Electric field vector	[V m^{-1}]
$\mathbf{F_{idx}}$	Force	[pN – nN]
$\mathbf{H}$	Magnetic field vector	[A m^{-1}]
$\omega_{idx} = \frac{2\pi c}{\lambda_{idx}}$	Angular frequency	[rad s^{-1}]
$\mathbf{\Phi}_{idx}$	Optical phase	[rad]
ϕ_{idx}	Angle of convergence	[rad]
ρ	Volume charge density	[C m^{-3}]
θ_{idx}	Angle of incidence	[rad]
$\varepsilon = \varepsilon_{rel} \cdot \varepsilon_0$	Absolute electric permittivity	[C V^{-1} m^{-1}]
ε_{rel}	Relative electric permittivity	[—]
φ_{idx}	Angle of refraction	[rad]
ϱ_{idx}	Material density	[kg m^{-3}]
ϑ_{idx}	Angle of reflection	[rad]
ξ	Particle size parameter	[—]
$C^{SR/SB}$	Spontaneous Raman/Brillouin response coefficient	[—]

c_{idx}	Speed of light in material ($idx = 0$ for vacuum)	[m s^{-1}]
$g^{R/B}$	Small signal Raman/Brillouin gain coefficient	[m W^{-1}]
I	Optical intensity	[W m^{-2}]
j	General running index	[—]
K	Wall correction factor	[—]
$k_{idx} = \frac{2\pi}{\lambda_{idx}}$	Angular wavenumber	[rad nm^{-1}]
MFD	Mode field diameter $(1/e^2)$	[µm]
$n^{(NL)}$	Nonlinear index of refraction	[—]
n_{idx}	Refractive index	[—]
P_{idx}	Optical power	[mW – kW]
r_{core}	Fibre core radius	[µm]
r_{ptcl}	Particle radius	[µm]
th	Microstructure membrane thickness	[nm]
w_0	Beam waist	[µm]
z_R	Rayleigh length	[µm]

List of Figures

List of Tables

Bibliography

[1] T. H. Maiman, "Stimulated Optical Radiation in Ruby," *Nature*, vol. 187, pp. 493–494, Aug. 1960. Number: 4736 Publisher: Nature Publishing Group.

[2] L. S. Collaboration and e. a. Virgo Collaboration, "Observation of Gravitational Waves from a Binary Black Hole Merger," *Physical Review Letters*, vol. 116, p. 061102, Feb. 2016. Publisher: American Physical Society.

[3] A. P. Young, M. J. Olsen, N. Driscoll, R. Flick, R. Gutierrez, R. Guza, E. Johnstone, and F. Kuester, "Comparison of Airborne and Terrestrial Lidar Estimates of Seacliff Erosion in Southern California," *Photogrammetric Engineering & Remote Sensing*, vol. 76, pp. 421–427, Apr. 2010.

[4] A. Houard, P. Walch, T. Produit, V. Moreno, B. Mahieu, A. Sunjerga, C. Herkommer, A. Mostajabi, U. Andral, Y.-B. André, M. Lozano, L. Bizet, M. C. Schroeder, G. Schimmel, M. Moret, M. Stanley, W. A. Rison, O. Maurice, B. Esmiller, K. Michel, W. Haas, T. Metzger, M. Rubinstein, F. Rachidi, V. Cooray, A. Mysyrowicz, J. Kasparian, and J.-P. Wolf, "Laser-guided lightning," *Nature Photonics*, pp. 1–5, Jan. 2023. Publisher: Nature Publishing Group.

[5] C. S. Enwemeka, V. V. Bumah, and D. S. Masson-Meyers, "Light as a potential treatment for pandemic coronavirus infections: A perspective," *Journal of Photochemistry and Photobiology B: Biology*, vol. 207, p. 111891, June 2020.

[6] Q. Liang, Y.-C. Chan, J. Toscano, K. K. Bjorkman, L. A. Leinwand, R. Parker, E. S. Nozik, D. J. Nesbitt, and J. Ye, "Breath analysis by ultra-sensitive broadband laser spectroscopy detects SARS-CoV-2 infection," *Journal of Breath Research*, vol. 17, no. 3, p. 036001, 2023. Publisher: IOP Publishing.

[7] J. Ballato and P. Dragic, "Glass: The Carrier of Light - A Brief History of Optical Fiber," *International Journal of Applied Glass Science*, vol. 7, no. 4, pp. 413–422, 2016. eprint: https://ceramics.onlinelibrary.wiley.com/doi/pdf/10.1111/ijag.12239.

[8] R. F. Cregan, B. J. Mangan, J. C. Knight, T. A. Birks, P. S. J. Russell, P. J. Roberts, and D. C. Allan, "Single-Mode Photonic Band Gap Guidance of Light in Air," *Science*, vol. 285, pp. 1537–1539, Sept. 1999. Publisher: American Association for the Advancement of Science Section: Report.

[9] X. Liu, "Evolution of Fiber-Optic Transmission and Networking toward the 5G Era," *iScience*, vol. 22, pp. 489–506, Dec. 2019.

[10] J. B. Rosolem, *Power-Over-Fiber Applications for Telecommunications and for Electric Utilities*. IntechOpen, June 2017. Publication Title: Optical Fiber and Wireless Communications.

[11] "Lockheed Martin delivers record 300-kW laser weapon to US military," Sept. 2022. Section: Military.

[12] M. Zaeh, J. Moesl, J. Musiol, and F. Oefele, "Material processing with remote technology revolution or evolution?," *Physics Procedia*, vol. 5, pp. 19–33, 2010.

[13] T. Okuda, Y. Fujiya, S. Goya, and A. Inoue, "Mitsubishi Heavy Industries, Ltd. Global Website | Technical Review," June 2020.

[14] "Mitsubishi Heavy Industries, Ltd. Global Website | Completely Rewrite Industry's Understanding of Transmitting High Quality Laser Processing Light over Long Distances."

[15] E. Khalkhal, M. Rezaei-Tavirani, M. R. Zali, and Z. Akbari, "The Evaluation of Laser Application in Surgery: A Review Article," *Journal of Lasers in Medical Sciences*, vol. 10, no. Suppl 1, pp. S104–S111, 2019.

[16] S. Liu, Y. He, H. Xie, Y. Ge, Y. Lin, Z. Yao, M. Jin, J. Liu, X. Chen, Y. Sun, and B. Wang, "A State-of-the-Art Review of Radioactive Decontamination Technologies: Facing the Upcoming Wave of Decommissioning and Dismantling of Nuclear Facilities," *Sustainability*, vol. 14, p. 4021, Jan. 2022. Number: 7 Publisher: Multidisciplinary Digital Publishing Institute.

[17] K. Shima, S. Ikoma, K. Uchiyama, Y. Takubo, M. Kashiwagi, and D. Tanaka, "5-kW single stage all-fiber Yb-doped single-mode fiber laser for materials processing," in *Fiber Lasers XV: Technology and Systems*, vol. 10512, p. 105120C, International Society for Optics and Photonics, Feb. 2018.

[18] B. Fu, W. Seidelman, Y. Liu, T. Kent, M. Carswell, Y. Zhang, and R. Yang, "Towards virtualized welding: Visualization and monitoring of remote welding," in *2014 IEEE International Conference on Multimedia and Expo (ICME)*, pp. 1–6, July 2014. ISSN: 1945-788X.

[19] S. Hegde, B. Satish Shenoy, and K. N. Chethan, "Review on carbon fiber reinforced polymer (CFRP) and their mechanical performance," *Materials Today: Proceedings*, vol. 19, pp. 658–662, Jan. 2019.

[20] N. Pisani, E. Numkam Fokoua, I. A. K. Davidson, F. Poletti, R. Slavík, D. Lowe, G. Machin, and G. Sutton, "Toward Gamma Ray Immune Fibre-Optic Phosphor Thermometry for Nuclear Decommissioning," *International Journal of Thermophysics*, vol. 43, p. 47, Jan. 2022.

[21] B. C. DeLoach Jr., R. C. Miller, and S. Kaufman, "Sound Alerter Powered Over an Optical Fiber," *Bell System Technical Journal*, vol. 57, no. 9, pp. 3309–3316, 1978. _eprint: https://onlinelibrary.wiley.com/doi/pdf/10.1002/j.1538-7305.1978.tb02205.x.

[22] F. Benabid, J. C. Knight, G. Antonopoulos, and P. S. J. Russell, "Stimulated Raman Scattering in Hydrogen-Filled Hollow-Core Photonic Crystal Fiber," *Science*, vol. 298, pp. 399–402, Oct. 2002. Publisher: American Association for the Advancement of Science Section: Report.

[23] F. Couny, F. Benabid, P. J. Roberts, P. S. Light, and M. G. Raymer, "Generation and Photonic Guidance of Multi-Octave Optical-Frequency Combs," *Science*, vol. 318, pp. 1118–1121, Nov. 2007. Publisher: American Association for the Advancement of Science Section: Report.

[24] A. D. Pryamikov, A. S. Biriukov, A. F. Kosolapov, V. G. Plotnichenko, S. L. Semjonov, and E. M. Dianov, "Demonstration of a waveguide regime for a silica hollow - core microstructured optical fiber with a negative curvature of the core boundary in the spectral region > 3.5 µm," *Optics Express*, vol. 19, pp. 1441–1448, Jan. 2011. Publisher: Optica Publishing Group.

[25] F. Yu, W. J. Wadsworth, and J. C. Knight, "Low loss silica hollow core fibers for 3–4 µm spectral region," *Optics Express*, vol. 20, pp. 11153–11158, May 2012. Publisher: Optica Publishing Group.

[26] J. M. Fini, J. W. Nicholson, R. S. Windeler, E. M. Monberg, L. Meng, B. Mangan, A. DeSantolo, and F. V. DiMarcello, "Low-loss hollow-core fibers with improved single-modedness," *Optics Express*, vol. 21, pp. 6233–6242, Mar. 2013. Publisher: Optica Publishing Group.

[27] A. N. Kolyadin, A. F. Kosolapov, and I. A. Bufetov, "Optical discharge propagation along hollow-core optical fibres," *Quantum Electronics*, vol. 48, p. 1138, Dec. 2018.

[28] F. Poletti, N. V. Wheeler, M. N. Petrovich, N. Baddela, E. Numkam Fokoua, J. R. Hayes, D. R. Gray, Z. Li, R. Slavík, and D. J. Richardson, "Towards high-capacity fibre-optic communications at the speed of light in vacuum," *Nature Photonics*, vol. 7, pp. 279–284, Apr. 2013. Number: 4 Publisher: Nature Publishing Group.

[29] A. Hartung, J. Kobelke, A. Schwuchow, K. Wondraczek, J. Bierlich, J. Popp, T. Frosch, and M. A. Schmidt, "Double antiresonant hollow core fiber – guidance in the deep ultraviolet by modified tunneling leaky modes," *Optics Express*, vol. 22, pp. 19131–19140, Aug. 2014. Publisher: Optica Publishing Group.

[30] J. R. Hayes, F. Poletti, M. S. Abokhamis, N. V. Wheeler, N. K. Baddela, and D. J. Richardson, "Anti-resonant hexagram hollow core fibers," *Optics Express*, vol. 23, pp. 1289–1299, Jan. 2015. Publisher: Optica Publishing Group.

[31] W. Belardi, "Design and Properties of Hollow Antiresonant Fibers for the Visible and Near Infrared Spectral Range," *Journal of Lightwave Technology*, vol. 33, no. 21, pp. 4497–4503, 2015. Conference Name: Journal of Lightwave Technology.

[32] G. Tsiminis, K. J. Rowland, E. P. Schartner, N. A. Spooner, T. M. Monro, and H. Ebendorff-Heidepriem, "Single-ring hollow core optical fibers made by glass billet extrusion for Raman sensing," *Optics Express*, vol. 24, pp. 5911–5917, Mar. 2016. Publisher: Optica Publishing Group.

[33] M. B. S. Nawazuddin, N. V. Wheeler, J. R. Hayes, S. R. Sandoghchi, T. D. Bradley, G. T. Jasion, R. Slavík, D. J. Richardson, and F. Poletti, "Lotus-Shaped Negative Curvature Hollow Core Fiber With 10.5 dB/km at 1550 nm Wavelength," *Journal of Lightwave Technology*, vol. 36, pp. 1213–1219, Mar. 2018. Conference Name: Journal of Lightwave Technology.

[34] S.-f. Gao, Y.-y. Wang, W. Ding, D.-l. Jiang, S. Gu, X. Zhang, and P. Wang, "Hollow-core conjoined-tube negative-curvature fibre with ultralow loss," *Nature Communications*, vol. 9, p. 2828, July 2018. Number: 1 Publisher: Nature Publishing Group.

[35] F. Amrani, J. H. Osório, F. Delahaye, F. Giovanardi, L. Vincetti, B. Debord, F. Gérôme, and F. Benabid, "Low-loss single-mode hybrid-lattice hollow-core photonic-crystal fibre," *Light: Science & Applications*, vol. 10, p. 7, Jan. 2021. Number: 1 Publisher: Nature Publishing Group.

[36] G. T. Jasion, H. Sakr, J. R. Hayes, S. R. Sandoghchi, L. Hooper, E. N. Fokoua, A. Saljoghei, H. C. Mulvad, M. Alonso, A. Taranta, T. D. Bradley, I. A. Davidson, Y. Chen, D. J. Richardson, and F. Poletti, "0.174 dB/km Hollow Core Double Nested Antiresonant Nodeless Fiber (DNANF)," in *2022 Optical Fiber Communications Conference and Exhibition (OFC)*, pp. 1–3, Mar. 2022.

[37] T. Matsui, K. Nakajima, and T. Sakamoto, "Effective mode-field diameter for few-mode fibers for considering splice loss characteristics," *Applied Optics*, vol. 56, pp. 7484–7490, Sept. 2017. Publisher: Optical Society of America.

[38] C. Röhrer, C. A. Codemard, G. Kleem, T. Graf, and M. A. Ahmed, "Preserving Nearly Diffraction-Limited Beam Quality Over Several Hundred Meters of Transmission Through Highly Multimode Fibers," *Journal of Lightwave Technology*, vol. 37, pp. 4260–4267, Sept. 2019. Publisher: IEEE.

[39] D. S. Bykov, O. A. Schmidt, T. G. Euser, and P. S. J. Russell, "Flying particle sensors in hollow-core photonic crystal fibre," *Nature Photonics*, vol. 9, pp. 461–465, July 2015.

[40] G. P. Agrawal, *Nonlinear Fiber Optics*. Lecture Notes in Physics, Berlin, Heidelberg: Springer, 2000.

[41] W. H. Renninger and F. W. Wise, "Optical solitons in graded-index multimode fibres," *Nature Communications*, vol. 4, p. 1719, Apr. 2013. Number: 1 Publisher: Nature Publishing Group.

[42] J. C. Knight, T. A. Birks, P. S. J. Russell, and D. M. Atkin, "All-silica single-mode optical fiber with photonic crystal cladding," *Optics Letters*, vol. 21, pp. 1547–1549, Oct. 1996. Publisher: Optical Society of America.

[43] S. Johnson, M. Ibanescu, M. Skorobogatiy, O. Weisberg, T. Engeness, M. Soljacic, S. Jacobs, J. Joannopoulos, and Y. Fink, "Low-loss asymptotically single-mode propagation in large-core OmniGuide fibers," *Optics Express*, vol. 9, no. 13, p. 748, 2001.

[44] R. Ryf, S. Randel, A. Gnauck, C. Bolle, A. Sierra, S. Mumtaz, M. Esmaeelpour, E. Burrows, R.-J. Essiambre, P. Winzer, D. Peckham, A. McCurdy, and J. Lingle, Robert, "Mode-Division Multiplexing Over 96 km of Few-Mode Fiber Using Coherent 6 $\,\times\,$6 MIMO Processing," *Lightwave Technology, Journal of*, vol. 30, pp. 1–1, Feb. 2012.

[45] D. Gloge, "Weakly Guiding Fibers," *Applied Optics*, vol. 10, pp. 2252–2258, Oct. 1971. Publisher: Optical Society of America.

[46] I. Technical Committee, "ISO 11146-2:2021," 2021.

[47] G. A. Thomas, B. I. Shraiman, P. F. Glodis, and M. J. Stephen, "Towards the clarity limit in optical fibre," *Nature*, vol. 404, pp. 262–264, Mar. 2000. Bandiera_abtest: a Cg_type: Nature Research Journals Number: 6775 Primary_atype: Research Publisher: Nature Publishing Group.

[48] E. A. J. Marcatili and R. A. Schmeltzer, "Hollow metallic and dielectric waveguides for long distance optical transmission and lasers," *The Bell System Technical Journal*, vol. 43, pp. 1783–1809, July 1964. Conference Name: The Bell System Technical Journal.

[49] F. Poletti, M. N. Petrovich, and D. J. Richardson, "Hollow-core photonic bandgap fibers: technology and applications," *Nanophotonics*, vol. 2, pp. 315–340, Dec. 2013. Publisher: De Gruyter Section: Nanophotonics.

[50] F. Benabid and P. J. Roberts, "Linear and nonlinear optical properties of hollow core photonic crystal fiber," *Journal of Modern Optics*, vol. 58, pp. 87–124, Jan. 2011. Publisher: Taylor & Francis _eprint: https://doi.org/10.1080/09500340.2010.543706.

[51] P. J. Roberts, D. P. Williams, B. J. Mangan, H. Sabert, F. Couny, W. J. Wadsworth, T. A. Birks, J. C. Knight, and P. S. J. Russell, "Realizing low loss air core photonic crystal fibers by exploiting an antiresonant core surround," *Optics Express*, vol. 13, pp. 8277–8285, Oct. 2005. Publisher: Optica Publishing Group.

[52] S.-J. Im, A. Husakou, and J. Herrmann, "Guiding properties and dispersion control of kagome lattice hollow-core photonic crystal fibers," *Optics Express*, vol. 17, pp. 13050–13058, July 2009. Publisher: Optica Publishing Group.

[53] C. Wei, R. J. Weiblen, C. R. Menyuk, and J. Hu, "Negative curvature fibers," *Advances in Optics and Photonics*, vol. 9, pp. 504–561, Sept. 2017.

[54] Y. Y. Wang, N. V. Wheeler, F. Couny, P. J. Roberts, and F. Benabid, "Low loss broadband transmission in hypocycloid-core Kagome hollow-core photonic crystal fiber," *Optics Letters*, vol. 36, pp. 669–671, Mar. 2011. Publisher: Optical Society of America.

[55] M. A. Duguay, Y. Kokubun, T. L. Koch, and L. Pfeiffer, "Antiresonant reflecting optical waveguides in SiO2-Si multilayer structures," *Applied Physics Letters*, vol. 49, pp. 13–15, Dec. 1986. Publisher: American Institute of Physics Publising LLC.

[56] W. Shere, G. T. Jasion, E. Numkam Fokoua, and F. Poletti, "Understanding the impact of cladding modes in multi-mode hollow-core anti-resonant fibres," *Optical Fiber Technology*, vol. 71, p. 102919, July 2022.

[57] W. Shere, E. N. Fokoua, G. T. Jasion, and F. Poletti, "Designing multi-mode anti-resonant hollow-core fibers for industrial laser power delivery," *Optics Express*, vol. 30, pp. 40425–40440, Oct. 2022. Publisher: Optica Publishing Group.

[58] X. Hu and A. Schülzgen, "Design of Negative Curvature Hollow Core Fiber Based on Reinforcement Learning," *Journal of Lightwave Technology*, vol. 38, pp. 1959–1965, Apr. 2020. Conference Name: Journal of Lightwave Technology.

[59] W. Zheng, Y. Qin, Y. Qin, Y. Qin, O. Xu, O. Xu, M. Xiang, M. Xiang, D. Peng, D. Peng, S. Fu, S. Fu, J. Li, J. Li, and J. Li, "Wideband low confinement loss anti-resonant hollow core fiber with nested U-shape tube," *Optics Express*, vol. 29, pp. 24182–24192, July 2021. Publisher: Optica Publishing Group.

[60] Y. Wang and W. Chang, "Multi-nested antiresonant hollow-core fiber with ultralow loss and single-mode guidance," *Optics Express*, vol. 31, pp. 18250–18264, May 2023. Publisher: Optica Publishing Group.

[61] M. I. Hasan, N. Akhmediev, and W. Chang, "Positive and negative curvatures nested in an antiresonant hollow-core fiber," *Optics Letters*, vol. 42, pp. 703–706, Feb. 2017.

[62] G. T. Jasion, D. J. Richardson, and F. Poletti, "Novel Antiresonant Hollow Core Fiber Design with Ultralow Leakage Loss Using Transverse Power Flow Analysis," in *Optical Fiber Communication Conference (OFC) 2019 (2019), paper Th3E.2*, p. Th3E.2, Optica Publishing Group, Mar. 2019.

[63] X. Chen, X. Hu, L. Yang, J. Peng, H. Li, N. Dai, and J. Li, "Double negative curvature anti-resonance hollow core fiber," *Optics Express*, vol. 27, pp. 19548–19554, July 2019.

[64] Y. Zhu, W. Li, F. Gao, X. Xu, and N. Song, "Small-core hollow-core nested antiresonant nodeless fiber with semi-circular tubes," *Optics Express*, vol. 30, pp. 20373–20388, June 2022. Publisher: Optica Publishing Group.

[65] G. T. Jasion, J. R. Hayes, N. V. Wheeler, Y. Chen, T. D. Bradley, D. J. Richardson, and F. Poletti, "Fabrication of tubular anti-resonant hollow core fibers: modelling, draw dynamics and process optimization," *Optics Express*, vol. 27, pp. 20567–20582, July 2019. Publisher: Optica Publishing Group.

[66] C. M. B. Cordeiro, A. K. L. Ng, and H. Ebendorff-Heidepriem, "Ultra-simplified Single-Step Fabrication of Microstructured Optical Fiber," *Scientific Reports*, vol. 10, p. 9678, June 2020. Number: 1 Publisher: Nature Publishing Group.

[67] E. Arrospide, I. Bikandi, I. Larrañaga, X. Cearsolo, J. Zubia, and G. Durana, "Harnessing Deep-Hole Drilling to Fabricate Air-Structured Polymer Optical Fibres," *Polymers*, vol. 11, p. 1739, Nov. 2019. Number: 11 Publisher: Multidisciplinary Digital Publishing Institute.

[68] W. Talataisong, R. Ismaeel, T. H. R. Marques, S. Abokhamis Mousavi, M. Beresna, M. A. Gouveia, S. R. Sandoghchi, T. Lee, C. M. B. Cordeiro, and G. Brambilla, "Mid-IR Hollow-core microstructured fiber drawn from a 3D printed PETG preform," *Scientific Reports*, vol. 8, p. 8113, May 2018. Number: 1 Publisher: Nature Publishing Group.

[69] G. T. Jasion, J. S. Shrimpton, Y. Chen, T. Bradley, D. J. Richardson, and F. Poletti, "MicroStructure Element Method (MSEM): viscous flow model for the virtual draw of microstructured optical fibers," *Optics Express*, vol. 23, pp. 312–329, Jan. 2015. Publisher: Optica Publishing Group.

[70] M. H. Frosz, R. Pennetta, M. T. Enders, G. Ahmed, and P. S. J. Russell, "Non-invasive real-time characterization of hollow-core photonic crystal fibers using whispering gallery mode spectroscopy," *Optics Express*, vol. 27, pp. 30842–30851, Oct. 2019. Publisher: Optica Publishing Group.

[71] L. Budd, A. Taranta, E. N. Fokoua, and F. Poletti, "Non-Invasive Measurement of Hollow-Core Antiresonant Fiber Structure," in *2021 IEEE Photonics Conference (IPC)*, pp. 1–2, 2021. ISSN: 2575-274X.

[72] J. C. Travers, W. Chang, J. Nold, N. Y. Joly, and P. S. J. Russell, "Ultrafast nonlinear optics in gas-filled hollow-core photonic crystal fibers [Invited]," *JOSA B*, vol. 28, pp. A11–A26, Dec. 2011.

[73] W. Ni, C. Yang, Y. Luo, R. Xia, P. Lu, D. J. J. Hu, S. Danto, P. P. Shum, and L. Wei, "Recent Advancement of Anti-Resonant Hollow-Core Fibers for Sensing Applications," *Photonics*, vol. 8, p. 128, Apr. 2021. Number: 4 Publisher: Multidisciplinary Digital Publishing Institute.

[74] T. W. Kelly, P. Horak, I. A. Davidson, M. Partridge, G. T. Jasion, S. Rikimi, A. Taranta, D. J. Richardson, F. Poletti, and N. V. Wheeler, "Gas-induced differential refractive index enhanced guidance in hollow-core optical fibers," *Optica*, vol. 8, pp. 916–920, June 2021. Publisher: Optica Publishing Group.

[75] M. K. Garbos, T. G. Euser, O. A. Schmidt, S. Unterkofler, and P. S. J. Russell, "Doppler velocimetry on microparticles trapped and propelled by laser light in liquid-filled photonic crystal fiber," *Optics Letters*, vol. 36, pp. 2020–2022, June 2011. Publisher: Optical Society of America.

[76] R. Zeltner, S. Xie, R. Pennetta, and P. S. Russell, "Broadband, Lensless, and Optomechanically Stabilized Coupling into Microfluidic Hollow-Core Photonic Crystal Fiber Using Glass Nanospike," *ACS Photonics*, vol. 4, pp. 378–383, Feb. 2017. Publisher: American Chemical Society.

[77] F. Benabid, J. C. Knight, and P. S. J. Russell, "Particle levitation and guidance in hollow-core photonic crystal fiber," *Optics Express*, vol. 10, pp. 1195–1203, Oct. 2002.

[78] F. Benabid, F. Couny, J. C. Knight, T. A. Birks, and P. S. J. Russell, "Compact, stable and efficient all-fibre gas cells using hollow-core photonic crystal fibres," *Nature*, vol. 434, pp. 488–491, Mar. 2005. Number: 7032 Publisher: Nature Publishing Group.

[79] P. S. J. Russell, P. Hölzer, W. Chang, A. Abdolvand, and J. C. Travers, "Hollow-core photonic crystal fibres for gas-based nonlinear optics," *Nature Photonics*, vol. 8, pp. 278–286, Apr. 2014. Number: 4 Publisher: Nature Publishing Group.

[80] P. Zhao, Y. Zhao, H. Bao, H. L. Ho, W. Jin, S. Fan, S. Gao, Y. Wang, and P. Wang, "Mode-phase-difference photothermal spectroscopy for gas detection with an anti-resonant hollow-core optical fiber," *Nature Communications*, vol. 11, p. 847, Feb. 2020. Number: 1 Publisher: Nature Publishing Group.

[81] J. Kapit and A. P. M. Michel, "Dissolved gas sensing using an anti-resonant hollow core optical fiber," *Applied Optics*, vol. 60, pp. 10354–10358, Nov. 2021. Publisher: Optica Publishing Group.

[82] E. N. Fokoua, S. A. Mousavi, G. T. Jasion, D. J. Richardson, and F. Poletti, "Loss in hollow-core optical fibers: mechanisms, scaling rules, and limits," *Advances in Optics and Photonics*, vol. 15, pp. 1–85, Mar. 2023. Publisher: Optica Publishing Group.

[83] F. Poletti, "Nested antiresonant nodeless hollow core fiber," *Optics Express*, vol. 22, pp. 23807–23828, Oct. 2014.

[84] H. A. HAUS, W. P. HUANG, S. KAWAKAMI, and N. A. WHITAKER, "Coupled-mode theory of optical waveguides," *Coupled-mode theory of optical waveguides*, vol. 5, no. 1, pp. 16–23, 1987. Place: New York, NY Publisher: Institute of Electrical and Electronics Engineers.

[85] W.-P. Huang, "Coupled-mode theory for optical waveguides: an overview," *JOSA A*, vol. 11, pp. 963–983, Mar. 1994. Publisher: Optica Publishing Group.

[86] F. Yu, P. Song, D. Wu, T. Birks, D. Bird, and J. Knight, "Attenuation limit of silica-based hollow-core fiber at mid-IR wavelengths," *APL Photonics*, vol. 4, p. 080803, Aug. 2019. Publisher: American Institute of Physics.

[87] J. Jackle and K. Kawasaki, "Intrinsic roughness of glass surfaces," *Journal of Physics: Condensed Matter*, vol. 7, no. 23, p. 4351, 1995.

[88] D. Gloge, "Optical-fiber packaging and its influence on fiber straightness and loss," *The Bell System Technical Journal*, vol. 54, no. 2, pp. 245–262, 1975. Conference Name: The Bell System Technical Journal.

[89] H. H. Lim and T. Taira, ">50 MW peak power, high brightness Nd:YAG/Cr^{4+}:YAG microchip laser with unstable resonator," *Optics Express*, vol. 30, pp. 5151–5158, Feb. 2022. Publisher: Optica Publishing Group.

[90] S. M. Abokhamis Mousavi, *Exploring optical nonlinearity in gas-filled hollow core fibre.* phd, University of Southampton, May 2018.

[91] Y. Shimoji, A. T. Fay, R. S. F. Chang, and N. Djeu, "Direct measurement of the nonlinear refractive index of air," *JOSA B*, vol. 6, pp. 1994–1998, Nov. 1989. Publisher: Optica Publishing Group.

[92] P. Kabaciński, T. M. Kardaś, Y. Stepanenko, and C. Radzewicz, "Nonlinear refractive index measurement by SPM-induced phase regression," *Optics Express*, vol. 27, pp. 11018–11028, Apr. 2019. Publisher: Optica Publishing Group.

[93] C. Jauregui, J. Limpert, and A. Tünnermann, "High-power fibre lasers," *Nature Photonics*, vol. 7, pp. 861–867, Nov. 2013. Number: 11 Publisher: Nature Publishing Group.

[94] H. C. H. Mulvad, S. Abokhamis Mousavi, V. Zuba, L. Xu, H. Sakr, T. D. Bradley, J. R. Hayes, G. T. Jasion, E. Numkam Fokoua, A. Taranta, S.-U. Alam, D. J. Richardson, and F. Poletti, "Kilowatt-average-power single-mode laser light transmission over kilometre-scale hollow-core fibre," *Nature Photonics*, pp. 1–6, May 2022. Publisher: Nature Publishing Group.

[95] T. D. Bradley, J. R. Hayes, Y. Chen, G. T. Jasion, S. R. Sandoghchi, R. Slavik, E. N. Fokoua, S. Bawn, H. Sakr, I. Davidson, A. Taranta, J. P. Thomas, M. N. Petrovich, D. Richardson, and F. Poletti, "Record Low-Loss 1.3dB/km Data Transmitting Antiresonant Hollow Core Fibre," in *2018 European Conference on Optical Communication (ECOC)*, pp. 1–3, Sept. 2018.

[96] H. Sakr, T. D. Bradley, G. T. Jasion, E. R. N. Fokoua, S. R. Sandoghchi, I. A. Davidson, A. A. Taranta, G. Guerra, W. Shere, Y. Cheng, J. R. Hayes, D. J. Richardson, and F. Poletti, "Hollow Core NANFs with Five Nested Tubes and Record Low Loss at 850, 1060, 1300 and 1625nm | IEEE Conference Publication | IEEE Xplore," July 2021.

[97] D. Marcuse, "Loss analysis of single-mode fiber splices," *Bell System Technical Journal*, vol. 56, no. 5, pp. 703–718, 1977.

[98] R. E. Wagner and W. J. Tomlinson, "Coupling efficiency of optics in single-mode fiber components," *Applied Optics*, vol. 21, pp. 2671–2688, Aug. 1982. Publisher: Optical Society of America.

[99] S. Xie, R. Pennetta, and P. S. J. Russell, "Self-alignment of glass fiber nanospike by optomechanical back-action in hollow-core photonic crystal fiber," *Optica*, vol. 3, pp. 277–282, Mar. 2016.

[100] C. Wang, R. Yu, C. Xiong, J. Zhu, and L. Xiao, "Ultralow-loss fusion splicing between antiresonant hollow-core fibers and antireflection-coated single-mode fibers with low return loss," *Optics Letters*, vol. 48, pp. 1120–1123, Mar. 2023. Publisher: Optica Publishing Group.

[101] M. Komanec, D. Suslov, S. Zvánovec, Y. Chen, T. Bradley, S. R. Sandoghchi, E. R. Numkam Fokoua, G. T. Jasion, M. N. Petrovich, F. Poletti, D. J. Richardson, and R. Slavík, "Low-Loss and Low-Back-Reflection Hollow-Core to Standard Fiber Interconnection," *IEEE Photonics Technology Letters*, vol. 31, no. 10, pp. 723–726, 2019. Conference Name: IEEE Photonics Technology Letters.

[102] D. Suslov, M. Komanec, E. R. Numkam Fokoua, D. Dousek, A. Zhong, S. Zvánovec, T. D. Bradley, F. Poletti, D. J. Richardson, and R. Slavík, "Low loss and high performance interconnection between standard single-mode fiber and antiresonant hollow-core fiber," *Scientific Reports*, vol. 11, p. 8799, Apr. 2021. Number: 1 Publisher: Nature Publishing Group.

[103] Y. Cui, Y. Cui, W. Huang, W. Huang, Z. Zhou, Z. Zhou, H. Li, H. Li, M. Wang, M. Wang, M. Wang, Z. Chen, Z. Chen, Z. Chen, Z. Wang, Z. Wang, and Z. Wang, "Highly efficient and stable coupling of kilowatt-level continuous wave laser into hollow-core fibers," *Chinese Optics Letters*, vol. 20, p. 040602, Apr. 2022. Publisher: Chinese Optical Society.

[104] J. Kepler, *De cometis libelli tres : I. Astronomicus, theoremata continens de motu cometarum, ubi demonstratio apparentiarum & altitudinis cometarum qui annis 1607. & 1618. conspecti sunt, nova & [paraidoxon]. II. Physicus, continens physiologiam cometarum nouam & [paraidoxon]. III. Astrologicus, de significationibus cometarum annorum 1607 & 1618.* Augustae Vindelicorum, [Augsburg]: Typis Andreae Apergeri, sumptibus Sebastiani Mylii Bibliopolae Augustani, 1619.

[105] A. Ashkin, "Acceleration and Trapping of Particles by Radiation Pressure," *Physical Review Letters*, vol. 24, pp. 156–159, Jan. 1970. Publisher: American Physical Society.

[106] A. Ashkin and J. M. Dziedzic, "Optical Levitation by Radiation Pressure," *Applied Physics Letters*, vol. 19, pp. 283–285, Oct. 1971. Publisher: American Institute of Physics.

[107] A. Ashkin, J. M. Dziedzic, J. E. Bjorkholm, and S. Chu, "Observation of a single-beam gradient force optical trap for dielectric particles," *Optics Letters*, vol. 11, May 1986. Publisher: Optica Publishing Group.

[108] Z. Gong, Y.-L. Pan, G. Videen, and C. Wang, "Optical trapping and manipulation of single particles in air: Principles, technical details, and applications," *Journal of Quantitative Spectroscopy and Radiative Transfer*, vol. 214, pp. 94–119, July 2018.

[109] G. Pesce, P. H. Jones, O. M. Maragò, and G. Volpe, "Optical tweezers: theory and practice," *The European Physical Journal Plus*, vol. 135, p. 949, Dec. 2020.

[110] P. Zemánek, G. Volpe, A. Jonáš, and O. Brzobohatý, "Perspective on light-induced transport of particles: from optical forces to phoretic motion," *Advances in Optics and Photonics*, vol. 11, pp. 577–678, Sept. 2019. Publisher: Optical Society of America.

[111] J. Chen, J. Ng, Z. Lin, and C. T. Chan, "Optical pulling force," *Nature Photonics*, vol. 5, pp. 531–534, Sept. 2011. Number: 9 Publisher: Nature Publishing Group.

[112] J. Lin and Y.-q. Li, "Optical trapping and rotation of airborne absorbing particles with a single focused laser beam," *Applied Physics Letters*, vol. 104, p. 101909, Mar. 2014.

[113] A. Urvoy, Z. Vendeiro, J. Ramette, A. Adiyatullin, and V. Vuletić, "Direct Laser Cooling to Bose-Einstein Condensation in a Dipole Trap," *Physical Review Letters*, vol. 122, p. 203202, May 2019. Publisher: American Physical Society.

[114] L. Wang, S. Wang, Q. Zhao, and X. Wang, "Macroscopic laser pulling based on the Knudsen force in rarefied gas," *Optics Express*, vol. 31, pp. 2665–2674, Jan. 2023. Publisher: Optica Publishing Group.

[115] P. P. Crooker, W. B. Colson, and J. Blau, "Representation of a Gaussian beam by rays," *American Journal of Physics*, vol. 74, pp. 722–727, July 2006. Publisher: American Association of Physics Teachers.

[116] K. S. Malik and B. R. Boruah, "Optical force calculation in the ray-optics regime for beams with arbitrary complex amplitude profiles," *Optics Letters*, vol. 47, pp. 4151–4154, Aug. 2022. Publisher: Optica Publishing Group.

[117] A. Ashkin, "Forces of a single-beam gradient laser trap on a dielectric sphere in the ray optics regime," *Biophysical Journal*, vol. 61, pp. 569–582, Feb. 1992.

[118] T. X. Phuoc, "A numerical study of the radiation forces on an absorbing particle using the ray optics approach," *Optics Communications*, vol. 241, pp. 271–277, Nov. 2004.

[119] D. S. Bykov, S. Xie, R. Zeltner, A. Machnev, G. K. L. Wong, T. G. Euser, and P. S. J. Russell, "Long-range optical trapping and binding of microparticles in hollow-core photonic crystal fibre," *Light: Science & Applications*, vol. 7, p. 22, June 2018.

[120] H. G. Alinezhad and S. N. S. Reihani, "Optimal condition for optical trapping of large particles: tuning the laser power and numerical aperture of the objective," *JOSA B*, vol. 36, pp. 3053–3059, Nov. 2019. Publisher: Optica Publishing Group.

[121] H. C. Hamaker, "The London—van der Waals attraction between spherical particles," *Physica*, vol. 4, pp. 1058–1072, Oct. 1937.

[122] N. Al Quddus, W. A. Moussa, and S. Bhattacharjee, "Motion of a spherical particle in a cylindrical channel using arbitrary Lagrangian–Eulerian method," *Journal of Colloid and Interface Science*, vol. 317, pp. 620–630, Jan. 2008.

[123] E. N. Fokoua, R. Slavik, D. J. Richardson, and F. Poletti, "Limits of Coupling Efficiency into Hollow-Core Antiresonant Fibers," in *Conference on Lasers and Electro-Optics (2021), paper STu1Q.4*, p. STu1Q.4, Optica Publishing Group, May 2021.

[124] B. Siwicki, R. M. Carter, J. D. Shephard, F. Yu, J. C. Knight, and D. P. Hand, "Negative-Curvature Anti-Resonant Fiber Coupling Tolerances," *Journal of Lightwave Technology*, vol. 37, pp. 5548–5554, Nov. 2019. Conference Name: Journal of Lightwave Technology.

[125] V. Zuba, H. C. H. Mulvad, R. Slavík, H. Sakr, F. Poletti, D. J. Richardson, and E. N. Fokoua, "Experimental Investigation into Optimum Laser Coupling Efficiency into Hollow-Core NANFs," in *Conference on Lasers and Electro-Optics (2022), paper SW4K.1*, p. SW4K.1, Optica Publishing Group, May 2022.

[126] V. Zuba, H. C. H. Mulvad, R. Slavík, H. Sakr, F. Poletti, D. J. Richardson, and E. N. Fokoua, "Limits of Coupling Efficiency into Hollow-core Antiresonant Fibres," *Journal of Lightwave Technology*, pp. 1–10, 2023. Conference Name: Journal of Lightwave Technology.

[127] H. T. Nguyen, G. Stepniewski, A. Filipkowski, R. Kasztelanic, D. Pysz, H. L. Van, R. Stepien, M. Klimczak, W. Krolikowski, and R. Buczynski, "Transmission of an optical vortex beam in antiresonant fibers generated in an all-fiber system," *Optics Express*, vol. 30, pp. 45635–45647, Dec. 2022. Publisher: Optica Publishing Group.

[128] S. Jamali, V. Wittig, J. Börner, R. Bracke, and A. Ostendorf, "Application of high powered Laser Technology to alter hard rock properties towards lower strength materials for more efficient drilling, mining, and Geothermal Energy production," *Geomechanics for Energy and the Environment*, vol. 20, p. 100112, Dec. 2019.

[129] D. J. Benford, T. J. Powers, and S. H. Moseley, "Thermal conductivity of Kapton tape," *Cryogenics*, vol. 39, pp. 93–95, Jan. 1999.

[130] S. Rikimi, Y. Chen, Y. Chen, M. C. Partridge, T. D. Bradley, I. A. K. Davidson, A. A. Taranta, F. Poletti, M. N. Petrovich, M. N. Petrovich, D. J. Richardson, and N. V. Wheeler, "Growth of Ammonium Chloride on Cleaved End-Facets of Hollow Core Fibers," in *Conference on Lasers and Electro-Optics (2020), paper SF2P.4*, p. SF2P.4, Optical Society of America, May 2020.

[131] E. Honea, R. S. Afzal, M. Savage-Leuchs, J. Henrie, K. Brar, N. Kurz, D. Jander, N. Gitkind, D. Hu, C. Robin, A. M. Jones, R. Kasinadhuni, and R. Humphreys, "Advances in fiber laser spectral beam combining for power scaling," in *Components and Packaging for Laser Systems II*, vol. 9730, pp. 181–189, SPIE, Apr. 2016.

[132] T. Bonhoff, P. Loosen, J. Stollenwerk, and M. Schniedenharn, "Experimental and theoretical analysis of thermo-optical effects in protective window for selective laser melting," *undefined*, 2017.

[133] N. Ashok, S. Han, Y. L. Lee, and W. Shin, "Cladding pump light stripper study for high power fiber laser applications," in *Components and Packaging for Laser Systems III*, vol. 10085, p. 1008514, International Society for Optics and Photonics, Feb. 2017.

[134] L. Yin, M. Yan, Z. Han, H. Wang, H. Shen, and R. Zhu, "High power cladding light stripper using segmented corrosion method: theoretical and experimental studies," *Optics Express*, vol. 25, pp. 8760–8776, Apr. 2017.

[135] S. Zou, H. Chen, J. Zhang, H. Yu, Z. Zhang, J. Sun, and X. Lin, "Cladding Light Stripper of High Average Stripped Power Density With High Attenuation of 39

dB and Low Temperature Rise," *IEEE Photonics Journal*, vol. 10, pp. 1–10, Feb. 2018.

[136] J. Anderegg, S. J. Brosnan, and P. A. Thielen, "System and method to remove light from cladding," Mar. 2008.

[137] D. C. Jones, C. R. Bennett, M. A. Smith, and A. M. Scott, "High-power beam transport through a hollow-core photonic bandgap fiber," *Optics Letters*, vol. 39, pp. 3122–3125, June 2014. Publisher: Optical Society of America.

[138] S. Hädrich, J. Rothhardt, S. Demmler, M. Tschernajew, A. Hoffmann, M. Krebs, A. Liem, O. d. Vries, M. Plötner, S. Fabian, T. Schreiber, J. Limpert, and A. Tünnermann, "Scalability of components for kW-level average power few-cycle lasers," *Applied Optics*, vol. 55, pp. 1636–1640, Mar. 2016.

[139] G. Palma-Vega, G. Palma-Vega, F. Beier, F. Beier, F. Stutzki, S. Fabian, T. Schreiber, R. Eberhardt, A. Tünnermann, and A. Tünnermann, "High Average Power Transmission Through Hollow-core Fibers," in *Laser Congress 2018 (ASSL) (2018), paper ATh1A.7*, p. ATh1A.7, Optical Society of America, Nov. 2018.

[140] X. Zhu, D. Wu, Y. Wang, F. Yu, Q. Li, Y. Qi, J. Knight, S. Chen, and L. Hu, "Delivery of CW laser power up to 300 watts at 1080 nm by an uncooled low-loss anti-resonant hollow-core fiber," *Optics Express*, vol. 29, pp. 1492–1501, Jan. 2021. Publisher: Optical Society of America.

[141] X. Zhu, X. Zhu, F. Yu, F. Yu, D. Wu, S. Chen, Y. Jiang, L. Hu, and L. Hu, "Laser-induced damage of an anti-resonant hollow-core fiber for high-power laser delivery at 1 µm," *Optics Letters*, vol. 47, pp. 3548–3551, July 2022. Publisher: Optica Publishing Group.

[142] M. A. Cooper, J. Wahlen, J. C. A. Zacarias, D. C. Delgado, I. Divliansky, J. Antonio-Lopez, A. Schulzgen, and R. A. Correa, "KW single mode CW laser transmission in an anti-resonant hollow-core fiber," in *Laser Technology for Defense and Security XVII*, vol. PC12092, p. PC120920C, SPIE, May 2022.

[143] M. Cooper, J. Wahlen, S. Yerolatsitis, D. Delgado, D. Parra, B. Tanner, P. Ahmadi, O. Jones, M. S. Habib, I. Divliansky, J. Antonio-Lopez, A. Schülzgen, and R. A. Correa, "2.2 kW Single-Mode Narrow-Linewidth Laser Delivery Through a Hollow-Core Fiber," Aug. 2023.

[144] C. Park, A. Sim, S. Ahn, H. Kang, and E.-J. Chun, "Influence of laser surface engineering of AISI P20-improved mold steel on wear and corrosion behaviors," *Surface and Coatings Technology*, vol. 377, p. 124852, Nov. 2019.

[145] P. A. Rona, "The changing vision of marine minerals," *Ore Geology Reviews*, vol. 33, pp. 618–666, June 2008.

[146] J. Temple, "This geothermal startup showed its wells can be used like a giant underground battery," July 2023.

[147] M. Michieletto, J. K. Lyngsø, C. Jakobsen, J. Lægsgaard, O. Bang, and T. T. Alkeskjold, "Hollow-core fibers for high power pulse delivery," *Optics Express*, vol. 24, pp. 7103–7119, Apr. 2016. Publisher: Optical Society of America.

[148] P. Jaworski, F. Yu, R. R. J. Maier, W. J. Wadsworth, J. C. Knight, J. D. Shephard, and D. P. Hand, "Picosecond and nanosecond pulse delivery through a hollow-core Negative Curvature Fiber for micro-machining applications," *Optics Express*, vol. 21, pp. 22742–22753, Sept. 2013. Publisher: Optical Society of America.

[149] L. Liang, J. Guan, X. Zhu, Y. Wang, D. Wu, F. Yu, and Y. Han, "Delivery of Nearly Diffraction-Limited Picosecond Laser Pulses in the Air-Filled Anti-Resonant Hollow-Core Fiber at 1 µm Wavelength," *Photonics*, vol. 10, p. 416, Apr. 2023. Number: 4 Publisher: Multidisciplinary Digital Publishing Institute.

[150] C. Yan, H. Li, Z. Huang, X. Wang, D. Liu, X. Liu, J. Pan, Z. Luo, F. Yang, Y. Zheng, R. Yin, H. Yu, Y. Leng, L. Song, M. Pang, and X. Jiang, "Highly stable, flexible delivery of microjoule-level ultrafast pulses in vacuumized anti-resonant hollow-core fibers for active synchronization," *Optics Letters*, vol. 48, pp. 1838–1841, Apr. 2023. Publisher: Optica Publishing Group.

[151] I. A. Bufetov, A. N. Kolyadin, A. F. Kosolapov, V. P. Efremov, and V. E. Fortov, "Catastrophic damage in hollow core optical fibers under high power laser radiation," *Optics Express*, vol. 27, pp. 18296–18310, June 2019.

[152] M. J. Renn, D. Montgomery, O. Vdovin, D. Z. Anderson, C. E. Wieman, and E. A. Cornell, "Laser-Guided Atoms in Hollow-Core Optical Fibers," *Physical Review Letters*, vol. 75, pp. 3253–3256, Oct. 1995. Publisher: American Physical Society.

[153] M. J. Renn, R. Pastel, and H. J. Lewandowski, "Laser Guidance and Trapping of Mesoscale Particles in Hollow-Core Optical Fibers," *Physical Review Letters*, vol. 82, pp. 1574–1577, Feb. 1999. Publisher: American Physical Society.

[154] J. K. Lyngsø, B. J. Mangan, C. Jakobsen, and P. J. Roberts, "7-cell core hollow-core photonic crystal fibers with low loss in the spectral region around 2 µm," *Optics Express*, vol. 17, pp. 23468–23473, Dec. 2009. Publisher: Optica Publishing Group.

[155] R. Thurn and W. Kiefer, "Raman-Microsampling Technique Applying Optical Levitation by Radiation Pressure," *Applied Spectroscopy*, vol. 38, pp. 78–83, Jan. 1984. Publisher: SAGE Publications Ltd STM.

[156] R. Omori, T. Kobayashi, and A. Suzuki, "Observation of a single-beam gradient-force optical trap for dielectric particles in air," *Optics letters*, vol. 22, pp. 816–8, July 1997.

[157] D. R. Burnham and D. McGloin, "Holographic optical trapping of aerosol droplets," *Optics Express*, vol. 14, pp. 4175–4181, May 2006.

[158] D. McGloin, D. R. Burnham, M. D. Summers, D. Rudd, N. Dewar, and S. Anand, "Optical manipulation of airborne particles: techniques and applications," *Faraday Discussions*, vol. 137, pp. 335–350, Oct. 2008. Publisher: The Royal Society of Chemistry.

[159] M. D. Summers, D. R. Burnham, and D. McGloin, "Trapping solid aerosols with optical tweezers: A comparison between gas and liquid phase optical traps," *Optics Express*, vol. 16, pp. 7739–7747, May 2008. Publisher: Optica Publishing Group.

[160] M. Najlah, I. Parveen, M. A. Alhnan, W. Ahmed, A. Faheem, D. A. Phoenix, K. M. G. Taylor, and A. Elhissi, "The effects of suspension particle size on the performance of air-jet, ultrasonic and vibrating-mesh nebulisers," *International Journal of Pharmaceutics*, vol. 461, pp. 234–241, Jan. 2014.

[161] N. Magome, M. I. Kohira, E. Hayata, S. Mukai, and K. Yoshikawa, "Optical Trapping of a Growing Water Droplet in Air," *The Journal of Physical Chemistry B*, vol. 107, pp. 3988–3990, Apr. 2003. Publisher: American Chemical Society.

[162] E. Corbanie, M. Matthijs, J. van Eck, J. Remon, W. Landman, and C. Vervaet, "Deposition of differently sized airborne microspheres in the respiratory tract of chickens," *Avian Pathology*, vol. 35, pp. 475–485, Dec. 2006. Publisher: Taylor & Francis _eprint: https://doi.org/10.1080/03079450601028845.

[163] D. Jakubczyk, M. Kolwas, G. Derkachov, K. Kolwas, and M. Zientara, "Evaporation of micro-droplets: The "radius-square-law" revisited," *Acta Physica Polonica A*, vol. 122, no. 4, pp. 709–716, 2012.

[164] D. Jakubczyk, G. Derkachov, M. Kolwas, and K. Kolwas, "Combining weighting and scatterometry: Application to a levitated droplet of suspension," *Journal of Quantitative Spectroscopy and Radiative Transfer*, vol. 126, pp. 99–104, Sept. 2013.

[165] M. J. Renn and R. Pastel, "Particle manipulation and surface patterning by laser guidance," *Journal of Vacuum Science & Technology B: Microelectronics and Nanometer Structures Processing, Measurement, and Phenomena*, vol. 16, pp. 3859–3863, Nov. 1998. Publisher: American Institute of Physics.

[166] D. Caviezel, C. Narayanan, and D. Lakehal, "Adherence and bouncing of liquid droplets impacting on dry surfaces," *Microfluidics and Nanofluidics*, vol. 5, pp. 469–478, Oct. 2008.

[167] D. A. Bolleddula, A. Berchielli, and A. Aliseda, "Impact of a heterogeneous liquid droplet on a dry surface: Application to the pharmaceutical industry," *Advances in Colloid and Interface Science*, vol. 159, pp. 144–159, Sept. 2010.

[168] O. A. Schmidt, M. K. Garbos, T. G. Euser, and P. S. J. Russell, "Reconfigurable Optothermal Microparticle Trap in Air-Filled Hollow-Core Photonic Crystal Fiber," *Physical Review Letters*, vol. 109, p. 024502, July 2012. Publisher: American Physical Society.

[169] J. Hwang, D. Choi, S. Han, S. Y. Jung, J. Choi, and J. Hong, "Potential toxicity of polystyrene microplastic particles," *Scientific Reports*, vol. 10, p. 7391, Apr. 2020. Number: 1 Publisher: Nature Publishing Group.

[170] O. A. Schmidt, M. K. Garbos, T. G. Euser, and P. S. J. Russell, "Metrology of laser-guided particles in air-filled hollow-core photonic crystal fiber," *Optics Letters*, vol. 37, pp. 91–93, Jan. 2012.

[171] K. Rodriguez, "Wayback Machine," 2010.

[172] R. Zeltner, R. Pennetta, S. Xie, and P. S. J. Russell, "Flying particle microlaser and temperature sensor in hollow-core photonic crystal fiber," *Optics Letters*, vol. 43, pp. 1479–1482, Apr. 2018. Publisher: Optical Society of America.

[173] S. Rikimi, Y. Chen, T. W. Kelly, I. A. Davidson, G. T. Jasion, M. Partridge, K. Harrington, T. D. Bradley, A. A. Taranta, F. Poletti, M. N. Petrovich, D. J. Richardson, and N. V. Wheeler, "Internal Gas Composition and Pressure in As-drawn Hollow Core Optical Fibers," *Journal of Lightwave Technology*, vol. 40, pp. 4776–4785, July 2022. Conference Name: Journal of Lightwave Technology.

[174] P. Measor, S. Kühn, E. J. Lunt, B. S. Phillips, A. R. Hawkins, and H. Schmidt, "Hollow-core waveguide characterization by optically induced particle transport," *Optics Letters*, vol. 33, pp. 672–674, Apr. 2008. Publisher: Optical Society of America.

[175] H.-M. Tzeng, K. F. Wall, M. B. Long, and R. K. Chang, "Laser emission from individual droplets at wavelengths corresponding to morphology-dependent resonances," *Optics Letters*, vol. 9, pp. 499–501, Nov. 1984. Publisher: Optica Publishing Group.

[176] D. McGloin, "Droplet lasers: a review of current progress," *Reports on Progress in Physics*, vol. 80, no. 5, p. 054402, 2017. Publisher: IOP Publishing.

[177] D. Grass, J. Fesel, S. G. Hofer, N. Kiesel, and M. Aspelmeyer, "Optical trapping and control of nanoparticles inside evacuated hollow core photonic crystal fibers," *Applied Physics Letters*, vol. 108, p. 221103, May 2016.

[178] A. Vinante, C. Timberlake, and H. Ulbricht, "Levitated Micromagnets in Superconducting Traps: A New Platform for Tabletop Fundamental Physics Experiments," *Entropy*, vol. 24, p. 1642, Nov. 2022. Number: 11 Publisher: Multidisciplinary Digital Publishing Institute.

[179] S. E. R. Medaer, D. D. Francesca, E. N. Fokoua, F. Poletti, D. Ricci, B. Schmauss, A. Taranta, and I. Toccafondo, "Near-zero Radiation Induced Attenuation in Nested Anti-resonant Nodeless Hollow-core Fibers at 1550 nm," in *Optical Fiber Communication Conference (OFC) 2023 (2023), paper W4D.4*, p. W4D.4, Optica Publishing Group, Mar. 2023.

[180] M. N. Romodina, S. Xie, F. Tani, and P. S. J. Russell, "Backward jet propulsion of particles by femtosecond pulses in hollow-core photonic crystal fiber," *Optica*, vol. 9, pp. 268–272, Mar. 2022. Publisher: Optica Publishing Group.

[181] H. Pettersson, "Cosmic Spherules and Meteoritic Dust," *Scientific American*, vol. 202, no. 2, pp. 123–135, 1960. Publisher: Scientific American, a division of Nature America, Inc.

List of Publications

V. Zuba, H. C. H. Mulvad, R. Slavík, H. Sakr, F. Poletti, D. J. Richardson, and E. Numkam Fokoua, "Experimental Investigation into Optimum Laser Coupling Efficiency into Hollow-Core NANFs", Conference on Lasers and Electro-Optics (CLEO), Optica Publishing Group, SW4K.1, pp. 1-2, May 2022, doi: 10.1364/CLEO-SI.2022.SW4K.1

H. C. H. Mulvad, S. Abokhamis Mousavi, V. Zuba, L. Xu, H. Sakr, T. D. Bradley, J. R. Hayes, G. T. Jasion, E. Numkam Fokoua, A. Taranta, S.-U. Alam, D. J. Richardson, and F. Poletti, "Kilowatt-average-power single-mode laser light transmission over kilometre-scale hollow-core fibre", Nature Photonics, vol.16, pp. 448–453, May 2022, doi: 10.1038/s41566-022-01000-3

V. Zuba, H. C. H. Mulvad, R. Slavík, H. Sakr, F. Poletti, D. J. Richardson, and E. Numkam Fokoua, "Limits of Coupling Efficiency Into Hollow-Core Antiresonant Fibres", Journal of Lightwave Technology (JLT), vol. 41, no. 19, pp. 6374–6382, 2023, doi: 10.1109/JLT.2023.3279701